Kinetics of Biochemical Systems Analyzed by Numerical Simulations

Marek Kochańczyk

Doctoral thesis advisor:

Tomasz Lipniacki

Institute of Fundamental Technological Research,

Polish Academy of Sciences

Warsaw 2018

Contents

Abstract

Living cells process information about their internal state as well as environmental cues to make decisions on their physiological activity or epigenetic identity. Coordinated biochemical processes that enable informed cellular decision-making are (*i*) inherently stochastic, (*ii*) organized spatially within the cell, (*iii*) based on nonlinear regulatory elements, and often (*iv*) marked by combinatorial complexity. These immanent features of cell signaling should be considered both separately—to gain insight through application of mathematical methods—and simultaneously—to understand more realistic cellular milieu. While there are numerous studies in which these features are considered in isolation, construing and analyzing models that combine them is far less common. This thesis comprises results of studies of model cell signaling systems in which at least two of the above-mentioned features are considered simultaneously. The studies, published in seven research articles (listed separately), were performed by creating computational models and analyzing their properties by means of numerical simulations, in part with the use of an author-created software tool.

Intricate relations between spatial and stochastic phenomena were demonstrated in generic biochemical systems, either monostable or bistable, where only kinase, phosphatase, and substrate molecules were present. Results for such simplified systems, obtained by performing kinetic Monte Carlo simulations on the lattice, can be summarized as follows:

- In a monostable generic reaction cycle the membrane, an analytical formula was found that describes the dependence of the effective macroscopic reaction rate coefficients on the microscopic rate constants and effective (molecular crowding-dependent) diffusivity of reactants. The analytical result was confirmed to agree with numerical results of stochastic simulations on the lattice for a wide range of reactant concentrations and diffusivities.

- In a bistable system on the membrane it was demonstrated that a spontaneous onset of activity can be radically more probable in subdomains characterized by slower diffusion. A local immobilization of reactants may lead to global activation of membrane proteins by a mechanism that involves stochastic fluctuations followed by the propagation of a semi-deterministic traveling wave.

The software tool capable of performing on-lattice simulations of diffusing and reacting molecules, Spatkin , was developed in the form of a general-purpose simulator of reaction–diffusion systems, that works at the single-molecule resolution in two spatial dimensions. The tool can account for internal chemical states of molecules (to accommodate, *e.g.*, post-translational modifications), implementing so-called rule-based approach to modeling of biomolecular interactions.

Complex dynamics arising from multiple nonlinearities (intertwined negative and positive feedback loops) in conjunction with either stochasticity or/and spatial organization is studied in models of specific cell signaling systems: the NF-κB network controlling innate immune responses, p53 network involved in DNA damage response, and the ERK network responsible for growth factor signaling. Results for these systems, obtained mainly through Gillespie algorithm-based simulations of Markov chain models and numerical bifurcation analyses of their deterministic approximations, demonstrate that:

- In the NF-κB system, a positive feedback arising due to the autocrine regulation via TNFα is responsible for the existence of limit-cycle oscillations of nucleus-localized NF-κB in non-stimulated wild-type cells and for bistability in cells that lack an NF-κB inhibitor, A20: wild-type cells characterized by high secretion of TNFα or high expression of its receptor exhibit sustained nuclear NF-κB oscillations, which may start spontaneously due to stochastic fluctuations, whereas A20-deficient cells exhibit long-lasting NF-κB activation in response to a short-pulsed TNFα stimulation, even at low TNFα expression.

- At the conditions of persistent DNA damage, the dynamical structure of the p53 core network allows for the coexistence of a stable limit cycle, associated with cell cycle arrest, and a stable steady state, characterized by a high level of a p53 phosphoform that induces apoptosis. The coexistence is possible because of a Neimark–Sacker bifurcation. The two solutions delineate distinct temporal core-system responses, that can be unambiguously interpreted by two subordinated bistable modules responsible for controlling cell cycle arrest and apoptosis.

- Experimentally observed pulses of phosphorylated ERK, of frequency that depends on the level of growth factor stimulation, can be explained within a computational model that exhibits relaxation oscillations. Detailed bifurcation analysis shows that particular regulatory roles can be associated with each considered feedback loop. Spatial modeling suggests that, in addition to time-scale separation, subcellular organization of feedback loops can be important for the mechanism of activation of growth factor signaling.

Overall, results contained in this thesis suggest that biochemical implementations of cellular decision-making mechanisms may tread a fine balance between stochastic and deterministic phenomena. Likely, cells need to actively maintain conditions that allow them to operate at such a boundary. Computational models of biological systems, created and analyzed from this perspective, explain how coupled nonlinear regulatory elements are capable of biochemical information processing in the presence of noise. The models are able to reproduce or predict the behavior of both "normal" cells and cells that are perturbed—as a result of application of molecular engineering techniques or due to an oncogenic transformation.

Streszczenie

Kinetyka układów biochemicznych
analizowana za pomocą symulacji numerycznych

Komórki organizmów żywych przetwarzają informacje dotyczące ich wewnętrznego stanu oraz bodźce pochodzące ze środowiska zewnętrznego, dzięki czemu mogą podejmować decyzje dotyczące swojej bieżącej aktywności fizjologicznej bądź, w dłuższej skali czasu, epigenetycznej tożsamości. Skoordynowane procesy biochemiczne, które pozwalają na podejmowanie takich decyzji, są: (i) stochastyczne, (ii) zorganizowane przestrzennie w komórce, (iii) oparte na nieliniowych elementach regulacyjnych oraz często (iv) wykazują znaczną złożoność kombinatoryczną. Te własności komórkowych układów sygnalizacyjnych powinny być analizowane zarówno z osobna—umożliwiając zastosowanie metod matematycznych—jak i razem—aby zrozumieć realistyczne uwarunkowania mechanizmów zaangażowanych w przetwarzanie sygnałów w komórce. Wymienionym własnościom rozważanym z osobna poświęcono wiele prac, natomiast łączne ujęcia tychże są rzadsze. Niniejsza rozprawa zawiera wyniki analiz modeli komórkowych układów sygnalizacyjnych, w których uwzględnione zostały co najmniej dwie spośród wyżej wymienionych własności. Opublikowane w siedmiu artykułach badania przeprowadzono tworząc modele obliczeniowe i badając ich własności za pomocą symulacji numerycznych z wykorzystaniem oprogramowania skonstruowanego przez autora.

Współzależność zjawisk stochastycznych i przestrzennych została przeanalizowana w uogólnionych modelach jedno- i dwustabilnych układów biochemicznych, w których dla uproszczenia występują jedynie kinazy, fosfatazy oraz ich substraty. Badając takie układy z wykorzystaniem metody kinetycznego Monte Carlo na sieci pokazano, że:

- Dla cyklu reakcji na błonie, mającego jeden stan stabilny, można analitycznie opisać zależność makroskopowych współczynników temp reakcji od współczynników mikroskopowych i efektywnych (zależnych od zatłoczenia molekularnego) współczynników dyfuzji reagentów, a otrzymany wynik analityczny jest zgodny z wynikami symulacji dla szerokiego zakresu stężeń i współczynników dyfuzji reagentów.

- W dwustabilnym układzie reakcji na błonie komórkowej samoczynna aktywacja jest bardziej prawdopodobna w obszarach reaktora charakteryzujących się wolniejszą dyfuzją. Lokalne unieruchomienie reagentów może prowadzić do aktywacji całego reaktora z użyciem mechanizmu, w którym lokalna aktywacja wynikająca ze stochastycznej fluktuacji daje początek propagującej się semi-deterministycznie fali biegnącej.

Narzędzie numeryczne do prowadzenia symulacji dyfundujących na sieci i reagujących cząsteczek przygotowano w postaci programu komputerowego SPATKIN pozwalającego na symulację dowolnych układów reakcji–dyfuzji z jednocząsteczkową rozdzielczością. Narzędzie uwzględnia stan wewnętrzny cząsteczek (np. modyfikacje potranslacyjne), implementując tzw. modelowanie oparte na regułach (ang. rule-based modeling).

Złożona nieliniowa dynamika regulowana działaniem wielu pętli sprzężeń zwrotnych dodatnich i ujemnych w połączeniu ze stochastycznością i/albo przestrzenną organizacją była przedmiotem badań prowadzonych na modelach trzech biologicznie istotnych sieci sygnalizacyjnych kontrolujących odpowiedź na stres: sieci kluczowego dla wrodzonej odpowiedzi odpornościowej czynnika transkrypcyjnego NF-κB, sieci czynnika transkrypcyjnego p53 zaangażowanego w odpowiedź na uszkodzenie DNA, oraz kaskady kinaz aktywującej ERK pod wpływem czynników wzrostu. Symulacje stochastyczne w postaci łańcuchów Markowa przeprowadzone według algorytmu Gillespiego oraz numeryczne analizy bifurkacyjne ich deterministycznych przybliżeń pokazały, że:

- Sprzężenie zwrotne dodatnie wynikające z autokrynnej stymulacji poprzez TNFα jest odpowiedzialne za oscylacje (cykl graniczny) jądrowej frakcji NF-κB w niestymulowanych komórkach typu dzikiego oraz za dwustabilność w komórkach pozbawionych A20 – inhibitora NF-κB. Komórki typu dzikiego o wysokim poziomie ekspresji TNFα lub jego receptora wykazują niegasnące oscylacje jądrowej frakcji NF-κB, które mogą być zainicjowane wskutek stochastycznej fluktuacji; komórki pozbawione A20 w odpowiedzi na krótką pulsową stymulację TNFα wykazują długotrwałą aktywację NF-κB, nawet gdy poziom ekspresji TNFα jest niski.

- W warunkach trwałego uszkodzenia DNA dynamiczna struktura sieci regulatorowej p53 wykazuje współistnienie stabilnego cyklu granicznego, istotnego dla fosfoformy p53 indukującej wstrzymanie cyklu komórkowego, oraz stabilnego stanu stacjonarnego, w którym wysoki poziom osiąga fosfoforma p53 indukująca apoptozę. Oba rozwiązania, których współistnienie umożliwia bifurkacja Neimarka–Sackera, wyznaczają odmienne w czasie odpowiedzi układu, które są jednoznacznie interpretowane przez dwa podporządkowane moduły kontrolujące wstrzymanie cyklu komórkowego i apoptozę.

- Pokazano, że eksperymentalnie obserwowane pulsy aktywności kinazy ERK, o częstotliwości zależnej od poziomu stymulacji czynnikiem wzrostu, można wyjaśnić w ramach modelu wykazującego relaksacyjne oscylacje. Przeprowadzając analizę bifurkacyjną, przypisano znaczenie dla dynamiki aktywacji ERK każdemu sprzężeniu zwrotnemu, które zostało uwzględnione w modelu. Dodatkowo modelowanie przestrzenne wykazało, że subkomórkowa organizacja sprzężeń może mieć znaczenie dla mechanizmu aktywacji rozważanej ścieżki.

Uzyskane wyniki sugerują, że komórkowe mechanizmy podejmowania decyzji działają na pograniczu zjawisk stochastycznych i deterministycznych. W komórce pogranicze to istotnie zależy od—i prawdopodobnie może być kontrolowane przez—określone warunki biofizyczne. Osadzone w tym kontekście obliczeniowe modele układów biologicznych wyjaśniają, jak sprzężone, nieliniowe elementy regulacyjne mogą w obecności szumu molekularnego przetwarzać informację biochemiczną, pozwalając zrozumieć zachowanie komórek zarówno „normalnych", jak i zmodyfikowanych przez zastosowanie metod inżynierii molekularnej bądź wskutek transformacji nowotworowej.

Structure of the thesis

This thesis consists of the following seven original articles:

A **Stochastic transitions in a bistable reaction system on the membrane**
Kochańczyk M, Jaruszewicz J, Lipniacki T[@]
Journal of the Royal Society Interface **10**, 20130151 (2013)   Impact Factor 2013: 3.856

B **Effective reaction rates in diffusion-limited phosphorylation–dephosphorylation cycles**
Szymańska P[⊙], Kochańczyk M[⊙], Miękisz J, Lipniacki T[@]
Physical Review E, **91**, 022702 (2015)   Impact Factor 2015: 2.252

C **Effective reaction rates for diffusion-limited reaction cycles**
Nałęcz-Jawecki P, Szymańska P, Kochańczyk M, Miękisz J, Lipniacki T[@]
The Journal of Chemical Physics **143**, 215102 (2015)   Impact Factor 2015: 2.894

D **SPATKIN: a simulator for rule-based modeling of biomolecular site dynamics on surfaces**
Kochańczyk M,[@] Hlavacek WS, Lipniacki T
Bioinformatics **33**, 3667–3669 (2017)   Impact Factor 2016: 7.307

E **Spontaneous NF-κB activation by autocrine TNFα signaling: A computational analysis**
Pękalski J, Zuk PJ, Kochańczyk M, Junkin M, Kellog R, Tay S, Lipniacki T[@]
PLOS One **8**, e78887 (2013)   Impact Factor 2013: 3.534

F **Feedbacks, bifurcations, and cell fate decision-making in the p53 system**
Hat B[⊙], Kochańczyk M[⊙], Bogdał MN, Lipniacki T[@]
PLOS Computational Biology **12**, e1004787 (2016)   Impact Factor 2016: 4.542

G **Relaxation oscillations and hierarchy of feedbacks in MAPK signaling**
Kochańczyk M,[@] Kocieniewski P, Kozłowska E, Jaruszewicz-Błońska J, Sparta B, Pargett M, Albeck JG, Hlavacek WS, Lipniacki T[@]
Scientific Reports **6**, 38244 (2017)   Impact Factor 2016: 4.259

All spatial kinetic Monte Carlo simulations of generic systems, described in articles A, B, C, were performed with an author-created software tool described in article D. In articles E, F, G, computational models of specific regulatory systems are formulated and analyzed.

Full-text articles along with supplementary materials are provided in Section 6.
Signed declarations of author contributions are provided in Section 7.

Impact Factors are given for the year of publication according to the Journal Citation Reports. For recent publications, the latest available values are given.

[⊙] Co-first authors.
[@] Corresponding author.

The author of this thesis has authored or co-authored several other original research articles *not* included in the thesis:

- **Cell fate in antiviral response arises in the crosstalk of IRF, NF-κB and JAK/STAT pathways**
  Czerkies M, Korwek Z, Prus W, Kochańczyk M, Jaruszewicz-Błońska J, Tudelska K, Błoński S, Kimmel M, Brasier AR, Lipniacki T
  Nature Communications **9**, 493 (2018)　　　　　　　Impact Factor 2016: 12.124

- **Information processing in the NF-κB pathway**
  Tudelska K, Markiewicz J, Kochańczyk M, Czerkies M, Prus W, Korwek Z, Abdi A, Błoński S, Kaźmierczak B, Lipniacki T
  Scientific Reports **7**, 15926 (2017)　　　　　　　Impact Factor 2016: 4.259

- **RAF1/BRAF dimerization integrates the signal from RAS to ERK and ROKα**
  Varga A, Ehrenreiter K, Aschenbrenner B, Kocieniewski P, Kochanczyk M, Lipniacki T, Baccarini M
  Science Signaling **10**, eaai8482 (2017)　　　　　　Impact Factor 2016: 6.830

- **Importins promote high-frequency NF-κB oscillations increasing information channel capacity**
  Korwek Z, Tudelska K, Nałęcz-Jawecki P, Czerkies M, Prus W, Markiewicz J, Kochańczyk M, Lipniacki T
  Biology Direct **11**, 61 (2016)　　　　　　　　　Impact Factor 2016: 2.856

- **A mathematical model of bimodal epigenetic control of miR-193a in ovarian cancer stem cells**
  Cheng FHC, Aguda BD, Tsai J-C, Kochańczyk M, Lin JMJ, Chen GCW, Lai H-C, Nephew KP, Hwang T-W, Chan MWY
  PLOS One **9**, e116050 (2014)　　　　　　　　　Impact Factor 2014: 3.234

- **Levels of pro-apoptotic regulator Bad and anti-apoptotic regulator Bcl-x$_L$ determine the type of the apoptotic logic gate**
  Bogdał MN, Hat B, Kochańczyk M, Lipniacki T
  BMC Systems Biology **7**, 67 (2013)　　　　　　　Impact Factor 2013: 2.853

- **Dynamics of a stochastic spatially extended system predicted by comparing deterministic and stochastic attractors of the corresponding birth–death process**
  Żuk PJ, Kochańczyk M, Jaruszewicz J, Bednorz W, Lipniacki T
  Physical Biology **5**, 055002 (2012)　　　　　　　Impact Factor 2012: 2.620

- **Prediction of functionally important residues in globular proteins from unusual central distances of amino acids**
  Kochańczyk M
  BMC Structural Biology **11**, 34 (2011)　　　　　　Impact Factor 2011: 2.476

- **In silico structural study of random amino acid sequence proteins not present in nature**
  Prymula K, Piwowar M, Kochańczyk M, Flis L, Malawski M, Szepieniec T, Evangelista G, Minervini G, Polticelli F, Wiśniowski Z, Sałapa K, Matczyńska E, Roterman I
  Chemistry & Biodiversity **6**, 2311–36 (2009)　　　Impact Factor 2009: 1.926

- **Prediction of functional sites based on the fuzzy oil drop model**
  Bryliński M, Prymula K, Jurkowski W, Kochańczyk M, Stawowczyk E, Konieczny L, Roterman I
  PLoS Computational Biology **3**, e94 (2007)　　　　Impact Factor 2007: 6.236

- **Localization of ligand binding site in proteins identified in silico**
  Bryliński M, Kochańczyk M, Broniatowska E, Roterman I
  Journal of Molecular Modeling **13**, 665–75 (2007)　　Impact Factor 2007: 1.669

1   Motivation

The phenomenon of life eludes a simple definition but undeniably and crucially relies on multiple tightly coupled biochemical processes.[1] These processes take place in cells—highly structured and dynamic biochemical reactors that take up resources from the environment and cooperate in order to survive and proliferate.[2] Cells are required to properly interpret and robustly respond to specific biochemical signals in fluctuating external conditions. Cellular information processing and decision making may affect current metabolic activity of the cell or alter its gene expression profile, having consequences at multiple scales in time and space.[3]

The repertoire of possible physiological responses or developmental paths appear to be limited to a predefined set of "programs". The most clear examples are dichotomous survival strategies of unicellular organisms[4] and diverse epigenetic identities of differentiated cells of multicellular organisms.[5] In mathematical terms, these "programs" can be associated with attractors of a dynamical system. The sole dynamical structure of a system of biochemical reactions does not fully prescribe its behavior, because particular properties of the intracellular milieu[6] impose a strong impact on biochemical processes occurring therein: the influence of randomness, inherent in chemical reactions, is often amplified by a relatively small number of reacting molecules; diffusive transport is hindered by fibrillar and membranous obstacles; cooperativity and saturation, not to mention feedback loops, render biochemical kinetics non-linear.

These properties, described in more detail in the Background section, have to be reflected in mathematical models of cellular processes. Only then can they reproduce the rich repertoire of, sometimes illusively chaotic, cell behaviors that are observed in experiments. For instance, commitment to and persistence in a given "program" may be analyzed in terms of (noise-induced) transitions between respective attractor basins.[7] Development of models of cell signaling systems with a strong support from experimental data has been enabled by recent progress in experimental single-cell techniques,[8] such as digital polymerase chain reaction, fluorescence-activated cell sorting, microfluidic cell cultures, and, probably most importantly, fluorescence microscopy which, when applied to live cells with fluorescently tagged molecules, can provide a wealth of temporal and spatial data, and to a great extent capture heterogeneity of cell populations.

---

[1]Berg J. *et al.*, *Biochemistry*, 8th ed. (Macmillan Learning, London, England, 2015).
[2]Alberts B. *et al.*, *Molecular Biology of the Cell*, 6th ed. (Garland Science, New York, USA, 2014).
[3]Lim W. *et al.*, *Cell Signaling: Principles and Mechanisms* (Garland Science, New York, USA, 2014).
[4]Ptashne M., *A Genetic Switch: Phage Lambda Revisited* (Cold Spring Harbor Laboratory Press, USA, 2004).
[5]Lang A. H. *et al.* (2014) *PLOS Comput. Biol.* **10**, e1003734.
[6]Phillips R. *et al.*, *Physical Biology of the Cell*, 2nd ed. (Garland Science, New York, USA, 2012).
[7]Choi M. *et al.* (2012) *Sci. Signal.* **5**, ra83.
[8]Lindström S. & Andersson-Svahn H., eds., *Single-Cell Analysis* (Humana Press, New York, USA, 2012).

Data originating from such cell-biology experiments are more and more of quantitative character, supporting the stance from which biology is viewed as the "mathematics' new physics."[9] The multitude and diversity of biomolecules and vastness of the network of their interactions, however, rule out direct application of traditional analytical approaches. Even when, under some assumptions, analytical methods are applicable, they need to be confronted with results of computer simulations (that may be free of some of these assumptions). Computer simulations can also utilize exactly solvable microscopic models in order to calibrate more coarse-grained simulational approaches (similarly as quantum mechanical calculations can be used to parameterize classical mechanical force fields pervasive in molecular dynamics simulations). A multi-resolution "computational microscope" appears to be an ideal tool to move across spatial and temporal scales of biological organization. Phenomenological computational models are an indispensable and convenient vehicle to integrate and concisely summarize the affluence of data—to the extent that biology, if desired to be seen, akin to physics, from a generalized, systems perspective, probably can only be computational.

Models in systems biology are solutions to inverse problems—educated guesses on the structure and time scales of a regulatory network given its experimentally observed behavior. Viewed as executable metaphors that propose and put to test specific design principles, computational models and associated numerical methods help also to understand fundamental biophysical principles and emergent phenomena underlying the workings of the cell. Useful models not only quantitatively describe observations but also offer predictions, although the border between the two is often blurred. High descriptive or predictive power of computational models of the key regulatory networks make them relevant for understanding from the systems perspective the roots of pathological cell malfunction[10] and multimodal impact of therapeutic agents,[11] raising hopes to contribute to strengthening the available medical armamentarium.[12,13]

[9]Cohen J. E. (2004) *PLoS Biol.* **2**, e439.
[10]Huang S. *et al*. (2009) *Semin. Cell Dev. Biol.* **20**, 869–876.
[11]Arrell D. K. & Terzic A. (2010) *Clin. Pharmacol. Ther.* **88**, 120–125.
[12]Ideker T. & Sharan R. (2008) *Genome Res.* **18**, 644–652.
[13]Wolkenhauer O. *et al*. (2013) *Pediatr. Res.* **73**, 502–507.

2 Background

2.1 Molecular noise

Biochemical processes have an inextricable stochastic component, referred to as the *intrinsic noise*, that results from randomness of diffusive collisions of biomolecules and from their discreteness. When the copy numbers of biomolecules per cell are low, relative changes of their abundance, resulting from randomness in their production and degradation, can be significant. Since the copy numbers of genes are usually as low as 1 or 2, gene activation is notoriously noisy.[14, 15] Messenger RNA is reported to be produced in random bursts[16] of varying magnitude.[17] In populations of cells, intrinsic noise is sufficient to introduce phenotypic heterogeneity.[18] In the presence of nonlinear response to signal, intrinsic noise is predicted to be able to increase system sensitivity by means of *stochastic focusing*.[19, 20]

Ambient sources of uncertainty, that affect cellular processes of interest in a random manner, in the form of fluctuations of environmental conditions and variability of the intracellular state, are collectively termed *extrinsic noise*.[21] The extrinsic differences among cells result primarily from uneven distribution of proteins, molecular machines, and organelles upon cell division.[22] Dual reporter studies suggest that the intrinsic and extrinsic contributions to non-genetic cell variability can be considered to a some extent independently.[23, 24, 25]

Although molecular noise imposes stringent limits on the accuracy of sensing by single cells,[26, 27, 28] at the level of the whole cell population the noise-generated phenotypic heterogeneity may turn out advantageous in the case when external conditions change.[29, 30]

[14] Novick A. & Weiner M. (1957) *Proc. Natl Acad. Sci. USA* **43**, 553–566.

[15] McAdams H. H. & Arkin A. (1999) *Trends Genet.* **15**, 65–69.

[16] Raj A. *et al.* (2006) *PLoS Biol.* **4**, e309.

[17] Suter D. M. *et al.* (2011) *Science* **332**, 472–474.

[18] Spudich J. L. & Koshland D. E. (1976) *Nature* **262**, 467–471.

[19] Harton M. D. & Batchelor E. (2017) *J. Mol. Biol.* **429**, 1143–1154.

[20] Paulsson J. *et al.* (2000) *Proc. Natl Acad. Sci. USA* **97**, 7148–7153.

[21] Newman J. R. S. *et al.* (2006) *Nature* **441**, 840–846.

[22] Huh D. & Paulsson J. (2011) *Nat. Genet.* **43**, 95–100.

[23] Elowitz M. B. *et al.* (2002) *Science* **297**, 1183–1186.

[24] Swain P. S. *et al.* (2002) *Proc. Natl Acad. Sci. USA* **99**, 12795–12800.

[25] Hilfinger A. & Paulsson J. (2011) *Proc. Natl Acad. Sci. USA* **108**, 12167–12172.

[26] Bialek W. & Setayeshgar S. (2005) *Proc. Natl Acad. Sci. USA* **102**, 10040–10045.

[27] Suderman R. *et al.* (2017) *Proc. Natl Acad. Sci. USA* **114**, 5755–5760.

[28] Tudelska K. *et al.* (2017) *Sci. Rep.* **7**, 15926.

[29] Balaban N. Q. *et al.* (2004) *Science* **305**, 1622–1625.

[30] Thattai M. & van Oudenaarden A. (2004) *Genetics* **167**, 523–530.

2.2 Spatial organization of cell signaling

Specificity of interacting molecules is augmented by intricacies of subcellular structures that localize and spatially organize components of biochemical systems. Spatial segregation or confinement of biomolecules is a simple mean of attaining modularity and limiting crosstalk. Most straightforwardly, the cell is compartmentalized into cytoplasm and nucleus, and delimited by the plasma membrane. Cells have to select, preprocess and convey relevant messages—such as the presence of a cytokine or presentation of a protein on the surface of a neighboring cell— from outside to cell interior so that a subsequent chain of events can adjust current cell behavior or, on a longer time scale, modulate gene expression.[31]

Signaling through many pathways is initiated at the plasma membrane[32] upon ligand binding by receptors that subsequently multimerize and self-activate by trans-autophosphorylation or conformational changes.[33] The number of receptors per cluster[34] and the number of clusters that need to be formed to induce a fully-fledged cell response can be very low.[35] Slow diffusion of membrane proteins (of order of $0.1\,\mu m^2 s^{-1}$, which is in turn at least an order of magnitude lower than in the cytosol[36]) and their partitioning into semi-permeable submicron-sized membrane regions[37] cause that membrane receptors and their clusters work virtually in isolation, enhancing noise at the initial stages of signal transduction.[38] Estimation of the fidelity of measuring the concentration of a chemoattractant by (individual) membrane receptors has been the subject of a seminal 1970s paper by Berg & Purcell.[39] Biochemical reactions on the plasma membrane are expected to be *diffusion-limited* and also strongly influenced by the presence of chemically inert, but sometimes non-specifically interacting, molecular "crowders".[40] These effects are significant due to the essentially two-dimensional geometry of the membrane and the fact that as much as nearly half of the membrane surface area is occupied by proteins.[41]

To relay the signal to the cell interior, activated membrane receptors recruit specialized cytoplasmic adaptor proteins.[42] These adaptors subsequently recruit cytoplasmic messengers that get activated, usually through phosphorylation, and after unbinding leave diffusively the membrane-proximal zone. Their activity can be quenched by cytosolic phosphatases,

[31]Kholodenko B. N. *et al*. (2010) *Nat. Rev. Mol. Cell. Biol.* **11**, 414–426.
[32]Grecco H. E. *et al*. (2011) *Cell* **144**, 897–909.
[33]Lemmon M. A. & Schlessinger J. (2010) *Cell* **141**, 1117–1134.
[34]Clayton A. H. A. *et al*. (2005) *J. Biol. Chem.* **280**, 30392–30399.
[35]Tay S. *et al*. (2010) *Nature* **466**, 267–271.
[36]Frick M. *et al*. (2007) *Curr. Biol.* **17**, 462–467.
[37]Kusumi A. *et al*. (2005) *Annu. Rev. Biophys. Biomol. Struct.* **34**, 351–378.
[38]Ladbury J. E. & Arold S. T. (2012) *Trends Biochem. Sci.* **37**, 173–178.
[39]Berg H. C. & Purcell E. M. (1977) *Biophys. J.* **20**, 193–219.
[40]Zhou H.-X. (2009) *J. Phys. Chem. B* **113**, 7995–8005.
[41]Lindén M. *et al*. (2012) *PLoS Comput. Biol.* **8**, e1002431.
[42]Kholodenko B. N. *et al*. (2000) *Trends Cell Biol.* **10**, 173–178.

generating a *gradient* of phosphorylated substrate, that extends into the cytoplasm.[43] It is worth to remind that when a biochemical signal is propagated diffusively, its magnitude is damped over time and its spatial range scales as the square root of time. To mitigate both these limitations, in the presence of a positive feedback the signal can be propagated with a non-decreasing strength and constant velocity by means of a chemical *traveling wave*[44] (resembling the calcium wave that is initiated at the sperm entry point and spreads across the fertilized egg). Detailed spatial aspects of the cell signaling mechanisms that underlie the processes of cell motility and migration reckon the directional character of external cues.[45]

If, ultimately, gene expression is to be affected, to enter the nucleus, transcription factors either need to be post-translationally modified to undergo a conformational rearrangement, exposing a sequence called nuclear localization signal (NLS), or have to be released from inhibitors that sequester them in the cytoplasm by covering NLS, or have to bind to a protein that contains NLS. After transcription factors are imported to the nucleus and enhance or repress expression of specific genes, they can be shepherded back to the cytoplasm by exposing their own nuclear export signal (NES) or through complexation with an NES-endowed partner.[46] The mechanisms of nuclear import and export are often coupled, giving rise to an oscillatory *nucleocytoplasmic shuttling*, readily observable in live-cell imaging experiments.[47]

2.3   Combinatorial complexity in cell signaling

The state of a signaling system is encoded in protein covalent post-translational modifications.[48] The most common modifications involved in signaling are phosphorylation (possible on serine, threonine and tyrosine residues) and, to a lesser extent, ubiquitylation and acetylation (both possible on lysine residues).[49] Phosphorylation, catalyzed by kinases, is predominantly associated with activation, wheres dephosphorylation, by phosphatases, with the loss of activity. Interestingly, substrates of kinases can themselves be kinases that become activated after phosphorylation.[50] Such multi-level *kinase cascades* are considered to be potent cellular signal amplification devices.

Most proteins consist of multiple domains, and domains may contain multiple phosphorylatable sites.[51] *Multisite phosphorylation* can occur independently on each residue or follow

[43]Niethammer P. *et al*. (2004) *Science* **303**, 1862–1866.
[44]Gelens L. *et al*. (2014) *Mol. Biol. Cell* **25**, 3486–3493.
[45]Parent C. A. & Devreotes P. N. (1999) *Science* **284**, 765–770.
[46]Görlich D. & Kutay U. (1999) *Annu. Rev. Cell Dev. Biol.* **15**, 607–660.
[47]Carlotti F. *et al*. (2000) *J. Biol. Chem.* **275**, 41028–41034.
[48]Deribe Y. L. *et al*. (2010) *Nat. Struct. Mol. Biol.* **17**, 666–672.
[49]Derouiche A. *et al*. (2012) *Curr. Opin. Biotechnol.* **23**, 585–590.
[50]Lewis T. S. *et al*. (1998) *Adv. Cancer Res.* **74**, 49–139.
[51]Holmberg C. I. *et al*. (2002) *Trends Biochem. Sci.* **27**, 619–627.

a well-defined order.[52] In some systems—when a kinase is able to confer phosphate groups to multiple residues at a single encounter—multisite phosphorylation can be processive,[53] in others—when the residues get phosphorylated upon multiple encounters—distributive;[54] the exact mode can depend on kinase concentration[55] as well as specificity and the relation of diffusivity to the phosphorylation and dephosphorylation reaction rates.[56]

For a protein with multiple phosphorylation sites (say, n), the number of possible states of phosphorylation can be very large (2^n). This *combinatorial complexity* is further aggravated when such multi-site proteins form complexes[57] [for a dimer, the number of possible states is $(2^n)^2$]. Another layer of conceptual complexity is caused by the coexistence of isoforms (paralogs or splice variants) whose similarity and redundancy may turn out elusive.[58] Combinatorial complexity cannot be avoided in characterization of signaling networks because specific patterns of post-translational modifications may exert distinct impact on protein activity, stability, intracellular localization, and, crucially for the cell signaling networks, protein interactions and binding affinity.[59]

An established strategy to concisely represent systems marked by combinatorial complexity is the *rule-based* approach,[60] in which molecules are represented as objects that hold internal information about covalent modifications, discrete conformational states, and bound partners. Reactions that can occur between such objects are expressed in terms of local rules, that specify only the partial information about reacting objects that is relevant for a given reaction or class of reactions (assuming in this way that a given chemical reaction or class of reactions can occur independently of the state that is not specified in the rule). A review by Chylek *et al.* (2014)[61] provides a comprehensive introduction to the fundamental concepts of rule-based modeling as well as a guide to the standards-setting software tool in this area, BioNetGen.

2.4   Nonlinear regulatory elements

Various signaling networks appear to contain analogous elementary regulatory modules and recurrent interaction motifs. It is desirable to know how they work in isolation (and in somewhat abstract terms, independent of the concrete network) to gain intuition and then be able

---

[52] Posada J. & Cooper J. A. (1992) *Science* **255**, 212–215.

[53] Aoki K. *et al.* (2011) *Proc. Natl Acad. Sci. USA* **108**, 12675–12680.

[54] Gunawardena J. (2007) *Biophys. J.* **93**, 3828–3834.

[55] Ferrell J. E. & Bhatt R. R. (1997) *J. Biol. Chem.* **272**, 19008–19016.

[56] Dushek O. *et al.* (2011) *Biophys. J.* **100**, 1189–1197.

[57] Hlavacek W. S. *et al.* (2003) *Biotechnol. Bioeng.* **84**, 783–794.

[58] Desideri E. *et al.* (2015) *Cell* **161**, 967–970.

[59] Kuriyan J. & Cowburn D. (1997) *Annu. Rev. Biophys. Biomol. Struct.* **26**, 259–288.

[60] Faeder J. R. *et al.* (2009) *Methods Mol. Biol.* **500**, 113–167.

[61] Chylek L. A. *et al.* (2014) *Wiley Interdiscip. Rev. Syst. Biol. Med.* **6**, 13–36.

to understand their role in complete (and concrete) signaling networks.

To gain full enzymatic activity, some kinases that participate in kinase cascades require bisphosphorylation.[62] Kinases for which monophosphorylation is not sufficient to relay the signal allow the cascade to filter weak signals and noise.[63] Due to the requirement of double phosphorylation across the consecutive levels of the pathway and phosphorylation level-dependent enzymatic activity, kinase cascades are capable of highly nonlinear amplification of perceptible signals, akin to activation of a highly cooperative enzyme.[64,65] Such *ultrasensitive* response can be promoted by other mechanisms such as positive feedback,[66] competition,[67] or *saturation* ("zero-order ultrasensitivity") that occurs when two molecules bind with high affinity and a surplus of molecules of one kind causes that nearly all molecules of the other kind are sequestered. Free molecules of the latter kind appear when their overall abundance surpasses the abundance of the sequestering molecules (which is often achieved by a rapid degradation of the sequestering molecules).

Positive feedbacks, often implicated in thresholding and amplifying the input signal at the initial steps of signaling pathways,[68] may give rise to bistability, that is, coexistence of two stable stationary states.[69] Bistable systems are archetypal models of binary cellular decision-making mechanisms that assign to an input signal one of two predefined responses ("on" or "off"). When the two stable steady states coexist for intermediate levels of the input signal, the system may exhibit hysteresis ("reversible bistability") for an input signal that varies within its full dynamic range. When the two stable steady states coexist for small (large) signal inputs, the system may be locked in the on-state (off-state) even when the input signal becomes very low (very large; "irreversible bistability").[70]

Spontaneous transitions between the (meta)stable states of bistable systems are enabled by noise[71] (and, of note, some systems are observed to be effectively bistable only in the presence of noise[72]). The behavior of spatial, stochastic bistable systems depends on reactor dimensionality.[73] Multisite phosphorylation[74] or positive feedback[75] may give rise to ultrasensitivity on the plasma membrane. In spatially extended domains, bistable reaction–diffusion

[62]Anderson N. G. *et al.* (1990) *Nature* **343**, 651–653.
[63]Hooshangi S. *et al.* (2005) *Proc. Natl Acad. Sci. USA* **102**, 3581–3586.
[64]Goldbeter A. & Koshland D. E. (1981) *Proc. Natl Acad. Sci. USA* **78**, 6840–6844.
[65]Huang C. Y. & Ferrell J. E. (1996) *Proc. Natl Acad. Sci. USA* **93**, 10078–10083.
[66]Trunnell N. B. *et al.* (2011) *Mol. Cell* **41**, 263–274.
[67]Kim S. Y. & Ferrell J. E. (2007) *Cell* **128**, 1133–1145.
[68]Sparta B. *et al.* (2015) *J. Biol. Chem.* **290**, 24784–24792.
[69]Markevich N. I. *et al.* (2004) *J. Cell Biol.* **164**, 353–359.
[70]Xiong W. & Ferrell J. E. (2003) *Nature* **426**, 460–465.
[71]Blake W. J. *et al.* (2003) *Nature* **422**, 633–637.
[72]Samoilov M. *et al.* (2005) *Proc. Natl Acad. Sci. USA* **102**, 2310–2315.
[73]Elf J. & Ehrenberg M. (2004) *Syst. Biol.* **1**, 230–236.
[74]Dushek O. *et al.* (2011) *Biophys. J.* **100**, 1189–1197.
[75]Das J. *et al.* (2009) *J. Chem. Phys.* **130**, 245102.

systems admit traveling wave solutions.[76] Heteroclinic fronts of such chemical waves connect regions in which distinct stationary states dominate, and shift in space leading to the spread of one of the states, ultimately homogenizing the whole reactor. It has been proposed that in bistable kinase–phosphatase circuits, a traveling wave of phosphorylated substrates may propagate from the cell surface to its interior[77] (this should not be confused with an earlier-mentioned generation of a stationary gradient of phosphoproteins).

To turn off signaling or adapt to a constant signal, neglect fluctuations, and maintain general homeostasis, cellular processes are ubiquitously constrained with negative feedback loops.[78] Activated systems that employ negative feedbacks are able to reset, and thus respond in a pulse-like manner. When the negative feedback is delayed—usually due to transcription and translation—with respect to the signal that does not cease, the regulatory system may exhibit damped or sustained oscillations. Many, if not most, prokaryotic transcription factors are known to (directly or indirectly) self-repress;[79,80] two best known eukaryotic transcription factors that oscillate are NF-κB (nucleocytoplasmic shuttling[81]) and p53 (protein abundance in a cell[82]). Oscillatory responses may be sensitive to input signal in terms of either their amplitude or frequency. The effect depends on the type of bifurcation in which a closed orbit in the phase space is born, the most important types being supercritical Hopf, subcritical Hopf featured by a cyclic fold, and the saddle-node-on-invariant-circle (SNIC) bifurcation.[83] In Hopf points, limit cycles are born with zero amplitude and finite period, whereas in SNIC, limit cycles have infinite period and non-zero amplitude. Simplified diagrams of the phase space near the critical parameter values can be found, *e.g.*, in the article by Hat *et al.* (2009; figure 1).[84]

Systems with interlocked positive and negative feedback loops often exhibit rich nonlinear dynamical behavior that depends on network connectivity and characteristic time scales associated with the feedback loops. Three cases of such complex systems, relevant to the further described regulatory networks, are depicted in Scheme 1. When a positive feedback loop is embedded in a negative feedback loop and operates at a faster time scale than the negative feedback loop [Scheme 1, case (*i*)], the system can periodically switch between two predefined states (active/inactive) with a frequency that depends on the level of stimulation. Time profiles may consist of a fast activation phase and a phase of (often slow) relaxation to

[76] Keener J. & Sneyd J., *Mathematical Physiology* (Springer, New York, USA, 1998), pp. 268–298.

[77] Markevich N. I. *et al.* (2006) *Mol. Syst. Biol.* **2**, 61.

[78] Becskei A. & Serrano L. (2000) *Nature* **405**, 590–593.

[79] Keseler I. M. *et al.* (2005) *Nucleic Acids Res.* **33**, D334–D337.
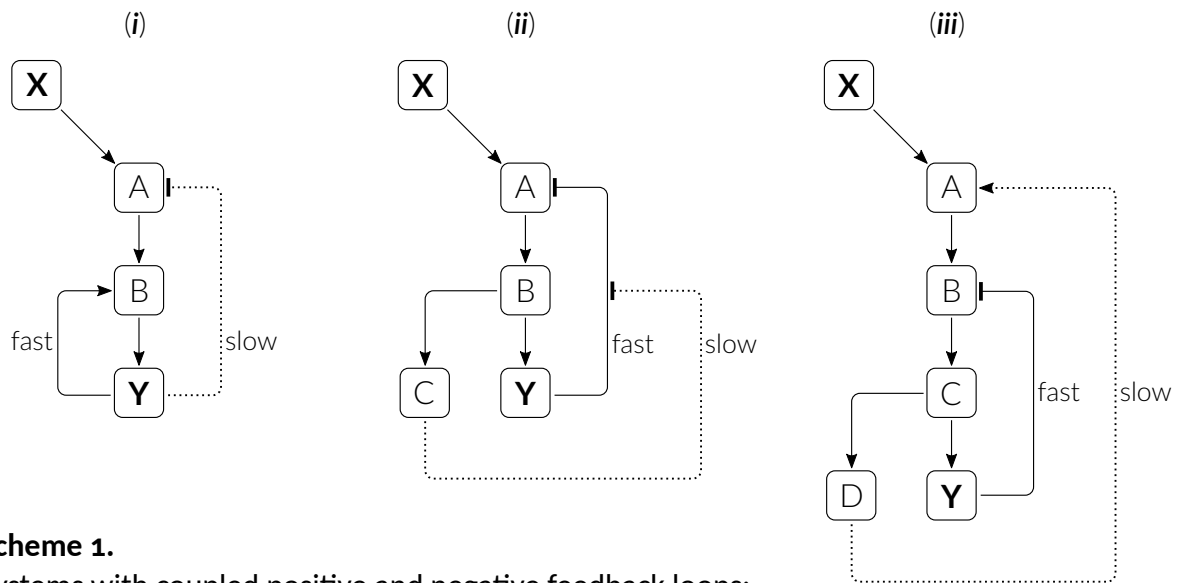
[80] Stekel D. J. & Jenkins D. J. (2008) *BMC Syst. Biol.* **2**, 6.

[81] Nelson D. E. *et al.* (2004) *Science* **306**, 704–708.

[82] Geva-Zatorsky N. *et al.* (2006) *Mol. Syst. Biol.* **2**, 2006.0033.

[83] Strogatz S., *Nonlinear Dynamics and Chaos*, 2nd ed. (Westview Press, Boulder, USA, 2015).

[84] Hat B. *et al.* (2009) *IET Syst. Biol.* **3**, 342–355.

Scheme 1.

Systems with coupled positive and negative feedback loops:
(***i***) fast positive feedback loop embedded in a relatively slower negative feedback loop,
(***ii***) slow positive feedback loop counteracts a relatively faster negative feedback loop,
(***iii***) fast negative feedback loop embedded in a relatively slow positive feedback loop.
In all panels, X – input, Y – output.

a state in which subsequent activation is possible, resembling time profiles of a *relaxation oscillator*. When a slow positive feedback loop turns off a relatively faster negative feedback [Scheme 1, case (***ii***)], after an input signal appears, the system exhibits oscillatory behavior. A short-lasting input signal does not activate the slow positive feedback loop, the system generates damped oscillations and returns to an initial state; a long-lasting input signal, however, can break the negative feedback loop so the system can switch to a state other than the initial one. When a fast negative feedback loop is embedded in a relatively slow (delayed) positive feedback loop [Scheme 1, case (***iii***)], the system initially triggered by a signal can oscillate autonomously (*i.e.*, when the signal ceases), and may generate relaxation oscillations.

In addition to feedbacks, regulation can be implemented with *feed-forward loops*. In the coherent-positive feed forward motif, two parallel paths of different time scales culminate in the same target. Since temporal coincidence of activation through both branches is required to relay the signal further, this mechanism, resembling the AND logic gate, can be used to generate responses to signals that last for a sufficiently long time.[85] Incoherent feed-forward loops (motifs that contain both positive and negative paths) may be used to generate a pulse-like response and achieve adaptation to the input signal.[86] The book by Alon (2006)[87] contains a complete classification of elementary signaling motifs.

[85] Mangan S. & Alon U. (2003) *Proc. Natl Acad. Sci. USA* **100**, 11980–11985.
[86] Ferrell J. E. (2016) *Cell Syst.* **2**, 62–67.
[87] Alon U., *An Introduction to Systems Biology* (Taylor & Francis, Abingdon-on-Thames, UK, 2006).

3   Objectives

The foundational assumption underlying the work presented in this thesis is that idealized computational models are instrumental in studying cellular biochemical processes. The detailed research objectives were as follows:

1. **Characterize the interplay between spatial and stochastic effects in a bistable reaction system on the membrane.** Mechanisms of transitions between both states of the bistable system and estimates of the associated mean first-passage times have been expected to depend on both the reactor volume and diffusion coefficients of reactants; these parameters jointly control the effective stochasticity by determining the size of subreactors, into which the membrane can be imaginably decomposed and in which molecules are diffusively well communicated. The transitions can be characterized by means of spatial stochastic simulations at the single-molecule resolution, that are able to capture both the intrinsic noise resulting from diffusion-limited molecule encounters and propagation of heteroclinic traveling fronts.

2. **Determine the effective macroscopic reaction rates in diffusion-limited reaction cycles on the membrane.** Chemical kinetics in a ubiquitous singling motif, in which the same phosphorylatable molecule can be a substrate for either kinases or phosphatases (depending on its current phosphostate), has been expected to depend in a non-trivial way on concentrations and microscopic reaction rates of both the enzymes and on the diffusion coefficient of all the reactants. Such prototypical system on the membrane can be simulated using the same approach as above.

3. **Develop a computer program for performing on-lattice kinetic Monte Carlo simulations in the form of a general-purpose tool.** The tool should simulate exactly the stochastic chemical kinetics in the form of a continuous-time Markov chain and, by implementing the rule-based approach, account for possible post-translational modifications and creation or disruption of macromolecular complexes. Such tool shall enable a user to define systems of biochemical reactions in a straightforward manner akin to conventions used in writing chemical reactions, and should make possible visualization of simulated spatial trajectories.

4. **Explain spontaneous oscillatory nuclear translocations of NF-κB.** Transcription factor NF-κB is a crucial player in the processes involved in innate immunity and the dynamics of its nucleocytoplasmic shuttling is known to impact gene expression patterns.[88]

---

[88]Zambrano S. *et al*. (2016) *eLife* **5**, e09100.

Model-based analysis has been expected to explain why in cells characterized by high secretion of TNFα and its receptor, NF-κB can exhibit spontaneous oscillations (of nuclear location), that can start spontaneously, *i.e.*, without an external cell stimulation.[89] Additionally, the model should provide an explanation to the fact that in cells that lack A20, an NF-κB inhibitor, even low TNFα expression can be sufficient for generating qualitatively different, non-oscillatory and sustained, NF-κB nuclear location in response to a short pulse of TNFα.[90]

5. **Explain why cancer cells known to have diverse expression levels of phosphatases Wip1 and PTEN exhibit a broad spectrum of p53 responses.** Arguably, the p53 network is the most important pathway involved in preventing carcinogenesis. Upon DNA damage, cellular abundance of p53 exhibits oscillatory dynamics[91] that leads to the cell cycle arrest; if the damaged DNA turns out to be irreparable, the level of p53 eventually rises, inducing apoptosis, controlled cell death.[92] The regulatory core of the p53 network is controlled by two negative feedback loops (one of which is regulated by Wip1) responsible for oscillations and two antagonistic positive feedback loops (regulated by Wip1 and PTEN) responsible for bistability. The objective was to understand from the dynamical systems point of view how switching from the limit cycle to the "apoptotic" steady state is achieved, allowing in this way for making an unanimous cell fate decision, and how it depends on the rates of expression of Wip1 and PTEN.

6. **Explain the mechanism of growth-factor dose-dependent oscillations of the phospho-ERK in the mammalian MAPK cascade.** Upon extracellular growth-factor stimulation, the signal is transmitted through a multi-tier cascade of mitogen-activated protein kinases (MAPKs) that results in ERK phosphorylation. Phospho-ERK is able to exhibit kinase activity and is a central activator of various regulatory proteins implicated in proliferation and differentiation. Very recently, it has been observed that the level of phospho-ERK in the cell can oscillate with a period that depends on the concentration of epidermal growth factor (EGF).[93] The aim was to formulate a model of MAPK signaling downstream of the EGF receptor to elucidate how interlinked feedback loops allow for the experimentally observed amplitude-to-frequency encoding.

[89]Turner D. A. *et al*. (2010) *J. Cell Sci.* **123**, 2834–2843.
[90]Werner S. L. *et al*. (2008) *Genes Dev.* **22**, 2093–2101.
[91]Batchelor E. *et al*. (2008) *Mol. Cell* **30**, 277–289.
[92]Purvis J. E. *et al*. (2012) *Science* **336**, 1440–1444.
[93]Albeck J. G. *et al*. (2013) *Mol. Cell* **49**, 249–261.

4 Methods

4.1 Ordinary differential equations

Systems of coupled autonomous ordinary differential equations (ODEs) serve as a standard tool for mathematical modeling of the kinetics of regulatory networks. Each individual equation describes the rate of change of the concentration of a single biochemical species. The ODEs usually assume the form of intuitive "book-keeping" equations, $\mathrm{d}s(t)/\mathrm{d}t = s_+ - s_-$, in which the influx terms (written collectively as s_+) and the outflux terms (represented by s_-) account for the appearance and loss of molecules due to the processes of mRNA or protein biosynthesis, post-translational modifications, molecular complex formation or break-up, intercompartmental translocations, or degradation (considered most often as a spontaneous process, a chemical first-order reaction). The changes of concentrations are modeled as continuous processes, which is a reasonable assumption when the number of molecules is large. Chemical kinetics usually follows the mass-action law, that is, the assumption that the rate of change depends on the product of instantaneous concentration of reactant(s) and a kinetic rate constant. Occasionally, when substrates are more abundant than enzymes and their binding is saturable, Michaelis–Menten-type terms appear as a coarse-graining of three events: formation of the enzyme–substrate complex, conversion of the complexed substrate into a product, and enzyme–product complex break-up. Such terms have the form $s/(S_{\mathrm{max}/2} + s)$, where $S_{\mathrm{max}/2}$ is the Michaelis–Menten constant, *i.e.*, the concentration of substrate s for which the speed of the reaction reaches its half-maximum. If, in addition to saturation kinetics, a given reaction is cooperative, Hill-type terms may appear instead, $s^h/(S^h_{\mathrm{max}/2} + s^h)$, with the Hill coefficient $h \geq 1$ increasing with the strength of cooperativity.

All the ODE systems analyzed in this thesis were integrated within BioNetGen that seamlessly embeds a state-of-the-art solver, Cvode (from the Sundials suite). The solver comprises a variable-order multistep integrator from the family of backward differentiation formulas featured by a preconditioned Krylov subspace-based method for the solution of linear systems, the generalized minimal residual method. The scheme is appropriate for stiff systems (computational models often take into account processes occurring on different time scales) and its optionally multi-threaded implementation in Cvode can handle relatively large systems of equations (for example, the solver has been shown to be able to simulate kinetics of a model consisting of more than 1000 ODEs generated according to the rule-based approach[94]).

The dynamics of the systems of ODEs depends on multiple parameters that describe the

---

[94]Barua D. *et al.* (2012) *J. Immunol.* **189**, 646–658.

abundance of biomolecules in a cell as well as the kinetic rate constants of chemical reactions. It is important to characterize sensitivity of these systems with respect to the key parameters—those related to an external stimulation or to the presence or effectiveness of the key regulatory molecules. Due to the often-nonlinear kinetics of modeled networks, a slight change of an analyzed parameter may give rise to a qualitative change of system dynamics in critical points. I have performed all bifurcation analyses reported in this thesis (articles $\boxed{E}$, $\boxed{F}$, $\boxed{G}$) in MATLAB (MathWorks, Natick, MA, USA) with a numerical parameter-continuation package, MATCONT,[95] that implements a pseudo-arclength predictor–corrector continuation algorithm.[96] The package allows for the location and continuation of equilibria, limit cycles, and homoclinic orbits, the detection and continuation of (co-dimension 1 or 2) bifurcations, and the analysis of eigenvalues and Floquet multipliers. Within MATCONT it is practicable to analyze systems of up to about 50 ODEs.

4.2   Partial differential equations

The use of ODEs is appropriate when—in addition the the large number of interacting molecules—the reactor of interest (the cell or a cellular compartment) is well mixed. The reactor can be considered well mixed when the time to reaction, being the inverse of the fastest chemical rate, is larger than the characteristic time τ in which a molecule of diffusivity D covers a distance comparable to the diameter of the reactor ℓ, $\tau \propto \ell^2/D$. In non-well-mixed reactors, local concentrations of molecules can vary over space. This can be accounted for with the use of the reaction–diffusion partial differential equations (PDEs) of the form $\partial s(\boldsymbol{x}, t)/\partial t = D\nabla^2 s + s_+ - s_-$, in which the first term expresses diffusion of s, whereas the remaining part represents fluxes resulting from chemical reactions (and is thus identical to the right-hand side of an ODE that would be appropriate in the well-mixed limit). Numerical solutions of the systems of PDEs presented in this thesis were obtained in COMSOL MULTIPHYSICS (Comsol Inc., Sweden) with a LU decomposition-based finite element method solver.

4.3   Kinetic Monte Carlo in the well-mixed limit

The continuous description in terms of differential equations does not allow to account for inherent randomness of biochemical processes. When the impact of intrinsic noise on system dynamics is expected to be non-negligible, one can describe system kinetics in terms of a continuous-time (discrete-state) Markov chain (CTMC). The states are defined by the abundances of all possible molecular species (expressed in natural numbers). When a chemical reaction occurs, the change of a state alters the abundance(s) by a discrete amount, usually

---

[95]Kuznetsov Y. A., *Elements of Applied Bifurcation Theory*, 3rd ed. (Springer, New York, USA, 2004).
[96]Keller H. B., *Lectures on Numerical Methods in Bifurcation Problems* (Springer Verlag, New York, USA, 1987).

just by one. In this approach, reaction rates are replaced with propensities, *i.e.*, probabilities that a given reaction occurs per unit time; propensities depend only on the current state of the system. Probability densities of state transitions in Markov processes satisfy the Chapman–Kolmogorov equation, whose differential form, the master equation, is written in terms of propensities.[97]

Despite the fact that the master equation fully characterizes time evolution of probability densities of the states of the system, it is analytically intractable for all but simplest cases. Realizations of CTMCs can be obtained by Monte Carlo simulations according to the Gillespie algorithm,[98] a staple of computational systems biology. In a single step of this iterative algorithm, the time to a next event is calculated from the exponential distribution whose mean is the inverse of the sum of propensities of all events that can happen in the simulated system. An event is then selected with a probability that is proportional to its propensity, and realized, moving the system to another state. Probability densities of system states can be estimated by performing multiple stochastic simulations.

It should be stressed that the Gillespie algorithm is inherently serial. Any algorithmic speed-ups, consisting in, *e.g.*, taking longer leaps in time and then firing multiple reactions, lead to inexact sampling of the CTMC.[99] All stochastic simulations in the well-mixed limit reported in this thesis were performed according to the (exact) Gillespie algorithm as implemented in BioNetGen.

4.4   Kinetic Monte Carlo on the lattice

To account for both the inherent stochasticity of biochemical reactions and the spatial location of molecules one can apply the kinetic Monte Carlo approach with explicit tracking of spatial positions of individual molecules. As an approximation, internal spatial structure of molecules may be neglected and space can be discretized using a regular lattice, nodes of which can be occupied by a molecule or be empty. Such spatial coarse-graining allows for efficient simulation of Brownian dynamics at intermediate reactant densities and greatly simplifies searching for neighboring molecules. This is of key importance for the method because bimolecular reactions are allowed to occur only between the molecules that occupy neighboring lattice nodes.

Within on-lattice kinetic Monte Carlo simulations, one can reproduce the exact state-to-state dynamics of the underlying time-continuous Markov process: events—biochemical reactions and diffusive hops between neighboring lattice nodes—are selected from a catalog of

[97] Van Kampen N. G., *Stochastic Processes in Physics & Chemistry*, 3rd ed. (North Holland, Amsterdam, 2007).
[98] Gillespie D. T. (1977) *J. Phys. Chem.* **81**, 2340–2361.
[99] Gillespie D. T. (2001) *J. Chem. Phys.* **115**, 1716–1733.

all possible events and fired with propensities proportional to their respective rate constants. The catalog of possible events is always complete as, after simulating any event, it is updated by considering every possible new event that may happen in the updated system. Complete updates are feasible due to the fact that the space is discretized and updates are local on the lattice. The method is rejection-free unless there are distinguished regions of diminished diffusivity defined on the lattice. In the limit of infinite diffusion, the algorithmic approach is equivalent to the Gillespie algorithm used for simulations of well-mixed systems;[100] for fast diffusion and larger reactors, where the grain size becomes irrelevant, simulation results correspond to that obtained with finite-element method-based solvers for PDEs. All kinetic Monte Carlo simulations reported in articles A , B , C were performed using SPATKIN, a software tool developed by me, described in article D .

---

[100] Stamatakis M. & Vlachos D. G. (2011) *Comput. Chem. Eng.* **35**, 2602–2610.

5 Overview of results

5.1 Biochemical kinetics in spatial stochastic systems

5.1.1 Kinetics of spatially extended bistable reaction systems

In article $\boxed{A}$, I investigated the mechanisms of macroscopic state-to-state transitions available to a bistable spatially extended system. To this end, I developed a spatial stochastic simulator, described in article $\boxed{D}$, and used it to perform massively parallel kinetic Monte Carlo simulations of a generic system of membrane-bound autophosphorylating kinases and phosphatases. The calculations were carried out on two-dimensional triangular lattices in a cluster environment, taking years of the aggregate single-CPU time. I compared these simulations with the simulations of the Markov process in the perfectly mixed reactor and with the deterministic approximation, *i.e.*, reaction–diffusion partial differential equations.

I have demonstrated that—while in the limit of infinite diffusion the stationary probability density (SPD) in the spatial on-lattice kinetic Monte Carlo simulations converges to the SPD obtained from Gillespie algorithm simulations of the well-mixed system—for smaller diffusivities the SPD is qualitatively different from the case of the well-mixed system: the bimodality of the SPD can emerge or vanish. I have shown that the fraction of the SPD concentrated in the vicinity of the two attracting states depends on the speed of diffusion and on both the volume and shape of the reactor. In large reactors, state-to-state transitions turned out to follow from the propagation of semi-deterministic traveling waves. These waves may be induced either stochastically due to a fluctuation or deterministically as a result of an externally triggered state transition in a subregion of the reactor. I also demonstrated that at slow diffusion, for some parameters, the reactor may exhibit a dynamical structure of perpetual local activations and inactivations, and refrain from assuming uniformly a single steady state (see supplementary materials).

Importantly, it has turned out that while the expected time to transition on the membrane (mean first-passage time, MFPT) increases exponentially with the volume of the reactor in the well-mixed regime, it decreases as 1/volume in a structured (poorly mixed) reactor, rendering the MFPT a non-monotonic function of the reactor volume. I have shown that the volume for which MFPT reaches its maximum (as well as the value of the maximum) increases with motility.

Taken together, these results allowed me to put forward a mechanism in which the coexistence of stochastic and deterministic effects can give rise to global activation of membrane proteins in response to a localized cue as subtle as a local immobilization of a small fraction of membrane proteins.

5.1.2   Effective reaction rates in diffusion-limited reaction cycles

Reaction cycles, in which substrate is modified by antagonistic enzymes, such as the phosphorylation–dephosphorylation cycles, are ubiquitous in cellular signal transduction, allowing for substrate reuse and signal amplification. In article B , we investigated kinetics of a generic cycle on the plasma membrane by means of kinetic Monte Carlo simulations on the triangular lattice. I have set up simulations and performed associated analyses (determined spatial correlation functions) in the cluster environment. This allowed us to numerically establish and explain the non-linear dependence of the effective macroscopic reaction rate coefficients as well as the steady state of the phosphorylated substrate fraction on the diffusion coefficient and concentrations of opposing enzymes: kinases and phosphatases.

In article C , starting from the microscopic bimolecular reaction rate constants and using estimates of the mean first-passage time for an enzyme–substrate encounter, we derived diffusion-dependent effective macroscopic reaction rate coefficients for a generic reaction cycle. Analytical predictions derived by other co-authors were verified using on-lattice kinetic Monte Carlo simulations that I helped to set up and run in the cluster environment. The proposed formulas estimate the steady-state concentrations and effective reaction rates for a wide range of microscopic reaction rates and concentrations of reactants.

The proposed analysis can capture the behavior of a reaction cycle in which the steady state is qualitatively controlled by diffusion. For low diffusivity, *i.e.*, when reaction kinetics is diffusion-controlled, the steady state is imposed by the more abundant enzyme, while for high diffusivity, *i.e.*, in the reaction-controlled limit, it is imposed by the enzyme which has higher effective activity. Recent studies suggest that high concentration of membrane "crowders" can maintain membrane proteins close to a percolation threshold and various subcellular environments appear to exist on the verge of the sol–gel transition. One can expect that abrupt, localized changes of effective diffusivity can exert impact on biochemical reaction kinetics implicated in signal transduction.

5.1.3   Spatkin: a simulator for spatial rule-based modeling

In article D , I described a novel computational tool to simulate stochastic reaction–diffusion kinetics of biochemical systems on biological membranes at the single-molecule resolution. In the limit of infinite diffusion, the approach is equivalent to the Gillespie algorithm, whereas for fast diffusion and larger reactors, simulation results are consistent with that obtained by solving corresponding systems of partial differential equations.

Importantly, the tool supports rule-based modeling and thus can be used to simulate systems encompassing a potentially high number of molecular states. I have implemented a network-free approach, which does not require a complete expansion of the network of

possible molecular states: the network of interactions is computed on-the-fly for existing molecular species (as in, *e.g.*, NFsim[101]) and updated locally after any reaction fires. In this way, the tool can tame combinatorial explosion of states inherent to models in which molecules possess multiple sites. Spatkin is thus well-suited for modeling cell signaling processes occurring on membranes. Models are defined using a variant (superset of a subset) of the BioNetGen language.[102] Article D contains a concise description of software implementation and capabilities.

With pre-release versions of Spatkin, I analyzed spatial and stochastic effects such as spontaneous traveling wave initiation in a bistable reaction system (article A) and spatial correlations in simple linear phosphorylation–dephosphorylation systems (article B). In addition, the software was helpful in determining macroscopic reaction rate coefficients (article C). The simulator, written in C++, has been embedded within a GUI. GPL-licensed source code of Spatkin, executable binaries, detailed user manual, and example input files are available at `http://pmbm.ippt.pan.pl/software/spatkin`.

5.2   Nonlinear dynamics of systems with multiple feedbacks

5.2.1   The NF-κB network

In article E, we analyzed, mainly theoretically, the regulatory system of NF-κB, the major transcription factor controlling innate immune responses. Its activity is tightly controlled by negative feedback loops mediated by IκBα and A20 proteins, see Scheme 2. Up to our knowledge, there were no studies on the dynamical role of the positive feedback loop arising due to the TNFα autocrine regulation, which introduces an important positive feedback loop to the regulatory system.

I performed bifurcation analysis of the deterministic approximation of the Markov chain model of the system. Bifurcation analyzes obtained in MatCont complemented stochastic simulations obtained in BioNetGen, showing that the TNFα-mediated positive feedback assures the existence of limit-cycle oscillations in unstimulated wild-type cells and introduces bistability in A20-deficient cells
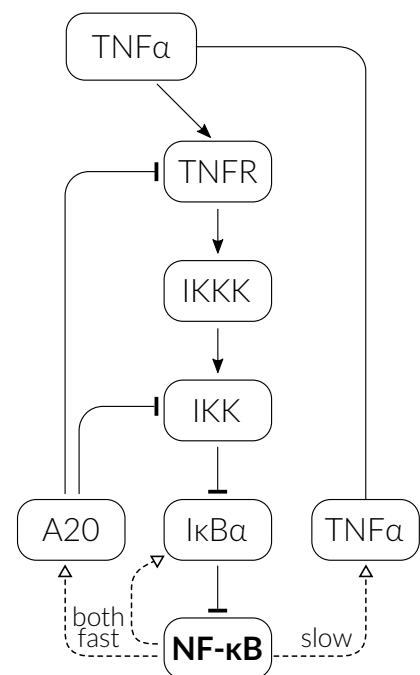
Scheme 2
A simplified diagram of the NF-κB regulatory network. Dashed lines with empty arrowheads represent transcription and translation.

[101]Sneddon M. W. *et al.* (2011) *Nat. Methods* **8**, 177–183.
[102]Harris L. A. *et al.* (2016) *Bioinformatics* **32**, 3366–3368.

in which one of the negative feedback loops is broken. We also demonstrated that cells of significant autocrine potential, *i.e.*, cells characterized by high expression of TNFα and its receptor, TNFR1, may exhibit sustained cytoplasmic–nuclear NF-κB oscillations which could start spontaneously due to stochastic fluctuations.

In A20-deficient cells, even a small TNFα expression rate qualitatively influences system kinetics leading to long-lasting NF-κB activation in response to a short-pulsed TNFα stimulation. As a consequence, cells with impaired A20 expression or increased TNFα secretion rate are expected to have elevated NF-κB activity even in the absence of stimulation. This may lead to chronic inflammation and promote cancer due to the persistent activation of the anti-apoptotic genes regulated by NF-κB. There is growing evidence that A20 mutations correlate with several types of lymphomas, and elevated TNFα secretion is characteristic of many cancers. Interestingly, A20 loss or dysfunction also leaves the organism vulnerable to septic shock and massive apoptosis triggered by the uncontrolled TNFα secretion that at high levels overcomes the anti-apoptotic action of NF-κB.

5.2.2   The p53 network

Transcription factor p53 is a key node of the complex regulatory network that coordinates important cellular processes including DNA repair, cell cycle arrest, and apoptosis, and has been intensively studied both experimentally and theoretically over the last decades.

Scheme 3

A simplified diagram of the core of the p53 regulatory network. Dashed lines with empty arrowheads represent transcription and translation.
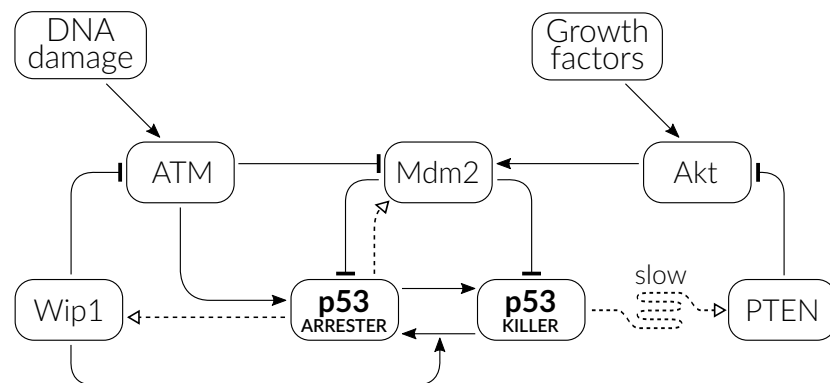
In article $\boxed{\text{F}}$, we have investigated the topology of interconnected feedback loops of the p53 network (Scheme 3) with the aim to construct a Markov chain model of the system, which allows for stochastic yet unambiguous cell fate decisions. The resulting model consists of the regulatory core and two slaved bistable modules responsible for cell cycle arrest and apoptosis. The regulatory core is controlled by two negative feedback loops (regulated by Mdm2 and Wip1) responsible for oscillations, and two antagonistic positive feedback loops (regulated by Wip1 and PTEN) responsible for bistability. By means of bifurcation analysis I was able to capture the recurrent solutions that shape temporal responses of the stochastic system. The direct transition from the limit-cycle oscillations to the "apoptotic" steady state
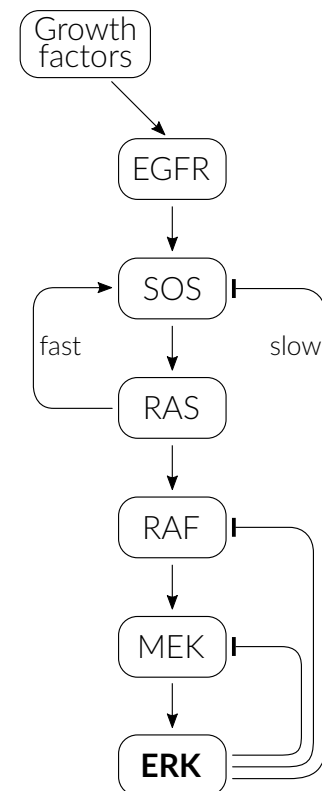
has turned out to be enabled by the existence of a subcritical Neimark–Sacker bifurcation (occurring and studied rarely in the context of regulatory networks). By means of stochastic simulations, I have shown that the specific competition of negative and positive feedbacks allows for the unbiased and proportionate cell fate decisions preceded by the oscillatory phase, in which cell cycle is arrested and the cell has a chance to repair its DNA. I have demonstrated that the initial level of phosphatase PTEN correlates well with the apoptotic potential of cells.

Our analysis provided an explanation why cancer cell lines known to have vastly diverse expression levels of phosphatases Wip1 and PTEN can exhibit a broad spectrum of qualitatively different responses to DNA damage. The model allows for system-level analysis of the possible outcomes of different chemo- and radiotherapies with respect to the expression levels of Wip1 and PTEN, and proteins or miRNAs regulating these two nodes.

5.2.3   The ERK network

Intense experimental and theoretical research on MAPK signaling demonstrated that in a canonical MAPK pathway that involves SOS, RAS, RAF, MEK, and ERK, signal transmission is controlled by multiple negative as well as positive feedback loops. How these feedbacks cooperate in information processing remains elusive.

In article G, we demonstrated that the canonical MAPK/ERK cascade (Scheme 4) can transform graded inputs into pulses that encode information about stimulation dose in their duration and frequency, as recently observed by our experimental collaborator.[103] Together with my supervisor, I have formulated a computational model for MAPK signaling downstream of the EGF receptor to elucidate how interlinked feedback loops allow for the experimentally observed amplitude-to-frequency encoding. The model has helped to unravel the origin of relaxation oscillations that arise because the RAS–SOS positive feedback loop is nested within the negative feedback loop that encompasses RAS and the kinases RAF, MEK,

Scheme 4
A simplified diagram of the MAPK regulatory network.

and ERK that inhibits SOS via phosphorylation. This negative feedback operates on a longer time scale than the positive feedback loop, and, as the bifurcation analysis that I performed in MᴀᴛCᴏɴᴛ indicates, it changes switch-like behavior into relaxation oscillations, consistent

---

[103]Albeck J. G. *et al.* (2013) *Mol. Cell* **49**, 249–261.

with experimentally observed dose-dependent pulses. Two auxiliary negative feedback loops, from ERK to MEK and from ERK to RAF, placed downstream of the positive feedback, shape the temporal ERK activity profile but are dispensable for generation of oscillations. Therefore, we have demonstrated that the positive feedback introduces a hierarchy among negative feedback loops, such that the effect of a negative feedback depends on its position with respect to the positive feedback loop.

Furthermore, I have shown that the system is capable of conversion of stimulation gradients into spatially organized pulses of ERK activity. By analyzing the regulatory system in the spatial context (by solving reaction–diffusion PDEs in Comsol Multiphysics), I have demonstrated that the combination of the positive feedback involving slow-diffusing membrane components, RAS and SOS, with negative feedbacks involving faster-diffusing cytoplasmic components, RAF, MEK, and ERK, leads to local excitation/global inhibition (LEGI) dynamics. We propose that this mechanism allows the MAPK signaling pathway for generating directional responses to localized (paracrine) growth factor stimulation.

Original articles

Stochastic transitions in a bistable reaction system on the membrane

Marek Kochańczyk[1], Joanna Jaruszewicz[1] and Tomasz Lipniacki[1,2]

[1]Institute of Fundamental Technological Research, Polish Academy of Sciences, Warsaw 02106, Poland
[2]Department of Statistics, Rice University, Houston, 77005 TX, USA

Transitions between steady states of a multi-stable stochastic system in the perfectly mixed chemical reactor are possible only because of stochastic switching. In realistic cellular conditions, where diffusion is limited, transitions between steady states can also follow from the propagation of travelling waves. Here, we study the interplay between the two modes of transition for a prototype bistable system of kinase–phosphatase interactions on the plasma membrane. Within microscopic kinetic Monte Carlo simulations on the hexagonal lattice, we observed that for finite diffusion the behaviour of the spatially extended system differs qualitatively from the behaviour of the same system in the well-mixed regime. Even when a small isolated subcompartment remains mostly inactive, the chemical travelling wave may propagate, leading to the activation of a larger compartment. The activating wave can be induced after a small subdomain is activated as a result of a stochastic fluctuation. Such a spontaneous onset of activity is radically more probable in subdomains characterized by slower diffusion. Our results show that a local immobilization of substrates can lead to the global activation of membrane proteins by the mechanism that involves stochastic fluctuations followed by the propagation of a semi-deterministic travelling wave.

1. Introduction

Living cells receive stimuli and process information with a circuitry of interacting genes and proteins. From the mathematical perspective, cell fates can be identified with attractors of the dynamical system defined by the interaction network [1]. Accordingly, cellular decisions correspond to transitions between multiple steady states of this dynamical system [2], allowing for phenotypical differentiation of genetically uniform cells [3]. Remarkably, many key biological regulatory and signalling modules are controlled by bistable switches, often leading to binary cellular responses of crucial importance, such as death or survival, senescence or proliferation [4,5]. In this work, we consider state-to-state transitions leading to the activation of proteins diffusing on the plasma membrane.

1.1. State-to-state transitions in homogeneous and heterogeneous reactors

Transitions between steady states in the perfectly mixed chemical reactor are possible only because of stochastic switching. (The classic monographs on stochastic processes covering material used in this study are those by van Kampen [6], Gardiner [7] and Nicolis & Prigogine [8].) In well-mixed reactors, however, the expected time to switch τ depends exponentially on the system size, $\tau \propto \exp(\alpha V)$, $\alpha > 0$, assuming a constant concentration of molecules N/V [9]. The number of reacting molecules in the plasma membrane is of order $N = 10^3$ to 10^5 [10,11], implying an infinitesimal rate of switching between macroscopic states of activity and inactivity in the well-mixed approximation. In spatially extended reactors, the characteristic size of the well-mixed subcompartment is effectively controlled by diffusion. Relatively small diffusion coefficients of membrane proteins, $D \approx 10^{-2}$ to 10^{-1} $\mu m^2 s^{-1}$ [12,13], coinciding with fast reaction rate constants of order $c \approx 1/s$ [14] imply a correlation length $\lambda \propto \sqrt{D/c}$ shorter than 1 μm. The membrane can be therefore heterogeneous without any molecular

structure imposed by cytoskeletal corrals, protein scaffolds or lipid rafts. In stochastic spatially extended bistable systems, the diffusion-limited number of interacting molecules controls the transition rates between macroscopic states. Interestingly, even when in the deterministic approximation a system is mono-stable, the volume of the well-mixed stochastic reactor can serve as a 'bifurcation parameter' controlling the emergence of noise-induced bimodality [15].

In deterministic spatially extended reactors, transitions between steady states of bistable systems can result from the propagation of heteroclinic travelling waves. (See the book by Murray [16] for an extensive introduction.) A local state-to-state transition can initiate the propagation of a travelling front driving the whole system towards the 'more stable' steady state, in which the system would eventually persist. Crucially, for a bistable birth–death process, the deterministically preferred steady state (global deterministic attractor) can be different from the steady state in which the stationary probability distribution (SPD) concentrates (global stochastic attractor) [17,18]. For gradient systems, the macroscopic (deterministic) state-coexistence line in the parameter space is obtained for the potential which exhibits minima of equal depth. In spatially extended systems, this coexistence line corresponds to standing heteroclinic wave solutions. The stochastic state-coexistence line results from the solution of the (stochastic) chemical master equation, and in particular cases can be found analytically in the limit of zero noise by the Maxwell-type construction [19]. This implies that the spatially extended reactor may remain in a stochastically preferred steady state until a local but sufficiently large fluctuation initiates a semi-deterministic transition of the whole reactor to the state preferred in the deterministic approximation [20].

Simulations of Newtonian hard sphere dynamics provided evidence [21] that in the bistable perfectly stirred system the global attractor is correctly defined by the (stochastic) master equation, while using the Fokker–Planck equation with either linear (additive) or nonlinear (multiplicative) noise may lead to incorrect predictions [9]. Baras *et al.* [21] used the Bird's direct simulation Monte Carlo method [22] to study the chemical kinetics in a homogeneous Boltzmann gas by associating the entire system volume with a single collisional cell. The method was proposed to perform simulations of rarified gas for which the Knudsen number is greater than 1, which is equivalent to the assumption of perfect homogeneity. By employing on-lattice kinetic Monte Carlo (KMC) simulations, we recapitulate here this result in the infinite diffusion limit (see [23]). We will demonstrate, however, that in reactors characterized by finite diffusion the global attractor can be prescribed either through the deterministic or through the stochastic approach, depending on the diffusion coefficient. Interestingly, the deterministic description in which the system is modelled by means of reaction–diffusion equations predicts the same global attractor as that obtained in the Langevin approach based on the macroscopic (deterministic) law of evolution into which an external additive noise term is incorporated. This places the discrepancy between the master equation and the diffusion approximation in the new context.

1.2. State-to-state transitions in biological membrane systems

The highly organized structure of cells, comprising zones of confinement [24,25] or altered motility [26–28], should allow signalling systems to employ intricately both transition modes, i.e. stochastic switching and semi-deterministic travelling wave propagation. Thus far, selected aspects of these phenomena have been investigated in the context of membrane-proximal signalling and spontaneous cell polarization. It has been shown that the self-recruitment of cytoplasmic proteins to the cell membrane leads to the generation of a single cluster of active molecules and thus may define a unique axis of cell polarity [29]. A local increase in the density of molecules in the presence of positive feedback is able to work as an activating switch [30]. In the context of Ras nanoswitches, it has been demonstrated that at uniform slow motility the sole positive feedback in the interaction network of membrane-anchored proteins generates expanding activity patches [31]. In excitable networks, transient clans of activated molecules emerge and vanish spontaneously, even without directional spatial cues [32,33]. Spatio-temporal oscillations of membrane-recruited Min proteins in *Escherichia coli* were demonstrated to be enabled by the inherent noise [34]; on the other hand, macroscopically stable homogeneous oscillations can be abolished by local fluctuations, depending critically on the size and dimensionality of the reactor [35]. In stimulated thin neuronal protrusions, it has been observed that slowly diffusing autocatalytic CaMKII kinases exhibit pulsatile compartmentalized activity [36]; a spatially extended bistable system can spontaneously generate subregions, where different steady states dominate [37]. Self-organized foci of activity can generate activating travelling waves [38]. Propagation of waves can give rise to long-lasting cell polarity when the fast-diffusing inhibitor accumulates proportionally to the amount of slow-diffusing activated molecules so that the wavefront can be stalled. This mechanism, known as wave pinning, has been investigated for bistable systems [39,40]. When the diffusion coefficient of the inhibitor is very large (in principle, infinite), the mechanism of polarization is known as the local excitation, global inhibition [41,42].

1.3. Overview of results

In order to provide a comprehensive view and to be able to recognize new mechanisms of macroscopic state-to-state transitions available in spatially extended systems, we study a generic bistable system of membrane-bound autophosphorylating kinases and phosphatases by means of KMC simulations on the hexagonal lattice. These simulations are compared with the simulations of the Markov process in the perfectly mixed reactor and with the deterministic approximation, i.e. reaction–diffusion partial differential equations (PDEs).

In the limit of infinite diffusion, unsurprisingly, the SPD in the spatial on-lattice KMC simulations converges to the SPD obtained from Gillespie algorithm simulations of the well-mixed system. For slower diffusion, however, we observe that the SPD is qualitatively different from the case of the perfectly mixed system; specifically, the bimodality can emerge or vanish. We demonstrate that the probability mass fraction concentrated in the stochastically and deterministically preferred steady states depends on the speed of diffusion and properties of the reactor, such as volume and shape. We show that the state-to-state transitions in large reactors can follow from the propagation of semi-deterministic travelling waves. These waves can be induced deterministically by the externally triggered state transition in a sub-volume of the spatially extended reactor; they can

also arise spontaneously as a result of local stochastic fluctuations. We found that the expected time to transition on the membrane grows exponentially with diffusivity. For a given diffusion coefficient, the expected time to transition increases exponentially with the volume of the reactor V as long as the reactor is perfectly mixed, and then it decreases as $1/V$. At slow diffusion, for some parameters, the reactor may exhibit a dynamical structure of perpetual local activations and inactivations, and refrain from assuming uniformly a single steady state. Finally, we identify a novel mechanism in which the coexistence of stochastic and deterministic effects can give rise to the global activation of membrane proteins in response to a localized cue.

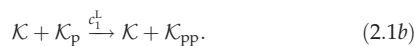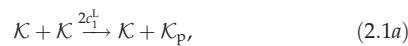## 2. Material and methods

2.1. Model

The analysed system of reactions involves two molecular species: kinases and phosphatases. Each kinase molecule contains two indistinguishable phosphorylation sites, hence it can assume three states: dephosphorylated, monophosphorylated or bisphosphorylated. The (auto)phosphorylation activity of a kinase increases with its phosphorylation level. Phosphatases are explicitly present in the system although they are not modified in any process.

The interaction network comprises the variant of the two-step phosphorylation–dephosphorylation motif, where kinases autophosphorylate one another and are dephosphorylated by phosphatases, which act non-specifically with respect to the level of phosphorylation of a substrate kinase [15,43]. The system encompasses the simplest case of the ubiquitous multi-site phosphorylation and exhibits bistability [44,45]. Since it consists of eight reactions, it may be viewed as far from minimal [46]; however, in contrast to other small bistable systems [47,48], all its reactions are bimolecular and elementary (i.e. only one of two reacting molecules changes its state), rendering the system appropriate for microscopic lattice-based simulations of diffusion-influenced reaction kinetics.
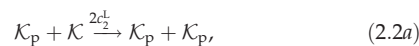
2.2. Reaction–diffusion system: kinetic Monte Carlo on the lattice

The spatial and stochastic simulations of the system are performed using the on-lattice KMC at the single molecule resolution. Molecules are allowed to hop between adjacent sites of a hexagonal lattice with propensity proportional to the diffusion coefficient. It is assumed that two molecules cannot occupy the same lattice site. Kinases $\mathcal{K}$ and phosphatases $\mathcal{P}$ can react only when in adjacent sites according to the following rules:
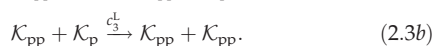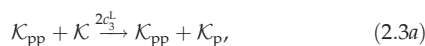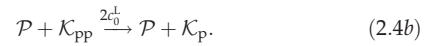
Phosphorylation by a dephosphorylated kinase:

$$\mathcal{K} + \mathcal{K} \xrightarrow{2c_1^{\mathrm{L}}} \mathcal{K} + \mathcal{K}_{\mathrm{p}}, \tag{2.1a}$$

$$\mathcal{K} + \mathcal{K}_{\mathrm{p}} \xrightarrow{c_1^{\mathrm{L}}} \mathcal{K} + \mathcal{K}_{\mathrm{pp}}. \tag{2.1b}$$

Phosphorylation by a monophosphorylated kinase:

$$\mathcal{K}_{\mathrm{p}} + \mathcal{K} \xrightarrow{2c_2^{\mathrm{L}}} \mathcal{K}_{\mathrm{p}} + \mathcal{K}_{\mathrm{p}}, \tag{2.2a}$$

$$\mathcal{K}_{\mathrm{p}} + \mathcal{K}_{\mathrm{p}} \xrightarrow{c_2^{\mathrm{L}}} \mathcal{K}_{\mathrm{p}} + \mathcal{K}_{\mathrm{pp}}. \tag{2.2b}$$

Phosphorylation by a bisphosphorylated kinase:

$$\mathcal{K}_{\mathrm{pp}} + \mathcal{K} \xrightarrow{2c_3^{\mathrm{L}}} \mathcal{K}_{\mathrm{pp}} + \mathcal{K}_{\mathrm{p}}, \tag{2.3a}$$

$$\mathcal{K}_{\mathrm{pp}} + \mathcal{K}_{\mathrm{p}} \xrightarrow{c_3^{\mathrm{L}}} \mathcal{K}_{\mathrm{pp}} + \mathcal{K}_{\mathrm{pp}}. \tag{2.3b}$$

Dephosphorylation (by a phosphatase):

$$\mathcal{P} + \mathcal{K}_{\mathrm{p}} \xrightarrow{c_0^{\mathrm{L}}} \mathcal{P} + \mathcal{K}, \tag{2.4a}$$

$$\mathcal{P} + \mathcal{K}_{\mathrm{pp}} \xrightarrow{2c_0^{\mathrm{L}}} \mathcal{P} + \mathcal{K}_{\mathrm{p}}. \tag{2.4b}$$

The relative activity of a kinase increases strongly with its phosphorylation level: $c_1 < c_2 < c_3$ (parameter values are given in the electronic supplementary material, table S1). Two molecules can diffuse away without reacting; on the other hand, a series of reactions involving two molecules is allowed, and such consecutive events are more probable at small diffusion coefficients when contacts last longer. The total numbers of kinases $N_{\mathcal{K}}$ and phosphatases $N_{\mathcal{P}}$ are constant in a simulation and their fractional surface concentrations (i.e. the fraction of lattice sites occupied by a species) are assumed to be $\rho_{\mathcal{K}} = 0.4$ and $\rho_{\mathcal{P}} = 0.1$, respectively. For the sake of simplicity, we assume the same motility M of kinases and phosphatases; the propensity of hopping to a neighbouring empty site of a hexagonal lattice is $M/6$. We will consider both spatially uniform and non-uniform motility to account for subdomains of slower diffusion, e.g. large lipid rafts [27]. In a two-dimensional reactor, the macroscopic diffusion coefficient D depends on the total fractional concentration of membrane molecules $\rho = \rho_{\mathcal{K}} + \rho_{\mathcal{P}}$ and the lattice constant ℓ,

$$D = \frac{(1-\rho)\ell^2 M}{4}. \tag{2.5}$$

The lattice constant is equal to the characteristic mean centre-to-centre spacing between neighbouring membrane proteins, which is of order $\ell = 10$ nm [49].

2.3. Spatially homogeneous Markov process: Gillespie algorithm

The Gillespie algorithm for KMC was employed for stochastic simulations in the limit of the perfectly mixed chemical reactor [50]. To provide a basis for the comparison of well-mixed Gillespie (superscript G) with on-lattice (superscript L) KMC simulations, kinetic rate constants $c_1^{\mathrm{L}}, c_2^{\mathrm{L}}, c_3^{\mathrm{L}}, c_0^{\mathrm{L}}$ have to be rescaled according to the general rule

$$c_i^{\mathrm{G}} = \frac{n_{\mathrm{c}}}{V} c_i^{\mathrm{L}}, \tag{2.6}$$

which reflects the fact that the propensity of each reaction in the perfectly mixed reactor is inversely proportional to the volume (or, here, surface) of the reactor V and is proportional to the number of possible contacts ($n_c = 6$ for the hexagonal lattice). The scaling ensures that in the limit of $M \to \infty$ the SPD obtained in on-lattice KMC simulations converges to that obtained with Gillespie KMC simulations (see the electronic supplementary material, figure S1c) [23].

2.4. Spatially extended deterministic approximation: partial differential equations

We will also consider the deterministic limit of the on-lattice KMC described by a system of PDEs. For this approximation, kinetic rate constants $c_1^{\mathrm{L}}, c_2^{\mathrm{L}}, c_3^{\mathrm{L}}, c_0^{\mathrm{L}}$ are scaled according to the following rules:

$$c_i = 6\rho_{\mathcal{K}} c_i^{\mathrm{L}} =: \Omega_{\mathcal{K}} c_i^{\mathrm{L}} \text{ for } i \in \{1,2,3\}, \tag{2.7a}$$

$$c_0 = 6\rho_{\mathcal{P}} c_0^{\mathrm{L}} =: \Omega_{\mathcal{P}} c_0^{\mathrm{L}}. \tag{2.7b}$$

These coefficients are used to parametrize dimensionless reaction–diffusion PDEs. Since we assume that the diffusion coefficient of kinase molecules is independent of their phosphorylation level, we may introduce fractional concentrations of dephosphorylated, monophosphorylated and bisphosphorylated kinases denoted by
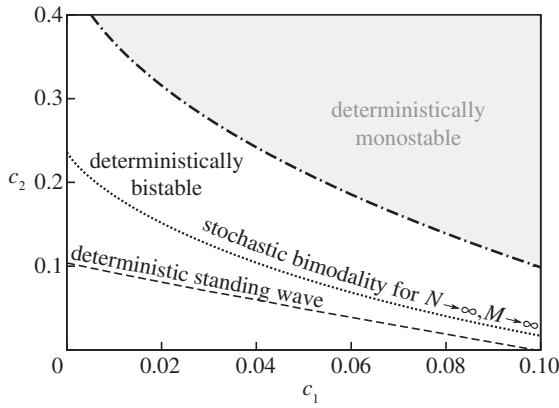
Figure 1. Bistability region of equations (2.8a−c) in the parameter space of (c_1, c_2); remaining parameters are fixed: $c_3 = 4$ and $c_0 = 1$. The region is divided into two lines: the deterministic coexistence line (dashed), obtained numerically in COMSOL, and the stochastic coexistence line (dotted), obtained numerically as an approximate limit of curves determined for increasing numbers of molecules in the perfectly mixed regime. Above and below these lines global deterministic and stochastic attractors converge in the active and inactive steady state, respectively. Between these lines, the well-mixed stochastic system is preferentially inactive, while activating travelling waves may propagate.

k, k_p and k_{pp} ($k + k_p + k_{pp} = 1$). The fraction of phosphorylated kinases, $k_p + k_{pp}$, will be considered as a measure of activity of the system. The resulting PDEs read as follows:

$$\frac{\partial k}{\partial t} = D\nabla^2 k + c_0 k_p - 2(c_1 k + c_2 k_p + c_3 k_{pp})k, \tag{2.8a}$$

$$\frac{\partial k_p}{\partial t} = D\nabla^2 k_p + 2(c_1 k + c_2 k_p + c_3 k_{pp})k + 2c_0 k_{pp}$$
$$- (c_1 k + c_2 k_p + c_3 k_{pp})k_p - c_0 k_p, \tag{2.8b}$$

$$\frac{\partial k_{pp}}{\partial t} = D\nabla^2 k_{pp} + (c_1 k + c_2 k_p + c_3 k_{pp})k_p - 2c_0 k_{pp}. \tag{2.8c}$$

Evolution of the above system was simulated using the finite-element method implemented in COMSOL MULTIPHYSICS (Comsol Inc., Sweden).

For a certain range of parameters, equations (2.8a−c) exhibit bistability (figure 1). The stable steady state corresponding to a high and a low value of $k_p + k_{pp}$ will be referred to as the active and the inactive state, respectively. For default parameters: $c_0 = 1$, $c_1 = 0.02$, $c_3 = 4$ (see the electronic supplementary material, table S1) and $c_2 = 0.2$, in the active state $k_p + k_{pp} = 0.86$ and in the inactive state $k_p + k_{pp} = 0.07$ (see the electronic supplementary material, figure S1b).

2.5. Estimation of the stationary probability distribution for rarely switching systems

An important characteristic of (homogeneous or heterogeneous) stochastic bistable systems is the expected time to switch from one to the other steady state, or the mean first-passage time (MFPT). Numerical estimates of the MFPT for activation τ_{on} and deactivation τ_{off} can be obtained from running multiple (parallel) simulations with initial conditions in both basins of attraction. When switches are too rare to provide a reliable estimation of the SPD from a single trajectory, MFPTs allow one to quantify relative probabilities of finding a system in the basin of attraction of the active steady state $p_{on} = \tau_{off}/(\tau_{on} + \tau_{off})$ and inactive steady state $p_{off} = 1 - p_{on}$.

If n independent simulations of the initially inactive system were running until finite times $T_{1 \leq i \leq n}$, it could happen that spontaneous activations were observed only in a fraction of

trajectories at times $\tau_i \leq T_i$. Then one can use the maximum-likelihood estimate for τ_{on},

$$\tau_{on} = \sum_{i=1}^{n} \frac{\min(\tau_i, T_i)}{n_{on}}, \tag{2.9}$$

where n_{on} is the number of observed *on* switches [51]; τ_{off} can be estimated analogously.

3. Results

3.1. General considerations

We are interested primarily in macroscopic state-to-state transitions of a bistable reaction–diffusion Markov process on the membrane. Depending on the chemical reaction rate parameters, diffusion coefficients of molecules and the size of the domain, the process can be approximated by means of the perfectly mixed stochastic system, perfectly mixed deterministic system or the spatially extended deterministic system:

— The reactor can be considered as perfectly mixed when its diameter L is smaller than the characteristic distance λ travelled by a molecule in the characteristic time τ_r between two subsequent reactions. In estimations of λ and τ_r, we employ the rate constant c_0, because the dephosphorylation reaction is both relatively fast and density-independent (ρ_P is constant, while densities of kinases at a particular phosphorylation level evolve in time). We assign $\tau_r = 1/c_0$ and obtain $\lambda = 2\sqrt{D\tau_r} = 2\sqrt{D/c_0}$ [6,52]. When $\lambda > L$, the positions of a molecule subjected to subsequent reaction events can be regarded as uncorrelated.

— The process in the well-mixed reactor can be considered in the deterministic approximation when MFPTs of macroscopic state-to-state transitions are longer than the duration of other processes modifying the system; for instance, the duration of the cell cycle T. The characteristic MFPT τ grows exponentially with the size of the well-mixed reactor [9],

$$\tau = \left(\frac{1}{c_0}\right) \exp(\rho_P V). \tag{3.1}$$

When $\tau \gg T$, the process can be considered as deterministic, in the sense that the chance for a stochastic transition in the considered time interval T is negligible.

— In the non-mixed reactor, the volume of the mixed subcompartment in two dimensions can be defined as $V_0 = D/c_0$. The characteristic transition time for such a sub-volume is

$$\tau_0 = \left(\frac{1}{c_0}\right) \exp(\rho_P V_0). \tag{3.2}$$

As we will see, a stochastic transition in any subcompartment, depending on parameters, may trigger travelling waves leading to the macroscopic state-to-state transition of the whole reactor. In large reactors for which $V_0 < V$, the MFPT for such locally induced transition τ^* is given as the waiting time of V/V_0 concurrent processes,

$$\tau^* = \left(\frac{V_0}{V}\right)\left(\frac{1}{c_0}\right) \exp(\rho_P V_0) = \left(\frac{V_0}{V}\right)\tau_0. \tag{3.3}$$

It is assumed here that the expected time to switch is much longer than the time of the wavefront propagation over the whole reactor, and that every local ignition can effectively give rise to a propagating front. When $\tau^* \gg T$, the process can be considered deterministic: the
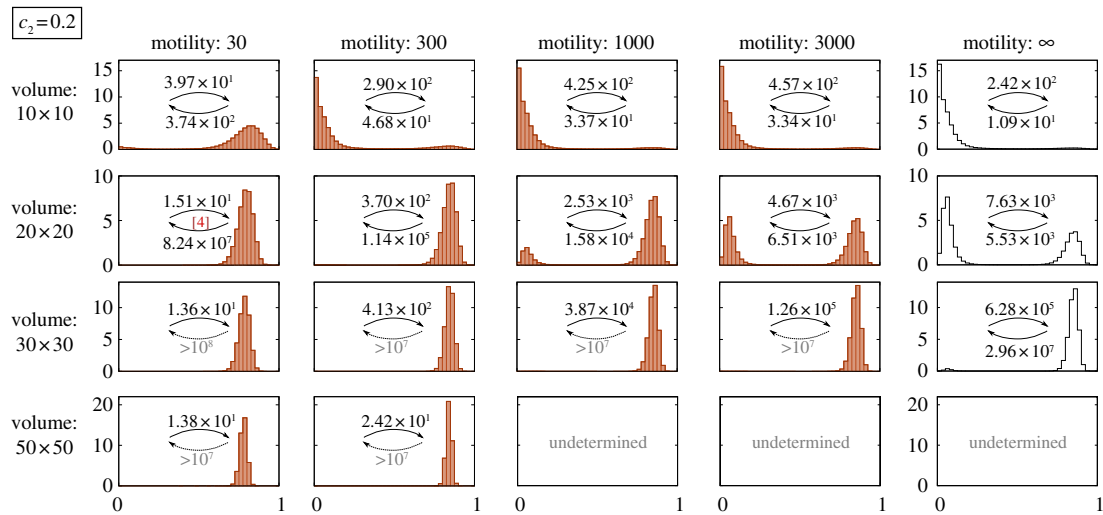
Figure 2. SPDs for different motility coefficients and square domains of different sizes. The lattice-based KMC simulations were performed on toroidal domains (i.e. square domains with periodic boundary conditions) for ($c_1 = 0.02$, $c_2 = 0.2$) and the remaining parameters with their default values: $c_3 = 4$, $c_0 = 1$. In the last column, SPDs were obtained using (spatially homogeneous) Gillespie algorithm simulations. The MFPTs τ_{on} and τ_{off} are shown in each panel. A small number in square brackets reports the number of observed switches n_{on} or n_{off} if smaller than 20. The SPD is marked as 'undetermined' when no switches were observed during simulations. (Online version in colour.)

chance for a stochastic state-to-state transition is negligible at the considered time scale.

Although in the above considerations we used D, in the further analysis of the on-lattice system the speed of diffusion will be expressed in terms of the motility M. According to equation (2.5), for default parameters in non-dimensionalized units $M = 8D$.

3.2. Different preferred steady states of the stochastic system and its deterministic approximation

The bistability domain of equations (2.8a–c) in the (c_1, c_2) parameter space for fixed $c_3 = 4$ and $c_0 = 1$ is shown in figure 1. The domain is divided by the $c_2(c_1)$ line (dashed) on which the standing wave solutions exist. These heteroclinic solutions connect the active and inactive stable steady states. For parameters from above the dashed line, travelling waves propagate from the active to the inactive state. This can be interpreted as the domination of the active steady state. For parameters below the line, the travelling waves propagate in the opposite direction, i.e. the inactive state is dominant. This deterministic separatrix (dashed line) can be compared with the separatrix for the stochastic perfectly mixed system (dotted line). For parameters from the latter line the SPD of the perfectly mixed process described by reactions (2.1a–2.4b) remains bimodal in the limit of the infinite reactor volume. In the same limit, for parameters above (below) the line, the SPD converges to the Dirac delta in the active (inactive) steady state [17]. Interestingly, these two separatrices do not overlap and they delineate a region where the system of PDEs prefers the active state, while the stochastic perfectly mixed system in the limit of the infinite reactor volume is inactive. The divergence of these separatrices suggests that for realistic reactors characterized by a finite diffusion the choice between the active and the inactive state depends on the speed of diffusion and the size or even shape of the reactor [20].

3.3. Diffusion and size of the reactor control system activity

Here, we analyse the expected activity of the kinase–phosphatase system by means of the SPD obtained in on-lattice KMC simulations, as a function of the compartment volume (surface) V and reactants motility coefficient M. First, let us remember that when $M \rightarrow \infty$ the SPD from on-lattice KMC simulations converges to that obtained from Gillespie KMC simulations ($M = \infty$). For $M = 3000$, the difference is still discernible (last two columns in figure 2) but the agreement becomes nearly perfect for $M = 10\,000$ (see the electronic supplementary material, figure S1c). In figure 2, we consider the case of ($c_1 = 0.02$, $c_2 = 0.2$), for which the stochastic system and its deterministic approximation are preferentially in the active state. As shown, the probability of the active state increases with V for finite M as well as in the limit of the perfectly mixed reactor ($M = \infty$, last column in figure 2). For large motility ($M \geq 300$), the active state probability increases from nearly 0 to almost 1 as the compartment volume increases from $V = 10 \times 10$ to $V = 30 \times 30$. It demonstrates that the relative stability of steady states is controlled by the volume of the reactor. For perfectly mixed systems, this effect has been reported previously by Zheng *et al.* [53].

In figure 3, we consider a more interesting case of ($c_1 = 0.02$, $c_2 = 0.15$), for which the stochastic perfectly mixed system is preferentially in the inactive state, but its deterministic approximation is preferentially active. In this case, in addition to the compartment volume, the activity of the system is controlled by the substrate motility M. For chosen parameters, the system is preferentially in the active state for small motility ($M = 30$) and in the inactive state for large motility ($M \geq 1000$). For intermediate values ($100 \leq M \leq 300$), the choice of the dominant state is controlled by the volume of the reactor. The tendency of the system to inactivate as $M \rightarrow \infty$ is visible also in figure 2, although it is pronounced only for small system volumes, for which the perfectly mixed system remains prevalently in the inactive state.
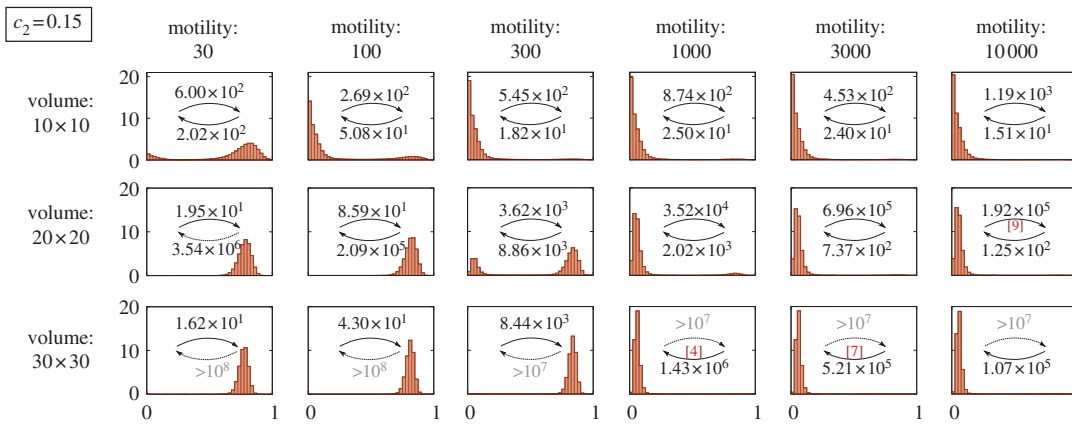
Figure 3. SPDs for different motility coefficients and square domains of different sizes. The simulations are in the same set-up as for figure 2 but with kinase activity coefficient $c_2 = 0.15$ (instead of $c_2 = 0.2$). (Online version in colour.)

In the subsequent analysis, we employ the mean first-passage time of the transition from the inactive to active steady state τ_{on} and the time for the reverse transition τ_{off}. At large substrate motility ($M \geq 1000$), MFPTs (given in each panel of figures 2 and 3) increase dramatically with the volume of the compartment. It is known that in a perfectly mixed reactor MFPTs increase exponentially with its volume [9]. In the case of finite motility, the situation is more complicated. Let us consider the case of a fixed motility for which one can determine a characteristic distance λ and the well-mixed sub-volume V_0. When the reactor diameter exceeds λ, it should be considered as a composition of multiple ($\approx V/V_0$) well-mixed sub-reactors. In such a structured reactor, the transition to the active steady state can result from a stochastic switch occurring in any of these sub-reactors, followed by the propagation of the activating wave, as discussed in §3.4. In this regime, τ_{on} decreases with the number of well-mixed sub-compartments ($\approx V/V_0$), and thus it is inversely proportional to the volume of the reactor, $\tau_{on} \propto 1/V$. These diverging limiting behaviours jointly result in the non-monotonic dependence of τ_{on} on the volume of the reactor (figure 4a): τ_{on} increases exponentially until the volume of the reactor V exceeds the volume of the well-mixed compartment V_0, and then decreases with the reactor volume as $\tau_{on} \propto 1/V$. Since larger motility implies larger perfectly mixed sub-volumes, the volume of the reactor for which the MFPT reaches its maximum increases with motility. The activation and inactivation processes are not symmetric, because for given parameters either activating or inactivating travelling waves may propagate. For the parameters considered in figure 4a, the activating travelling waves propagate. As a result, after a local inactivation, the activity is promptly recovered by waves from surrounding subcompartments, and thus the only possible mode of transition towards inactivity requires simultaneous inactivation of the whole reactor. Consequently, while τ_{on} decreases for small motility ($V > V_0$ regime) and increases for large motility ($V < V_0$ regime), τ_{off} grows exponentially with V in both regimes (figures 2 and 3).

Irrespective of the volume of the reactor and for both considered values of c_2, one can observe that for sufficiently low motility the active state is preferred. There are two properties of the system that give rise to such behaviour at decreased motility: (i) in addition to the less effective distributive mechanism, the more effective processive phosphorylation reactions are more likely to happen (when two kinase molecules stay in
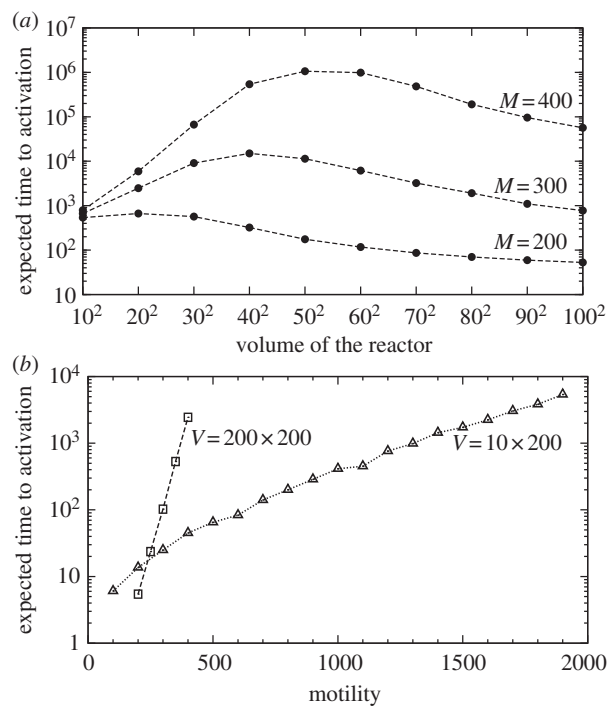

Figure 4. (a) Mean first-passage time for activation τ_{on} as a function of the volume V of the square-shaped reactor with periodic boundary conditions, obtained in on-lattice KMC simulations for three values of motility and ($c_1 = 0.02$, $c_2 = 0.15$), and other parameters with default values. For small V, τ_{on} grows exponentially with V (well-mixed regime), while for large V, τ_{on} decreases as $1/V$. Every τ_{on} is a maximum-likelihood estimate from a time series with fixed censoring time, calculated based on thousands of trajectories and at least $n_{on} = 10$ observed switches. (b) Dependence of τ_{on} on the motility M for reactors of two different geometries, for the same parameters as in (a). For the square-shaped reactor, the expected τ_{on} grows exponentially with increasing motility M; for the long rectangular reactor with periodic boundary conditions, τ_{on} grows faster than $\sim \exp(\sqrt{M})$ but slower than $\sim \exp(M)$.

contact longer, it is more probable that the substrate kinase will be phosphorylated twice by the same catalytic kinase; also, once the substrate kinase is phosphorylated it becomes more amenable to 'fire back' and to activate the first kinase) and (ii) the catalytic capacity of less abundant phosphatase molecules becomes dampened after they saturate their
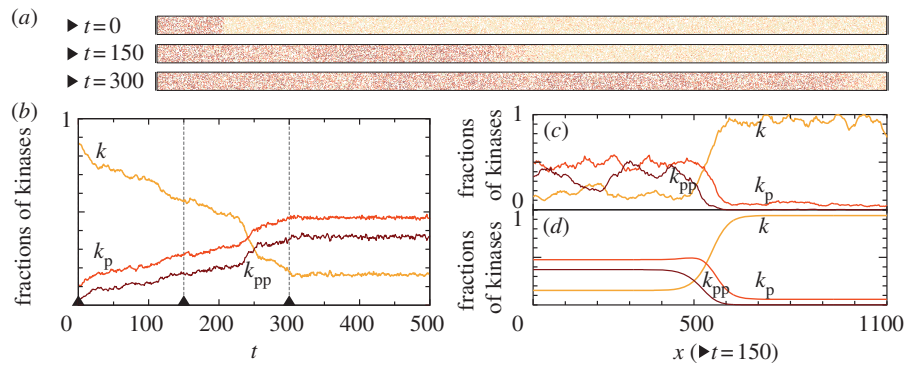
Figure 5. Kinase activity wave propagation on the cylindrical domain 30×1100 for parameters ($c_1 = 0.02$, $c_2 = 0.15$) and $M = 3000$. At $t = 0$, a fragment of the cylinder (30×100) is in the active state. (*a*) Three snapshots from an on-lattice KMC simulation. (*b*) Time profile of the kinase activity profile integrated over the whole domain. (*c*) Kinase activity profile across the domain at time $t = 150$, averaged using the sliding window of width $w = 11$. (*d*) Kinase activity profile obtained from corresponding PDEs in COMSOL. (Online version in colour.)

neighbourhoods (a phosphatase molecule can dephosphorylate all kinases in its vicinity, rendering itself idle).

3.4. Propagation of waves of kinase activity on cylindrical domains

In this section, we consider travelling wave propagation on long cylindrical domains. Elongated thin membrane protrusions constitute, for example, pseudopodia of motile cells and dendritic spines of neurons. First, we focus on parameters ($c_1 = 0.02$, $c_2 = 0.15$) lying in the range in which the preferred steady states for well-mixed and spatially extended reactors diverge (figure 1). For these parameters and large motility, $M = 3000$, the 30×30 reactor is principally inactive (figure 3). However, in a semi-one-dimensional array of a large number of such reactors the activating travelling waves can propagate as predicted by the deterministic approximation, equations ($2.8a$–c). In figure $5a$, we show snapshots from on-lattice KMC simulations of the stochastic travelling wave in the cylindrical domain 30×1100 (top–bottom boundary conditions are periodic, left–right reflecting). At $t = 0$, the left 30×100 area ('seed') is assigned to be in the active steady state and the rest of the cylinder, 30×1000, is set to the inactive state. At the very beginning of the simulation, the transition between the active and the inactive region becomes smooth and a wave profile is formed, which then propagates so that eventually the whole reactor adopts the active steady state (figure $5a,b$). This surprising divergence of system behaviours in a small 30×30 and in a long 30×1100 reactor is due to the fact that motility $M = 3000$ renders the small reactor mixed, but it is by far too small to mix the longer reactor: $30/2 < \lambda \ll 1100$, where $30/2$ is the effective diameter of the 30×30 reactor in periodic boundary conditions, and $\lambda = \sqrt{M/(2c_0)}$. Therefore, in the long reactor, the system converges to the attractor preferred by the deterministic approximation. Moreover, since the number of molecules on the wavefront (the width of which grows $\propto \sqrt{M/c_0}$) is quite large, the stochastic wave profile resembles the deterministic profile obtained from PDEs (figure $5c,d$).

For parameters (c_1,c_2) below the deterministic standing wave line (figure 1), the travelling wave can propagate in the opposite direction such that the whole system becomes inactive, provided that the diffusion is sufficiently fast, as discussed in §3.5 (see the electronic supplementary material, figure S6).
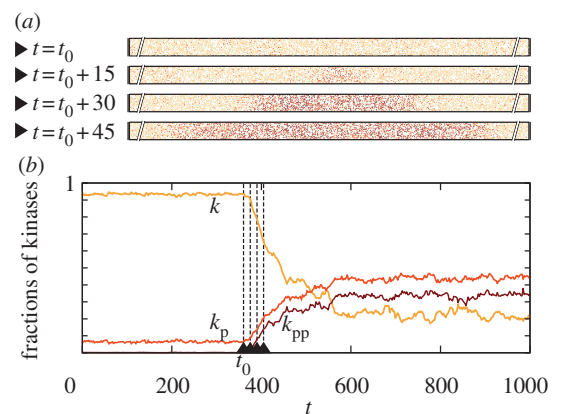

Figure 6. Spontaneous initiation of the activity wave in a subdomain of the cylindrical domain 20×1000 for parameters ($c_1 = 0.02$, $c_2 = 0.15$) and $M = 1000$. The expected waiting time for the activation is $\tau_{on} = 596$ s. (*a*) Four snapshots from an on-lattice KMC simulation (inessential parts of the reactor are truncated) and (*b*) time profile. (Online version in colour.)

With increasing motility, the velocity of the wave in on-lattice KMC simulations approaches the velocity in PDEs, which is $\propto \sqrt{Mc_0}$ (see the electronic supplementary material, figure S3). The number of molecules on the length of the wavefront increases with motility and, as a consequence of the reduced noise, at higher motilities the activating front propagates more steadily. The size of the activating seed also increases with motility and at higher motilities seeds are more likely to be swept away (see the electronic supplementary material, figure S2). Consequently, as we will see in §3.5, at large motility the stochastic wave initiations are much less frequent: they need the creation of a larger seed, and thus the initiating stochastic fluctuation must involve a larger number of molecules.

3.5. Spontaneous wave activation

The two already discussed transition modes, the stochastic switching in a well-mixed system and semi-deterministic travelling wave propagation in a spatially extended system, can work in conjunction. The initially inactive system can be excited owing to a local fluctuation, which could in turn initiate an activating travelling wave. We investigate this mechanism in the system with ($c_1 = 0.02$, $c_2 = 0.15$) and $M = 1000$ in the semi-one-dimensional reactor of $V = 20 \times 1000$ (figure 6). A spontaneous local activation, occurring in
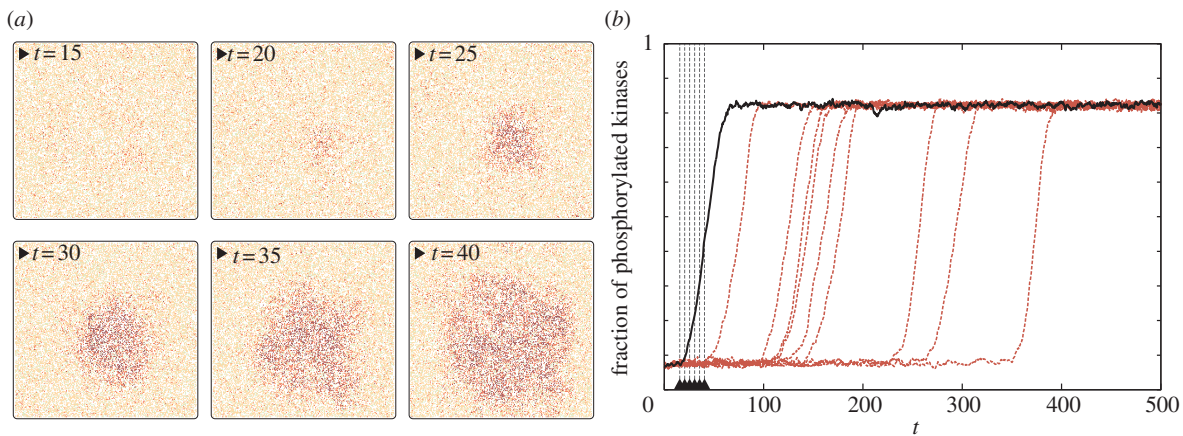
(a)

▶ t = 15   ▶ t = 20   ▶ t = 25

▶ t = 30   ▶ t = 35   ▶ t = 40

(b)

Figure 7. Spontaneous initiation of the activity wave on the square domain 200×200 for parameters ($c_1 = 0.02$, $c_2 = 0.15$) and $M = 300$. For larger motility $M = 1000$, activity waves were not self-initiated. Snapshots in (a) correspond to the trajectory represented by the solid black line in (b). (Online version in colour.)

a random place of the reactor, gives rise to two fronts, which propagate in opposite directions, driving the whole reactor to the active state. The average time to switch on was estimated as $\tau_{on}^{20 \times 1000} = 596$ (from $n_{on} = 16$ switches). Based on the analysis in §§3.3 and 3.4, the activation mechanism can be understood as follows: the 20×1000 reactor can be considered as an array of 50 smaller 20×20 sub-reactors. These small sub-reactors switch on and off with switching times $\tau_{on}^{20 \times 20} = 3.52 \times 10^4$, $\tau_{off}^{20 \times 20} = 2.02 \times 10^3$ (figure 3). Thus, the expected time to switch on in the whole reactor can be estimated as $\tau_{on} = \tau_{on}^{20 \times 20}/50 = 700$, which agrees (unexpectedly well) with the measured $\tau_{on}^{20 \times 1000} = 596$.

The same reasoning fails for a two-dimensional reactor of $V = 200 \times 200$. For the same parameters, a spontaneous activation was not observed in long simulations (with total simulation time $\approx 2 \times 10^4$). In the two-dimensional case, the spontaneously appearing seeds of activity are extinguished by the inactive neighbourhood more easily than in the reactor of cylindrical geometry. The spontaneous activation was observed only after reducing motility to $M = 300$ (figure 7).

Increasing motility increases the number of communicated molecules and thus reduces the switch rate: τ_{on} grows exponentially with the motility in the case of the two-dimensional reactor (figure 4b). One could expect that $\tau_{on}(M)$ for the one-dimensional reactor grows $\propto \exp(\sqrt{M})$. However, such dependence does not fit well to obtained data points, although it yields a better fit than $\tau_{on} \propto \exp(M)$. The divergence from the '$\propto \exp(\sqrt{M})$' prediction can be due to the fact that in the cylindrical reactor $\tau_{on}(M)$ spans the large range of motilities involving the change of the stochastically preferred steady state (figure 3).

The observation that the reduced motility increases the probability of system activation suggests that regions of reduced diffusivity can serve as ignition points for the activation of the whole reactor. We verified this hypothesis by performing simulations of the 200×200 domain with a spatially varying diffusion coefficient. The overall motility was set to $M = 1000$, while in a circular region of $r = 14$ motility was reduced 10 times to $M_{patch} = 100$. In order to minimize possible peculiarities caused by the sharp jump on the brink of the patch, the motility in its vicinity was increasing linearly, concentrically until reaching the outer circle of radius $r' = r + 10$, beyond which $M = 1000$. Within this set-up, we observed that

the patch of lowered diffusivity acts as an ignition centre: stochastic activation switches are much more probable in this region, and the local activation, with some probability, again, can start the semi-deterministic travelling wave (figure 8). As one can expect, τ_{on} decreases sharply with the radius of the patch (see the electronic supplementary material, figure S7).

For completeness, it should be noted that, when the stochastic and deterministic global attractors coincide in the active state (which happens for parameters c_1 and c_2 above the stochastic bimodality curve in figure 1), the initially inactive system is more likely to be activated by local stochastic fluctuations: for small diffusion, the activating seeds plausibly appear in several places simultaneously, giving rise to several travelling fronts (see the electronic supplementary material, figure S4).

In the already considered case of ($c_1 = 0.02$, $c_2 = 0.06$) depicted in the electronic supplementary material, figure S6, the stochastic and deterministic global attractors coincide in the inactive state. In this case, simultaneous local inactivations can occur probably in various places of the compartment. To avoid spontaneous switching and illustrate the possibility of the propagation of the inactivating wave, we considered $M = 10\,000$ in the wider 50×1100 reactor, where stochastic switches are rare.

Interestingly, in the 30×1000 toroidal domain at $M = 300$, the reactor is able to maintain a fractional activity (see the electronic supplementary material, figure S5). Since in the parameter space the point ($c_1 = 0.02$, $c_2 = 0.06$) is closer to the curve of the deterministic standing wave than point ($c_1 = 0.02$, $c_2 = 0.2$), it can be expected that for ($c_1 = 0.02$, $c_2 = 0.06$) inactivating travelling waves are not formed as easily as activating waves for ($c_1 = 0.02$, $c_2 = 0.2$). Hence, scattered local *on* or *off* switches do not propagate; they render the reactor dynamically yet persistently spatially structured. As a consequence, most of the probability mass is contained between stable steady states of the deterministic system, in contrast to all previously analysed cases.

4. Discussion

In this study, in order to understand the principal mechanisms of biochemical information processing and cellular
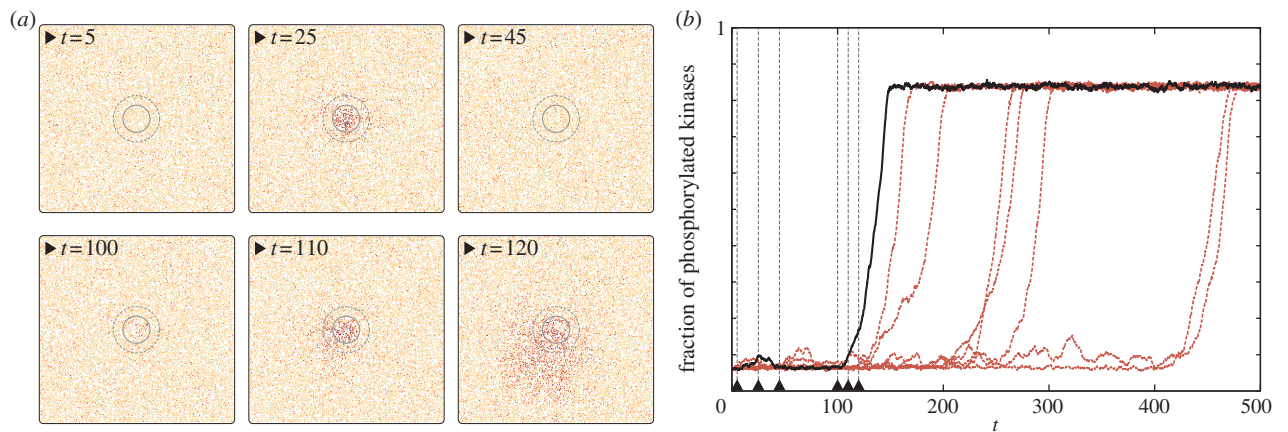
(a)

(b)

Figure 8. Activity wave initiation in the domain 200 × 200 owing to the locally reduced motility coefficient ($M = 100$ in the inner circle, $M = 1000$ outside the outer circle, and gradually increasing M in between circles) for parameters ($c_1 = 0.02$, $c_2 = 0.15$). Snapshots in (a) correspond to the trajectory represented by the solid black line in (b). (Online version in colour.)

decision-making, we systematically investigated transition modes available to a generic bistable reaction system in the spatially extended reactor. We used primarily microscopic simulations on the two-dimensional lattice complemented by the analysis of approximations neglecting either stochasticity or spatial resolution. In the well-mixed compartment (the size of which is determined by the diffusion coefficient), the transition rates between macroscopic steady states of the system decrease exponentially with the number of reacting molecules or the size of the compartment. In larger, non-mixed compartments, transition rates are controlled by the number of diffusively communicated molecules, which is typically much smaller than the total number of molecules. We demonstrated that the local stochastic state-to-state transitions occasionally initiate travelling waves, which expand in the semi-deterministic manner leading to the (in)activation of the whole reactor: either a local activation or inactivation can be amplified spatially, depending on the reaction rate constants. At increasing diffusivity, more molecules become communicated and local transitions become less probable. On the other hand, travelling waves can propagate only when the diffusion is sufficiently fast. At large diffusion coefficients, the wavefronts are thicker, contain more molecules and thus are less affected by fluctuations. As a result, in the limit of large diffusion, the velocity of a wavefront in the discrete stochastic system converges to that of its deterministic approximation modelled by PDEs.

Importantly, there exists a range of parameters for which the macroscopic, stochastically preferred steady state (or global stochastic attractor, i.e. the state which is prevalently occupied in a perfectly mixed regime) is different from the steady state preferred deterministically (or global deterministic attractor, i.e. the state which expands as a result of the propagation of travelling waves) [17,20]. We demonstrated that in this range of parameters, even when a small compartment is predominantly inactive, a travelling wave may spread the active state over the larger reactor. If parameters are such that global stochastic and deterministic attractors converge (in either the active or inactive state), the system is effectively monostable, i.e. the escapes from the 'less stable' macroscopic steady state can arise spontaneously with a high probability. Consequently, the reactor settles in the more stable steady state or remains

spatially heterogeneous with its regions flipping between steady states, giving rise to transient clans of activated molecules [37]. Our macroscopic analysis thus implies that the well-known mechanism of state-to-state transitions arising in bistable reaction–diffusion systems is restricted only to the sub-domain of the bistability domain in the parameter space. Only these bistable systems which exploit in the parameter space the region of diverging stochastic and deterministic attractors are expected to be both resistant to spontaneous autoactivation (caused by stochastic switching) and sensitive to external stimuli (allowing for deterministic activation by means of the propagation of travelling waves). This physiologically relevant region in the parameter space (delineated by two separatrices in figure 1) grows with the increasing differences between reaction rate constants, $c_1 < c_2 < c_3$. We note that the catalytic activity of a kinase can grow with its phosphorylation level even stronger than is assumed in the analysed system, i.e. kinetic rate constants can span several orders of magnitude: $c_1 \ll c_2 \ll c_3$ [54].

In living cells, travelling waves may be induced by an external stimulus; for example, upon binding of a specific extracellular ligand (antigen and chemoattractant) by membrane receptors. We demonstrated that partial immobilization of a tiny fraction of kinases on the membrane may lead to the global activation of the system. Since the locally constrained motility does not lead to a locally increased surface concentration of molecules, this activation mechanism is different from the recently proposed density-dependent switch [30]. In the mechanism introduced here, there is an inherent threshold number of activated clustered molecules required for triggering a travelling wave with a sufficiently high probability. It has been proposed theoretically and recently investigated numerically that a tiny fraction of membrane receptors clustered upon binding of antigens are capable of initiating immunogenic responses in B cells (see [55] and references therein). In other cases, proteins can become co-sequestered in lipid microdomains after the activation. Such confinement reduces their lateral diffusion and presumably facilitates subsequent signalling events [56].

We analysed exhaustively the SPD with respect to the diffusion coefficient and size of the reactor. In the context of the recruitment of cytoplasmic proteins to the membrane milieu,

Abel *et al.* [57] showed that decreasing motility or altering the depth of a submembrane layer promotes or suppresses SPD bimodality, depending on the topology of the interaction network. In their case, the unimodal distribution arises from averaging over the reactor and peaks between two steady states. In the system analysed in this study, the unimodality results from the preference of one of two steady states of the deterministic approximation. We showed that the SPD is controlled by both the motility of molecules and the volume of the reaction chamber. In our case, a single reaction rate parameter dictates the state to which the system converges at the increasing diffusivity. We found that, despite the system being bistable, the SPDs may be bimodal only in small well-mixed compartments. Large compartments have, generically, unimodal SPDs analogously to the perfectly mixed systems of large numbers of molecules [20,58].

In a spatially extended system, which in the case of slow diffusion can be considered as a composition of multiple well-mixed reactors, the expected time to activation has been shown to shorten with increasing volume, which is in stark contrast to a perfectly mixed reactor, for which the time increases exponentially with the volume. Furthermore, spatially extended reactors of similar volumes but different geometries can have vastly different expected times to activation. In a two-dimensional reactor, the minimal size of the 'nucleation centre' required for the initiation of a wave is larger than in a semi-one-dimensional reactor, and thus the expected time to the stochastic activation is longer. Propagation of waves is also dependent on the reactor geometry. In a semi-one-dimensional reactor, the front curvature is negligible, while in a two-dimensional reactor the curvature reduces the velocity of the travelling front, and may prohibit spreading of the wave when the initial cluster is too small [55].

Our work provides further evidence that biochemical reactions on the membrane can be reproduced only with spatial stochastic simulations. In addition to the discussed phenomena, in which local stochastic fluctuations lead to global state-to-state transitions not captured by deterministic reaction–diffusion equations, we found that in the discrete system the effective reaction rates are controlled by the diffusion. It can be observed that, in the case of slow diffusion, the more effective processive phosphorylation mode prevails over the less efficient distributive mechanism, boosting the system's activity [59,60]. Additionally, molecular crowding (and self-crowding), which is reflected explicitly in our lattice-based simulations and is expected to be significant at assumed surface densities of reacting molecules, facilitates consecutive phosphorylation events [61,62]. In the well-mixed approximation, kinases are dephosphorylated at the rate proportional to the product of phosphatase activity and the number of phosphatases. Phosphatases, which are modelled explicitly in spatial simulations, can become unemployed after dephosphorylating all their neighbouring kinases, resulting in the reduction of their effective enzymatic activity [63].

The applied method of on-lattice KMC simulates the master equation in continuous time and discretized space at the single event and single molecule resolution. For large systems, such simulations are inevitably computationally demanding, but provide accurate estimations of MFPTs, which are crucial for the performed analysis. Spatially or temporally coarse-grained algorithms have lower computational cost but also lower, in fact unknown, accuracy. The results presented in this paper consumed years of aggregate CPU time of a computer cluster, but in the hope that they could be used to calibrate faster approximate algorithms.

In summary, transitions in a bistable system on the membrane employ both stochastic and deterministic effects. Transitions between macroscopic steady states of spatially extended systems are qualitatively different from transitions available in well-mixed compartments. These transitions employ travelling waves that can be initiated spontaneously as a result of stochastic fluctuations. We demonstrated that the SPD and MFPTs depend strongly on the diffusion coefficient, size and shape of the reactor. These factors (in addition to reaction rates) decide the activity (or inactivity) of a spatially extended bistable system.

References

1. Huang S, Eichler G, Bar-Yam Y, Ingber DE. 2005 Cell fates as high-dimensional attractor states of a complex gene regulatory network. *Phys. Rev. Lett.* **94**, 128701. (doi:10.1103/PhysRevLett.94.128701)

2. Ozbudak EM, Thattai M, Lim HN, Shraiman BI, Oudenaarden AV. 2004 Multistability in the lactose utilization network of *Escherichia coli*. *Nature* **427**, 737–740. (doi:10.1038/nature02298)

3. Smits WK, Kuipers OP, Veening J-W. 2006 Phenotypic variation in bacteria: the role of feedback regulation. *Nat. Rev. Microbiol.* **4**, 259–271. (doi:10.1038/nrmicro1381)

4. Ferrell JE. 2002 Self-perpetuating states in signal transduction: positive feedback, double-negative feedback and bistability. *Curr. Opin. Cell Biol.* **14**, 140–148. (doi:10.1016/S0955-0674(02)300314-9)

5. Das J, Ho M, Zikherman J, Govern C, Yang M, Weiss A, Chakraborty AK, Roose JP. 2009 Digital signaling and hysteresis characterize Ras activation in lymphoid cells. *Cell* **136**, 337–351. (doi:10.1016/j.cell.2008.11.051)

6. van Kampen N. 2007 *Stochastic processes in physics and chemistry*. Amsterdam, The Netherlands: Elsevier.

7. Gardiner CW. 1985 *Handbook of stochastic methods for physics, chemistry and the natural sciences*, 2nd edn. Berlin, Germany: Springer.

8. Nicolis G, Prigogine I. 1977 *Self-organization in non-equilibrium systems*. Hoboken, NJ: Wiley.

9. Vellela M, Qian H. 2009 Stochastic dynamics and non-equilibrium thermodynamics of a bistable chemical system: the Schlögl model revisited. *J. R. Soc. Interface* **6**, 925–940. (doi:10.1098/rsif.2008.0476)

10. Kasai RS, Suzuki KGN, Prossnitz ER, Koyama-Honda I, Nakada C, Fujiwara TK, Kusumi A. 2011 Full characterization of GPCR monomer–dimer dynamic equilibrium by single molecule imaging. *J. Cell. Biol.* **192**, 463–480. (doi:10.1083/jcb.201009128)

11. Kalay Z, Fujiwara TK, Kusumi A. 2012 Confining domains lead to reaction bursts: reaction kinetics in the plasma membrane. *PLoS ONE* **7**, e32948. (doi:10.1371/journal.pone.0032948)

12. Elowitz MB, Surette MG, Wolf PE, Stock JB, Leibler S. 1999 Protein mobility in the cytoplasm of *Escherichia coli*. *J. Bacteriol*. **181**, 197–203.

13. Ramadurai S, Holt A, Krasnikov V, van den Bogaart G, Killian JA, Poolman B. 2009 Lateral diffusion of membrane proteins. *J. Am. Chem. Soc*. **131**, 12 650–12 656. (doi:10.1021/ja902853g)

14. Faeder JR, Hlavacek WS, Reischl I, Blinov ML, Metzger H, Redondo A, Wofsy C, Goldstein B. 2003 Investigation of early events in FcεRI-mediated signaling using a detailed mathematical model. *J. Immunol*. **170**, 3769–3781.

15. Bishop LM, Qian H. 2010 Stochastic bistability and bifurcation in a mesoscopic signaling system with autocatalytic kinase. *Biophys. J*. **98**, 1–11. (doi:10.1016/j.bpj.2009.09.055)

16. Murray JD. 2007 *Mathematical biology*. New York, NY: Springer.

17. Nicolis G, Lefever R. 1977 Comment on the kinetic potential and the Maxwell construction in non-equilibrium chemical phase transitions. *Phys. Lett. A* **62**, 469–471. (doi:10.1016/0375-9601(77)90069-X)

18. Baras F, Malek Mansour M. 1997 Microscopic simulations of chemical instabilities. *Adv. Chem. Phys*. **100**, 393–474. (doi:10.1002/9780470141595.ch5)

19. Ge H, Qian H. 2009 Thermodynamic limit of a nonequilibrium steady state: Maxwell-type construction for a bistable biochemical system. *Phys. Rev. Lett*. **103**, 148103. (doi:10.1103/PhysRevLett.103.148103)

20. Zuk PJ, Kochańczyk M, Jaruszewicz J, Bednorz W, Lipniacki T. 2012 Dynamics of a stochastic spatially extended system predicted by comparing deterministic and stochastic attractors of the corresponding birth–death process. *Phys. Biol*. **9**, 055002. (doi:10.1088/1478-3975/9/5/055002)

21. Baras F, Malek Mansour M, Pearson JE. 1996 Microscopic simulation of chemical bistability in homogeneous systems. *J. Chem. Phys*. **105**, 8257–8261. (doi:10.1063/1.472679)

22. Bird GA. 1994 *Molecular gas dynamics and the direct simulation of gas flows*. Oxford, UK: Clarendon.

23. Stamatakis M, Vlachos DG. 2011 Equivalence of on-lattice stochastic chemical kinetics with the well-mixed chemical master equation in the limit of fast diffusion. *Comput. Chem. Eng*. **35**, 2602–2610. (doi:10.1016/j.compchemeng.2011.05.008)

24. Potma EO, de Boeij WP, Bosgraaf L, Roelofs J, van Haastert PJ, Wiersma DA. 2001 Reduced protein diffusion rate by cytoskeleton in vegetative and polarized dictyostelium cells. *Biophys. J*. **81**, 2010–2019. (doi:10.1016/S0006-3495(01)75851-1)

25. Sbalzarini IF, Mezzacasa A, Helenius A, Koumoutsakos P. 2005 Effects of organelle shape on fluorescence recovery after photobleaching. *Biophys. J*. **89**, 1482–1492. (doi:10.1529/biophysj.104.057885)

26. Luby-Phelps K. 2000 Cytoarchitecture and physical properties of cytoplasm: volume, viscosity, diffusion, intracellular surface area. *Int. Rev. Cytol*. **192**, 189–221. (doi:10.1016/S0074-7696(08)60527-6)

27. Lu S, Ouyang M, Seong J, Zhang J, Chien S, Wang Y. 2008 The spatiotemporal pattern of Src activation at lipid rafts revealed by diffusion-corrected FRET imaging. *PLoS Comput. Biol*. **4**, e1000127. (doi:10.1371/journal.pcbi.1000127)

28. Kalwarczyk T *et al*. 2011 Comparative analysis of viscosity of complex liquids and cytoplasm of mammalian cells at the nanoscale. *Nano Lett*. **11**, 2157–2163. (doi:10.1021/nl2008218)

29. Altschuler SJ, Angenent SB, Wang Y, Wu LF. 2008 On the spontaneous emergence of cell polarity. *Nature* **454**, 886–889. (doi:10.1038/nature07119)

30. Jilkine A, Angenent SB, Wu LF, Altschuler SJ. 2011 A density-dependent switch drives stochastic clustering and polarization of signaling molecules. *PLoS Comput. Biol*. **7**, e1002271. (doi:10.1371/journal.pcbi.1002271)

31. Das J, Kardar M, Chakraborty AK. 2009 Positive feedback regulation results in spatial clustering and fast spreading of active signaling molecules on a cell membrane. *J. Chem. Phys*. **130**, 245102. (doi:10.1063/1.3149861)

32. Postma M, Roelofs J, Goedhart J, Gadella TWJ, Visser AJWG, Haastert PJMV. 2003 Uniform cAMP stimulation of Dictyostelium cells induces localized patches of signal transduction and pseudopodia. *Mol. Biol. Cell*. **14**, 5019–5027. (doi:10.1091/mbc.E03-08-0566)

33. Hecht I, Kessler DA, Levine H. 2010 Transient localized patterns in noise-driven reaction–diffusion systems. *Phys. Rev. Lett*. **104**, 158301. (doi:10.1103/PhysRevLett.104.158301)

34. Fange D, Elf J. 2006 Noise-induced Min phenotypes in *E. coli*. *PLoS Comput. Biol*. **2**, e80. (doi:10.1371/journal.pcbi.0020080)

35. Malek Mansour M, Dethier J, Baras F. 2001 Onset of homogeneous oscillations in reactive systems. *J. Chem. Phys*. **114**, 9265–9275. (doi:10.1063/1.1367389)

36. Lee S-JR, Escobedo-Lozoya Y, Szatmari EM, Yasuda R. 2009 Activation of CaMKII in single dendritic spines during long-term potentiation. *Nature* **458**, 299–304. (doi:10.1038/nature07842)

37. Elf J, Ehrenberg M. 2004 Spontaneous separation of bi-stable biochemical systems into spatial domains of opposite phases. *Syst. Biol*. **1**, 230–236. (doi:10.1049/sb:20045021)

38. Arai Y, Shibata T, Matsuoka S, Sato JM, Yanagida T, Ueda M. 2010 Self-organization of the phosphatidylinositol lipids signaling system for random cell migration. *Proc. Natl Acad. Sci. USA* **107**, 12 399–12 404. (doi:10.1073/pnas.0908278107)

39. Mori Y, Jilkine A, Edelstein-Keshet L. 2008 Wave-pinning and cell polarity from a bistable reaction–diffusion system. *Biophys. J*. **94**, 3684–3697. (doi:10.1529/biophysj.107.120824)

40. Walther GR, Marée AFM, Edelstein-Keshet L, Grieneisen VA. 2012 Deterministic versus stochastic cell polarisation through wave-pinning. *Bull. Math. Biol*. **74**, 2570–2599. (doi:10.1007/s11538-012-9766-5)

41. Xiong Y, Huang C-H, Iglesias PA, Devreotes PN. 2010 Cells navigate with a local-excitation, global-inhibition-biased excitable network. *Proc. Natl Acad. Sci. USA* **107**, 17 079–17 086. (doi:10.1073/pnas.1011271107)

42. Jilkine A, Edelstein-Keshet L. 2011 A comparison of mathematical models for polarization of single eukaryotic cells in response to guided cues. *PLoS Comput. Biol*. **7**, e1001121. (doi:10.1371/journal.pcbi.1001121)

43. Huang Q, Qian H. 2009 Ultrasensitive dual phosphorylation dephosphorylation cycle kinetics exhibits canonical competition behavior. *Chaos* **19**, 033109. (doi:10.1063/1.3187790)

44. Lisman JE. 1985 A mechanism for memory storage insensitive to molecular turnover: a bistable autophosphorylating kinase. *Proc. Natl Acad. Sci. USA* **82**, 3055–3057. (doi:10.1073/pnas.82.9.3055)

45. Markevich NI, Hoek JB, Kholodenko BN. 2004 Signaling switches and bistability arising from multisite phosphorylation in protein kinase cascades. *J. Cell. Biol*. **164**, 353–359. (doi:10.1083/jcb.200308060)

46. Wilhelm T. 2009 The smallest chemical reaction system with bistability. *BMC Syst. Biol*. **3**, 90. (doi:10.1186/1752-0509-3-90)

47. Schlögl F. 1971 On thermodynamics near a steady state. *Z. Physik*. **248**, 446–458. (doi:10.1007/BF01395694)

48. Ferrell JE, Xiong W. 2001 Bistability in cell signaling: how to make continuous processes discontinuous, and reversible processes irreversible. *Chaos* **11**, 227–236. (doi:10.1063/1.1349894)

49. Phillips R, Ursell T, Wiggins P, Sens P. 2009 Emerging roles for lipids in shaping membrane-protein function. *Nature* **459**, 379–385. (doi:10.1038/nature08147)

50. Gillespie DT. 1977 Exact stochastic simulation of coupled chemical reactions. *J. Phys. Chem*. **81**, 2340–2361. (doi:10.1021/j100540a008)

51. Lawless JF. 2003 *Statistical models and methods for lifetime data*. Hoboken, NJ: Wiley-Interscience.

52. Kuramoto Y. 1974 Effects of diffusion on the fluctuations in open chemical systems. *Prog. Theor. Phys*. **52**, 711–713. (doi:10.1143/PTP.52.711)

53. Zheng Q, Ross J, Hunt KLC, Hunt PM. 1992 Stationary solutions of the master equation for single and multi-intermediate autocatalytic chemical systems. *J. Chem. Phys*. **96**, 630–640. (doi:10.1063/1.462446)

54. Alessi DR, Saito Y, Campbell DG, Cohen P, Sithanandam G, Rapp U, Ashworth A, Marshall CJ, Cowley S. 1994 Identification of the sites in MAP kinase kinase-1 phosphorylated by p74raf-1. *EMBO J*. **13**, 1610–1619.

55. Hat B, Kazmierczak B, Lipniacki T. 2011 B cell activation triggered by the formation of the small receptor cluster: a computational study. *PLoS Comput. Biol*. **7**, e1002197. (doi:10.1371/journal.pcbi.1002197)

56. Wang Q, Zhang X, Zhang L, He F, Zhang G, Jamrich M, Wensel TG. 2008 Activation-dependent

hindrance of photoreceptor G protein diffusion by lipid microdomains. *J. Biol. Chem.* **283**, 30 015 – 30 024. (doi:10.1074/jbc. M803953200)

57. Abel SM, Roose JP, Groves JT, Weiss A, Chakraborty AK. 2012 The membrane environment can promote or suppress bistability in cell signaling networks. *J. Phys. Chem. B* **116**, 3630 – 3640. (doi:10.1021/jp2102385)

58. Jaruszewicz J, Zuk PJ, Lipniacki T. 2013 Type of noise defines global attractors in bistable molecular regulatory systems. *J. Theor. Biol.* **317**, 140 – 151. (doi:10.1016/j.jtbi.2012.10.004)

59. Takahashi K, Tanase-Nicola S, ten Wolde PR. 2010 Spatio-temporal correlations can drastically change the response of a MAPK pathway. *Proc. Natl Acad. Sci. USA* **107**, 2473 – 2478. (doi:10.1073/pnas. 0906885107)

60. Mugler A, Bailey AG, Takahashi K, ten Wolde PR. 2012 Membrane clustering and the role of rebinding in biochemical signaling. *Biophys. J.* **102**, 1069 – 1078. (doi:10.1016/j.bpj.2012.02.005)

61. Zhou H-X. 2009 Crowding effects of membrane proteins. *J. Phys. Chem. B* **113**, 7995 – 8005. (doi:10.1021/jp8107446)

62. Aoki K, Yamada M, Kunida K, Yasuda S, Matsuda M. 2011 Processive phosphorylation of ERK MAP kinase in mammalian cells. *Proc. Natl Acad. Sci. USA* **108**, 12 675 – 12 680. (doi:10.1073/pnas.1104030108)

63. Dushek O, van der Merwe PA, Shahrezaei V. 2011 Ultrasensitivity in multisite phosphorylation of membrane-anchored proteins. *Biophys. J.* **100**, 1189 – 1197. (doi:10.1016/j.bpj.2011.01.060)

ELECTRONIC SUPPLEMENTARY MATERIAL

Stochastic transitions in a bistable reaction system on the membrane

Marek Kochańczyk, Joanna Jaruszewicz, and Tomasz Lipniacki

This material features the article published in the *Journal of the Royal Society Interface*, 2013.

Supplementary table

Parameters of the analysed system used in simulations

Parameter	Dimensionless values			Dimensional values for $c_0 = 10/\text{s}$, $\ell = 0.01\ \mu\text{m}$
	On-lattice KMC	Gillespie KMC	PDEs	On-lattice KMC
c_0	1.667	$10/V$	1	$10/\text{s}$
c_1	0.008333	$0.05/V$	0.02	$0.05/\text{s}$
c_2	$\{0.025,\ 0.0625,\ 0.08333\}$	$\{0.15/V,\ 0.375/V,\ 0.5/V\}$	$\{0.06,\ 0.15,\ 0.2\}$	$\{0.15/\text{s},\ 0.375/\text{s},\ 0.5/\text{s}\}$
c_3	1.667	$10/V$	4	$10/\text{s}$
M	18 to 6000	∞	18 to 6000	300 to $10\,000/\text{s}$
D	2.25 to 750	∞	2.25 to 750	3.75×10^{-3} to $1.25\ \mu\text{m}^2/\text{s}$
l	1	—	1	$0.01\ \mu\text{m}$
$\rho_{\mathcal{K}}$	0.4	—	—	$4619/\mu\text{m}^2$
$\rho_{\mathcal{P}}$	0.1	—	—	$1155/\mu\text{m}^2$

TABLE S1: *Parameters of the analysed system.* Parameters are described in the main text. Only c_2 and M (and D) vary between simulations; other parameters, referred to as default parameters in the main text, are the same in all simulations.

Physiological relevance of parameter values used in simulations:

- Rate constants of reactions on the membrane can be as fast as 100/s [S1]; the relation $c_1 < c_2 < c_3$ reflects the strong boost to the catalytic activity of a kinase resulting from the increase in the number of its phosphorylated sites [S2].

- Diffusion coefficients of membrane proteins lie in the range of 10^{-2} to 10^{-1} $\mu m^2/s$ (which is at least an order of magnitude lower than in the cytoplasm) [S3, S4].

- The lattice constant ℓ is assumed to correspond exactly to the average centre-to-centre spacing of neighbouring membrane proteins [S5]. At $\ell = 10$ nm compartment volumes analysed in simulations correspond well to sizes of plasma membrane confinement zones, which e.g. in NRK cells have the mean diameter of about 230 nm as revealed by single-particle tracking experiments [S6]; on the other hand, as we consider isolated chambers, transient trapping of proteins in zones of confinement is not reflected in simulations.

- A significant fraction of the membrane surface can be covered by proteins [S7]. The surface density of membrane proteins is of order of $100/\mu m^2$, but in some cases can be even as high as $10\,000/\mu m^2$ [S8]. (The calculation of dimensional densities of molecules involves the formula for the surface of a hexagon: $A = \frac{\sqrt{3}}{2}\ell^2$.)

Supplementary references:

S1 Faeder, J. R., Hlavacek, W. S., Reischl, I., Blinov, M. L., Metzger, H., Redondo, A., Wofsy, C. & Goldstein, B. 2003 Investigation of early events in FcεRI-mediated signaling using a detailed mathematical model. *J. Immunol.* **170**, 3769–3781.

S2 Alessi, D. R., Saito, Y., Campbell, D. G., Cohen, P., Sithanandam, G., Rapp, U., Ashworth, A., Marshall, C. J. & Cowley, S. 1994 Identification of the sites in MAP kinase kinase-1 phosphorylated by p74raf-1. *EMBO J.* **13**, 1610–1619.

S3 Elowitz, M. B., Surette, M. G., Wolf, P. E., Stock, J. B. & Leibler, S. 1999 Protein mobility in the cytoplasm of Escherichia coli. *J. Bacteriol.* **181**, 197–203.

S4 Ramadurai, S., Holt, A., Krasnikov, V., van den Bogaart, G., Killian, J. A. & Poolman, B. 2009 Lateral diffusion of membrane proteins. *J. Am. Chem. Soc.* **131**, 12650–12656. (doi:10.1021/ja902853g)

S5 Phillips, R., Ursell, T., Wiggins, P. & Sens, P. 2009 Emerging roles for lipids in shaping membrane-protein function. *Nature* **459**, 379–385. (doi:10.1038/nature08147)

S6 Kusumi, A., Nakada, C., Ritchie, K., Murase, K., Suzuki, K., Murakoshi, H., Kasai, R. S., Kondo, J. & Fujiwara, T. 2005 Paradigm shift of the plasma membrane concept from the two-dimensional continuum fluid to the partitioned fluid: high-speed single-molecule tracking of membrane molecules. *Annu. Rev. Biophys. Biomol. Struct.* **34**, 351–378. (doi:10.1146/annurev.biophys.34.040204.144637)

S7 Zhou, H.-X. 2009 Crowding effects of membrane proteins. *J. Phys. Chem. B* **113**, 7995–8005. (doi:10.1021/jp8107446)

S8 Kalay, Z., Fujiwara, T. K. & Kusumi, A. 2012 Confining domains lead to reaction bursts: reaction kinetics in the plasma membrane. *PLoS One* **7**, e32948. (doi:10.1371/journal.pone.0032948)

Supplementary figures

Gillespie algorithm versus on-lattice KMC for large motility

(*a*)

| Inactive state | Transition | Active state |

(*b*)

Gillespie KMC simulation ($M = \infty$)   On-lattice KMC simulation ($M = 10^4$)

Fraction of singly and doubly phosphorylated kinases

Stable steady states of PDEs for ($c_1 = 0.02$, $c_2 = 0.2$):

Active $\begin{cases} k = 0.14, \\ k_{\mathrm{p}} = 0.47, \\ k_{\mathrm{pp}} = 0.39 \end{cases}$

Inactive $\begin{cases} k = 0.93, \\ k_{\mathrm{p}} = 0.07, \\ k_{\mathrm{pp}} = 0 \end{cases}$

(*c*)

Inactive   *Active*

Stationary probability distribution

1.28×10^4 $M = \infty$ 1.28×10^4

1.10×10^4 $M = 10^4$ 1.12×10^4

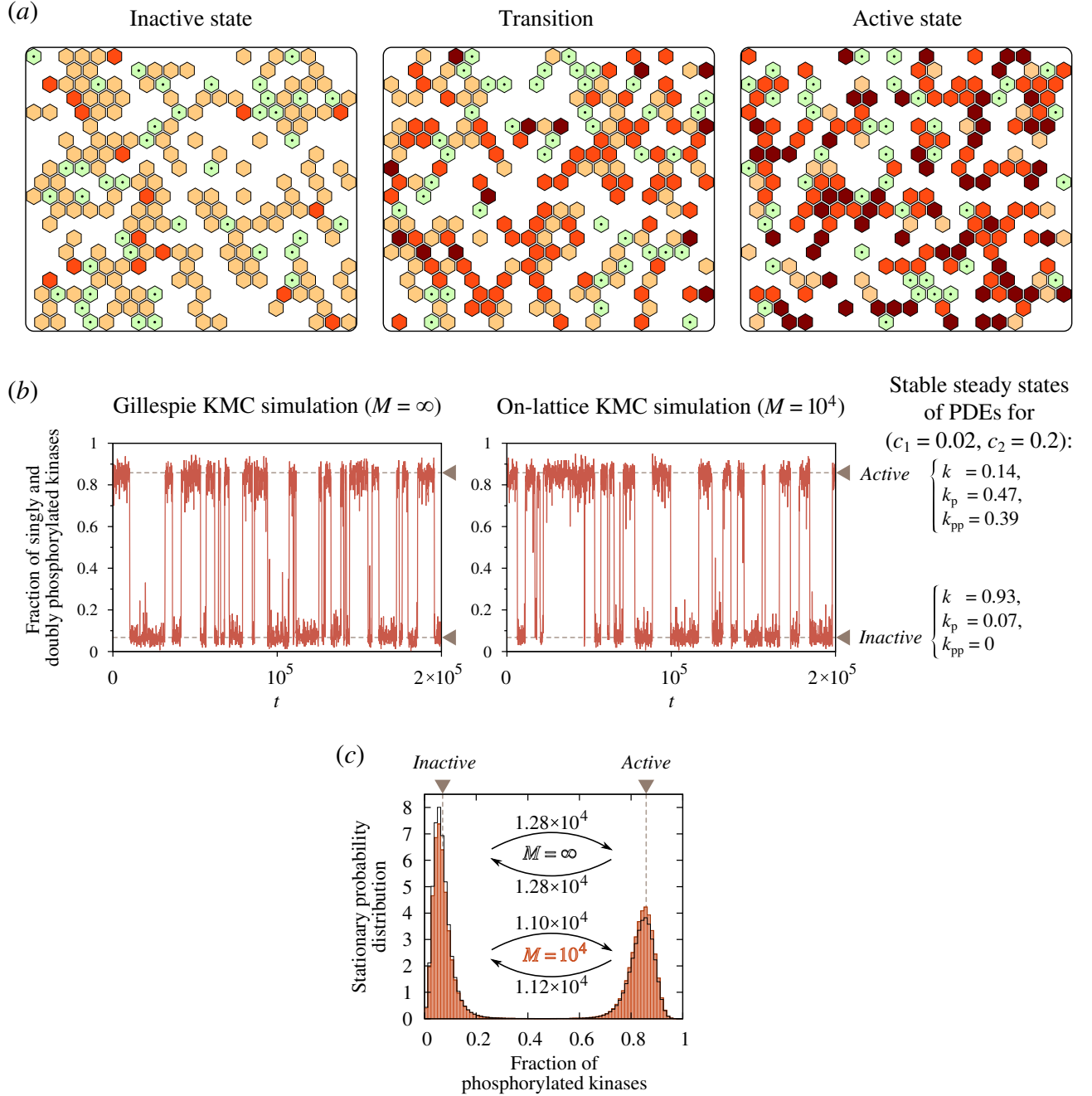Fraction of phosphorylated kinases

FIGURE S1: *Comparison of KMC on the lattice simulations for large motility coefficient $M = 10^4$ and the corresponding spatially homogeneous Markov process simulated with Gillespie algorithm.* Domain size: 20×20, periodic boundary conditions; parameters: ($c_1 = 0.02$, $c_2 = 0.2$). (*a*) Three snapshots from on-lattice KMC simulations (dephosphorylated kinases – orange, monophosphorylated – red, bisphosphorylated – brown; phosphatases – pale green, marked with a dot). (*b*) Trajectories of the fraction of phosphorylated kinases $k_{\mathrm{p}} + k_{\mathrm{pp}}$ from the Gillespie algorithm and on-lattice KMC simulations. (*c*) Bimodal stationary probability distribution of $k_{\mathrm{p}} + k_{\mathrm{pp}}$ calculated from long on-lattice (boxes) and Gillespie algorithm (thick black overlay) KMC simulations. MFPTs τ_{on} and τ_{off} are shown for both methods.

3

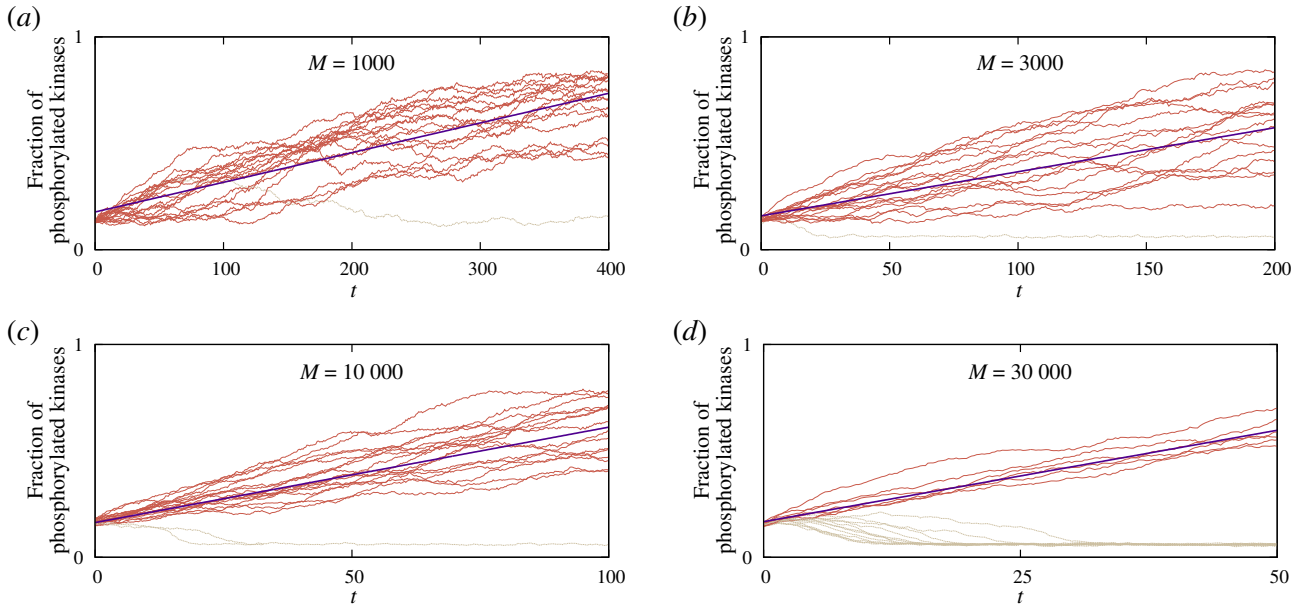# Propagation of induced travelling waves in the semi-1-D reactor

FIGURE S2: *Fraction of phosphorylated kinases $k_p + k_{pp}$ averaged over the whole reactor 30×1100 during the induced wave propagation.* Travelling wave velocities shown in figure S3 were estimated from linear fits to these trajectories. When the "seed" had become deactivated, so that the travelling wave did not form, the corresponding trajectory was not taken into account in fitting (dashed pale lines). At higher diffusivities the probability that the initially active area ("seed") is swept away and cannot induce the wave is larger.
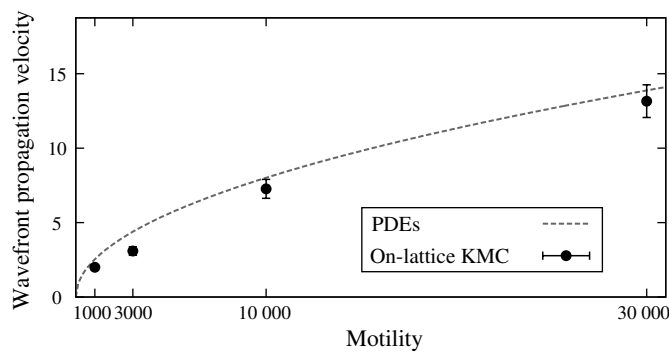

FIGURE S3: *Travelling wave velocity as a function of motility.* Velocities were calculated from simulations of PDEs and estimated in on-lattice KMC simulations for $(c_1 = 0.02, c_2 = 0.15)$ (figure S2). Error bars – SD.

4

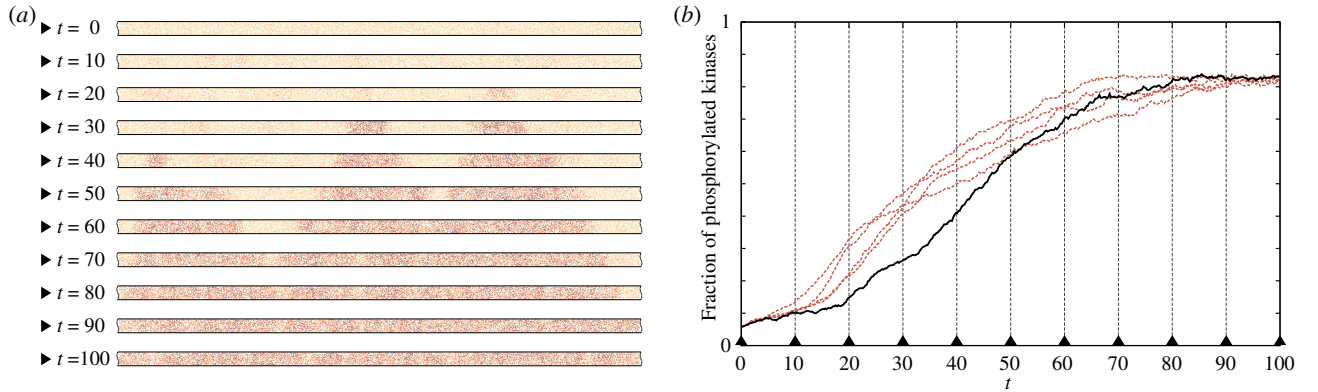# Coinciding stochastically and deterministically preferred steady states

FIGURE S4: *Simultaneous spontaneous activation on the long toroidal domain 30×1000.* Parameters: $(c_1 = 0.02, c_2 = 0.2)$ and $M = 300$. (a) Snapshots from the on-lattice KMC simulation, (b) five example time profiles of phosphorylated kinases $k_\mathrm{p} + k_\mathrm{pp}$. Snapshots in ($a$) correspond to the trajectory represented by the solid black line in (b).
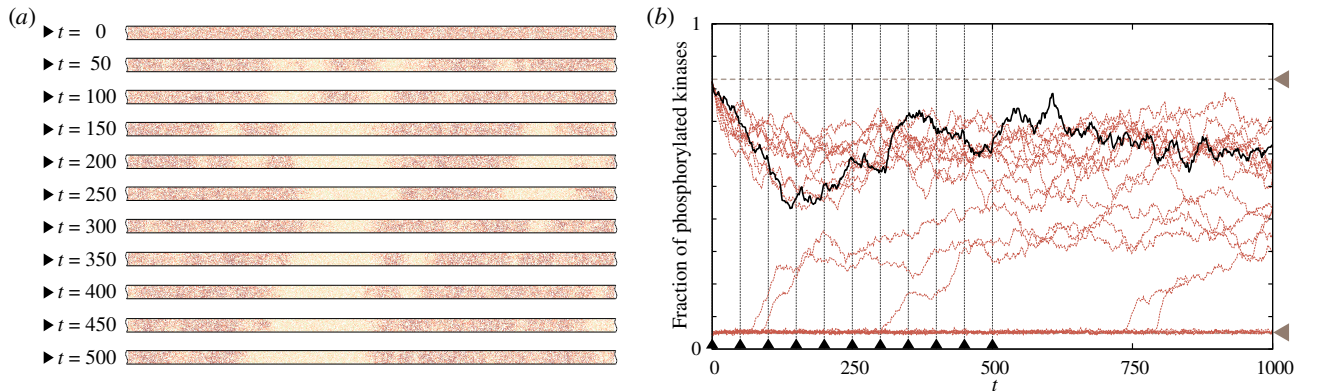

FIGURE S5: *Self-sustaining transient patches of activity in a toroidal domain 30×1000.* Parameters: $(c_1 = 0.02, c_2 = 0.06)$ and $M = 300$. (a) Snapshots from the on-lattice KMC simulation, (b) time profiles of $10 + 10$ trajectories starting from the spatially homogeneous active and inactive steady states (horizontal dashed lines). Snapshots in (a) correspond to the trajectory represented by the solid black line in (b).
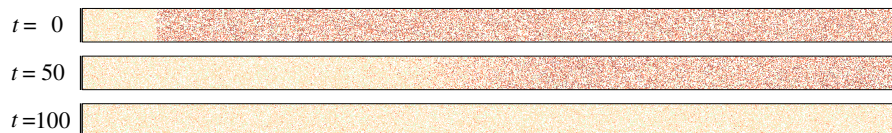

FIGURE S6: *Kinase inactivity wave propagation on the cylindrical domain 50×1000 for very large motility $M = 10\,000$. Three snapshots from an on-lattice KMC simulation.* Parameters: $(c_1 = 0.02, c_2 = 0.06)$.
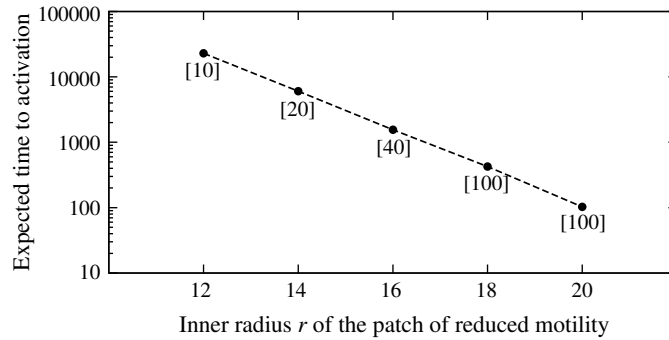
Activation due to a locally reduced motility

FIGURE S7: *Dependence of the expected time to activation τ_{on} on the radius of the patch of lowered motility $M_{\mathrm{patch}} = 100$ with the overall motility $M = 1000$ obtained from on-lattice KMC simulations.* Parameters: ($c_1 = 0.02$, $c_2 = 0.06$) as in figure 8 in the main text. The expected τ_{on} is estimated based on n_{on} observed switches given in square brackets.

Supplementary movies

Movies are available on-line at:

http://pmbm.ippt.gov.pl/publications/supplementary/
Kochanczyk-2013-JRSocInterface-Movies.zip

MOVIE S1: *Activity wave initiation on the square domain due to the locally reduced motility coefficient.* System parameters as in figure 8 in the main text.

MOVIE S2: *Self-sustaining transient patches of activity in a toroidal domain.* All parameters as in figure S5.

Effective reaction rates in diffusion-limited phosphorylation-dephosphorylation cycles

Paulina Szymańska*

College of Inter-Faculty Individual Studies in Mathematics and Natural Sciences, University of Warsaw, 02-089 Warsaw, Poland

Marek Kochańczyk*

Institute of Fundamental Technological Research, Polish Academy of Sciences, 02-106 Warsaw, Poland

Jacek Miękisz

Institute of Applied Mathematics and Mechanics, University of Warsaw, 02-097 Warsaw, Poland

Tomasz Lipniacki†

Institute of Fundamental Technological Research, Polish Academy of Sciences, 02-106 Warsaw, Poland
and Department of Statistics, Rice University, Houston, Texas 77005, USA

We investigate the kinetics of the ubiquitous phosphorylation-dephosphorylation cycle on biological membranes by means of kinetic Monte Carlo simulations on the triangular lattice. We establish the dependence of effective macroscopic reaction rate coefficients as well as the steady-state phosphorylated substrate fraction on the diffusion coefficient and concentrations of opposing enzymes: kinases and phosphatases. In the limits of zero and infinite diffusion, the numerical results agree with analytical predictions; these two limits give the lower and the upper bound for the macroscopic rate coefficients, respectively. In the zero-diffusion limit, which is important in the analysis of dense systems, phosphorylation and dephosphorylation reactions can convert only these substrates which remain in contact with opposing enzymes. In the most studied regime of nonzero but small diffusion, a contribution linearly proportional to the diffusion coefficient appears in the reaction rate. In this regime, the presence of opposing enzymes creates inhomogeneities in the (de)phosphorylated substrate distributions: The spatial correlation function shows that enzymes are surrounded by clouds of converted substrates. This effect becomes important at low enzyme concentrations, substantially lowering effective reaction rates. Effective reaction rates decrease with decreasing diffusion and this dependence is more pronounced for the less-abundant enzyme. Consequently, the steady-state fraction of phosphorylated substrates can increase or decrease with diffusion, depending on relative concentrations of both enzymes. Additionally, steady states are controlled by molecular crowders which, mostly by lowering the effective diffusion of reactants, favor the more abundant enzyme.

I. INTRODUCTION

Cellular information is transmitted and processed by complex networks of coupled biochemical reactions. Dynamics of these networks is governed by reaction rates, which are strongly influenced by diffusivity of reactants [1], their subcellular localization, and nonspecific molecular crowding [2–4].

The aim of our study is to analyze the dependence of effective macroscopic reaction rate coefficients on diffusion in cycles of coupled antagonistic reactions. Such cycles, exemplified by the phosphorylation-dephosphorylation cycle or the GTPase cycle (Fig. 1), are crucial for cellular signal transduction. In the ubiquitous motif of the phosphorylation-dephosphorylation cycle, substrate molecules are phosphorylated and dephosphorylated by kinases and phosphatases, respectively. For example, in the GTPase cycle [5], GTPases such as Ras exist in either of two signaling states: GTP-bound Ras is active (as it can recruit Raf and trigger MAPK kinase cascade signaling), while GDP-bound Ras is inactive. GTPase-activating proteins (GAPs) assist in the transition from the

GTP-bound to GDP-bound forms, while guanine nucleotide-exchange factors (GEFs) facilitate GDP dissociation followed by reloading of Ras with GTP. Overall, reversible regulatory motifs allow for substrate reuse and signal amplification, thus enabling rapid transmission of extracellular signals to effector proteins such as transcription factors.

In this study we focus on chemical kinetics in two-dimensional systems such as biological membranes. The two-dimensional (2D) systems have their own peculiarities and significantly differ from 3D systems but are very important for signal transduction. Signal transduction in numerous pathways is initiated by cytokine binding to membrane receptors, which transmit signal to secondary messengers, often by phosphorylation. Plasma membrane is a very crowded and nonhomogenous environment where reactions are expected to be diffusion controlled. This distinguishes plasma membrane from the cytoplasm, which is characterized by at least one order of magnitude faster diffusion and in which the characteristic reaction time scale is longer.

Since the seminal work of von Smoluchowski on kinetics of diffusion-limited association [6], there have been numerous attempts to derive effective macroscopic reaction rate coefficients (EMRRCs) that govern processes in a macroscale chemical reactor. These derivations were based mostly on

_____

*These authors contributed equally.
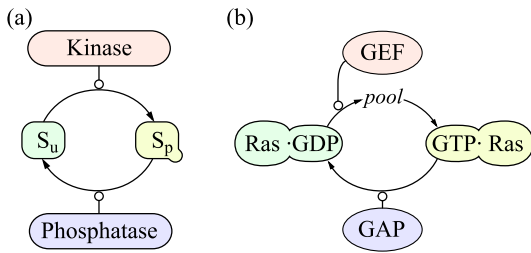†tlipnia@ippt.pan.pl

FIG. 1. (Color online) (a) A simple phosphorylation-dephosphorylation cycle; S_u, dephosphorylated substrate; S_p, phosphorylated substrate. (b) Ras GTPase cycle; GEF, guanine nucleotide-exchange factor; GAP, GT-ase activating protein.

microscopic models having a single-molecule resolution, continuous in space and time. Halfway between, the system can be described by means of a reaction-diffusion master equation, referred to as mesoscopic, as it averages out the kinetics over the microscopic length and time scales [7,8]. We will approach the microscopic limit by means of on-lattice kinetic Monte Carlo simulations, assuming that each lattice site can be either occupied by one molecule or empty. This approach, in contrast to mesoscopic description-based simulation methods, provides us with the single-molecule and single-reaction resolution, but simplifies the continuous space to a discretized lattice.

Reaction schemes studied thus far can be divided into reversible and irreversible. For the reversible case, even in equilibrium, reactions still take place and the steady state may be nontrivial. For the irreversible case, the system converges in most cases to a well-defined state in which all reactions cease; but the determination of time-dependent behavior still remains a challenging problem.

Irreversible reaction systems are as follows:

$A + B \rightarrow C$: Collins and Kimball [1] determined the time-dependent reaction rate in the case when only a fraction of collisions leads to dimer formation (extending the study of von Somoluchowski [6]) and analyzed two limits corresponding to diffusion control and reaction (activation energy) control. Further works by Naqvi [9], Emais and Fehder [10], and Torney and McConnel [11] showed essential differences between two- and three-dimensional systems. In three dimensions, the reaction rate "quickly" stabilizes at some positive value, while in two dimensions it decreases to zero as $1/\ln(t)$ [11]. A very similar reaction, $A + B \rightarrow \emptyset$, was considered by Toussaint and Wilczek in the context of particle-antiparticle annihilation [12] (see also Ref. [13]).

$A + B \rightarrow A + C$ and $A + B \rightarrow AB \rightarrow A + C$: Szabo considered this unidirectional reaction in the context of fluorescent quenching, where A is a quencher and B (C) are in excited (relaxed) states [14]. By employing various approaches, including that of von Smoluchowski, mean-field, mean first-passage time, he calculated the reaction rate to find that the agreement between these approaches is satisfactory only in the limit of small concentration and fast diffusion. For the Michaelis-Menten scheme, $A + B \rightleftharpoons AB \rightarrow A + C$, Kim *et al.* found that the long-time asymptotic relaxation of the deviation of the bound enzyme concentration from the steady-state value shows the power-law behavior $\propto (Dt)^{-1/2}$, where D is the diffusion coefficient [15]. The same scheme

has been analyzed by Park and Agmon [16,17]. In the latter work, Park and Agmon determined substrate concentration profiles developing near a static enzyme molecule. Also Zhou developed theoretical approaches and performed simulations to quantify the diffusion influence on binding and unbinding rates [18].

Reversible reaction systems are as follows:

$A + B \rightleftharpoons C$: Classical mass-action theory in the limit of infinite diffusion predicts exponential relaxation to the steady state. For diffusion-influenced kinetics, Zel'dovich and Ovchinnikov showed that the system follows power-law relaxation $\propto (Dt)^{-3/2}$ in 3D [19]. Then Berg calculated the diffusion-controlled dissociation constant [20], and, later, Agmon and Szabo determined the time-dependent kinetics for the fraction of dissociated A and B molecules for various initial and boundary conditions [21,22]. Szabo discussed three different approaches to the relaxation kinetics of the reversible association reactions that lead to nonexponential relaxation in the diffusion-limited case [22]. Sung and Lee provided an accurate theory of the diffusion-influenced reversible association reactions [23] which is in agreement with numerical results of Edelstein and Agmon [24] and correctly reduces to the von Smoluchowski's result in the irreversible limit. Takahashi *et al.* [25] considered a more complex double phosphorylation-dephosphorylation cycle based on this simple reaction scheme. They found that substrate rebindings, which arise more likely for slow diffusion, turn a distributive phosphorylation mechanism into a processive one leading to the loss of ultrasensitivity in the MAPK cascade. Processive phosphorylation is the mechanism of double phosphorylation happening at a single enzyme-substrate encounter. This phosphorylation mode is favored in the case of slow diffusion. In the distributive phosphorylation mechanism, occurring more likely for faster diffusions, the subsequent phosphorylations happen at different enzyme-substrate collisions and may be performed by different enzyme molecules. Recently, substrate rebinding was considered by van Zon *et al.*, who found that repressor-promoter rebindings slow down gene switching and therefore increase gene expression noise [26]. In the context of T-cell receptor (TCR) activation it was found that fast TCR-pMHC rebindings of shortly bound ligands can allow for kinetic proofreading-based TCR activation similar to that induced by ligands which bind for longer times [27].

$A + B \rightleftharpoons C + D$: In a series of papers, Agmon and colleagues obtained analytical solutions for the Green function and survival probabilities of the reversible reaction. They found that the asymptotic state (in three dimensions) is reached as $(Dt)^{-1/2}$, as in the irreversible case [28–30]. Recently, for the reversible Michaelis-Menten scheme, $A + B \rightleftharpoons AB \rightleftharpoons A + C$, Szabo and Zhou calculated the steady-state reaction rates in the case when substrate and product concentrations are effectively fixed, so bimolecular reactions can be treated as pseudo first order [31]. They found that, similarly to the irreversible Michaelis-Menten kinetics, the relaxation of free- and bound-enzyme concentrations to steady state follows the power law $\propto (Dt)^{-1/2}$.

The molecular crowding effect was studied and discussed in a considerable number of papers and reviews [2–4]. To-date results state that crowding, acting through volume exclusion, influences the reactions rates differently in different regimes.

In the diffusion-controlled regime it decreases the effective rate coefficients, whereas it increases them in the reaction-controlled regime. Also, it creates microdomains that can transiently cage substrates or enzymes [3,32–34]. In particular, it was shown experimentally and analyzed theoretically that substrate caging can change the distributive phosphorylation mode into the processive one [35]. Recently, it was shown by Weiss that molecular crowding renders fluids viscoelastic, which in turn leads to subdiffusion of tracer particles [36].

In this work we investigate the phosphorylation-dephosphorylation cycle consisting of two opposing reactions: $K + S_u \to K + S_p$ and $P + S_p \to P + S_u$, and analyze how EMRRCs and steady states depend on the diffusion and concentrations of enzymes (kinases, K, and phosphatases, P). In the considered model, the nonuniformity in spatial distribution of phosphorylated and dephosphorylated substrates is inherent to the system. At small densities of enzymes, each enzyme molecule is surrounded by a cloud of converted substrates. Since the scale of nonuniformity is controlled simultaneously by both enzymes, the effective phosphorylation and dephosphorylation rate coefficients are expected to be coupled.

The paper is organized as follows: In Sec. II we define our models and outline the methods used for numerical analysis; in Sec. III we provide analytical solutions for limiting cases; and in Sec. IV we present numerical results and highlight interesting effects. Discussion follows in Sec. V.

The paper is supplemented with four appendices: In Appendix A we show that EMRRCs are independent of the lattice size for sufficiently large lattices; in Appendix B we analyze the dependence of macroscopic diffusion on motility and density of molecules; in Appendix C we analyze nonequilibrium dynamics of the system of two opposing reactions (i.e., the basic model) and the system without the dephosphorylation reaction; and in Appendix D we consider a model variant in which phosphorylation and dephosphorylation proceed via formation of a transient enzyme-substrate complex.

II. MODELS AND METHODS

A. Numerical methods

All of the considered models introduced hereafter are analyzed by means of spatial kinetic Monte Carlo (KMC) simulations [37,38]. Molecules are placed on discrete sites of a two-dimensional triangular lattice which forms a square domain with periodic boundary conditions. The molecules diffuse freely by hopping to adjacent empty lattice sites. Their state can be modified due to chemical reactions, either unimolecular or bimolecular (involving two molecules occupying adjacent lattice sites). Diffusion and reaction events occur at defined rates called motilities and (microscopic) reaction rate constants, respectively. Motilities, m, are assumed to be equal for molecules of all types (unless otherwise specified). The propensity of hopping to a neighboring empty site on the triangular lattice is $m/6$. All allowed chemical reactions are defined together with their respective reaction rate constants.

At each step of the KMC simulation, a list of all events possible on the lattice is available. Time step is drawn at random from the exponential distribution with the rate parameter equal to the sum of the rates of all possible events. A

diffusion or reaction event is selected from the complete events list at random, with probability proportional to its rate. This approach is equivalent to a stochastic simulation according to the Gillespie algorithm [39] extended to account for additional diffusive events. Such construction allows for direct comparison of motility with reaction rate constants. After every event, the list of all events is updated. However, since the change in the system configuration after every simulation step is local, only a partial update of the list is necessary. By drawing events from the always-complete list, there is no need to simulate trial events that would be subsequently rejected, rendering the method efficient. The overall algorithm is essentially equivalent to the Bortz-Kalos-Lebowitz method applied previously to, e.g., studying dynamics of Ising spin glasses [40].

Initial distribution of molecules on the lattice is uniformly random. Simulations were performed on the 100×100 lattice to estimate EMRRCs in equilibrium; in the nonequilibrium case, the 300×300 lattice was used in order to obtain better statistics, while the spatial correlation functions were determined based on simulations performed on the 500×500 lattice. As shown in Appendix A, simulations performed on lattices of sizes equal or larger than 30×30 with a number of molecules of each type exceeding 50, give the EMRRCs estimates independent of the lattice size. EMRRCs in equilibrium were determined by averaging over 10 independent, long-run simulations of the system in equilibrium (assessed by invariance of nontrivial radial distribution functions or correlation length-based considerations [41]). Unless stated otherwise, the simulations were preceded by equilibration phase of 1000 and lasted at least 1000 each. In the nonequilibrium case we performed 1000 independent simulations to obtain satisfactory statistics (see Appendix C for further details).

Numerical results are supplemented by analytical expressions obtained in two extreme cases of zero and infinite motility. We also analyze how the steady states and effective motilities are influenced by nonspecific molecular crowders of varying motilities.

B. Phosphorylation-dephosphorylation cycle

We consider a phosphorylation-dephosphorylation cycle assuming that these processes are unidirectional reactions, occurring at their respective rates; the free energy expenditure featuring reaction cycles is neglected. Substrates are phosphorylated and dephosphorylated by kinases and phosphatases according to the following set of reactions:

$$K + S_u \xrightarrow{c} K + S_p, \tag{1a}$$

$$P + S_p \xrightarrow{d} P + S_u, \tag{1b}$$
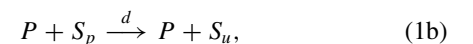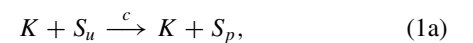
where S_u and S_p stand for dephosphorylated and phosphorylated substrates, respectively, and K represents the kinase and P the phosphatase. The symbols ρ_K, ρ_P, ρ_{S_u}, and ρ_{S_p} will denote surface densities, i.e., the fractions of lattice sites occupied by respective molecules. Coefficients c and d are the microscopic rate constants of phosphorylation and dephosphorylation reactions catalyzed by adjacent enzymes. In other words, c and d are propensities of respective reactions when an enzyme molecule is in contact with a substrate molecule.

Equations (1) should not be read as exact chemical balance equations; instead, they conform to an approximation in which the concentration and diffusion coefficient of ATP (phosphate donor) are sufficient to assume that ATP accessibility does not limit the phosphorylation reaction rate. Also the inorganic phosphate molecules produced in dephosphorylation reactions are not taken into account.

As a reference to the basic model defined by Eqs. (1) we also consider a model variant in which dephosphorylation is a first-order reaction, i.e.,

$$S_p \xrightarrow{d_0} S_u, \tag{2}$$

whereas phosphorylation still occurs via Eq. (1a). The *first-order dephosphorylation* (FOD) reaction is a simplification but it serves as an approximation when a particular phosphatase or its level are unknown. In order to compare FOD approximation with the basic model, we set $d_0 = 6\rho_P d$, which assures equal dephosphorylation efficiencies in the limit of infinite motility, as will be shown later.

The basic model does not account explicitly for the formation of the enzymatic encounter complex: Both the phosphorylation and dephosphorylation are considered to be single-step reactions. In reality, these reactions are multistep processes (enzyme-substrate binding, catalytic reaction, and enzyme-product dissociation). As shown in the Appendix D, this simplification does not significantly affect our key findings, at least when the enzyme sequestration is weak.

C. Macroscopic description and effective reaction rate coefficients

Time evolution of systems of reacting molecules is usually described by chemical mass-action kinetics equations, i.e., systems of ordinary differential equations for densities of substrates and products. Here we take into account the spatial and discrete nature of biochemical reactions and simulate numerically processes involving individual molecules. Our aim is to determine—based on the microscopic rate constants c and d—the effective reaction rate coefficients, which can be then used in the macroscopic description of the system.

We define the *effective macroscopic phosphorylation rate coefficient* c_{eff} and *effective macroscopic dephosphorylation rate coefficient* d_{eff} accordingly:

$$c_{\text{eff}} = \frac{n}{\rho_{S_u}\rho_K V \Delta t}, \tag{3a}$$

$$d_{\text{eff}} = \frac{n}{\rho_{S_p}\rho_P V \Delta t}, \tag{3b}$$

and refer to them collectively as to EMRRCs. In Eqs. (3), n is the number of (de)phosphorylation reactions that fired during a time interval Δt and V is the lattice surface area (i.e., total number of lattice sites). The densities of kinases, phosphatases, and substrates are denoted by ρ with a respective subscript: ρ_K, ρ_P, ρ_{S_u}, and ρ_{S_p}.

For the most part in our study, we will focus on the steady-state analysis where EMRRCs can be estimated based on long-run simulations, in which the number of reactions is determined over a satisfactorily long time interval Δt. Only in Appendix C will we perform simulations for the system which

is initially far from equilibrium to show that for the reversible phosphorylation-dephosphorylation cycle EMRRCs converge to their steady states. In this case, we will estimate EMRRCs within short time intervals by averaging over 1000 independent KMC simulations.

When the number of molecules present in the system is large we can write the following system of ordinary differential equations:

$$\frac{d}{dt}\rho_{S_u} = -c_{\text{eff}}\rho_K\rho_{S_u} + d_{\text{eff}}\rho_P\rho_{S_p}, \tag{4a}$$

$$\frac{d}{dt}\rho_{S_p} = c_{\text{eff}}\rho_K\rho_{S_u} - d_{\text{eff}}\rho_P\rho_{S_p}. \tag{4b}$$

These two equations are complementary, since their solutions satisfy $\rho_{S_u}(t) + \rho_{S_p}(t) = \rho_S = \text{const.}$ The steady-state solution of Eqs. (4) reads:

$$\rho_{S_u} = \frac{d_{\text{eff}}\rho_P}{c_{\text{eff}}\rho_K + d_{\text{eff}}\rho_P}\rho_S, \tag{5a}$$

$$\rho_{S_p} = \frac{c_{\text{eff}}\rho_K}{c_{\text{eff}}\rho_K + d_{\text{eff}}\rho_P}\rho_S. \tag{5b}$$

In the next section we will analyze the dependence of the steady-state solutions and EMRRCs on motility. EMRRCs provide more information than steady states alone; for example, they give the ATP turnover which can be measured by radioactively labeled ATP (γ-^{32}P-ATP). First, we will provide analytical results in the limits of zero and infinite motility. Then we will analyze numerically our model for finite, nonzero motilities.

III. ANALYTICAL RESULTS

A. Infinite-motility limit

We assume that in the *infinite-motility limit* the probability of finding a given molecule is uniform on the lattice. Thus, at any time the density of enzyme-substrate pairs is given by the product of densities multiplied by the number of potential neighbors, e.g., the kinase-dephosphorylated substrate pair density is equal to $6\rho_K\rho_{S_u}$. Therefore, the phosphorylation rate, i.e., the number of phosphorylation reactions per reactor volume per time, is equal to $6c\rho_K\rho_{S_u}$, which in light of Eq. (4) gives $c_{\text{eff}}^\infty = 6c$. The limit of infinite motility will be compared later with simulations performed for high motilities.

B. Zero-motility limit

The *zero-motility limit* is a singular limit, since without mixing the whole process is determined by initial positions of enzymes and substrates. For an arbitrarily small motility, however, the system relaxes after a sufficiently long time.

The zero-motility limit approximates the behavior of dense systems, in which diffusion is substantially reduced, but reactions still occur for substrates in the close vicinity of opposing enzymes. Increased density, together with reduced diffusion, features receptor clusterization, necessary, for example, for the initiation of B-cell receptor signaling [42–45] and TLR4-CD14 cluster formation preceding receptor internalization [46]. Formation of dense ordered patterns of proteins and other molecules has been intensively modeled in recent years (see Ref. [47] and references therein).

We start the analysis of this limit by calculating the steady-state densities of phosphorylated and dephosphorylated substrates, ρ_{S_p} and ρ_{S_u}:

$$\rho_{S_p} = p^+ \cdot \rho_S, \quad \rho_{S_u} = \rho_S - \rho_{S_p}, \tag{6}$$

where p^+ is the probability that a substrate molecule is in the phosphorylated state.

When the motility is zero, the probability that a given substrate molecule is phosphorylated depends solely on the number of neighboring kinases, i, and the number of neighboring phosphatases, j, and is equal to

$$p_{ij}^+ = \frac{ic}{ic + jd}. \tag{7}$$

The probability of having exactly i kinase and j phosphatase neighbors is

$$p_{ij} = \binom{6}{i} \rho_K^i \binom{6-i}{j} \rho_P^j (1 - \rho_K - \rho_P)^{6-i-j},$$
$$i, j \in \{0,1,\ldots,6\}, \quad 1 \leqslant i + j \leqslant 6 \tag{8}$$

and the probability that the substrate is in the phosphorylated state without contact with any enzyme molecule is equal to the probability that the substrate is in the phosphorylated state while in contact with at least one enzyme molecule. The Eq. (8) is exact only on infinite domains with infinite number of kinases and phosphatases; however, it serves as a good approximation when the number of enzymes of each type is much larger than 1. The infinitely small but nonzero motility means that substrates equilibrated in contact with the enzyme diffuse away maintaining their phosphorylation status which cannot change without a subsequent contact with an appropriate enzyme molecule.

Therefore, the probability p^+ is given by the conditional probability that a substrate molecule is phosphorylated when in contact with at least one enzyme molecule,

$$p^+ = \sum_{1 \leqslant i + j \leqslant 6} p_{ij} p_{ij}^+ \bigg/ \sum_{1 \leqslant i + j \leqslant 6} p_{ij}, \tag{9}$$

where the sum runs over all substrate molecules having contact with at least one enzyme molecule.

Now we will calculate EMRRCs in the steady state. Let us notice that in the zero-motility limit reactions occur only for the substrate molecules which have neighbors of different types (i.e., at least one kinase and one phosphatase). Let us recall that the probability that the substrate which has i neighboring kinases and j neighboring phosphatases is dephosphorylated is $jd/(ic + jd)$. The phosphorylation propensity is ic for the unphosphorylated substrate, while it is 0 for the phosphorylated substrate. Thus the effective phosphorylation propensity is $ic\,jd/(ic + jd)$. In the stationary state the number of the phosphorylation and dephosphorylation reactions per reactor volume per time must be equal, and thus the reaction rates are equal to $\rho_S \sum_{i,j \geqslant 1, i+j \leqslant 6} p_{ij}(ic\,jd)/(ic + jd)$ and, correspondingly, the effective phosphorylation and

dephosphorylation rate coefficients are equal to

$$c_{\text{eff}}^0 = \frac{\rho_S}{\rho_K \rho_{S_u}} \sum_{\substack{i,j \geqslant 1 \\ i + j \leqslant 6}} p_{ij} \frac{ic\,jd}{ic + jd}, \tag{10a}$$

$$d_{\text{eff}}^0 = \frac{\rho_S}{\rho_P \rho_{S_p}} \sum_{\substack{i,j \geqslant 1 \\ i + j \leqslant 6}} p_{ij} \frac{ic\,jd}{ic + jd}, \tag{10b}$$

where $\rho_S / \rho_{S_u} = 1/(1 - p^+)$ and $\rho_S / \rho_{S_p} = 1/p^+$, with p^+ given by Eq. (9).

One should keep in mind that rate coefficients c_{eff}^0 and d_{eff}^0 were derived under the steady-state assumption and, therefore, far from equilibrium their values can be substantially different. The phosphorylation and dephosphorylation rate coefficients obtained in the limit of zero motility give the lower bounds for EMRRCs. In the limit of $\rho_K \to 0$ and $\rho_P \to 0$, Eq. (8) implies $p_{ij} \approx p_{11} = 30\rho_K \rho_P$ (the probability of having more than one enzyme of each kind is negligibly small, so $p_{ij} = 0$ for $i, j > 1$) and therefore in this limit c_{eff}^0 and d_{eff}^0 are

$$c_{\text{eff}}^0 = \frac{30}{1 - p^+} \rho_P \frac{cd}{c + d}, \tag{11a}$$

$$d_{\text{eff}}^0 = \frac{30}{p^+} \rho_K \frac{cd}{c + d}. \tag{11b}$$

Constants c_{eff}^0 and d_{eff}^0 can be large in systems characterized by high densities of both kinases and phosphatases; however, according to Eqs. (11), they decrease to zero with the density of the opposing enzyme decreasing to zero.

C. Finite motility

We have analyzed two extreme cases of zero and infinite motility. In the infinite motility limit, also known as the *reaction-controlled limit*, the EMRRCs are proportional to the microscopic reaction propensities (for molecules in contact). In this limit, since $m \gg c$ and $m \gg d$, the probability that an enzyme reacts with a substrate at a single encounter is negligibly small and proportional to the microscopic rate constants c and d.

The small motility limit arises when the microscopic reaction rate constants c and d are fast when compared to motility. Processes characterized by low motility and large reaction propensities are called *diffusion limited*. For such processes the probability that an allowed reaction fires at every collision of molecules is close to 1. Therefore, for such processes EMRRCs are proportional to the collision frequency, which in turn is proportional to the motility m. Here the situation is more complex since even in the limit of zero motility the reaction rates are nonzero, as discussed in the previous section. Accordingly, one could expect the following macroscopic equation:

$$\frac{d}{dt} \rho_{S_p} = (\lambda m + c_{\text{eff}}^0) \rho_K \rho_{S_u} - (\lambda m + d_{\text{eff}}^0) \rho_P \rho_{S_p}, \tag{12}$$

where λ is some coefficient. In fact, the considered case is even more complicated, since, especially at low enzyme densities, the spatial distribution of the phosphorylated and dephosphorylated substrates is nonuniform. That is, the
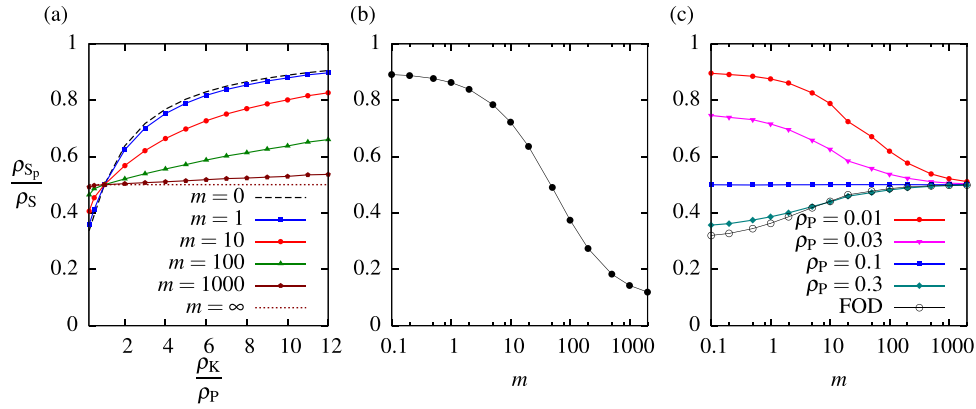
FIG. 2. (Color online) (a) Fractional density of phosphorylated substrates, ρ_{S_p}/ρ_S, as a function of the enzymes density ratio for different values of motility, m. Analytically computed limits of zero and infinite motility are marked with dashed and dotted lines. Parameters are: $\rho_S = 0.3$, $\rho_K = 0.1$, $c = 1/6\rho_K$, and $d = 1/6\rho_P$. In this series of simulations, the density of kinases was kept constant, while the density of phosphatases was varied from $\rho_P = \rho_K/0.25 = 0.4$ to $\rho_P = \rho_K/12 \approx 0.008$. By setting $d = 1/6\rho_P$, the change of phosphatases density was compensated by the proportional change of the microscopic dephosphorylation rate constant. (b) Fractional density of phosphorylated substrates as a function of m, in the case when the more abundant enzyme (kinase) has much lower catalytic activity. Simulations were performed for $\rho_S = 0.3$, $\rho_K = 0.1$, $\rho_P = 0.01$, $c = 1$, and $d = 100$. (c) Fractional density of phosphorylated substrate as a function of m for different values of phosphatase density ρ_P as well as for the first-order dephosphorylation model marked as FOD, with $d_0 = 1$. Simulations were performed for $\rho_S = 0.2$, $\rho_K = 0.1$, $c = 1/6\rho_K$, and $d = 1/6\rho_P$.

phosphorylated substrate molecules are more likely to be present in the vicinity of a kinase, while the dephosphorylated substrate molecules are more likely to be present in the vicinity of a phosphatase. As a result, even in the symmetric case of $c = d$ and $\rho_K = \rho_P$, in which the overall probability that a substrate is phosphorylated is $\frac{1}{2}$, kinase molecules collide much more often with phosphorylated substrates, which reduces the effective phosphorylation rate. Intuitively, this effect increases with decreasing density of enzymes which causes that each phosphatase molecule is surrounded by a cloud of dephospshorylated substrates and each kinase molecule by a cloud of phosphorylated substrates. We will analyze this effect in Sec. IVB by means of spatial correlation function.

As we will show below, in the general case of finite motility, EMRRCs are controlled simultaneously by the motility, both contact reaction propensies, and densities of both enzymes. Therefore, analytical determination of these rate coefficients is a challenging problem.

IV. NUMERICAL RESULTS

A. Steady-state dependence on enzyme density and motility

In this section we analyze numerically the dependence of the steady-state density of phosphorylated and dephosporylated substrates and EMRRCs on motility and densities of the opposing enzymes. The convergence of EMRRCs to their steady state in the phosphorylation-dephosphorylation cycle is demonstrated in Appendix C. In the same appendix the nonreversible dynamics of phosphorylation in the absence of phosphatase is considered.

Let us recall that in the infinite-motility limit the effective macroscopic phosphorylation and dephosphorylation rate coefficients are $c_{\text{eff}}^\infty = 6c$ and $d_{\text{eff}}^\infty = 6d$ and, correspondingly [due to Eq. (5)], the density of phosphorylated substrates is

$$\rho_{S_p} = \frac{c\rho_K}{c\rho_K + d\rho_P}\rho_S. \tag{13}$$

To keep the steady-state densities of phosphorylated and dephosphorylated substrates equal to $\frac{1}{2}$ in the limit of the infinite motility, we keep $c\rho_K = \text{const}$ and $d\rho_P = \text{const}$, that is, we set $c = 1/6\rho_K$ and $d = 1/6\rho_P$. We found that for finite motilities the phosphorylated substrate fraction increases with ρ_K/ρ_P (in the analysis we keep $\rho_K = 0.1$ and vary ρ_P), and we show that the smaller the motility is, the more pronounced this effect is, see Fig. 2(a). The dashed line for $m = 0$ tends to 1 with ρ_K/ρ_P tending to infinity. For low motility, $m = 1$, the numerically estimated ρ_{S_p} matches closely the *zero-motility limit*. Similarly, for large motilities, ρ_{S_p} is close to the *infinite-motility limit*. Because of the symmetry, for $\rho_K = \rho_P$ the phosphorylated substrate fraction is equal to $\frac{1}{2}$ for all motilities.

In Fig. 2(b) we show that when kinases are more abundant than phosphatases, but at the same time have much lower catalytic activity, the dependence of ρ_{S_p}/ρ_S on motility is strongly pronounced. At low motilities, substrates remain mostly in the phosphorylated state, $\rho_{S_p}/\rho_S \approx 0.9$, while at high motilities they are mostly dephosphorylated, $\rho_{S_p}/\rho_S \approx 0.1$. The above shows that, generically, in the regime of low motilities (*diffusion limited*) it is the density of enzymes that decides about the state of the system and for large motilities (*reaction-controlled* limit) crucial is the product of the microscopic reaction rate constants and densities.

In Fig. 2(c) we show that the density of phosphorylated substrate can either decrease or increase with motility depending on the enzyme densities ratio. For a fixed density of kinases ($\rho_K = 0.1$) we analyze the dependence of ρ_{S_p} on motility for four values of phosphatase densities, as well as for the FOD model. Since, as in Fig. 2(a), phosphatase microscopic reaction rate constant is set $d = 1/6\rho_P$, for increasing motility, ρ_{S_p}/ρ_S tends to $\frac{1}{2}$, regardless of the phosphatase density. However, for small motilities ρ_{S_p}/ρ_S depends strongly on the phosphatase density and, in general, differs from that for the FOD model. Only for a very high density ($\rho_P = 0.3$) does
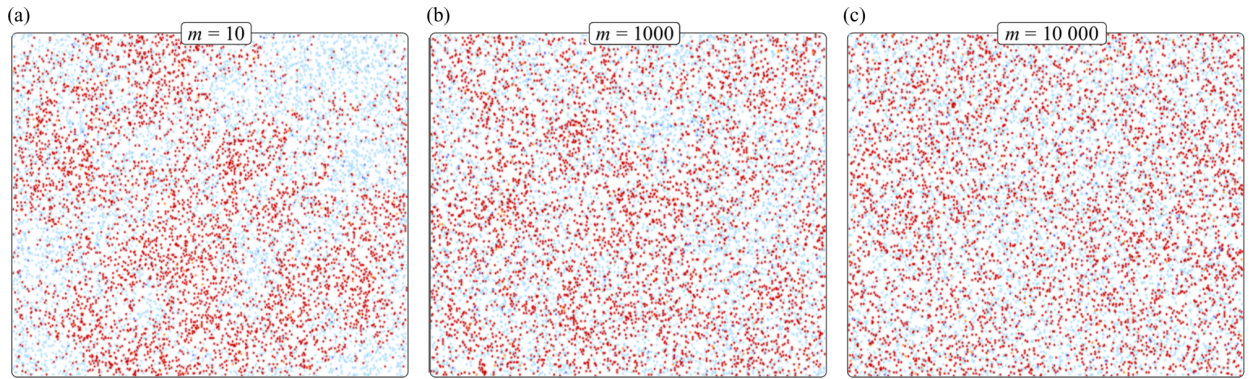
FIG. 3. (Color online) Three simulation snapshots of the 300×300 lattice showing spatial inhomogeneities of the distribution of the phosphorylated (red) and dephosphorylated (blue) substrates. For all panels $c = d = 100$, $\rho_S = 0.1$, and $\rho_K = \rho_P = 0.001$.

the fraction ρ_{S_p}/ρ_S closely match the FOD model prediction with $d_0 = 1$. This is due to the fact that for $\rho_P = 0.3$ the probability that a given substrate molecule is in contact with at least one phosphatase is high [equal to $1 - (0.7)^6 = 0.88$] and therefore the dephosphorylation is effectively of first order. This demonstrates that the FOD model cannot serve as a good approximation across a broad range of motilities.

B. Spatial correlation functions

The results shown in Fig. 2 can be explained as follows: for a decreased phosphatase density (compensated by a proportionally increased dephosphorylation rate constant d), phosphatases are surrounded by dephosphorylated substrates and therefore the effective dephosphorylation rate coefficient decreases. Intuitively, this effect becomes stronger for low motilities, for which substrates have a higher chance to be dephosphorylated after a single encounter with a phosphatase and vanishes in the limit of infinite motility, when the probability that a substrate molecule is in the phosphorylated state does not depend on its position.

It is well known that the rate of diffusion controls the steady state of the system in the case when opposing enzymes are spatially separated. As shown and discussed by Brown

and Kholodenko, when substrate phosphorylation occurs at the plasma membrane and dephosphorylation occurs in the cytoplasm, gradients of phosphorylated substrates arise, and the effectiveness of the phosphorylation process depends on diffusion [48,49]. Later, van Albada and ten Wolde demonstrated that the sharpness of the response decreases with the spatial separation of opposing enzymes [50]. It was also found that although clustering reduces signal for linear reaction kinetics, it can dramatically increase signal strength in the cases when substrates require double modification [51] or there exists a positive feedback between enzymes and substrates [42,52].

Here the spatial separation of enzymes is not imposed but results from the discreteness of the matter. Park and Agmon found time-dependent concentration profiles of unconverted substrate around a solitary nonmoving enzyme molecule for the Michaelis-Menten scheme [17]. The effect of formation of inhomogeneities is visualized in Fig. 3 for three different motilities, $m \in \{10, 1000, 10\,000\}$. For small motilities clouds of phosphorylated and dephosphorylated substrates are clearly visible, whereas for larger motilities the spatial distribution of phosphorylated and dephosphorylated substrates is nearly uniform. This effect is quantified in Fig. 4 where the normalized spatial correlation functions between kinases
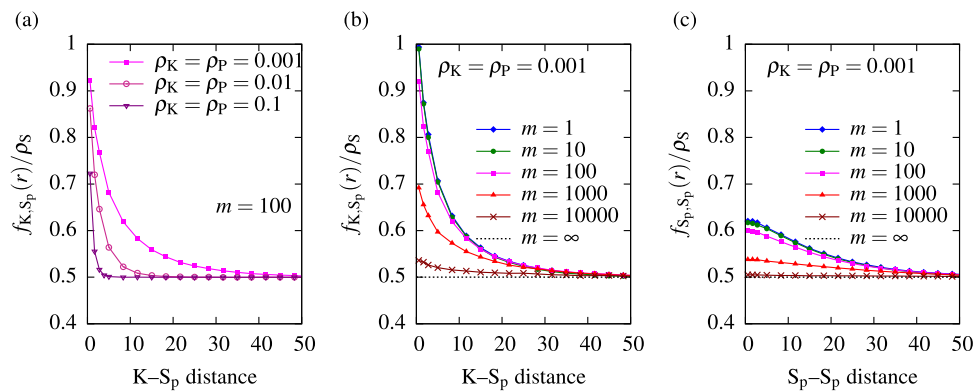
FIG. 4. (Color online) Spatial correlation functions. (a) Spatial correlation function between kinases and phosphorylated substrates $f_{K,S_p}(r)/\rho_S$ for motility $m = 100$ and three enzyme densities. (b) $f_{K,S_p}(r)/\rho_S$ for fixed enzyme densities $\rho_K = \rho_P = 0.001$ and six motilities m. (c) Spatial autocorrelation function for phosphorylated substrates $f_{S_p,S_p}(r)/\rho_S$. For all panels $c = d = 100$ and $\rho_S = 0.1$. Results shown come from averaging over 250 snapshots from independent numerical simulations on the 500×500 lattice.

and phosphorylated substrates, $f_{K,S_p}(r)/\rho_S$, and between phosphorylated substrates, $f_{S_p,S_p}(r)/\rho_S$, are plotted (r being the distance). Function $f_{K,S_p}(r)/\rho_S$ is calculated based on 250 snapshots from independent numerical simulations on the 500×500 lattice, long enough to reach the equilibrium distribution. From each snapshot, $f_{K,S_p}(r)$ is calculated as $\frac{1}{N_K}\sum_K N_{S_p}(r)/N(r)$, where N_K is the number of kinase molecules on the lattice, $N_{S_p}(r)$ is the number of phosphorylated substrates at the distance between r and $r + \Delta r$ from a given kinase, and $N(r)$ is the number of lattice sites at the distance between r and $r + \Delta r$. Then $f_{K,S_p}(r)$ is averaged over all snapshots. Function $f_{S_p,S_p}(r)/\rho_S$ is calculated analogously (i.e., the sum is over all pairs of phosphorylated substrate molecules).

As one could expect, the correlation length as well as the amplitude of the correlation function f_{K,S_p} increase with decreasing enzyme density, Fig. 4(a). Correlation length is of the order of the average distance between enzymes $1/\sqrt{\rho_K} = 1/\sqrt{\rho_P}$. For small motilities $f_{K,S_p}(1)/\rho_S \approx 1$, i.e., substrates adjacent to kinase are phosphorylated with probability close to 1. The $f_{S_p,S_p}(r)$ correlation function is smaller but the correlation length is longer. The $f_{S_p,S_p}(r)/\rho_S$ function may not reach 1 even for the smallest m, since phosphorylated substrates that are at the borders of clouds are in the close vicinity of dephosphorylated ones. The larger correlation length of $f_{S_p,S_p}(r)$ can result from fluctuations in kinase distribution. They can cause formation of transient, large "superclouds" of phosphorylated substrates surrounding several kinases. These clouds contribute to long-range correlation between phosphorylated substrates.

C. Effective macroscopic reaction rate coefficients

In this section we estimate EMRRCs on the basis of long-run numerical simulations. As was already discussed under Models and Methods, c_{eff} can be estimated according to Eq. (3). In Fig. 5 we show c_{eff}/c_{eff}^{∞} for three values of dephosphorylation rate constant d, as well as for the FOD model with $d_0 = 1$.

Effective macroscopic phosphorylation rate coefficient, c_{eff}, increases with reagents' motility and this effect is more visible for small dephosphorylation reaction rate constant d. This shows that the phosphorylation kinetics is strongly coupled with the dephosphorylation kinetics and therefore the effective macroscopic phosphorylation and dephosphorylation reaction rate coefficients cannot be estimated separately. Figure 5 shows that c_{eff} is a function of ρ_K, ρ_P, c, d, and m. The dependence of c_{eff} on motility is the strongest at the smallest considered enzyme densities, $\rho_K = \rho_P = 0.01$, see Fig. 5(c), and the weakest for the highest considered densities, $\rho_K = \rho_P = 0.2$, see Fig. 5(a), where $c_{eff}^0/c_{eff}^{\infty}$ is large. This, consistently with Fig. 2, is due to the fact that at high enzyme densities, substrates are constantly in contact with both kinases and phosphatases, and thus the phosphorylation and dephosphorylation reactions can occur almost independently of the diffusion. As shown for $\rho_K = \rho_P = 0.2$ and $\rho_K = \rho_P = 0.05$, Figs. 5(a) and 5(b), numerically estimated c_{eff} for $m = 0.1$ matches well the analytically calculated limit of c_{eff}^0; for $\rho_K = \rho_P = 0.01$, Fig. 5(c), the agreement is worse since the convergence of $c_{eff}(m)$ to c_{eff}^0 is slower.
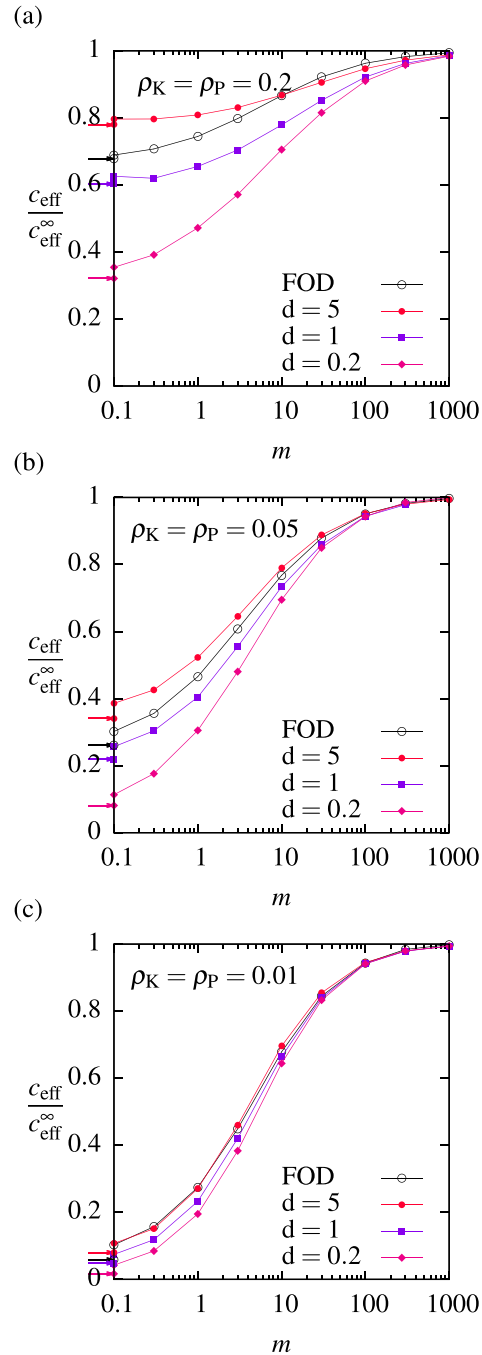

FIG. 5. (Color online) Scaled effective macroscopic phosphorylation rate coefficient c_{eff}/c_{eff}^{∞} as a function of motility m. Densities of enzymes are $\rho_K = \rho_P = 0.2$ in (a), $\rho_K = \rho_P = 0.05$ in (b), and $\rho_K = \rho_P = 0.01$ in (c). First-order dephosphorylation model marked as FOD, with $d_0 = 6\rho_P$, which corresponds to $d = 1$ in the basic model. Analytically calculated c_{eff}^0 are marked by respective arrows next to the vertical axis. For all panels $\rho_S = 0.3$, $c = 1$.

We will now analyze these effects in the limit when phosphorylation is a diffusion-driven process. As discussed above, such a limit can be achieved when diffusion-independent reactions are very infrequent compared to those driven by

diffusion, i.e., when

$$c_{\text{eff}}^0 \ll \lambda m, \quad d_{\text{eff}}^0 \ll \lambda m. \tag{14}$$

Simultaneously, the microscopic reaction rate constants, c and d, should be much larger than motility, so the probability of a reaction firing at a collision is close to 1,

$$c \gg m, \quad d \gg m. \tag{15}$$

These conditions are difficult to satisfy in numerical simulations, therefore to estimate the diffusion-limited contribution, λm, we subtract the analytically calculated zero-motility rate constant c_{eff}^0 from the numerically estimated c_{eff}. We will here assume high reaction propensities, $c = d = 1000$, and consider motilities $m \in [0,1000]$ and enzyme densities $\rho_E \in [0.0001, 0.1]$. The EMRRC is estimated, as previously, from long-run numerical simulations on the 100×100 lattice, based on Eq. (3).

First we investigate the symmetric case of $\rho_K = \rho_P =: \rho_E$. In Fig. 6(a) we show the dependence of $c_{\text{eff}}/c_{\text{eff}}^\infty$ on enzyme densities in a log-log scale for seven values of motility. The numerical predictions for small motilities, $m = 1$ and $m = 3$, lie close the theoretical prediction of the *zero-motility limit* (dashed line). It shows that for relatively small motilities and large enzyme densities the zero-motility contribution is a substantial part of the overall effective rate. The theoretically predicted c_{eff}^0 is the lower bound for the effective rate coefficient. The zero-motility contribution is proportional to the enzyme density and thus for intermediate motilities, $m \in \{10,30\}$, it becomes dominant as enzyme density increases.

In order to eliminate the zero-motility contribution from the effective rate coefficient, we show $(c_{\text{eff}} - c_{\text{eff}}^0)/c_{\text{eff}}^\infty$ with respect to enzyme densities [Fig. 6(b)] and with respect to motility [Fig. 6(c)]. In light of Eq. (12) we would expect $c_{\text{eff}} - c_{\text{eff}}^0 = \lambda m$ and therefore $(c_{\text{eff}} - c_{\text{eff}}^0)/c_{\text{eff}}^\infty$ to be proportional to m for fixed densities of enzymes, which is confirmed in Fig. 6(c). The average of gradients of lines on the log-log plot is equal to 0.99. We therefore numerically confirmed our heuristic prediction that in the small motility limit:

$$c_{\text{eff}} = c_{\text{eff}}^0 + \lambda(\rho_E)m. \tag{16}$$

Figure 6(b) confirms that the coefficient λ decreases (weakly) with decreasing enzyme density. As discussed in Sec. IVB, this dependence follows from the fact that, at low enzyme densities, enzymes are surrounded by clouds of converted substrates. This effect is quantified in Fig. 4(a) showing that spatial correlation function between kinase and phosphorylated substrate increases (in both amplitude and correlation length) with decreasing density of enzymes. The effective reaction rate is proportional to the density of unconverted substrates in lattice sites adjacent to the enzyme site. Therefore, it decreases to zero when the correlation function tends to 1 in $r = 1$ (adjacent sites).

D. Molecular crowding: Steady-state dependence on crowders' motility

Here we investigate the molecular crowding effect, i.e., we analyze how the densities of active substrates in the stationary state change due to the presence of additional molecules,
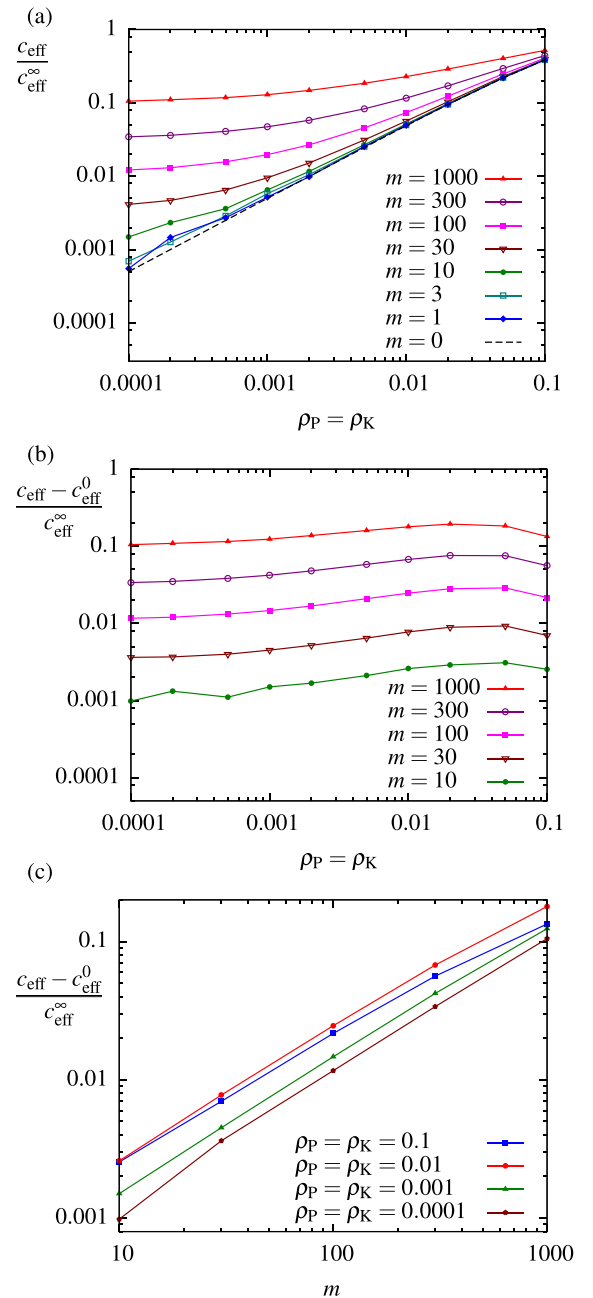

FIG. 6. (Color online) (a) Scaled effective macroscopic phosphorylation rate coefficient $c_{\text{eff}}/c_{\text{eff}}^\infty$ as a function of enzyme density $\rho_K = \rho_P$. (b) Scaled effective macroscopic phosphorylation rate constant with subtracted zero-motility contribution: $(c_{\text{eff}} - c_{\text{eff}}^0)/c_{\text{eff}}^\infty$ with respect to enzyme density. (c) $(c_{\text{eff}} - c_{\text{eff}}^0)/c_{\text{eff}}^\infty$ with respect to motility. For all panels $c = d = 1000$.

crowding agents, which do not react but occupy space and diffuse with a given motility m_C, not necessarily equal to m.

As shown in Fig. 9 in Appendix B, the presence of crowding agents leads to the decrease of effective motility of reacting molecules and this decrease is more pronounced for small motilities of crowding molecules and large motilities of reacting molecules [Fig. 9(b) versus Fig. 9(a)]. The reduction of the effective substrate motility either increases the fraction
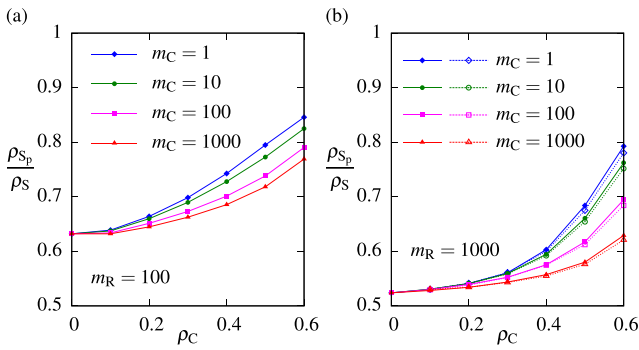
FIG. 7. (Color online) Phosphorylated substrate fractional density with respect to the density of crowding agents ρ_C. Reagents motility $m_R = 100$ in (a), $m_R = 1000$ in (b), and for four values of crowding agents motility m_C. Dashed lines refer to the simulations without crowding agents, with scaled reagents motility $\tilde{m}$, see Eq. (17). Other parameters are $\rho_S = 0.2$, $\rho_K = 0.09$, $\rho_P = 0.01$, $c = 1/6\rho_K$, and $d = 1/6\rho_P$.

of phosphorylated substrates in the stationary state, provided that $\rho_K > \rho_P$, or, because of the symmetry of the model, decreases this fraction for $\rho_P > \rho_K$. As shown in Fig. 7(b), the effect of crowding agents can be almost fully reproduced by the appropriate scaling of reagents motility,

$$\tilde{m}_R := m_R \frac{m_{\text{eff}}(\rho_R, \rho_C, m_R, m_C)}{m_{\text{eff}}(\rho_R, m_R)}, \qquad (17)$$

where $\rho_R = \rho_S - \rho_K - \rho_P$ is the fractional density of all reacting molecules assumed to have the same motility m_R. In the numerator of Eq. (17) there is the effective motility of reacting molecules of density ρ_R and motility m_R in the presence of crowding agents of density ρ_C and motility m_C, estimated in numerical simulations and given in Fig. 9(b). In the denominator of Eq. (17) there is the effective motility of reacting molecules of density ρ_R and motility m_R in the absence of additional molecules, given by the approximate Eq. (B5). This shows that the presence of chemically inert molecules can substantially change the balance between opposing reactions.

V. DISCUSSION

We investigated the correspondence between microscopic and macroscopic reaction rate coefficients in the model of the phosphorylation-dephosphorylation cycle with respect to diffusion (motility). The biological membrane is simplified to a two-dimensional triangular lattice where molecules are allowed to move with given motilities and react when in adjacent lattice sites with given propensities: microscopic reaction rate constants. Based on numerical simulations we estimated the steady state of the system (fraction of phosphorylated substrates) as well as EMRRCs as functions of reaction propensities, fractional densities of substrates, and motility. There are two opposing limits of infinite and zero motility, for which the EMRRC steady states were calculated analytically and confirmed numerically.

In the infinite motility limit, the positions of molecules are independent and therefore the macroscopic reaction rate is proportional to the product of enzyme and substrate densities and reaction propensities. This implies that the macroscopic reaction rate coefficients are equal to the microscopic propensities multiplied by the number of potential neighbors (which is 6 in our case of the triangular lattice). In this limit of infinite motility, the probability that a reaction fires at a substrate-enzyme collision is (infinitely) small and proportional to reaction propensity, and therefore the process can be considered as *reaction limited*.

In the limit of zero motility, reactions can occur only for the substrates which remain in contact with the opposing enzymes and therefore the zero-motility reaction rate coefficients decrease to zero with enzyme densities decreasing to zero, but can be significant for dense systems. In realistic conditions the limit of zero motility can be approached in very dense systems in which the effective diffusion is very low due to molecular crowding, and the probability that a substrate is trapped in contact with the opposing enzymes is high. This limit gives the lower bound for the effective reaction rate coefficients for nonzero motility.

For finite (small, but nonzero) motility we have shown the emergence of the contribution (proportional to molecules' motility) stemming from *diffusion-limited* reactions. In this regime (almost) all enzyme-substrate collisions lead to reactions. The most challenging is the regime of intermediate motilities, in which we found (based on numerical simulations) that the EMRRCs (and steady states of the system) depend in a nontrivial way on all microscopic reaction propensities and fractional densities of substrates. Precisely, the effective phosphorylation rate coefficient depends not only on the microscopic phosphorylation rate constant and kinase density but also on the dephosphorylation rate constant and phosphatase density. The parameters describing the activity and density of opposing enzymes influence the spatial distribution of phosphorylated substrate and, consequently, the probability that, e.g., a kinase molecule will collide with a dephosphorylated substrate. Generally, small enzyme densities give rise to clouds of phosphorylated and dephosphorylated substrates surrounding respective enzymes. However, the analytical estimation of macroscopic parameters for intermediate motility requires, and in our opinion deserves, more effort.

The analysis of the influence of molecular crowding on the steady state of the system showed that the presence of crowding molecules can be accounted for by modifying effective motility of reagents. Quite surprisingly, a system without crowding molecules but with appropriately reduced reagents motility predicts almost the same steady state as the system with crowding molecules. We have quantified the influence of molecular crowding on the effective motility of reagents and provided a semianalytical formula for the mentioned scaling.

The phosphorylation-dephosphorylation cycle was analyzed under the simplifying assumption in which the phosphorylation and dephosphorylation are treated as single-step reactions. In reality these processes involve at least three steps and require formation of a transient enzyme-substrate complex. In Appendix D we consider a model in which an enzyme and substrate can form a transient complex; we show that while enzyme-substrate binding is relatively short and, correspondingly, the enzyme sequestration is low, this more detailed model predicts almost the same steady states as the

original, more coarse-grained, model. In the case of more stable enzyme-substrate binding, we found that the level of enzyme (and substrate) sequestration substantially increases with motility and that, consequently, the sequestration modifies (quantitatively) steady-state dependence on motility. Analysis of this case requires further study.

In summary, our analysis is a step towards the determination of effective macroscopic reaction rate coefficients and steady states for ubiquitous cycles of opposing reactions with respect to the motility of substrates and enzymes and their densities. The presence of two antagonistic enzymes and discreteness of reacting substances lead to inhomogeneities in the phosphorylated and dephosphorylated substrate distribution. These inhomogeneities are large for slow diffusion and small enzyme densities, as indicated by spatial correlation functions. As a result, the effective catalytic activities depend on the diffusivity and enzymes densities: In the example presented in Fig. 2(b) kinases "win" at low motility, while at high motility phosphatases dominate, rendering most of the substrate dephosphorylated.

APPENDIX A: DEPENDENCE OF EMRRCS ON THE LATTICE SIZE

Here we analyze the influence of the lattice size on the estimated EMRRCs (see Fig. 8). The simulations were performed on lattices 300×300, 100×100, 30×30, and 10×10. For each lattice size and each parameter set [corresponding to parameters chosen for Fig. 5(b)] we performed 10 independent simulations with simulation times $t = 10^3$, $t = 9 \times 10^3$, $t = 100 \times 10^3$, $t = 900 \times 10^3$, i.e., inversely proportional to the lattice size, which assured that more than 5×10^4 reactions fired in each simulation. Each simulation was preceded by an equilibration phase lasting for 1000. We calculated the scaled effective macroscopic phosphorylation rate coefficient $c_{\mathrm{eff}}/c_{\mathrm{eff}}^{\infty}$ independently for each simulation, and then, based on the set of 10 simulations (for each lattice size and each parameter set),
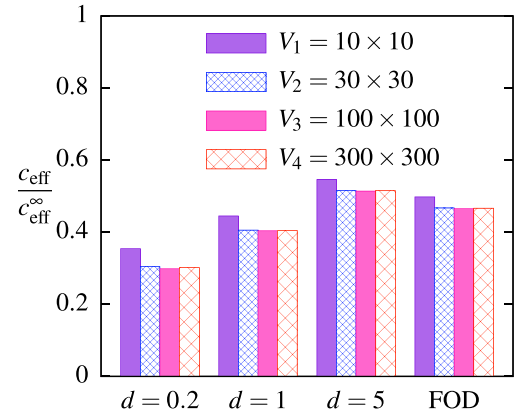

FIG. 8. (Color online) Scaled effective macroscopic phosphorylation rate coefficient $c_{\mathrm{eff}}/c_{\mathrm{eff}}^{\infty}$, estimated in simulations performed on lattices of different sizes. For all simulations $\rho_S = 0.3$, $c = 1$, $m = 1$, and $\rho_K = \rho_P = 0.05$. In the first-order dephosphorylation, model marked as FOD, $d_0 = 6\rho_P$, which corresponds to $d = 1$ in the basic model. The difference between the 10×10 lattice and the remaining lattices is statistically significant, the differences between larger lattices are of order of the statistical error.

we calculated the mean value of $c_{\mathrm{eff}}/c_{\mathrm{eff}}^{\infty}$ and the error of the mean. In each case the error of the mean was found smaller than 10^{-3}. In conclusion, we found that for assumed densities of molecules the differences between the 10×10 lattice and the remaining lattices are significant, while the differences between larger latices are of the order of the statistical error. One could expect that the dependence of EMRRCs on the lattice size can be stronger for systems of smaller molecule densities. In the analyzed system there are 45 phosphatases, 45 kinases, and 300 substrates on the 30×30 lattice.

APPENDIX B: MACROSCOPIC DIFFUSION COEFFICIENT AS A FUNCTION OF MOTILITY AND MOLECULES DENSITY

Here, in order to study the impact of molecular crowding on the phosphorylation-dephosphorylation kinetics, we analyze the impact of crowding agents on effective diffusion coefficient. The macroscopic diffusion coefficient, D, of a single tracer molecule having motility m depends on the total density of the crowding molecules ρ_C (i.e., the fraction of lattice sites occupied by molecules), their motility $m_C = m/\gamma$, and the lattice constant ℓ:

$$D = f(\rho_C, \gamma)(1 - \rho_C)\ell^2 m/4, \qquad (B1)$$

where f is the correlation function that can be approximated by the following formula [53,54]:

$$f(\rho_C, \gamma) = \frac{\left\{[(1 - \gamma)(1 - \rho_C)f_0 + \rho_C]^2 + 4\gamma(1 - \rho_C)f_0^2\right\}^{1/2} - [(1 - \gamma)(1 - \rho_C)f_0 + \rho_C]}{2\gamma(1 - \rho_C)f_0}, \qquad (B2)$$

where

$$f_0 = (1 - \alpha)/[1 + \alpha(2\gamma - 1)]. \qquad (B3)$$

The coefficient α depends on the lattice type; for the triangular lattice (considered here) $\alpha = 0.282$, for the square lattice $\alpha = 1 - 2/\pi$, and for the honeycomb (or hexagonal) lattice
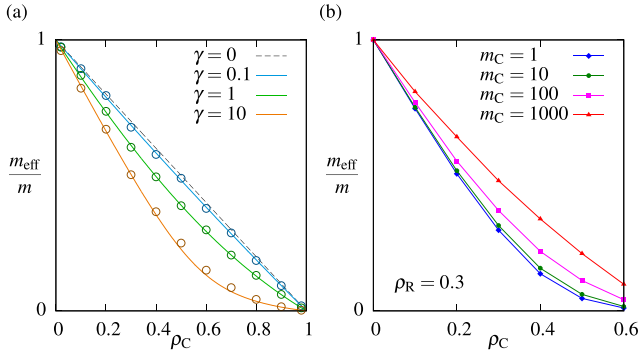
FIG. 9. (Color online) Scaled effective motility m_{eff}/m as a function of density of crowding molecules ρ_C and motility $m_C = m/\gamma$. (a) Effective motility of a tracer molecule in the presence of crowding molecules. Lines correspond to the theoretical result given by Eq. (B1), and circles mark results of corresponding numerical simulations. (b) Scaled effective motility m_{eff}/m of reacting molecules with fractional density $\rho_R = 0.3$ and motility $m = 1000$ in the presence of crowders. This result is used in simulations shown in Fig. 7(b).

$\alpha = 1/2$ [55]. The parameter $m_{\text{eff}} = f(\rho_C, \gamma)(1 - \rho_C)m$ will be considered as the effective motility of the tracer molecule in the presence of crowding molecules of density ρ_C and motility m_C.

The correlation function f satisfies $0 < f < 1$ for $0 < \gamma < \infty$. In the limit of $\gamma \to 0$, i.e., when crowding molecules move infinitely fast and a tracer molecule does not sense their positions, $f \to 1$; in the limit of $\gamma = \infty$, i.e., when crowding molecules do not move, the expression for

f reads:

$$f(\rho_C) = \max\left\{ 0, \frac{(1-\alpha) - \rho_C(1+\alpha)}{(1-\rho_C)(1-\alpha)} \right\}. \quad \text{(B4)}$$

According to the equation above, the diffusion coefficient of a tracer molecule drops to zero when the fractional density of immobile obstacles equals $\rho_{\text{crit}} = (1-\alpha)/(1+\alpha) = 0.56$, which agrees reasonably well with the percolation threshold of $1/2$ for the triangular lattice. In the case most interesting to us, i.e., when all molecules have the same motility ($\gamma = 1$), Eq. (B1) simplifies to

$$D(\rho_C, 1) = \frac{\sqrt{\rho_C^2 + 4(1-\rho_C)\left(\frac{1-\alpha}{1+\alpha}\right)^2} - \rho_C}{2\left(\frac{1-\alpha}{1+\alpha}\right)} \ell^2 m/4. \quad \text{(B5)}$$

The approximate Eq. (B1) agrees well with our simulation results presented in Fig. 9(a). In these simulations we estimated the effective motility of the tracer molecule $m_{\text{eff}} := \langle \text{Dist}^2 \rangle / \Delta t$, based on the mean-square distance $\langle \text{Dist}^2 \rangle$ covered by the tracer molecule in time Δt. To obtain reasonable statistics at a modest computational cost we performed simulations in which the number of tracer molecules was larger than 1 but always smaller than 1% of the number of crowding molecules. Finally, in order to analyze the influence of crowding molecules with a given motility on the effective motility of reacting molecules, we performed simulations in which the density of reacting molecules was 30%, while different densities and motilities of crowding molecules were considered, see Fig. 9(b). These results are used in Sec. IV D to interpret the effect of molecular crowding on the steady state of the reacting system.
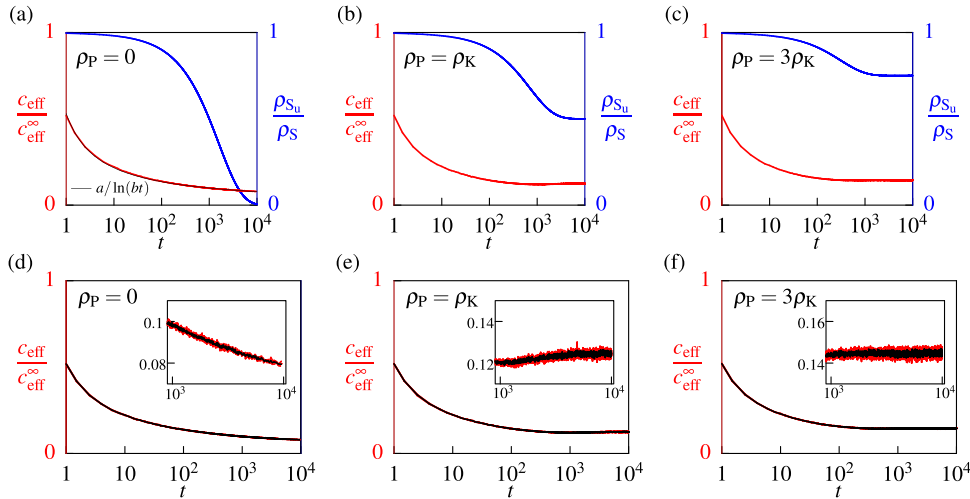
FIG. 10. (Color online) Scaled effective macroscopic phosphorylation rate coefficient $c_{\text{eff}}/c_{\text{eff}}^\infty$ and fractional density of phosphorylated substrates ρ_{S_p}/ρ_S as a function of time with initial density of phosphorylated substrate set zero. Simulations were performed for $\rho_K = 0.001$, $\rho_S = 0.3, m = 1, c = 1$, and $d = 1$. Two cases are considered: nonreversible phosphorylation (a) with $\rho_P = 0$ and a reversible phosphorylation-dephosphorylation cycle (b) and (c) with $\rho_P = \rho_K$ and $\rho_P = 3\rho_K$. The curves in panels (a), (b), and (c) result from averaging over 1000 independent simulations performed on the 300×300 lattice. In the nonreversible case, the fraction of dephosphorylated substrate drops to 0.5% at the end of simulations, leading to substantial fluctuations in the effective macroscopic phosphorylation rate coefficient. Coefficients of the fitting function in (a) are $a = 5.044$ and $b = 1.586$. In panels (d), (e), and (f) we compare $c_{\text{eff}}(t)/c_{\text{eff}}^\infty$ estimates based on 1000 simulations (black line) with the estimates based on 333 simulations (three red lines). The trajectories for $t > 1000$ are shown in the insets.
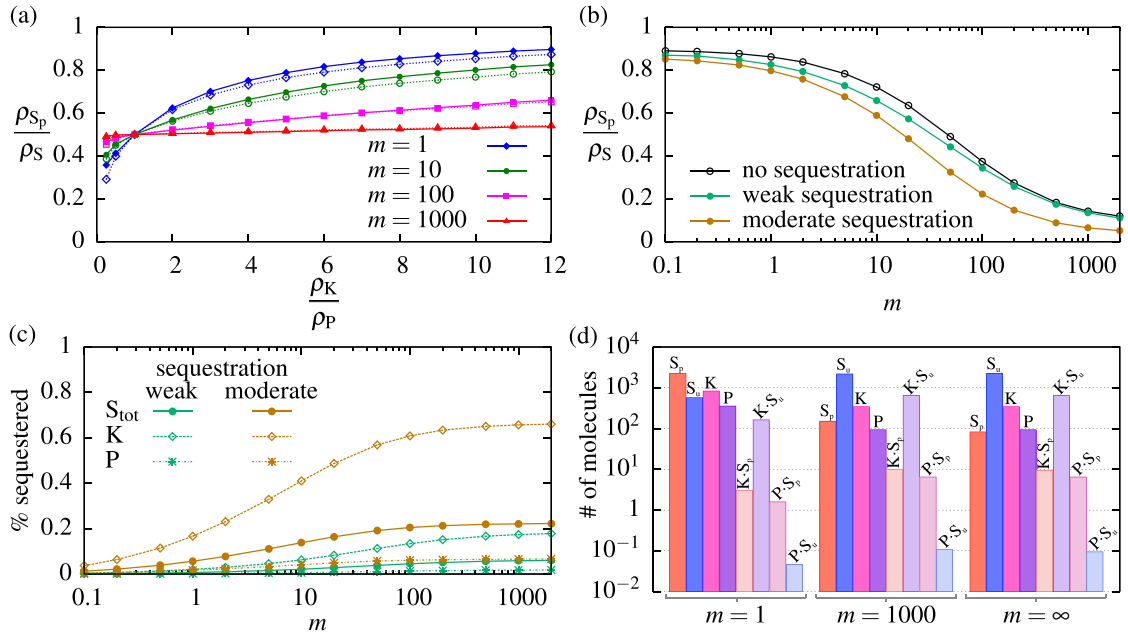
FIG. 11. (Color online) (a) Fractional density of phosphorylated substrates as a function of the enzyme ratio for different values of motility m. We compare the model variant in which the formation of a transient enzyme-substrate complex is explicitly included [the case of weak enzyme sequestration, Eqs. (D2); dotted lines] with the original model prediction shown in Fig. 2(a) (solid lines). The parameters used in the simulations of the basic (original) model: $\rho_S = 0.3$, $\rho_K = 0.1$, $c = 1/6\rho_K$, $d = 1/6\rho_P$; the parameters for the model variant considered are defined by Eqs. (D2). In the calculation of the phosphorylated substrate fraction only free (unbound) substrates are considered. (b) Fractional density of phosphorylated substrates as a function of m. We compare the original model prediction shown in Fig. 2(b) (black line) with the model variant in which the formation of a transient enzyme-substrate complex is explicitly included; two cases are considered: weak sequestration, Eqs. (D2), and moderate enzyme sequestration, Eqs. (D3). The parameters used in simulations are $\rho_S = 0.3$, $\rho_K = 0.1$, $\rho_P = 0.01$, $c = 1$, and $d = 100$. (c) Fraction of sequestered reactants for the weak and moderate sequestration cases as a function of m in simulations performed for (b). (d) Steady-state densities of all reactants and complexes in the case of moderate sequestration, Eqs. (D3), for three motilities: $m = 1$, $m = 1000$, and $m = \infty$. Values for finite motility come from simulations performed for (b). Values for infinite motility are given by the steady state of the corresponding system of ODEs.

APPENDIX C: SYSTEM EQUILIBRATION

In this appendix we numerically analyze system relaxation to the steady state. Within the framework of our main model we consider irreversible and reversible dynamics with the initial condition in which all substrates are dephosphorylated. In the irreversible case, Fig. 10(a), we assume that phosphatases are absent, while in the reversible case we assume that the density of phosphatases is either equal to, or 3 times higher than, the density of kinases, Figs. 10(b) and 10(c). In both cases, since at $t = 0$ all substrates are dephosphorylated, there is no correlation between the position of a substrate molecule and its phosphorylation status. Therefore, in the limit of $t \to 0$, the scaled effective macroscopic phosphorylation rate coefficient $c_{\text{eff}}/c_{\text{eff}}^{\infty} \to 1$; however, on the time scale of $1/c$ (when substrates being in contact with kinases are phosphorylated) it decreases to lower values.

In the irreversible case, Fig. 10(a), $\rho_{S_p}/\rho_S \to 0$, while the effective macroscopic phosphorylation rate coefficient decreases slowly with time. Torney and McConnel [11] showed theoretically that in two dimensions (in contrast to three dimensions) the reaction rate coefficient of the irreversible reaction $A + B \to \emptyset$ decreases logarithmically in time. The fit shown in Fig. 10(a) suggests that also for our reaction, $K + S_u \to K + S_p$, the reaction rate coefficient

decreases logarithmically as $a/\ln(bt)$, where $a = 5.044$ and $b = 1.586$.

In the reversible case considered in this study [see Figs. 10(b) and 10(c)], we observe that the effective macroscopic phosphorylation rate coefficient, as well as the density of phosphorylated substrate ρ_{S_p}/ρ_S, converge to the (positive) steady-state values. Interestingly, the convergence of the effective macroscopic phosphorylation rate coefficient is about one order of magnitude faster than the convergence of ρ_{S_p}/ρ_S, which shows that the steady-state values of EMRRCs can serve as a good approximation also when the system is far from its steady state.

The effective macroscopic phosphorylation rate coefficient shown in Figs. 10(a), 10(b), and 10(c) was calculated based on Eq. (3a) by averaging over 1000 independent simulations on the 300×300 lattice. The time interval Δt was adjusted in such a way that the cumulative number of reactions (in 1000 simulations) is not smaller than $50\,000$. Therefore, in the reversible case, Δt is of order of 1 during the whole simulation, while in the irreversible case (in which the frequency of phosphorylation events decreases substantially) Δt increases from 1 to about 200 at the end of simulation time. Since the time derivative of $c_{\text{eff}}(t)/c_{\text{eff}}^{\infty}$ also decreases, the increase of Δt does not contribute substantially to the error.

To demonstrate the accuracy of our $c_{\text{eff}}(t)/c_{\text{eff}}^{\infty}$ numerical estimates, in Figs. 10(d), 10(e), and 10(f), we compared the estimates based on 1000 simulations with three estimates, each based on 333 simulations. The difference between estimates based on 1000 and 333 simulations is visible only in the close-ups (insets).

APPENDIX D: ANALYSIS OF THE MODEL WITH TRANSIENT ENZYME–SUBSTRATE COMPLEXES

The phosphorylation-dephosphorylation cycle was analyzed under the simplifying assumption in which the phosphorylation and dephosphorylation are treated as single-step reactions. In reality, these processes involve at least three steps and require formation of a transient enzyme-substrate complex. It is therefore important to verify whether the analyzed effects are preserved when the more accurate description is considered. In the more detailed model, reactions (1) are replaced by

$$K + S_u \underset{c_2}{\overset{c_1}{\rightleftharpoons}} \{K \cdot S_u\} \overset{c_3}{\longrightarrow} \{K \cdot S_p\} \overset{c_4}{\longrightarrow} K + S_p, \quad \text{(D1a)}$$

$$P + S_p \underset{d_2}{\overset{d_1}{\rightleftharpoons}} \{P \cdot S_p\} \overset{d_3}{\longrightarrow} \{P \cdot S_u\} \overset{d_4}{\longrightarrow} P + S_u, \quad \text{(D1b)}$$
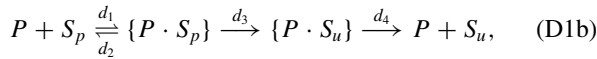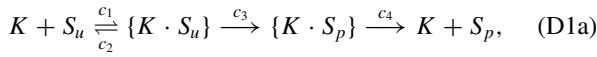
where curly brackets denote substrate complex.

We consider two sets of reaction rate constants corresponding to the short or longer enzyme-substrate binding, implying, respectively, either weak or stronger but still moderate enzyme sequestration. The constants for the two cases are

weak sequestration:

$$c_1 = 2c, \quad c_2 = 10c, \quad c_3 = 10c, \quad c_4 = 100c, \quad \text{(D2a)}$$

$$d_1 = 2d, \quad d_2 = 10d, \quad d_3 = 10d, \quad d_4 = 100d; \quad \text{(D2b)}$$

moderate sequestration:

$$c_1 = 10c, \quad c_2 = 9c, \quad c_3 = c, \quad c_4 = 100c, \quad \text{(D3a)}$$

$$d_1 = 10d, \quad d_2 = 9d, \quad d_3 = d, \quad d_4 = 100d. \quad \text{(D3b)}$$

For these two sets of constants a substrate being initially in contact with an enzyme molecule is modified with almost the same probability as in the original model. For this model variant we performed an analysis analogous to that shown in Fig. 2 (see Fig. 11). In the case of weak sequestration, we obtained the quantitatively similar dependence of fraction of phosphorylated substrate on enzyme density and on motility [Figs. 11(a) and 11(b)] as in the original model.

For stronger sequestration, for which the fraction of sequestered kinase exceeds 60% (for large motilities), the agreement with the original model [Fig. 11(b)] is only qualitative. Importantly, the fraction of sequestered enzymes and substrates significantly grows with motility. This is due to the fact that the increase of motility implies more enzyme-substrate encounters, and therefore increases their binding rate, not influencing the dissociation rate.

Overall, the analysis of the above model variant shows that the reported dependence of steady state on motility is independent of the details of the phosphorylation and dephosphorylation processes, as long as the fractions of sequestered enzymes and substrate are small, and results from the presence of opposing enzymes in the reaction network. However, for stronger enzyme-substrate binding, the fraction of sequestered reactants is higher (and dependent on their motility), and therefore the quantitative dependence of the phosphorylated substrate fraction on motility can differ and requires further study.

[1] F. C. Collins and G. E. Kimball, J. Colloid Sci. **4**, 425 (1949).

[2] R. J. Ellis, Curr. Opin. Struct. Biol. **11**, 114 (2001).

[3] D. Hall and A. P. Minton, Biochim. Biophys. Acta **1649**, 127 (2003).

[4] J. S. Kim and A. Yethiraj, Biophys. J. **96**, 1333 (2009).

[5] E. C. Stites, P. C. Trampont, Z. Ma, and K. S. Ravichandran, Science **318**, 463 (2007).

[6] M. von Smoluchowski, Z. Phys. Chem. **92**, 129 (1917).

[7] D. Fange, O. G. Berg, P. Sjöberg, and J. Elf, Proc. Natl. Acad. Sci. U.S.A. **107**, 19820 (2010).

[8] S. Hellander, A. Hellander, and L. Petzold, Phys. Rev. E **85**, 042901 (2012).

[9] K. R. Naqvi, Chem. Phys. Lett. **28**, 280 (1974).

[10] C. A. Emeis and P. L. Fehder, J. Am. Chem. Soc. **92**, 2246 (1970).

[11] D. C. Torney and H. M. McConnell, Proc. R. Soc. London A **387**, 147 (1983).

[12] D. Toussaint and F. Wilczek, J. Chem. Phys. **78**, 2642 (1983).

[13] C. E. Allen and E. G. Seebauer, J. Chem. Phys. **104**, 2557 (1996).

[14] A. Szabo, J. Phys. Chem **93**, 6929 (1989).

[15] H. Kim, M. Yang, M.-U. Choi, and K. J. Shin, J. Chem. Phys. **115**, 1455 (2001).

[16] S. Park and N. Agmon, J. Phys. Chem. B **112**, 5977 (2008).

[17] S. Park and N. Agmon, J. Phys. Chem. B **112**, 12104 (2008).

[18] H.-X. Zhou, J. Phys. Chem. B **101**, 6642 (1997).

[19] Y. B. Zel'dovich and A. A. Ovchinnikov, JETP Lett **26**, 440 (1977).

[20] O. G. Berg, J. Chem. Phys. **31**, 47 (1978).

[21] N. Agmon and A. Szabo, J. Chem. Phys. **92**, 5270 (1990).

[22] A. Szabo, J. Chem. Phys. **95**, 2481 (1991).

[23] J. Sung and S. Lee, J. Chem. Phys. **111**, 796 (1999).

[24] A. L. Edelstein and N. Agmon, J. Phys. Chem. **99**, 5389 (1995).

[25] K. Takahashi, S. Tanase-Nicola, and P. Rein ten Wolde, Proc. Natl. Acad. Sci. U.S.A. **107**, 2473 (2010).

[26] J. S. van Zon, M. J. Morelli, S. Tanase-Nicola, and P. R. ten Wolde, Biophys. J. **91**, 4350 (2006).

[27] C. C. Govern, M. K. Paczosa, C. A. K, and E. S. Huseby, Proc. Natl. Acad. Sci. U.S.A. **107**, 8724 (2010).

[28] A. V. Popov and N. Agmon, J. Chem. Phys. **117**, 5770 (2002).

[29] S. Park, K. J. Shin, and N. Agmon, J. Chem. Phys. **121**, 868 (2004).

[30] S. Park, K. J. Shin, A. V. Popov, and N. Agmon, J. Chem. Phys. **123**, 034507 (2005).

[31] A. Szabo and H.-X. Zhou, B. Kor. Chem. Soc. **33**, 925 (2012).

[32] A. P. Minton, J. Biol. Chem. **276**, 10577 (2001).

[33] S. Schnell and T. E. Turner, Prog. Biophys. Mol. Biol. **85**, 235 (2004).

[34] Z. Kalay, T. K. Fujiwara, and A. Kusumi, PLoS ONE **7**, e32948 (2012).

[35] K. Aoki, K. Takahashi, K. Kaizu, and M. Michiyuki, Sci. Rep. **3** (2013).

[36] M. Weiss, Phys. Rev. E **88**, 010101 (2013).

[37] M. Kochańczyk, J. Jaruszewicz, and T. Lipniacki, J. R. Soc. Interface **10**, 20130151 (2013).

[38] P. J. Zuk, M. Kochańczyk, J. Jaruszewicz, W. Bednorz, and T. Lipniacki, Phys. Biol. **9**, 055002 (2012).

[39] D. T. Gillespie, J. Phys. Chem **81**, 2340 (1977).

[40] A. B. Bortz, M. H. Kalos, and J. L. Lebowitz, J. Comput. Phys. **17**, 10 (1975).

[41] Y. Kuramoto, Prog. Theor. Phys. **52**, 711 (1974).

[42] B. Hat, B. Kazmierczak, and T. Lipniacki, PLoS Comput. Biol. **7**, e1002197 (2011).

[43] P. Tolar, H. W. Sohn, W. Liu, and S. K. Pierce, Immunol. Rev. **232**, 34 (2009).

[44] R. J. Brezski and J. G. Monroe, in *Multichain Immune Recognition Receptor Signaling* (Springer, Berlin, 2008), pp. 12–21.

[45] N. E. Harwood and F. D. Batista, Annu. Rev. Immunol. **28**, 185 (2009).

[46] H. Husebye, Ø. Halaas, H. Stenmark, G. Tunheim, Ø. Sandanger, B. Bogen, A. Brech, E. Latz, and T. Espevik, EMBO J. **25**, 683 (2006).

[47] J. Pękalski, A. Ciach, and N. G. Almarza, J. Chem. Phys. **140**, 114701 (2014).

[48] G. C. Brown and B. N. Kholodenko, FEBS Lett. **457**, 452 (1999).

[49] B. N. Kholodenko, Nat. Rev. Mol. Cell Biol. **7**, 165 (2006).

[50] S. B. van Albada and P. R. ten Wolde, PLoS Comput. Biol. **3**, e195 (2007).

[51] A. Mugler, A. Bailey, K. Takahashi, and P. R. ten Wolde, Biophys. J. **102**, 1069 (2012).

[52] B. Kazmierczak and T. Lipniacki, J. Theor. Biol. **259**, 291 (2009).

[53] H. van Beijeren and R. Kutner, Phys. Rev. Lett. **55**, 238 (1985).

[54] P. Almeida and W. Vaz, Handb. Biol. Phys. **1**, 305 (1995).

[55] K. Compaan and Y. Haven, Trans. Farad. Soc. **52**, 786 (1956).

CrossMark
click for updates

Effective reaction rates for diffusion-limited reaction cycles

Paweł Nałęcz-Jawecki,[1] Paulina Szymańska,[1] Marek Kochańczyk,[2] Jacek Miękisz,[3]
and Tomasz Lipniacki[2,4,a)]

[1]*College of Inter-Faculty Individual Studies in Mathematics and Natural Sciences, University of Warsaw, Warsaw, Poland*
[2]*Institute of Fundamental Technological Research, Polish Academy of Sciences, Warsaw, Poland*
[3]*Institute of Applied Mathematics and Mechanics, University of Warsaw, Warsaw, Poland*
[4]*Department of Statistics, Rice University, Houston, Texas 77005, USA*

Biological signals in cells are transmitted with the use of reaction cycles, such as the phosphorylation-dephosphorylation cycle, in which substrate is modified by antagonistic enzymes. An appreciable share of such reactions takes place in crowded environments of two-dimensional structures, such as plasma membrane or intracellular membranes, and is expected to be diffusion-controlled. In this work, starting from the microscopic bimolecular reaction rate constants and using estimates of the mean first-passage time for an enzyme–substrate encounter, we derive diffusion-dependent effective macroscopic reaction rate coefficients (EMRRC) for a generic reaction cycle. Each EMRRC was found to be half of the harmonic average of the microscopic rate constant (phosphorylation c or dephosphorylation d), and the effective (crowding-dependent) motility divided by a slowly decreasing logarithmic function of the sum of the enzyme concentrations. This implies that when c and d differ, the two EMRRCs scale differently with the motility, rendering the steady-state fraction of phosphorylated substrate molecules diffusion-dependent. Analytical predictions are verified using kinetic Monte Carlo simulations on the two-dimensional triangular lattice at the single-molecule resolution. It is demonstrated that the proposed formulas estimate the steady-state concentrations and effective reaction rates for different sets of microscopic reaction rates and concentrations of reactants, including a non-trivial example where with increasing diffusivity the fraction of phosphorylated substrate molecules changes from 10% to 90%. © *2015 AIP Publishing LLC.* [http://dx.doi.org/10.1063/1.4936131]

I. INTRODUCTION

In numerous cellular information-processing pathways, signaling is initiated on the plasma membrane. Upon ligand binding, membrane receptors are modified chemically, which enables them to transfer the extracellular signal to the secondary, intracellular messengers. Due to the presence of membrane-anchored enzymes of antagonistic catalytic activity, the activating modifications are reversible.[1] The membrane of mammalian cells of a diameter of order of 10 μm is considered to be a crowded environment, characterized by low diffusivity of order of 0.1–0.01 $\mu m^2/s$. Consequently, biochemical reactions on the plasma membrane are expected to be diffusion-controlled.[2]

The aim of this study is to derive the diffusion-controlled *effective macroscopic reaction rate coefficients*, EMRRCs, in the cycle of antagonistic reactions. Such cycles, exemplified by the phosphorylation–dephosphorylation cycle, ubiquitination–deubiquitination cycle, acetylation–deacetylation cycle, or the GTPase cycle, allow for fast substrate reuse and are of fundamental importance in cellular signal transduction and amplification, enabling rapid transmission of extracellular signals to effector proteins such as transcription factors.

There have been numerous attempts to derive diffusion-dependent EMRRCs that govern processes in a macroscale chemical reactor. Most of the existing results, discussed in more detail in the introduction to our previous study,[3] involved relatively simple reaction schemes. In short, the irreversible reaction schemes included the following:

- $A + B \rightarrow C$ or $A + B \rightarrow \emptyset$ considered initially by von Smoluchowski[4] and later by, i.a., Collins and Kimball,[5] Naqvi,[6] Emais and Fehder,[7] Torney and McConnel,[8] and Toussaint and Wilczek;[9,10]
- $A + B \rightarrow A + C$ and $A + B \rightarrow AB \rightarrow A + C$ studied by Szabo,[11] Zhou,[12] Kim *et al.*,[13] and Park and Agmon.[14,15]

There were also many studies on reversible reaction schemes such as the following:

- $A + B \rightleftharpoons C$ considered by Zel'dovich and Ovchinnikov,[16] Berg,[17] Edelstein, Gopich, Agmon, and Szabo.[18–21] Takahashi *et al.*[22] studied a more complex, double phosphorylation–dephosphorylation cycle based on this simple reaction scheme, and Dushek *et al.*[23] studied even longer chains of such cycles in membrane proteins. More recently, substrate rebinding was studied by van Zon *et al.*[24] and Govern *et al.*;[25]
- $A + B \rightleftharpoons C + D$ studied by Agmon and colleagues,[26–28] and by Szabo and Zhou.[29]

a)Electronic mail: tlipnia@ippt.pan.pl

In this theoretical work following our recent numerical study,[3] we will investigate a phosphorylation–dephosphorylation cycle, which consists of two reactions: $K + S_u \to K + S_p$, $P + S_p \to P + S_u$. In this scheme, substrate molecules (S) assume either the phosphorylated (S_p) or unphosphorylated (S_u) state upon reactions with two antagonistic enzymes: kinase (K) and phosphatase (P). We will derive the EMRRCs and steady states as functions of the coefficient of diffusion and concentrations of the enzymes. The differences between single-reaction schemes and the cycle of two antagonistic reactions are caused by the fact that in the case of limited diffusion the antagonistic enzymes introduce heterogeneity in concentrations of phosphorylated and unphosphorylated substrate molecules. Because the EMRRCs depend both on diffusivity and microscopic reaction rate constants in the case when phosphorylation and dephosphorylation rate constants are different, the steady-state phosphorylated substrate fraction depends on diffusion. This is in contrast to a single-reaction scheme, such as reversible dimerization, in which the steady-state fraction of dimerized enzymes does not depend on diffusion (see, e.g., Ref. 21).

We will approach the microscopic limit by analyzing on-lattice Monte Carlo kinetics of diffusing molecules undergoing coupled reactions. In the previous study,[3] we assumed that each lattice site can be either empty or occupied by a single molecule, and that phosphorylation and dephosphorylation reactions occur when substrate and enzyme molecules occupy adjacent lattice sites. Here, in contrast, we assume that substrate and enzyme molecules may enter the same lattice sites, and are required to be in the same lattice site in order to react. By the assumption that the substrate and enzyme molecules react only when present in the same lattice site, the reactions cease in the zero-diffusion limit. In the previous model, the substrate molecules having both a kinase molecule and a phosphatase molecule at adjacent sites were repeatedly converted between the phosphorylated and the unphosphorylated states, which resulted in (sometimes significant) zero-diffusion contribution to the macroscopic reaction rate coefficients. In the present model, there are no reactions firing in the zero-diffusion limit.

The paper is organized as follows: In Sec. II, we introduce the model and numerical methods, and discuss simulations performed to verify theoretical predictions. Sec. III is divided into four subsections in which we: (1) express the steady-state EMRRCs via the *mean first-passage time*, MFPT, in which a substrate molecule after changing its state upon the reaction with a given enzyme reaches an antagonistic enzyme molecule; (2) estimate this MFPT by the average number of steps, $w(\rho)$, until trapping a random walker in the system of randomly distributed traps with a given concentration, ρ; (3) give final estimates for the steady-state EMRRCs and compare them with numerical results; (4) compare these results with those of our previous study.[3] Finally, in Sec. IV we summarize and discuss the obtained results. The paper is supplemented by three appendices: In Appendix A, we give estimates of effective motility which due to crowding is a function of the concentration of diffusing molecules. In Appendix B, the average number of steps until trapping, $w(\rho)$, is estimated numerically. In Appendix C, we consider the

reversible dimerization problem $A + B \rightleftharpoons C$ to show that for this classic example our on-lattice numerical simulations and theory agree with the steady-state analytical solution obtained in the Brownian dynamics scheme.

II. METHODS

A. Model

We consider a generic phosphorylation–dephosphorylation cycle in which two enzymes act antagonistically on the substrate, S, which upon interaction with the kinase, K, or the phosphatase, P, may assume either the phosphorylated state, S_p, or unphosphorylated state, S_u, respectively. The interacting molecules are confined to the two-dimensional membrane represented by the triangular lattice (in which each site has six neighbors) with periodic boundary conditions. Diffusion of molecules is modeled with stochastic hops to adjacent lattice sites. Possible events, which are diffusive hops and enzymatic reactions (phosphorylations and dephosphorylations), occur with propensities defined by motility, m, and microscopic reaction rate constants, c and d, respectively. The propensity of hopping to a neighboring allowed lattice site is $m/6$. We assume that neither two enzyme nor two substrate molecules can enter the same lattice site. The enzyme and the substrate molecules, however, may enter the same lattice site and have to be in the same lattice site to react according to the following reaction scheme:

$$K + S_u \xrightarrow{c} K + S_p, \tag{1a}$$

$$P + S_p \xrightarrow{d} P + S_u. \tag{1b}$$

The molecules remain in the same lattice site after reacting, and then can leave the site independently with propensities defined by their motility. Microscopic phosphorylation and dephosphorylation rate constants, c and d, motility, m, and concentrations of the substrate, ρ_S, kinase, ρ_K, and phosphatase, ρ_P, as well as the volume of the reactor (i.e., the total number of lattice sites), V, define the model. Concentrations ρ are defined as numbers of molecules per reactor volume, i.e., fractions of lattice sites occupied by molecules of a given type. Concentrations of phosphorylated and unphosphorylated substrate are denoted by ρ_{S_p} and ρ_{S_u}.

In the proposed approach, the enzymatic reactions are modeled without considering explicitly the enzyme–substrate complex formation which allowed us to obtain analytical results. This assumption can be questionable in the case of high enzyme sequestration, however, in the case of the weak and moderate sequestrations, the explicit inclusion of the enzyme–substrate complexation does not qualitatively influence the phosphorylated substrate fraction in equilibrium, as we demonstrated in our previous numerical study.[3]

Our aim is to analytically derive formulas for the EMRRCs, c_{eff} and d_{eff}, as functions of microscopic reaction rates c and d and the remaining parameters of the model. The EMRRCs are defined as

$$c_{\text{eff}} = \frac{n_p}{\rho_{S_u} \rho_K V \Delta t}, \tag{2a}$$

$$d_{\text{eff}} = \frac{n_u}{\rho_{S_p} \rho_P V \Delta t}, \tag{2b}$$

Article C

215102-3   Nałęcz-Jawecki *et al.*   J. Chem. Phys. **143**, 215102 (2015)

where n_p and n_u are the numbers of phosphorylation and dephosphorylation reactions, respectively, that fired during a short time interval, Δt. We restrict our study to the steady-state values of EMRRCs, which can be determined by averaging over long time intervals.

When the number of molecules present in the system is large, EMRRCs govern the system of ordinary differential equations for ρ_{S_u} and ρ_{S_p},

$$\frac{d}{dt}\rho_{S_u} = -c_{eff}\rho_K\rho_{S_u} + d_{eff}\rho_P\rho_{S_p}, \tag{3a}$$

$$\frac{d}{dt}\rho_{S_p} = c_{eff}\rho_K\rho_{S_u} - d_{eff}\rho_P\rho_{S_p}. \tag{3b}$$

These two equations are complementary, since their solutions satisfy $\rho_{S_u}(t) + \rho_{S_p}(t) = \rho_S = $ const. The steady-state solution of Eq. (3) is

$$\rho_{S_u} = \frac{d_{eff}\rho_P}{c_{eff}\rho_K + d_{eff}\rho_P}\rho_S, \tag{4a}$$

$$\rho_{S_p} = \frac{c_{eff}\rho_K}{c_{eff}\rho_K + d_{eff}\rho_P}\rho_S. \tag{4b}$$

B. Numerical simulations

To verify the accuracy of the analytically derived formulas, the model will be analyzed by means of spatial kinetic Monte Carlo (KMC) simulations employing the software we described and used previously.[3,30,31] Before each step of the KMC simulation, a list of all possible events on the lattice is available. Time-step is drawn at random from the exponential distribution with the propensity parameter equal to the sum of the propensities of all possible events. A displacement or reaction event is selected from the complete list of events at random, with probability proportional to its propensity, and is executed. Then, before the next step, the list of all possible events is updated. Since the change in the system configuration after every simulation step is local, only a partial update of the list is necessary. By drawing events from the list which is always complete, there is no need to simulate trial events that would be subsequently rejected; this renders the method efficient. Such approach is equivalent to a stochastic simulation according to the Gillespie algorithm[32] applied to a spatially extended problem.

The EMRRCs were numerically estimated based on Eq. (2) using long-run simulations performed on the 300×300 lattice (except for simulations shown in Fig. 1, which were performed on smaller lattices as indicated in the figure caption, and simulations for Fig. 2(c), which were performed on the 1000×1000 lattice to estimate the dependence of accuracy of simulation-based estimates on the lattice size). For each analyzed set of parameters, we performed 3 independent simulations which were long enough to allow for at least 3×10^4 reaction firings; only for simulations shown in Fig. 1 we performed 9 independent simulations, with at least 5×10^3 reactions each. This allowed us to determine the EMRRCs numerically with the relative error smaller than 1%.

We used the same simulation code to estimate the average number of steps made by a single random walker until trapping by one of the randomly distributed immobile traps (see Appendix B). To analyze a broad range of trap concentrations,
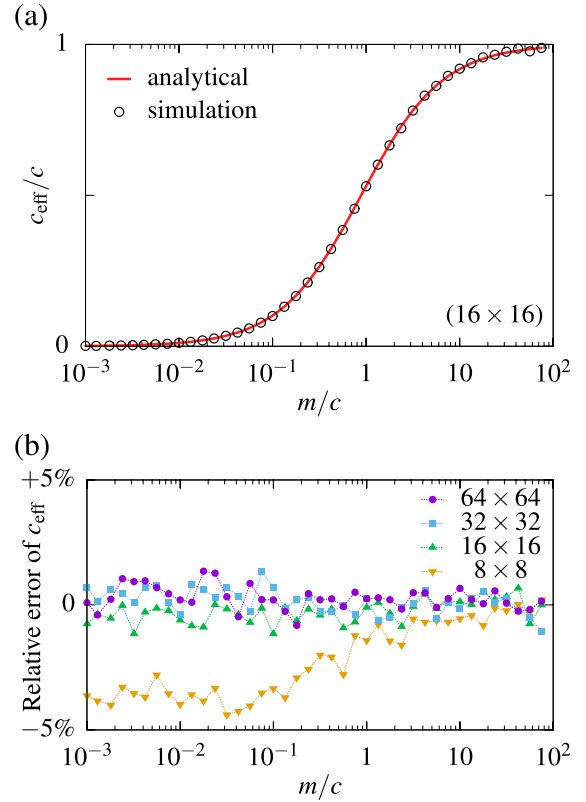

FIG. 1. Single enzyme pair model, analytical expression in Eq. (21) versus numerical estimates. (a) Normalized effective phosphorylation rate coefficient c_{eff}/c as a function of m/c for a reactor of size 16×16. (b) Relative percentage error of c_{eff} for four reactor volumes V: 8×8, 16×16, 32×32, and 64×64. For both panels $c = d$ and $\rho_K = \rho_P = 1/V$.

$\rho \in [0.0001; 0.1]$, simulations were performed on 1000×1000 lattices. The concentration of walkers was set to 0.001, which is a reasonable trade-off between the requirement of satisfactory statistics in a modest computational time and the requirement of a negligible number of collisions between walkers. After reaching a trap, a walker was immediately degraded. Since traps are immobile, the computational cost is proportional to the number of remaining walkers, and thus the simulations speed up with time, which allowed us to perform simulations until all walkers were trapped. For each set of parameters, the simulations were performed 1000 times, so the calculation of the average number of steps before trapping was based on averaging over 10^6 walkers. Finally, the average number of steps was calculated as $w = m \times \tau_{deg}$, where τ_{deg} is the average time to walker degradation. To verify the accuracy of our method, we performed analogous simulations in the case when analytical expression for w is known, i.e., when traps are distributed periodically.[33]

The on-lattice numerical simulations have the obvious limitations resulting from space discretization. It is therefore important to verify whether the proposed approach leads to correct results, at least for the classic reverse dimerization problem, $A + B \rightleftharpoons A \cdot B \overset{k}{\underset{q}{\rightleftharpoons}} C$, for which the analytical relation between the steady-state densities of A, B, and C molecules, $\rho_C = (k/q)\rho_A\rho_B$, is known for the Brownian-type dynamics. In Appendix C, we show that the same relation

Article C

215102-4   Nałęcz-Jawecki *et al.*   J. Chem. Phys. **143**, 215102 (2015)
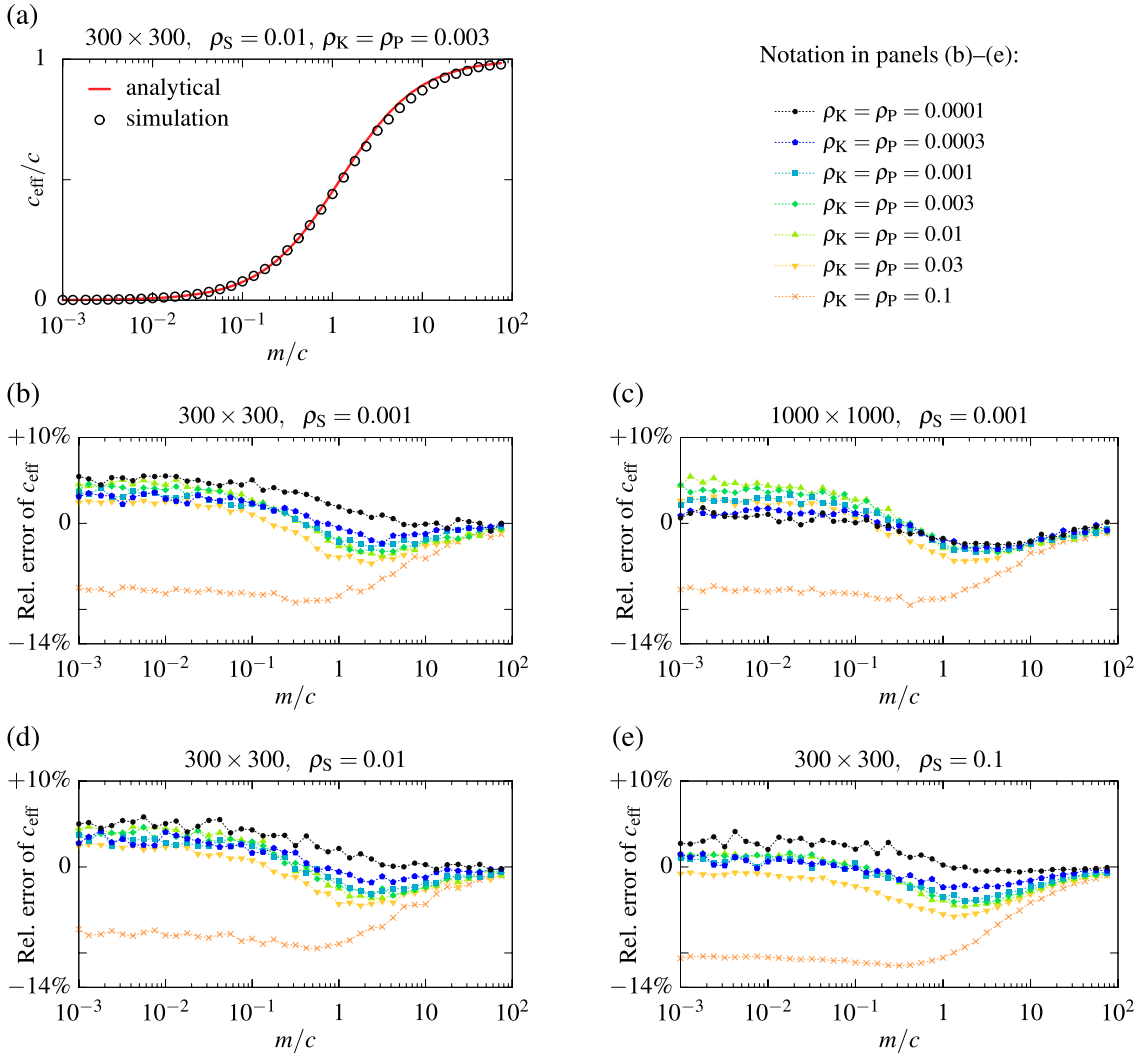
FIG. 2. Comparison of analytical expressions in Eq. (22) with numerical estimates in the fully symmetric case of $c = d$, $\rho_K = \rho_P$. (a) Normalized effective phosphorylation rate coefficient c_{eff}/c for $\rho_K = \rho_P = 0.003$ and substrate concentration $\rho_S = 0.01$. (b)–(e) Relative error of c_{eff}, i.e., (simulation value − analytical value)/analytical value, for seven values of $\rho_K = \rho_P \in \{0.0001; 0.1\}$. The substrate concentrations are $\rho_S = 0.001$ in panels (b) and (c), $\rho_S = 0.01$ in panel (d), and $\rho_S = 0.1$ in panel (e). Simulations for panel (c) were performed on the 1000×1000 lattice while remaining simulations were performed on 300×300 lattice. Please notice the difference between the relative errors of c_{eff} for the lowest enzyme densities (black dots) obtained in simulations performed on 300×300 and 1000×1000 lattices.

can be derived based on the on-lattice approach, in which dimers C arise from the geminate substrate pairs $A \cdot B$ that are formed when A and B molecules enter the same lattice site. We also demonstrate that this relation is satisfied by our numerical simulations to a good accuracy.

III. RESULTS

In the infinite-motility limit, the probability of finding a given molecule is uniform on the lattice. Thus, at any time the concentration of enzyme–substrate pairs is given by the product of their concentrations: the kinase–unphosphorylated substrate pair concentration equals $\rho_K \rho_{S_u}$, and the phosphatase–phosphorylated substrate pair concentration equals $\rho_P \rho_{S_p}$. The numbers of phosphorylation and dephosphorylation reactions that fired during a time interval Δt in a reactor of volume V are $c \, \rho_K \rho_{S_u} V \Delta t$ and $d \, \rho_P \rho_{S_p} V \Delta t$, and thus from definitions in Eq. (2) the EMRRCs

in the infinite-motility limit are equal to

$$c_{\text{eff}}^{\infty} = c, \qquad d_{\text{eff}}^{\infty} = d. \qquad (5)$$

In the case of finite motility, the concentration of enzyme–substrate pairs is smaller than the product of their concentrations so $c_{\text{eff}} < c$ and $d_{\text{eff}} < d$. This results from the spatiotemporal correlations: a substrate molecule located in the same lattice site as a kinase molecule has an increased chance of being in the phosphorylated state and, symmetrically, a substrate molecule located in the same lattice site as a phosphatase molecule has an increased chance of being in the unphosphorylated state.

A. Relation between MFPTs and EMRRCs

The steady-state fractions of unphosphorylated and phosphorylated substrate, ρ_{S_u}/ρ_S and ρ_{S_p}/ρ_S, can be expressed in terms of the average time intervals during which a substrate

molecule remains unphosphorylated, τ_u, and phosphorylated, τ_p,

$$\frac{\rho_{S_u}}{\rho_S} = \frac{\tau_u}{\tau_u + \tau_p}, \qquad \frac{\rho_{S_p}}{\rho_S} = \frac{\tau_p}{\tau_u + \tau_p}. \tag{6}$$

Now, using Eq. (4) we can express c_{eff} and d_{eff} through τ_u and τ_p,

$$c_{eff} = \frac{1}{\tau_u \rho_K}, \qquad d_{eff} = \frac{1}{\tau_p \rho_P}. \tag{7}$$

To calculate time intervals τ_u and τ_p, we split them into

$$\tau_u = \tau_{u_1} + \tau_{u_2}, \qquad \tau_p = \tau_{p_1} + \tau_{p_2}, \tag{8}$$

where τ_{u_1} (τ_{p_1}) is the MFPT in which a substrate molecule after being modified by a phosphatase (kinase) molecule meets a kinase (phosphatase) molecule for a first time, and τ_{u_2} (τ_{p_2}) is the average time after which a substrate molecule occupying initially the same lattice site as a kinase (phosphatase) molecule becomes phosphorylated (unphosphorylated).

Time intervals τ_u and τ_p depend on the effective motilities of enzyme and substrate molecules, $\tilde{m}_E$ and $\tilde{m}_S$. The effective motilities are lower than the nominal motility of all molecules, m, due to molecular crowding, and when $\rho_E \neq \rho_S$, then $\tilde{m}_E$ and $\tilde{m}_S$ differ because enzyme and substrate molecules are crowding agents only for themselves. The effective relative motility of enzyme and substrate molecules is $\tilde{M} = \tilde{m}_E + \tilde{m}_S$. The time between encounters of enzyme and substrate molecules scales inversely with $\tilde{M}$. Following the original paper by van Beijeren and Kutner[34] and our previous study,[3] we provide approximate formulas for $\tilde{m}_E$ and $\tilde{m}_S$ in Appendix A.

We first calculate τ_{u_2}. When an unphosphorylated substrate molecule and a kinase molecule meet in the same lattice site, two exclusive events are possible: either the substrate molecule gets phosphorylated or the molecules move apart before the reaction fires. The expected time for which an unphosphorylated substrate molecule and a kinase molecule remain in the same lattice site, τ_{short}, is inversely proportional to the sum of rates of these two events, $\tau_{short} = 1/(c + \tilde{M})$. With the probability of the phosphorylation event, which is $c/(c + \tilde{M})$, τ_{u_2} will be equal to τ_{short}, and with the probability of the separation event, which is $\tilde{M}/(c + \tilde{M})$, τ_{u_2} will be equal to τ_{long}, which is the expected time for substrate molecule phosphorylation in the case when it moves away from the kinase molecule. Taken together, τ_{u_2} can be expressed as

$$\tau_{u_2} = \frac{c}{c + \tilde{M}} \tau_{short} + \frac{\tilde{M}}{c + \tilde{M}} \tau_{long}, \tag{9}$$

where

$$\tau_{long} = \tau_{find} + \tau_{short} + \tau_{u_2}. \tag{10}$$

Here, τ_{find} is the average time for the substrate molecule to meet a kinase molecule (the same or another) under the condition that it is in a site adjacent to a site occupied by a kinase molecule. When the substrate molecule meets a kinase molecule, the initially considered situation reoccurs and therefore the third term is τ_{u_2}.

To calculate τ_{find} let us notice that since the fraction of lattice sites occupied by kinase molecules is equal to ρ_K,

on average every $1/\rho_K$ steps the substrate molecule meets a kinase molecule. This is, when a substrate molecule and a kinase molecule occupy the same lattice site, the expected number of steps after which the substrate molecule meets the same or another kinase molecule is $1/\rho_K$. Therefore, if these two molecules are located in adjacent lattice sites, i.e., when one step toward next meeting has already been done, the expected number of steps is $1/\rho_K - 1$. Thus,

$$\tau_{find} = \frac{1/\rho_K - 1}{\tilde{M}}. \tag{11}$$

Finally, Eqs. (9)–(11) together yield

$$\tau_{u_2} = \frac{c}{c + \tilde{M}} \frac{1}{c + \tilde{M}} + \frac{\tilde{M}}{c + \tilde{M}} \left(\frac{1/\rho_K - 1}{\tilde{M}} + \frac{1}{c + \tilde{M}} + \tau_{u_2} \right), \tag{12}$$

from which we obtain a simple expression for τ_{u_2} and an analogous expression for τ_{p_2},

$$\tau_{u_2} = \frac{1}{c \, \rho_K}, \qquad \tau_{p_2} = \frac{1}{d \, \rho_P}. \tag{13}$$

To complete calculations of τ_u and τ_p, we need to estimate τ_{u_1} and τ_{p_1}. These two MFPTs can be expressed as

$$\tau_{u_1} = \frac{w(\rho_P, \rho_K)}{\tilde{M}}, \qquad \tau_{p_1} = \frac{w(\rho_K, \rho_P)}{\tilde{M}}, \tag{14}$$

where $w(\rho_P, \rho_K)$ and $w(\rho_K, \rho_P)$ are the expected numbers of steps needed for a substrate molecule to reach a kinase and phosphatase molecule, respectively, after being converted by a phosphatase (kinase) molecule. Eventually, we arrive at the following formulas:

$$c_{eff} = \frac{1}{(\tau_{u_1} + \tau_{u_2})\rho_K} = \left(\frac{1}{c} + \frac{\rho_K \, w(\rho_P, \rho_K)}{\tilde{M}} \right)^{-1}, \tag{15a}$$

$$d_{eff} = \frac{1}{(\tau_{p_1} + \tau_{p_2})\rho_P} = \left(\frac{1}{d} + \frac{\rho_P \, w(\rho_K, \rho_P)}{\tilde{M}} \right)^{-1}. \tag{15b}$$

B. Estimation of MFPTs

The MFPTs τ_{u_1} and τ_{p_1}, Eq. (14), are simple functions of $w(\rho_P, \rho_K)$ and $w(\rho_K, \rho_P)$ which need to be estimated.

Under the assumption that the search for enzyme molecules of an appropriate type starts from a random position, functions $w(\rho_P, \rho_K)$ and $w(\rho_K, \rho_P)$ can be simplified to

$$w(\rho_P, \rho_K) = w(\rho_K), \qquad w(\rho_K, \rho_P) = w(\rho_P). \tag{16}$$

To understand when the above simplifying assumption is valid, let us consider the case when on the lattice there is only one kinase molecule and a large number of phosphatase molecules. In such a case, a substrate molecule phosphorylated on the kinase molecule will be dephosphorylated in its vicinity by one of the numerous phosphatase molecules, and therefore the next search for the single kinase molecule will start not from a random position with respect to the kinase molecule but more likely from its vicinity. Thus, in the considered case, the assumption is not valid for the phosphorylation reaction; however, since there is only one kinase molecule and thus the expected time to phosphorylation is relatively long, the

abundant phosphatase molecules change significantly their positions between two dephosphorylation reactions, so that one can assume that the search for a phosphatase molecule starts from a random position with respect to positions of phosphatase molecules.

Now, let us consider the system of N different enzyme molecules, E_i, $i = 1, \ldots, N$, and assume that each enzyme molecule E_i converts substrate molecules to the distinct state S_i with reaction rate q. Let us assume that $N \gg 1$ and let ρ_E denote the total concentration of all enzyme molecules. In light of the observation made in the previous paragraph, substrate molecules converted by E_i (i.e., in state S_i) will start their search for the remaining $N - 1$ enzyme molecules at a position that can be considered random (with respect to remaining enzyme molecules). Thus, the average time τ for which the substrate molecules will remain in each of states S_i is (by analogy to Eq. (8), with Eqs. (13) and (14), and since the concentration of $N - 1$ enzyme molecules is $\approx \rho_E$)

$$\tau = \frac{1}{q\,\rho_E} + \frac{w(\rho_E)}{\tilde{M}}. \tag{17}$$

The number of reactions per substrate molecule, per time, is equal to $r = 1/\tau$. Let us assume that one part of these enzyme molecules is kinase molecules and the rest are phosphatase molecules, so that $\rho_K + \rho_P = \rho_E$. Therefore, the probability that an unphosphorylated substrate molecule will be converted in the next reaction to the phosphorylated state is ρ_K/ρ_E, while with the probability of ρ_P/ρ_E it will be converted to another unphosphorylated state (such pseudo-conversions are possible because we assumed that each enzyme molecule converts the substrate to a distinct state). The number of real phosphorylation reactions (i.e., conversions from the unphosphorylated to the phosphorylated state) per unphosphorylated substrate molecule is $r_p = r \times \rho_K/\rho_E$, and therefore the average time spent by a substrate molecule in the unphosphorylated state is $\tau_u = 1/r_p = \tau \times \rho_E/\rho_K$.

From $c_{eff} = 1/(\tau_u \rho_K)$, Eq. (7), we obtain

$$c_{eff} = \left(\frac{1}{q} + \frac{1}{\tilde{M}} \rho_E\, w(\rho_E) \right)^{-1}. \tag{18}$$

To derive the above equation, we had to assume that all substrate states, S_i, are equiprobable, which requires $c = d = q$. In the case when $c \neq d$, we propose to replace q by c or d, appropriately, which leads to the following approximations for EMRRCs:

$$c_{eff} = \left[\frac{1}{c} + \frac{1}{\tilde{M}} (\rho_K + \rho_P)\, w(\rho_K + \rho_P) \right]^{-1}, \tag{19a}$$

$$d_{eff} = \left[\frac{1}{d} + \frac{1}{\tilde{M}} (\rho_K + \rho_P)\, w(\rho_K + \rho_P) \right]^{-1}, \tag{19b}$$

where, recall, $w(\rho)$ is the average number of steps until trapping a random walker in a system of randomly distributed traps of concentration ρ.

C. Final formulas and their numerical verification

As shown in Appendix B, $w(\rho) = w(1/V)$, where V is the volume of a reactor containing a single trap or a trap-specific

volume in a reactor with traps of concentration ρ, can be approximated by the following asymptotic formula:[33]

$$w(1/V) = \alpha V \log V + \beta V + O(1). \tag{20}$$

For the triangular lattice and a square-shaped reactor with periodic distribution of traps (or, equivalently, on finite lattices of volume $V = 1/\rho$ with periodic boundary conditions containing a single trap), coefficients were calculated by Montroll[33] and are as follows: $\alpha = \sqrt{3}/(2\pi)$, $\beta \approx 0.235$. When traps are distributed randomly, coefficients α' and β' were estimated numerically. After assuming $\alpha' = \alpha$, we obtained a good fit for $\beta' = 1.00$ (see Appendix B).

One can use Eq. (20) with coefficients α, β to estimate the effective reaction rate coefficients in idealized systems which in volume V contain a single pair of antagonistic enzyme molecules. In this case we return to Eq. (15) and, because in this case the substrate molecule searches always for a single enzyme molecule (kinase or phosphatase), we set $w(\rho_K, \rho_P) = w(\rho_P, \rho_K) = w(1/V)$. In this way, we obtain the following expressions for c_{eff} and d_{eff}:

$$c_{eff} = \left(\frac{1}{c} + \frac{\alpha \log V + \beta}{\tilde{M}} \right)^{-1}, \tag{21a}$$

$$d_{eff} = \left(\frac{1}{d} + \frac{\alpha \log V + \beta}{\tilde{M}} \right)^{-1}. \tag{21b}$$

In Fig. 1, we study the fully symmetric case ($c = d$) for a single pair of enzyme molecules and show that the formulas in Eq. (21) agree satisfactorily with results of numerical simulations. In panel (a), we plot the dependence of c_{eff} on the speed of diffusion for an example reactor of size 16×16. In panel (b), we show the relative error of our approximation for different sizes of the reactor, with always one kinase molecule, one phosphatase molecule, and one substrate molecule present in the reactor. We observe that for reactors of size 16×16 or larger, the discrepancy between formulas in Eq. (21) and results of numerical simulations is lower than 2%.

To obtain the EMRRCs in the limit of large reactor volume, with multiple enzyme molecules, we use our estimates of $w(\rho) = w(1/V)$ in the case when traps are randomly distributed (Appendix B). After setting $1/V = \rho_K + \rho_P$ from Eq. (19), we obtain

$$c_{eff} = \left[\frac{1}{c} + \frac{1}{\tilde{M}} \left(\alpha' \log \frac{1}{\rho_K + \rho_P} + \beta' \right) \right]^{-1}, \tag{22a}$$

$$d_{eff} = \left[\frac{1}{d} + \frac{1}{\tilde{M}} \left(\alpha' \log \frac{1}{\rho_K + \rho_P} + \beta' \right) \right]^{-1}, \tag{22b}$$

with $\alpha' = \alpha = \sqrt{3}/(2\pi)$, $\beta' = 1.00$. The steady-state concentrations of phosphorylated and unphosphorylated substrate fractions are given by Eq. (4).

In the next four figures we compare the EMRRCs given by Eq. (22) with numerical estimates. First, in Fig. 2, we consider the fully symmetric case in which $c = d$ and $\rho_K = \rho_P$. For substrate density $\rho_S \leqslant 0.1$ and enzyme densities $\rho_K, \rho_P \leqslant 0.03$ the relative error of c_{eff}, (simulation value − analytical value)/analytical value, remains below 5% and decreases with the enzyme density. This is visible in Fig. 2(c), for which simulations were performed on
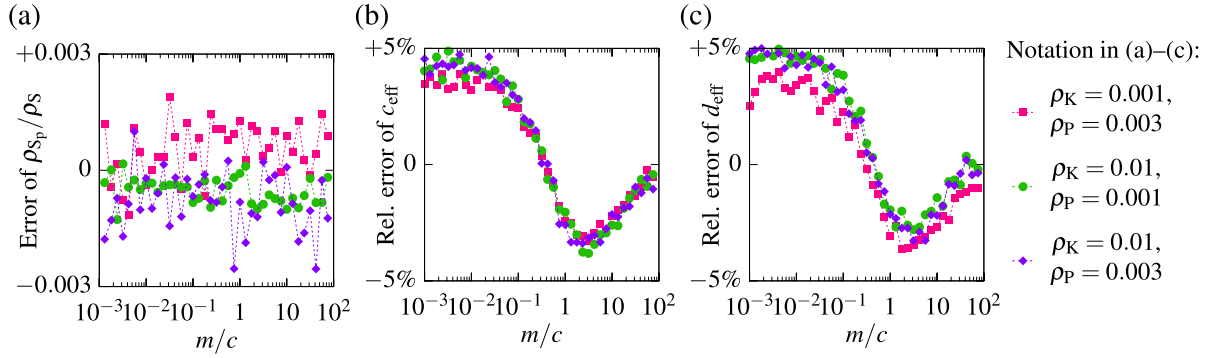
Article C

215102-7   Nałęcz-Jawecki *et al.*   J. Chem. Phys. **143**, 215102 (2015)

FIG. 3. Comparison of analytical expressions in Eqs. (22) and (23) versus numerical estimates. (a) Error of ρ_{S_p}/ρ_S. (b) and (c) Relative error of c_{eff} and d_{eff}. Three pairs of ρ_K and ρ_P were assumed: $\rho_K = 0.001$, $\rho_P = 0.003$ (pink squares); $\rho_K = 0.01$, $\rho_P = 0.001$ (green circles); and $\rho_K = 0.01$, $\rho_P = 0.003$ (violet diamonds). In all panels, the substrate concentration is $\rho_S = 0.01$ and $c = d$.

the 1000×1000 lattice. The remaining simulations were performed (for technical limitations) on the smaller 300×300 lattice, for which at the lowest enzyme concentration, $\rho_K = \rho_P = 10^{-4}$, the number of kinases (and phosphatases) is $N = 9$, and therefore the condition $N \gg 1$ is not satisfied.

The comparison of the results obtained in the simulation performed on the 300×300 and 1000×1000 lattices suggests that at least part of the discrepancy between the theory and simulations is introduced by the small size of the lattice.
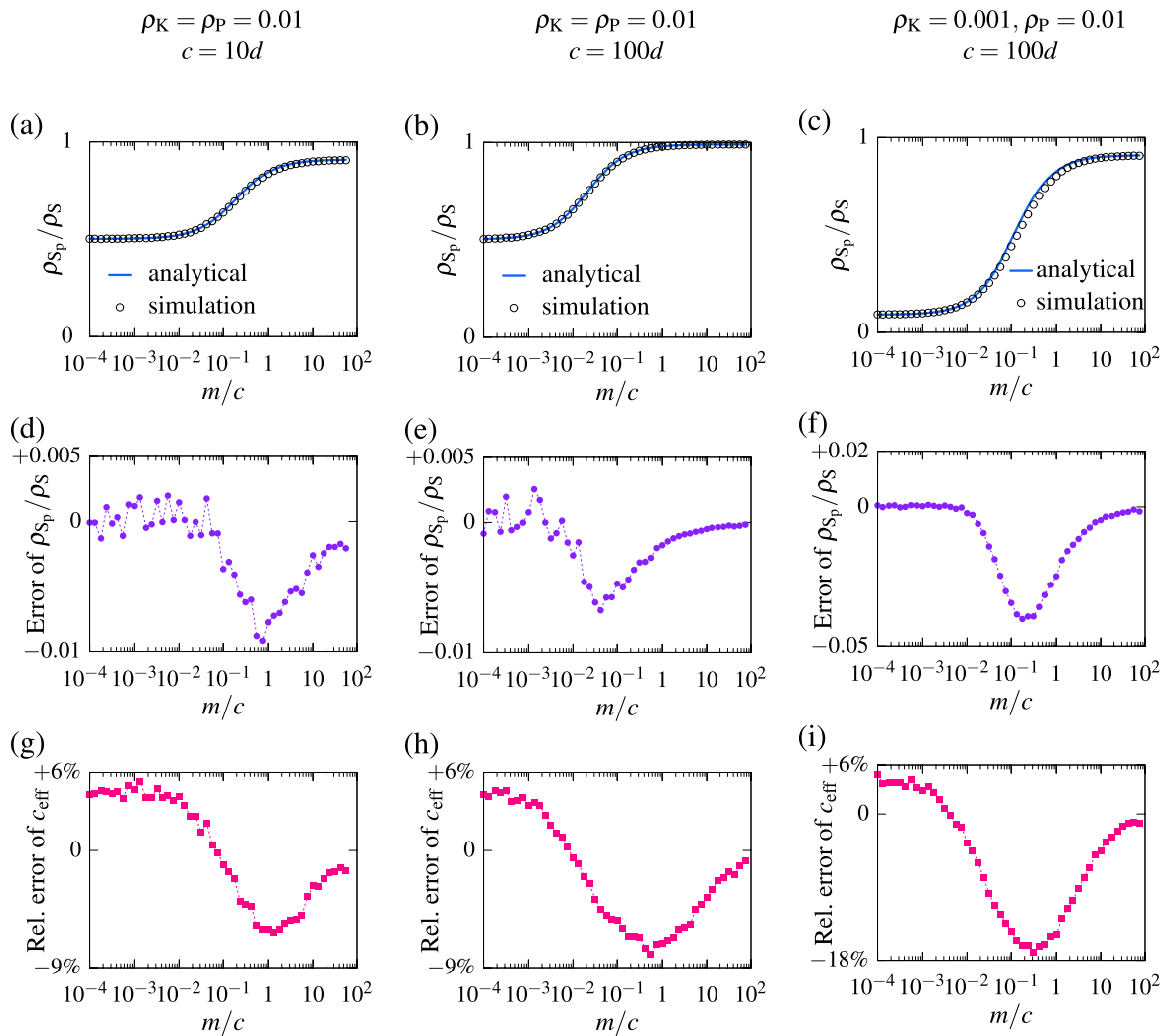

FIG. 4. Comparison of analytical expressions in Eqs. (4) and (22) versus numerical estimates. First row (panels (a)–(c)) shows phosphorylated substrate fraction ρ_{S_p}/ρ_S, second row (panels (d)–(f)) shows error of ρ_{S_p}/ρ_S, i.e., (simulation value − analytical value), third row (panels (g)–(i)) shows relative error of c_{eff}. In the first column (panels (a), (d) and (g)), $c = 10d$ and in the second column (panels (b), (e) and (h)) $c = 100d$; in the first and the second columns $\rho_K = \rho_P = 0.01$. In the third column (panels (c), (f) and (i)), $c = 100d$ with $\rho_K = 0.001$, $\rho_P = 0.01$. Substrate concentration is $\rho_S = 0.01$ for all panels.

Article C

215102-8   Nałęcz-Jawecki *et al.*   J. Chem. Phys. **143**, 215102 (2015)

In Fig. 3 we consider the case in which $c = d$, but $\rho_K \neq \rho_P$. Let us notice that Eq. (22) together with Eq. (4) implies that when $c = d$,

$$\frac{\rho_{S_p}}{\rho_S} = \frac{\rho_K}{\rho_K + \rho_P}. \tag{23}$$

Figure 3(a) shows a perfect agreement, with error less than 0.002, of Eq. (23) and the numerical estimate; Figures 3(b) and 3(c) show that EMRRCs are predicted with the accuracy of about 5%.

In Fig. 4 we consider asymmetric cases in which $c = 10d$ (first column) or $c = 100d$ (second column). In the third column we show results for the fully asymmetric case in which $c = 100d$ and $\rho_K = 0.1\rho_P$. In this case, in the limit of infinite diffusion, i.e., when $c_{\text{eff}} = c$ and $d_{\text{eff}} = d$, phosphorylation proceeds at the effective rate $\propto c \times \rho_K$ that is ten times greater than the effective dephosphorylation rate $\propto d \times \rho_P$. Consequently, the fraction of phosphorylated substrate is close to 0.9. In the opposite, diffusion-controlled limit, $c_{\text{eff}} \approx d_{\text{eff}}$ and therefore since phosphatase molecules are ten times more abundant, dephosphorylation proceeds ten times faster than phosphorylation, and as a result the phosphorylated substrate fraction is close to 0.1. This example demonstrates that the speed of diffusion can qualitatively influence the steady state of the system.

Finally, in Fig. 5 we consider the case when the phosphatase activity is 10 times higher than the kinase activity, $d = 10c$, and calculate the fraction of the phosphorylated substrate as a function of enzyme ratio. Four different motility values are considered. The results obtained for $m/c = 0.1$ lie close to those for the zero-diffusion limit, $m/c \to 0$, for which $\rho_{S_p}/\rho_S = \rho_K/(\rho_K + \rho_P)$; the results obtained for $m/c = 100$ lie close to those for the limit of infinite diffusion, $m/c \to \infty$, for which $\rho_{S_p}/\rho_S = c\rho_K/(c\rho_K + d\rho_P)$.
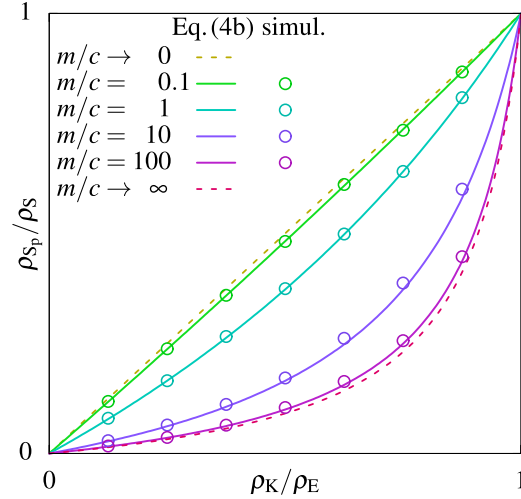

FIG. 5. Fraction of phosphorylated substrate ρ_{S_p}/ρ_S as a function of enzyme ratio ρ_K/ρ_E in the case when the phosphatase activity is 10 times higher than the kinase activity, $d = 10c$. Concentrations: $\rho_E = \rho_K + \rho_P = 0.006$ and $\rho_S = 0.01$.

D. Comparison with the previous study

As mentioned in the Introduction, this study follows our previous numerical study[3] in which the same reaction scheme was considered under the assumption that each lattice site can be occupied by no more than one molecule, and that an enzyme molecule reacts with a substrate molecule when located in adjacent lattice sites. Here, in contrast, we assumed that enzyme and substrate molecules are allowed to enter the same lattice site, and have to be in the same lattice site in order to react. This assumption substantially simplifies the problem and allowed us to obtain the (approximate) analytical results.
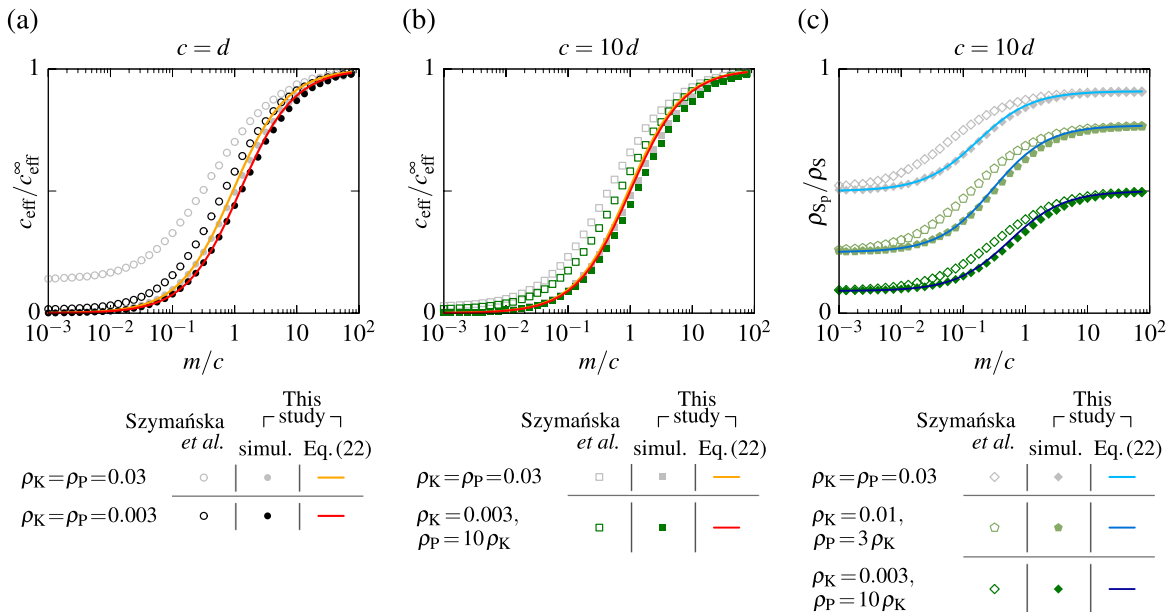
FIG. 6. Comparison of the current model with the model by Szymańska *et al.*[3] Solid lines present theoretical predictions of the current model. (a) Normalized effective phosphorylation rate coefficient, $c_{\text{eff}}/c_{\text{eff}}^{\infty}$, in the fully symmetric case: $c = d$, $\rho_K = \rho_P$ with ρ_K equal to 0.03 or 0.003. (b) Normalized effective phosphorylation rate coefficient, $c_{\text{eff}}/c_{\text{eff}}^{\infty}$, in the asymmetric case $c = 10d$, with $\rho_P = 0.03$ and ρ_K equal to 0.03 or 0.003. (c) Fraction of the phosphorylated substrate, ρ_{S_p}/ρ_S, for $c = 10d$, $\rho_P = 0.03$, and ρ_K equal to 0.03, 0.01, or 0.003.

Let us compare predictions of these two models. The assumption in the former model[3] implies a larger interaction radius and causes that there are on average six times more enzyme–substrate pairs than in the current model, thus in the infinite-diffusion limit the EMRRC was equal $c_{\text{eff}}^{\infty} = 6c$ (not just c as in the current model). Therefore, to compare the two models (Fig. 6), in the simulations according to the former model we divide microscopic constants c and d by 6, and normalize c_{eff} with respect to c_{eff}^{∞} for both models. The increase of the reaction radius that the effective distances between enzymes shortened, which for finite motility increased the EMRRCs with respect to the current model, Figs. 6(a) and 6(b). Additionally, because of the larger reaction radius the substrate molecules could have two antagonistic enzymes in their reaction volumes (consisting of six neighboring sites). Substrates having (at least) two antagonistic neighbors were sequentially phosphorylated and dephosphorylated, which led to nonzero c_{eff} in the zero-motility limit. The zero-motility EMRRCs are significant when the probability of having two antagonistic enzymes is large, i.e., for dense systems, Fig. 6(a). In reality, however, the sequential substrate modifications by the neighboring enzymes require the substrate molecule to expose its modified residue to the antagonistic enzyme. One can thus expect that in the case when both translational and rotational diffusions cease, the reactions are suppressed and therefore the EMRRCs should converge to zero in the limit of zero (translational and rotational) diffusion (as implicated by the current model).

Fig. 6(c) shows the discrepancy between steady-state phosphorylated substrate fractions predicted by two models, which arises when $c \neq d$ (for $c = d$, both models predict that $\rho_{S_p}/\rho_S = \rho_K/(\rho_K + \rho_P)$ independently of motility).

We expect that in the parameter region in which the discrepancy between these two models is significant (i.e., for very small motility and high enzyme concentration), the discrete lattice-based approach breaks, and the analysis should be based on the rigid body Brownian dynamics. The simulations should account for refractory times of enzyme molecules, ATP exchange kinetics, and for orientation of substrate and enzyme molecules.

IV. CONCLUSIONS

We derived formulas for the diffusion-controlled effective macroscopic reaction rate coefficients in a cycle of two reactions in which two antagonistic enzymes (here: kinase and phosphatase) modify the state of a substrate. Such cycles are ubiquitously utilized in biochemical signal transduction because they allow for rapid information transmission: substrate molecules are reused instead of being degraded and resynthesized.

We focused on two-dimensional reactors, which have their own peculiarities and are substantially different from three-dimensional reactors, but play an important role in regulatory pathways. Initial stages of signaling employ numerous types of membrane receptors that transmit signals by means of phosphorylation (and sometimes other modifications) of membrane-bound components. A large share of signal transduction takes place on membranes of various intracellular organelles. Biological membranes are considered crowded environment of relatively low diffusivity (at least an order of magnitude lower than in cytosol), and therefore reactions on membranes are expected to be diffusion-controlled. Importantly, effective diffusion coefficients of various substrates can be modified by transient binding to buffering proteins,[35] by the presence of crowding molecules, or through changes of viscoelastic properties of the membrane.

In this study, biochemical reactions on two-dimensional membranes are analyzed by means of Monte Carlo kinetic model on the square-shaped, triangular lattice. For this model, we propose a derivation in which the EMRRCs are expressed as the average time, τ_u (or τ_p), a substrate molecule spends between antagonistic reactions. This time, in turn, is the sum of time to find the antagonistic enzyme molecule, τ_{u_1} (or τ_{p_1}), and time to react after the first encounter with the enzyme molecule, τ_{u_2} (or τ_{p_2}). As the time τ_{u_2} (or τ_{p_2}) was found to be simply $\tau_{u_2} = 1/(c\,\rho_K)$ (or $\tau_{p_2} = 1/(d\,\rho_P)$), the main difficulty is in calculating time to find the antagonistic enzyme molecule, τ_{u_1} (or τ_{p_1}).

In solving this problem, we first noticed that phosphorylation and dephosphorylation reactions are correlated in space and time. Intuitively, it is clear when one enzyme, e.g., kinase, is much more abundant than the other enzyme. Then one may expect that after phosphorylation the search for the phosphatase molecules starts from one of the kinase molecules located in the vicinity of the phosphatase molecule which had previously dephosphorylated the substrate molecule, rather than from a random place with respect to the locations of phosphatase molecules. As a result, τ_{u_1} (or τ_{p_1}) depends on concentrations of both enzymes. After noticing this fact, we estimated τ_{u_1} and τ_{p_1} using the formula of Montroll,[33] which gives the average number of steps before trapping the random walker in a field of traps of concentration ρ. Coefficients of this formula were calculated by Montroll[33] for the case of periodically distributed traps; here, for the case of randomly distributed traps, we assumed that the first, leading-order coefficient has the same value as in the Montroll formula, and fits the value of the second coefficient using the results of numerical simulations.

The resulting macroscopic phosphorylation reaction rate coefficient c_{eff} has an intuitive form: it is half of the harmonic average of the microscopic phosphorylation rate constant, c, and the effective motility, $\tilde{M}$, divided by a slowly decreasing logarithmic function of enzyme concentration, $\rho_E = \rho_K + \rho_P$,

$$c_{\text{eff}} = \left(\frac{1}{c} + \frac{1}{\tilde{M}} f(\rho_E) \right)^{-1}. \qquad (24)$$

In the case when $c \ll \tilde{M}$, i.e., in the reaction-controlled limit, we have $c_{\text{eff}} \approx c$, while in the opposite, diffusion-controlled limit, $c \gg \tilde{M}$, $c_{\text{eff}} \approx \tilde{M}/f(\rho_E)$. In the last limit the logarithmic dependence of c_{eff} on enzyme concentration, $f(\rho_E) \propto \log(1/\rho_E)$, follows from the fact that the expected number of steps $w(\rho)$ till trapping in a system of randomly distributed traps with density ρ scales as $w(\rho) \propto \rho^{-1} \log(\rho^{-1})$ in the limit of $\rho \to 0$, when starting from a random position. In our case, the search for a kinase molecule starts after

dephosphorylation, which takes place in an approximately random position with respect to the kinases. In the case when search starts from a site neighboring a trap, the expected number of steps scales as $\tilde{w}(\rho) \propto \rho^{-1}$. Therefore, for example, in the classic reversible dimerization problem, an A molecule after the $A \cdot B$ dimer dissociation needs on average $\tilde{w}(\rho_B) = \rho_B^{-1}$ steps to find the same or another B molecule. This constitutes the main difference between reactions involving two antagonistic enzymes and simple reversible reactions.

Equation (24) together with analogous equation for d implies that when microscopic phosphorylation and dephosphorylation rate constants c and d differ, c_{eff} and d_{eff} scale differently with the motility. As a result, the steady-state phosphorylated substrate fraction can depend on the diffusivity. This is in contrast to single-reaction processes such as the reversible dimerization reaction $A + B \rightleftharpoons A \cdot B \overset{k}{\underset{q}{\rightleftharpoons}} C$ (considered in Appendix C) where the steady-state concentration of C does not depend on the diffusion coefficient.

The derived EMRRCs and the steady-state value of the phosphorylated substrate fraction agree with the numerical estimates with reasonable accuracy. Based on analytical considerations and results of numerical simulations, we may conclude that in the range of parameters,

$$m \in (0, \infty), \quad \rho_K \in (0, 0.03),$$
$$\rho_P \in (0, 0.03), \quad \rho_S \in (0, 0.1), \tag{25}$$

the analytical estimates of EMRRCs and the phosphorylated substrate fraction ρ_{S_p}/ρ_S satisfy the following:

- for $c = d$: [EMRRC relative error] < 5% and $[\rho_{S_p}/\rho_S]$ is exact;
- for $c \neq d$ with $c/d \in (0.01, 100)$: [EMRRC relative error] < 20% and $[\rho_{S_p}/\rho_S$ error] < 0.05.

Still, one should be aware of limitations of the on-lattice model, discussed in Sec. III D. These limitations can render our approximation non-satisfactory for dense systems characterized by a very small diffusivity.

In summary, the proposed analysis is able to capture the behavior of the system in which the steady state is qualitatively controlled by diffusion. For low diffusivity, i.e., when reaction kinetics is diffusion-controlled, the steady state is imposed by the more abundant enzyme, while for high diffusivity, i.e., in the reaction-controlled limit, it is imposed by the enzyme which has higher effective activity. More work and a more detailed description is needed in the case of high concentration of enzymes and membrane crowders that can maintain membrane proteins close to the percolation threshold.[36] In this limit, various subcellular environments exist on the verge of the sol–gel transition,[37] and one can expect the existence of localized, temporal abrupt changes of effective diffusivity which can impact biochemical reaction kinetics implicated in signal transduction.[38]

APPENDIX A: EFFECTIVE MOTILITY

Here, we briefly summarize the influence of molecular crowding on the effective motility, $\tilde{m}$. As discussed before,[3] the effective motility of a molecule having motility m depends on both the concentration of crowding molecules, ρ_C, and their motility, m_C. By the crowding molecules, we understand those whose presence in a lattice site prevents the considered molecule from moving to that lattice site. The expression for $\tilde{m}$ reads

$$\tilde{m} = m f(\rho_C, g)(1 - \rho_C), \tag{A1}$$

where f is the correlation function that can be approximated by the following formula:[34,39]

$$f(\rho_C, g) = \frac{\{[(1-g)(1-\rho_C)f_0 + \rho_C]^2 + 4g(1-\rho_C)f_0^2\}^{1/2}}{2g(1-\rho_C)f_0}$$
$$- \frac{[(1-g)(1-\rho_C)f_0 + \rho_C]}{2g(1-\rho_C)f_0}, \tag{A2}$$

where

$$f_0 = (1-a)/[1 + a(2g-1)] \tag{A3}$$

and g is the ratio of m/m_C. The coefficient a used in Eq. (A3) depends on the lattice type; for triangular lattice (considered here) $a = 0.282$, for square lattice $a = 1 - 2/\pi$, and for honeycomb (or hexagonal) lattice $a = 1/2$.[40] Since we consider only the case when all molecules have the same motility ($g = 1$), Eq. (A1) simplifies to

$$\tilde{m}(m, \rho_C, 1) = m \frac{\sqrt{\rho_C^2 + 4(1 - \rho_C)\left(\frac{1-a}{1+a}\right)^2} - \rho_C}{2\left(\frac{1-a}{1+a}\right)}. \tag{A4}$$

Recall that in the present model we assume that neither two enzyme molecules nor two substrate molecules can enter the same lattice site. This means that enzyme as well as substrate molecules play the role of crowding agents only for themselves. Accordingly, $\tilde{m}_X$ for $X \in \{S, K, P\}$ is given by

$$\tilde{m}_X = \begin{cases} \tilde{m}(m_X, \rho_S, 1) & \text{for} \quad X = S, \\ \tilde{m}(m_X, \rho_K + \rho_P, 1) & \text{for} \quad X \in \{K, P\}. \end{cases} \tag{A5}$$

APPENDIX B: ESTIMATION OF $w(\rho)$

Assuming that a walker has the same probability of starting from any non-trapping site, Montroll[33] obtained an analytical asymptotic formula for the average number of steps of a random walker, for walks on lattices with periodic distributions of traps, of concentration ρ, or, equivalently, on finite lattices of volume $V = 1/\rho$ with periodic boundary

conditions containing a single trap. The approximate formula reads

$$w_P(1/V) = \alpha V \log V + \beta V + \gamma + O(1/V), \qquad \text{(B1)}$$

where α is constant for a particular lattice structure ($\alpha = 1/\pi$ for square lattice, $\alpha = \sqrt{3}/(2\pi)$ for triangular lattice), whereas β and γ depend also on the shape of the reactor. For a triangular lattice and a square-shaped reactor, their values are $\beta \approx 0.235$ and $\gamma \approx -0.251$. We restricted ourselves to two first terms of the right-hand side of Eq. (B1). As discussed by Montroll,[33] the formula in Eq. (B1) agrees almost perfectly (with the error smaller than 0.1% for lattices of $V \geq 16$) with exact values.

To obtain the EMRRCs for large lattices with multiple enzyme molecules, we need to estimate $w(\rho) = w(1/V)$ in the case when traps are randomly distributed. Up to our best knowledge, despite several theoretical, e.g., Ref. 41, and numerical attempts, e.g., Refs. 42 and 43, this problem remains unsolved, i.e., precise estimates for $w(\rho)$ are not known.[44,45] Thus, we estimate $w(\rho)$ in numerical simulations (as described in Sec. II) and then fit the formula analogous to that obtained by Montroll[33] (cf. Eq. (2.16) in Ref. 41), i.e.,

$$w_R(\rho) = \alpha' \rho^{-1} \log(\rho^{-1}) + \beta' \rho^{-1}, \qquad \text{(B2)}$$

assuming that $\alpha' = \alpha$. Through fitting we obtained $\beta' = 1.00$. Use of α' and β' which were fitted simultaneously does not decrease the error.

We verified the accuracy of our approach by performing analogous simulations for periodic distribution of traps, i.e., in the case when analytical results are known. The small discrepancy between our numerical estimates and the formula derived by Montroll[33] (Fig. 7) justifies our numerical approach and suggests a reasonable accuracy of the fitted coefficient β' when traps are distributed randomly.

APPENDIX C: REVERSIBLE DIMERIZATION PROBLEM

We consider the classical reversible dimerization reaction $A + B \rightleftharpoons A \cdot B \underset{q}{\overset{k}{\rightleftharpoons}} C$, where $A \cdot B$ denotes the geminate A, B pair that occupies a single lattice site, while C denotes A, B heterodimer. Let ρ_C denote concentration of heterodimers and let ρ_A, ρ_B denote concentrations of A and B molecules that are free or in a geminate pair. This is $\rho_A = \rho_{A_{tot}} - \rho_C$ and $\rho_B = \rho_{B_{tot}} - \rho_C$, where $\rho_{A_{tot}}$ and $\rho_{B_{tot}}$ are the total concentrations of A and B molecules.

Since the molecules A and B are allowed to enter the same site, their positions are independent. Therefore, the geminate pair concentration will be given by $\rho_{A \cdot B} = \rho_A \rho_B$. In the steady state, geminate pairs $A \cdot B$ are in equilibrium with heterodimers C, i.e., $0 = d\rho_C/dt = k \rho_{A \cdot B} - q \rho_C$, which implies

$$\rho_C = \frac{k}{q} \rho_A \rho_B. \qquad \text{(C1)}$$

This agrees with the classic formula obtained in the Brownian dynamics model (see, e.g., Ref. 21). The formula implies that steady state concentrations are independent of diffusion, which is in contrast to the more complex reaction scheme
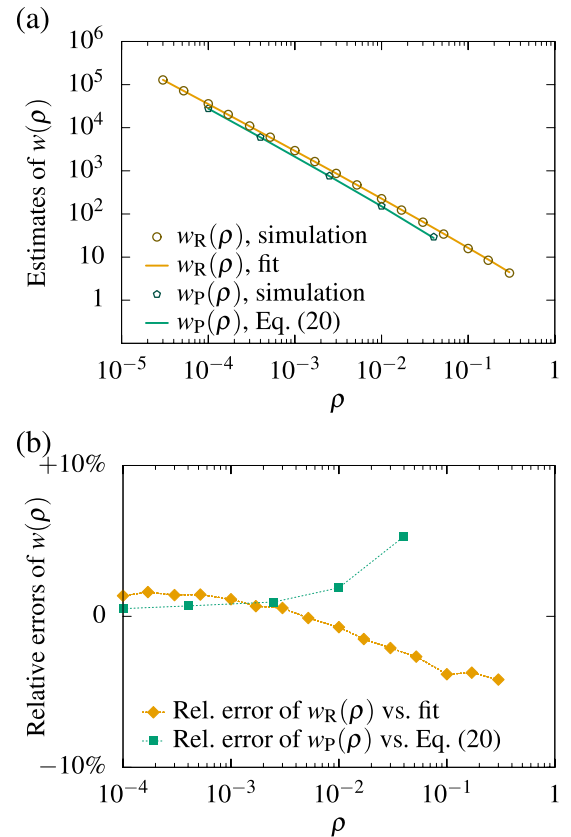

FIG. 7. Average number of steps of a random walker before trapping in periodically and randomly distributed traps. (a) Numerical estimates of $w_R(\rho)$ (random traps) and $w_P(\rho)$ (periodic traps) versus best fit (with $\alpha' = \alpha = \sqrt{3}/(2\pi)$, with fitted $\beta = 1.00$) or the Montroll formula[33] ($\alpha = \sqrt{3}/(2\pi)$ and $\beta = 0.235$). (b) The relative error between numerical estimate and fit, (simulation − fit)/fit, and between numerical estimate and Montroll formula, (simulation − Montroll)/Montroll, see Ref. 33. The fit was obtained for trap concentrations $\rho \in [0.000\,03; 0.03]$, i.e., when the concentration of traps is low enough so the asymptotic formula can hold but simultaneously the number of traps is not smaller than 30.

studied in this paper. We use this classic formula to check the accuracy of our numerical approach. In Fig. 8, we numerically calculate $q \rho_C/(k \rho_A \rho_B)$ as a function of motility, showing that
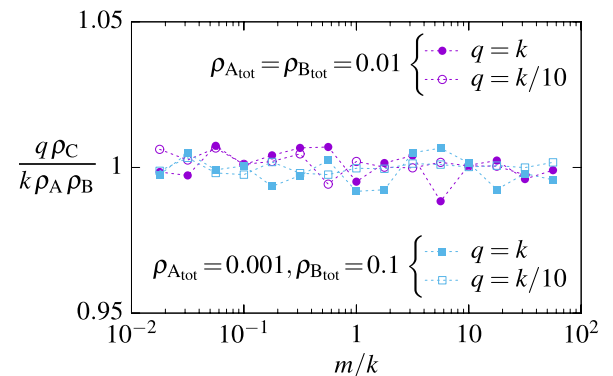

FIG. 8. Reversible dimerization problem: comparison of the numerically calculated steady-state concentrations with the analytical expression, Eq. (C1). Value of the expression $q \rho_C/(k \rho_A \rho_B)$ is plotted as a function of scaled motility, m/k. Four combinations of parameters $\rho_{A_{tot}}$, $\rho_{B_{tot}}$, k, and q are considered.

the error introduced by our numerical scheme is comparable to the statistical error of order of 1% for scaled motilities: $m/k \in (0.01, 100)$.

[1] O. Dushek, J. Goyette, and P. A. van der Merwe, Immunol. Rev. **250**, 258 (2012).

[2] H.-X. Zhou, G. Rivas, and A. P. Minton, Annu. Rev. Biophys. **37**, 375 (2008).

[3] P. Szymańska, M. Kochańczyk, J. Miękisz, and T. Lipniacki, Phys. Rev. E **91**, 022702 (2015).

[4] M. von Smoluchowski, Z. Phys. Chem. **92**, 129 (1917).

[5] F. C. Collins and G. E. Kimball, J. Colloid Sci. **4**, 425 (1949).

[6] K. R. Naqvi, Chem. Phys. Lett. **28**, 280 (1974).

[7] C. A. Emeis and P. L. Fehder, J. Am. Chem. Soc. **92**, 2246 (1970).

[8] D. C. Torney and H. M. McConnell, Proc. R. Soc. A **387**, 147 (1983).

[9] D. Toussaint and F. Wilczek, J. Chem. Phys. **78**, 2642 (1983).

[10] C. E. Allen and E. G. Seebauer, J. Chem. Phys. **104**, 2557 (1996).

[11] A. Szabo, J. Phys. Chem. **93**, 6929 (1989).

[12] H.-X. Zhou, J. Phys. Chem. B **101**, 6642 (1997).

[13] H. Kim, M. Yang, M.-U. Choi, and K. J. Shin, J. Chem. Phys. **115**, 1455 (2001).

[14] S. Park and N. Agmon, J. Phys. Chem. B **112**, 5977 (2008).

[15] S. Park and N. Agmon, J. Phys. Chem. B **112**, 12104 (2008).

[16] Y. B. Zel'dovich and A. A. Ovchinnikov, JETP Lett. **26**, 440 (1977).

[17] O. G. Berg, Chem. Phys. **31**, 47 (1978).

[18] N. Agmon and A. Szabo, J. Chem. Phys. **92**, 5270 (1990).

[19] A. Szabo, J. Chem. Phys. **95**, 2481 (1991).

[20] A. L. Edelstein and N. Agmon, J. Phys. Chem. **99**, 5389 (1995).

[21] I. V. Gopich and A. Szabo, J. Chem. Phys. **117**, 507 (2002).

[22] K. Takahashi, S. Tănase-Nicola, and P. R. ten Wolde, Proc. Natl. Acad. Sci. U. S. A. **107**, 2473 (2010).

[23] O. Dushek, P. A. van der Merwe, and V. Shahrezaei, Biophys. J. **100**, 1189 (2011).

[24] J. S. van Zon, M. J. Morelli, S. Tănase-Nicola, and P. R. ten Wolde, Biophys. J. **91**, 4350 (2006).

[25] C. C. Govern, M. K. Paczosa, A. K. Chakraborty, and E. S. Huseby, Proc. Natl. Acad. Sci. U. S. A. **107**, 8724 (2010).

[26] A. V. Popov and N. Agmon, J. Chem. Phys. **117**, 5770 (2002).

[27] S. Park, K. J. Shin, and N. Agmon, J. Chem. Phys. **121**, 868 (2004).

[28] S. Park, K. J. Shin, A. V. Popov, and N. Agmon, J. Chem. Phys. **123**, 034507 (2005).

[29] A. Szabo and H.-X. Zhou, Bull. Korean Chem. Soc. **33**, 925 (2012).

[30] P. J. Zuk, M. Kochańczyk, J. Jaruszewicz, W. Bednorz, and T. Lipniacki, Phys. Biol. **9**, 055002 (2012).

[31] M. Kochańczyk, J. Jaruszewicz, and T. Lipniacki, J. R. Soc., Interface **10**, 20130151 (2013).

[32] D. T. Gillespie, J. Phys. Chem. **81**, 2340 (1977).

[33] E. W. Montroll, J. Math. Phys. **10**, 753 (1969).

[34] H. van Beijeren and R. Kutner, Phys. Rev. Lett. **55**, 238 (1985).

[35] B. Kaźmierczak and Z. Peradzyński, J. Math. Biol. **62**, 1 (2011).

[36] B. J. Sung and A. Yethiraj, J. Phys. Chem. B **112**, 143 (2008).

[37] P. Li, S. Banjade, H.-C. Cheng, S. Kim, B. Chen, L. Guo, M. Llaguno, J. V. Hollingsworth, D. S. King, S. F. Banani, P. S. Russo, Q.-X. Jiang, B. T. Nixon, and M. K. Rosen, Nature **483**, 336 (2012).

[38] K. Jaqaman, H. Kuwata, N. Touret, R. Collins, W. S. Trimble, G. Danuser, and S. Grinstein, Cell **146**, 593 (2011).

[39] P. F. F. Almeida and W. L. C. Vaz, Handb. Biol. Phys. **1**, 305 (1995).

[40] K. Compaan and Y. Haven, Trans. Faraday Soc. **52**, 786 (1956).

[41] W. Den Hollander, J. Stat. Phys. **37**, 331 (1984).

[42] P. Scheunders and J. Naudts, Z. Phys. B **73**, 551 (1989).

[43] G. T. Barkema, P. Biswas, and H. van Beijeren, Phys. Rev. Lett. **87**, 170601 (2001).

[44] F. S. Henyey and V. Seshadri, J. Chem. Phys. **76**, 5530 (1982).

[45] After the acceptance of the manuscript, we learned from Frank den Hollander that based on results from Refs. 41 and 44 in the case of randomly distributed traps the following approximate analytical formula for the average number of steps before trapping can be obtained:

$$w_R^*(\rho) = \frac{A}{\rho} \left(\log \frac{c}{\rho} + \log\log \frac{c}{\rho} + \log\log \frac{c}{\rho} \Big/ \log \frac{c}{\rho} + 2K \Big/ \log \frac{c}{\rho} + \cdots \right),$$

where $A = \sqrt{3}/(2\pi)$, $C = 8\sqrt{3}\pi$, $K \cong 1.171953$. This formula is thought to be exact in the limit of $\rho \to 0$ and does not require parameter fitting, which is an undisputed advantage. In the regime explored in this paper, however, its accuracy is not better than that of formula (B2) and it produces more complex expressions for c_{eff} and d_{eff}.

OXFORD

Systems biology

SPATKIN: a simulator for rule-based modeling of biomolecular site dynamics on surfaces

Marek Kochańczyk[1],*, William S. Hlavacek[2] and Tomasz Lipniacki[1]

[1]Institute of Fundamental Technological Research, Warsaw 02-106, Poland and [2]Theoretical Division, Los Alamos National Laboratory, Los Alamos, NM 87545, USA

*To whom correspondence should be addressed.
Associate Editor: Jonathan Wren

Abstract

Summary: Rule-based modeling is a powerful approach for studying biomolecular site dynamics. Here, we present SPATKIN, a general-purpose simulator for rule-based modeling in two spatial dimensions. The simulation algorithm is a lattice-based method that tracks Brownian motion of individual molecules and the stochastic firing of rule-defined reaction events. Because rules are used as event generators, the algorithm is network-free, meaning that it does not require to generate the complete reaction network implied by rules prior to simulation. In a simulation, each molecule (or complex of molecules) is taken to occupy a single lattice site that cannot be shared with another molecule (or complex). SPATKIN is capable of simulating a wide array of membrane-associated processes, including adsorption, desorption and crowding. Models are specified using an extension of the BioNetGen language, which allows to account for spatial features of the simulated process.

Availability and implementation: The C++ source code for SPATKIN is distributed freely under the terms of the GNU GPLv3 license. The source code can be compiled for execution on popular platforms (Windows, Mac and Linux). An installer for 64-bit Windows and a macOS app are available. The source code and precompiled binaries are available at the SPATKIN Web site (http://pmbm.ippt.pan.pl/software/spatkin).

Contact: spatkin.simulator@gmail.com

Supplementary information: Supplementary data are available at *Bioinformatics* online.

1 Introduction

In living cells, information processing is enabled by networks of interacting biomolecules that typically have multiple modification and binding sites. Tracking the time- and condition-dependent states of these sites in a model is challenging because of the high or even infinite number of potentially populated chemical species. This challenge is overcome with rule-based modeling approaches, in which models are formulated in terms of rules for biomolecular interactions. With a rule-based approach, a large reaction network can be concisely represented by a relatively small set of rules, with each rule characterizing an interaction and an associated class of reactions (Chylek *et al.*, 2014). A complete list of reactions implied by rules can be generated before a numerical simulation, as with

BioNetGen (Harris *et al.*, 2016), or the rules may be used as event generators in a stochastic simulation algorithm, as with NFsim (Sneddon *et al.*, 2011). The latter approach enables one to analyze models consisting of rules that imply reaction networks too large to be generated.

There are many software packages that enable rule-based modeling but only a handful of them support spatial modeling. Tools that enable spatial rule-based modeling include MCell-R (Tapia Valenzuela, 2016), Simmune (Angermann *et al.*, 2012), Smoldyn (Andrews, 2017), SK (Sorokina *et al.*, 2013), SRsim (Gruenert *et al.*, 2010), SSC (Lis *et al.*, 2009) and VCell (Schaff *et al.*, 2016). Simmune, SSC and VCell depend on network generation, meaning that a list of possible reactions must be derived from rules before a
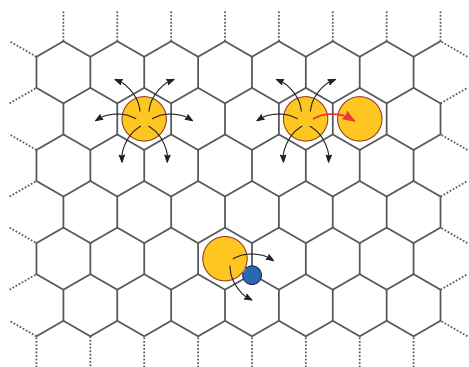
Fig. 1. Lattice confinement of (regular) molecules and binders. *Top left*: A molecule (orange) in a site of a triangular lattice can hop to one of unoccupied adjacent lattice sites. *Top right*: A molecule can jump to an occupied adjacent lattice site (red arrow) only when a complex formation reaction is allowed (and such an event has been selected). *Bottom*: Movements of a molecule bound to an (immobile) binder (blue), which is placed in a node of a dual lattice, are constrained so that the bond is not broken

simulation is performed. The remaining three simulators have the advantage of not relying on network generation.

Here, we present SPATKIN, which offers stochastic rule-based modeling capabilities that do not rely on prior network generation. The simulator tracks positions of individual molecules (not accounting for their internal spatial structure) in a two-dimensional space discretized using a triangular lattice. A comparison of SPATKIN with the most similar of the above-mentioned tools is provided in Section 4. Early-development-stage versions of SPATKIN have been used to study how diffusion and the intrinsic noise of biochemical reactions affect the initiation of traveling waves (Kochańczyk *et al.*, 2013; Zuk *et al.*, 2012). The software has been validated by comparing simulation results obtained for very fast diffusion (rendering the simulated reactor well-mixed) with the results obtained with (non-spatial) BioNetGen. For finite diffusivity, it was shown that the effective macroscopic rate constants determined using SPATKIN agree with analytical estimates for these rate constants (Nałecz-Jawecki *et al.*, 2015; Szymańska *et al.*, 2015) and that the traveling wave velocity agrees with that obtained in finite element-based simulations of analogous partial differential equations-defined systems (Kochańczyk *et al.*, 2013).

2 Approach

SPATKIN implements two-dimensional lattice-based Brownian dynamics (BD) and is designed for simulations of reaction–diffusion processes occurring on surfaces, such as the plasma membrane of a cell. Models and simulation protocols are specified using an extension of the BioNetGen language (BNGL), or to precise, a superset of a subset of BNGL. The extended language is referred to as SptBNGL. A complete, formal definition of SptBNGL, along with its comparison with BNGL, are provided in the User Manual. SptBNGL allows for the specification of boundary conditions, the diffusion properties of biomolecules and biomolecular complexes, and other information necessary to initialize SPATKIN simulations (e.g. starting positions of molecules).

SPATKIN does not rely on network generation. Rather, rules are directly used to generate reaction events. The event-generation procedure is a generalization of that used to generate reaction events in a conventional BD simulation, with use of a list of reactions being replaced by use of a list of rules. Immediately after simulation of a reaction or diffusion event, lists of possible events consistent with model rules are updated locally, which is efficient due to the hybrid

use of hierarchical space-partitioning trees and hash tables. The Monte Carlo method is rejection-free unless there are lattice subdomains of diminished diffusivity, which can be introduced to model traps or membrane heterogeneity (Kochańczyk *et al.*, 2013). As with other rule-based modeling software tools, the biomolecules and biomolecular complexes considered in a SPATKIN simulation are associated with graphs, with nodes representing functional components of biomolecules and edges representing bonds between components. The nodes may have textual attributes that represent internal states of biomolecular sites. Thus, SPATKIN differs from conventional BD simulators in that the molecular substructures of chemical species are explicitly tracked. However, the internal graph data structures of SPATKIN are not used to represent spatial configurations of complexes. Molecules and complexes are each taken to occupy a single lattice site, to the exclusion of other unconnected molecules.

There are two kinds of chemical entities: *molecules*, which represent membrane-tethered proteins and occupy hexagonal cells of a lattice, and *binders*, which can occupy the sites of a dual lattice (see Fig. 1). The main difference between these two types of entities is that regular molecules can assume different internal states and are capable of binding other molecules, whereas binders have no internal state and can only bind regular molecules. The concept of binders, which are always taken to be immobile, was introduced into SPATKIN to model immunogenic ligands that induce receptor clustering and immobilization. A single lattice node may contain no molecules, or a single (whole) molecule, or an (entire) complex of several (connected) molecules. Because of the constraints of a triangular lattice, any molecule can have up to six other molecules and six binders as neighbors, and any binder can be adjacent to a maximum of three molecules (see Fig. 1). The temporal evolution of a simulated system can be viewed as analogous to that of a cellular automaton in which a single event occurs in each time step.

We recommend using SPATKIN in conjunction with BioNetGen. As the latter tool implements an efficient version of Gillespie's direct method for well-mixed systems, it can be used to determine behavior in the infinite-diffusion limit and find starting parameter estimates for more expensive SPATKIN simulation studies. A model formulated in BNGL can be easily recast as a spatial model defined using SptBNGL. From this point, SPATKIN can be applied to investigate spatial effects, such as the possible consequences of diffusion-limited reaction rates or spatially varying diffusivity.

3 Implementation

SPATKIN comprises a simulator equipped with a parser for interpreting plain-text input files, which define models and simulation settings using the conventions of SptBNGL, and a tool for visualizing snapshots of system configurations. Both tools can be invoked from the command line or used within a GUI, which facilitates creation, editing and debugging of input files, and visualization of simulation results in the form of X–Y plots and lattice snapshots (see Fig. 2). The source code is written in C++; the build process is managed by CMake. The Spirit Parser Framework was used to develop the SptBNGL parser. The Cairo programming library was used to develop SPATKIN's visualization capabilities. The Qt framework was used to build the GUI. The GUI provides a multiple document interface (MDI), which enables running multiple stochastic simulations in parallel.

Supplementary Material online contains commented example input files. A detailed User Manual is available at the SPATKIN Web site.
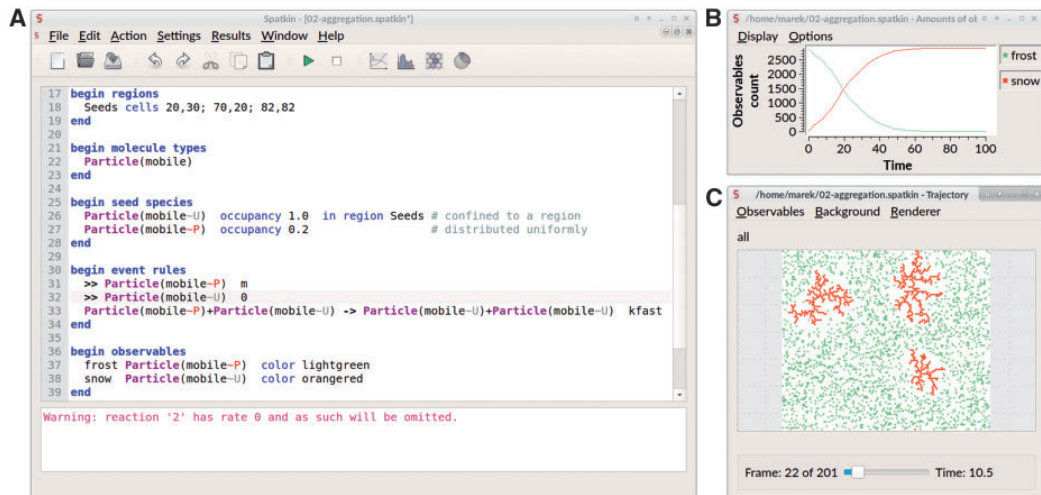
Fig. 2. SPATKIN GUI with (**A**) code editor as an MDI window and separate windows for viewing simulations results as (**B**) X–Y plots and (**C**) snapshots of system configurations

4 Comparison to similar tools

Among the three spatial and network-free rule-based modeling tools mentioned in Introduction, SK has the coarsest spatial resolution and SRSim has the finest spatial resolution. SK implements a next-subvolume method, in which reaction compartments are divided into subvolumes that are taken to be locally well mixed; translocations between subvolumes are treated as reactions. MCell-R integrates NFsim and MCell, providing a tool for off-lattice stochastic simulations of BD and diffusion-controlled reactions defined by rules specified in BNGL. Biomolecules and biomolecular complexes are treated as point particles in both SK and MCell-R. SRSim accounts for the space occupied by biomolecules (i.e. excluded-volume effects) and thus requires specification of the coarse structures of biomolecules, as well as geometric constraints on interactions. SRSim performs molecular dynamics simulations, requiring the user to specify a force field that governs biomolecular interactions.

In comparison to SK, SPATKIN offers greater spatial resolution, with the disadvantage of higher simulation cost. In contrast to MCell-R, SPATKIN is specialized to 2-D reaction systems. In comparison to SRSim, which performs force field-based simulations, SPATKIN, in which simulations are based on excluded-volume BD and chemical kinetics, allows for easier comparison of results against those produced by commonly used non-spatial simulators, making it possible to unambiguously identify diffusion effects.

There are two recently developed simulators, not mentioned thus far, that also consider excluded-volume effects: ReaDDy (Schöneberg and Noé, 2013) and SpringSaLaD (Michalski and Loew, 2016). These tools treat molecules as collections of beads. In ReaDDy, a force field governs diffusive bead movements. In SpringSaLaD, links between beads, modeled as springs, impose constraints on the relative positions of beads. These tools are distinct from SPATKIN, SK, MCell-R and SRSim in that they do not enable model formulation in terms of rules for interactions using a formal language.

Funding

Conflict of Interest: none declared.

References

Andrews,S.S. (2017) Smoldyn: particle-based simulation with rule-based modeling, improved molecular interaction, and a library interface. *Bioinformatics*, **33**, 710–717.

Angermann,B.R. *et al.* (2012) Computational modeling of cellular signaling processes embedded into dynamic spatial contexts. *Nat. Methods*, **9**, 283–289.

Chylek,L.A. *et al.* (2014) Rule-based modeling: a computational approach for studying biomolecular site dynamics in cell signaling systems. *WIREs Syst. Biol. Med.*, **6**, 13–36.

Gruenert,G. *et al.* (2010) Rule-based spatial modeling with diffusing, geometrically constrained molecules. *BMC Bioinformatics*, **11**, 307.

Harris,L.A. *et al.* (2016) BioNetGen 2.2: advances in rule-based modeling. *Bioinformatics*, **32**, 3366–3368.

Kochańczyk,M. *et al.* (2013) Stochastic transitions in a bistable reaction system on the membrane. *J. R. Soc. Interface*, **10**, 20130151.

Lis,M. *et al.* (2009) Efficient stochastic simulation of reaction–diffusion processes via direct compilation. *Bioinformatics*, **25**, 2289–2291.

Michalski,P.J. and Loew,L.M. (2016) SpringSaLaD: a spatial, particle-based biochemical simulation platform with excluded volume. *Biophys. J.*, **110**, 525–529.

Nałecz-Jawecki,P. *et al.* (2015) Effective reaction rates for diffusion-limited reaction cycles. *J. Chem. Phys.*, **143**, 215102.

Schaff,J.C. *et al.* (2016) Rule-based modeling with Virtual Cell. *Bioinformatics*, **32**, 2880–2882.

Schöneberg,J. and Noé,F. (2013) ReaDDy – a software for particle-based reaction-diffusion dynamics in crowded cellular environments. *PLoS One*, **8**, e74261.

Sneddon,M.W. *et al.* (2011) Efficient modeling, simulation and coarse-graining of biological complexity with NFsim. *Nat. Methods*, **8**, 177–183.

Sorokina,O. *et al.* (2013) A simulator for spatially extended kappa models. *Bioinformatics*, **29**, 3105–3106.

Szymańska,P. *et al.* (2015) Effective reaction rates in diffusion-limited phosphorylation-dephosphorylation cycles. *Phys. Rev. E*, **91**, 022702.

Tapia Valenzuela,J.J. (2016) A study on systems modeling frameworks and their interoperability. Ph.D. Thesis, University of Pittsburgh.

Zuk,P.J. *et al.* (2012) Dynamics of a stochastic spatially extended system predicted by comparing deterministic and stochastic attractors of the corresponding birth–death process. *Phys. Biol.*, **5**, 055002.

This **Supplementary Material** features the article

"SPATKIN: A simulator for rule-based modeling of biomolecular site dynamics on surfaces"

by Kochańczyk *et al.*, *Bioinformatics*, 2017

This document is intended as a practical introduction to SPATKIN, that demonstrates its capabilities by providing 10 annotated tutorial "μmodels":

All "μmodels" are shown in the form of complete, runnable inputs, and are included as separate files in the source code distribution of SPATKIN (in the directory doc/examples). An archive containing these files can be also downloaded directly from the software Web site. Additional SPATKIN documentation can be found in the User Manual.

Tutorial μmodel 1: Heterogeneous initial location of molecules

This example (see Listing 1) shows how user-defined regions can be used to place molecules in a non-homogeneous manner on the lattice. One region is used to constrain the initial placement of molecules A(x~U,y~U) (drawn grey), at time=0; other regions are filled with molecules B (red) and C (blue) in the course of simulation according to a temporally constrained emergence rule. Molecules B modify molecules A(x~U,y~U) into A(x~P,y~U) – green. Molecules C modify molecules A(x~U,y~U) into A(x~U,y~P) – yellow. Molecules A and B degrade slowly. Simulation shows how polarization can be introduced to the system and how it vanishes due to diffusion.

```
begin parameters
  m 3
  m2 10   k 0.1     # This is a free-format text, meaning that line breaks
  r 10   q 0.01     #  do not matter.
end


begin world
  topology plane   size 200 200
end


begin regions
  # Two basic primitives for defining regions are circles and rectangles.
  CircRgn   circle     100 100 50       # centerX centerY radius
  RectRgn   rectangle 100 150 200 100 # centerX centerY width height

  # Typical constructive geometry operations are supported:
  RgnX   !CircRgn                   # !a =: complement of set a
  RgnY   (CircRgn * RectRgn)        # (a * b) =: intersection of a and b
  RgnZ   (CircRgn - RectRgn)        # (a - b) =: subtraction of b from a
end


begin molecule types
  A(x,y)   B()   C()
end


begin seed species                              # Number of molecules or frac-
  A(x~U,y~U)  occupancy 0.1  in region RgnX  #  tional (region) occupancy
end                                             #  should be given here.
```

```
begin event rules
  # Diffusion, molecule emergence and degradation rules have prefix syntax.
  >> A()  m    #  |
  >> B()  m2   #  >- diffusion
  >> C()  m2   #  |


  # Following 2 rules for molecule insertion are both spatially and
  #  temporally constrained; effective rate of insertion is proportional
  #  to the number of unoccupied lattice nodes (here, in a region):
  ++ B()  k   in region RgnY  since 5  until 8
  ++ C()  k   in region RgnZ  since 5  until 8


  B() + A(x~U,y~U) -> B() + A(x~P,y~U)  r
  C() + A(x~U,y~U) -> C() + A(x~U,y~P)  r


  -- B()  q      -- C()  q    # Molecules B, C are degraded with rate q.
end

begin observables
    A  A(x~U,y~U)   color lightgrey       # All observables that
    Ax A(x~P,y~U)   color green           #  have assigned colors
    Ay A(x~U,y~P)   color gold            #  are recorded in the
    B  B()          color red             #  trajectory file.
    C  C()          color blue            #
end

begin simulation
    time end 300            # Total duration (in simulation time units).
    observer intervals 100  # No. time points at which logging occurs.
end
```

Listing 1: Tutorial input file 1 (doc/examples/tutorial/01-regions.spatkin).

Tutorial µmodel 2: Diffusion-limited aggregation

This example (Listing 2) demonstrates diffusion-limited aggregation in just 3 (effectively 2) rules (rules of zero rate are omitted).

```
begin parameters
  m        10
  kfast 10000
end


begin world
  topology plane  size 120 120
end


begin regions
  Seeds cells 20,30; 70,20; 82,82  # Region consists of single lattice nodes.
end


begin molecule types
  Particle(mobile)
end


begin seed species
  Particle(mobile~U)  occupancy 1.0  in region Seeds  # confined to a region
  Particle(mobile~P)  occupancy 0.2                    # distributed uniformly
end


begin event rules
  "Gogogo!":
  >> Particle(mobile~P)  m  # A named rule for diffusion.


  >> Particle(mobile~U)  0  # Anonymous rule (referred to as rule "2").


  # According to the above rules, molecule diffusivity depends on its state.
  Particle(mobile~P) + Particle(mobile~U)  ->
  Particle(mobile~U) + Particle(mobile~U)  kfast
end
```

```
begin observables
  frost Particle(mobile~P)  color lightgreen # An array of observables colors
  snow  Particle(mobile~U)  color orangered  #  has been predefined for user's
end                                          #  convenience (see user manual).


begin simulation
  time end 100         # If there are no more events, a warning will be issued.
  observer intervals 200
end
```

Listing 2: Tutorial input file 2 (doc/examples/tutorial/02-aggregation.spatkin).

Tutorial µmodel 3: State-dependent removal from the membrane

This example (Listing 3) is inspired by the fact that lipid modification, such as palmitoylation or farnesylation, can affect membrane attachment of proteins; for example, G protein α subunit is depalmitoylated upon stimulation and then translocates to cytosol.

```
begin parameters
  m1   10
  b   1
  d   10
  u   10
  x   0.1
end


begin world
  topology plane   size 100 100
end


begin regions   (* none *)   end


begin molecule types            # By defining relative molecular weights in
  Thioesterase(a)   weight 1   #  this manner, we assure that Thioesterase,
  AlphaS(palmito)   weight 0   #  which is assumed immobile, does not move
end                           #  upon binding/unbinding AlphaS.


begin seed species
  AlphaS(palmito~P)   1000      # site 'palmito' defined explicitly as unbound
  Thioesterase(a)       10    # site 'a'       defined explicitly as unbound
end


begin event rules
 >> Thioesterase(a)   0        # assumed immobile
 >> AlphaS(palmito) m1         # assumed mobile
 Thioesterase(a) + AlphaS(palmito~P)  ->Thioesterase(a!1).AlphaS(palmito~P!1) b
 Thioesterase(a!1).AlphaS(palmito~P!1)->Thioesterase(a!1).AlphaS(palmito~U!1) d
 Thioesterase(a!1).AlphaS(palmito~U!1)->Thioesterase(a) + AlphaS(palmito~U)   u
 -- AlphaS(palmito~U) x         # removal of depalmitoylated AlphaS from membrane
end
```

```
begin observables
  A_palmi   AlphaS(palmito~P!?) color lightpink # '?!' means that the status of
  A_depalmi AlphaS(palmito~U!?) color red       #  binding is irrelevant here
  T         Thioesterase()      color darkblue
end


begin simulation
  description "Depalmitoylation v0.1" # Descriptions are copied into results.
  duration 300                        # Bimolecular complexes are occasionally
  observer intervals 100              #  seen in trajectory as split hexagons.
end
```

Listing 3: Tutorial input file 3 (doc/examples/tutorial/03-depalmitoylation.spatkin).

Tutorial μmodel 4: Rule-based capabilities (1)

This example ([Listing 4](#)) demonstrates rule-based capabilities.

Each molecule S ("substrate") can be independently phosphorylated on 10 residues, meaning that S may assume one of $2^{10} = 1024$ phosphorylation states. Residues A, B, C, D, E can be phosphorylated by kinase K1 which is recruited and remains tethered in the circular region RgnL; residues F, G, H, I, J can be phosphorylated by kinase K2 that is recruited and remains tethered in the circular region RgnR (in this way, occurrence of several second-order reactions is constrained spatially). To become phosphorylated on all residues (dark red observable), S must visit both regions.

In the absence of phosphatase activity (parameter ku $= 0$), all S are ultimately phosphorylated but even a weak activity of uniformly distributed phosphatases (parameter ku $= 0.01$) prevents simultaneous phosphorylation of S on all residues.

```
begin parameters
  m     10.       # diffusivity
  kadd  0.1       # insertion rate
  kp    10.       # kinase activity
  ku    0.0       # phosphatase activity  <-- CHOOSE: ku=0 or ku=0.01
  occuS 0.1       # substrate occupancy
  occuP 0.03      # phosphatase ocupancy
end

begin world
  topology plane  size 200 100
end

begin regions
  RgnL  circle  50 50 30
  RgnR  circle 150 50 30
end

begin molecule types
  S(A,B,C,D,E,F,G,H,I,J) # a multi-site substrate
  K1()                   # a kinase
  K2()                   # another kinase
  P()                    # a phosphatase
end
```

```
begin seed species
  S(A~U,B~U,C~U,D~U,E~U,F~U,G~U,H~U,I~U,J~U)  occupancy occuS
  P()  occupancy occuP
end

begin event rules

  >> S() m  # By omitting diffusive rules for K1 and K2, they are
  >> P() m  #  made immobile.

  K1() + S(A~U) -> K1() + S(A~P) kp
  P()  + S(A~P) -> P()  + S(A~U) ku

  K1() + S(B~U) -> K1() + S(B~P) kp
  P()  + S(B~P) -> P()  + S(B~U) ku

  K1() + S(C~U) -> K1() + S(C~P) kp
  P()  + S(C~P) -> P()  + S(C~U) ku

  K1() + S(D~U) -> K1() + S(D~P) kp
  P()  + S(D~P) -> P()  + S(D~U) ku

  K1() + S(E~U) -> K1() + S(E~P) kp
  P()  + S(E~P) -> P()  + S(E~U) ku

  K2() + S(F~U) -> K2() + S(F~P) kp
  P()  + S(F~P) -> P()  + S(F~U) ku

  K2() + S(G~U) -> K2() + S(G~P) kp
  P()  + S(G~P) -> P()  + S(G~U) ku

  K2() + S(H~U) -> K2() + S(H~P) kp
  P()  + S(H~P) -> P()  + S(H~U) ku

  K2() + S(I~U) -> K2() + S(I~P) kp
  P()  + S(I~P) -> P()  + S(I~U) ku
```

```
  K2() + S(J~U) -> K2() + S(J~P) kp
  P()  + S(J~P) -> P()  + S(J~U) ku


  ++ K1() kadd  in region RgnL  since 1.0  until 3.0
  ++ K2() kadd  in region RgnR  since 5.0  until 7.0
end


begin observables
  S_10u     S(A~U,B~U,C~U,D~U,E~U,F~U,G~U,H~U,I~U,J~U) color blue
  S_5pNterm S(A~P,B~P,C~P,D~P,E~P,F~U,G~U,H~U,I~U,J~U) color gold
  S_5pCterm S(A~U,B~U,C~U,D~U,E~U,F~P,G~P,H~P,I~P,J~P) color pink
  S_10p     S(A~P,B~P,C~P,D~P,E~P,F~P,G~P,H~P,I~P,J~P) color darkred
  K1  K1() color black
  K2  K2() color dimgrey
  P   P()  color green
end


begin simulation
  time end 500
  observer intervals 100
end
```

Listing 4: Tutorial input file 4 (doc/examples/tutorial/04-rule_based_1.spatkin).

Tutorial μmodel 5: Rule-based capabilities (2)

This example (Listing 5) is a further demonstration of rule-based capabilities and extends the previous example. Additionally here, independently of their phosphostate, molecules S can form homodimers, so there are $(2^{10})^2/2 \simeq$ over half a million potential homodimer species (more than molecules in the simulation). Dimers in which one protomer is phosphorylated on A, B, C, D, E and the other is phosphorylated on F, G, H, I, J are stabilized (not allowed to dissociate).

```
begin parameters
  m      10.     # diffusivity
  kadd   0.1     # insertion rate
  kp     10.     # kinase activity
  ku     0.0     # phosphatase activity  <-- CHOOSE: ku=0 or ku=0.01
  occuS  0.1     # S occupancy
  occuP  0.03    # phosphatase ocupancy
  b      1       # S homodimerization
  d      1       # S-S un-dimerization
  stb    100     # S-S homodimer stabilization
end


begin world
    topology plane  size 200 100
end


begin regions
  RgnL  circle  50 50 30
  RgnR  circle 150 50 30
end


begin molecule types
  S(A,B,C,D,E,F,G,H,I,J,dim,stable)
  K1()   K2()   P()
end


begin seed species
  S(A~U,B~U,C~U,D~U,E~U,F~U,G~U,H~U,I~U,J~U,dim,stable~U) occupancy occuS
  P()   occupancy occuP
end
```

```
begin event rules
  >> S() m
  >> S(dim!1).S(dim!1) m   # diffusion of S-S dimer
  >> P() m

  K1() + S(A~U) -> K1() + S(A~P) kp
  P()  + S(A~P) -> P()  + S(A~U) ku

  K1() + S(B~U) -> K1() + S(B~P) kp
  P()  + S(B~P) -> P()  + S(B~U) ku

  K1() + S(C~U) -> K1() + S(C~P) kp
  P()  + S(C~P) -> P()  + S(C~U) ku

  K1() + S(D~U) -> K1() + S(D~P) kp
  P()  + S(D~P) -> P()  + S(D~U) ku

  K1() + S(E~U) -> K1() + S(E~P) kp
  P()  + S(E~P) -> P()  + S(E~U) ku

  K2() + S(F~U) -> K2() + S(F~P) kp
  P()  + S(F~P) -> P()  + S(F~U) ku

  K2() + S(G~U) -> K2() + S(G~P) kp
  P()  + S(G~P) -> P()  + S(G~U) ku

  K2() + S(H~U) -> K2() + S(H~P) kp
  P()  + S(H~P) -> P()  + S(H~U) ku

  K2() + S(I~U) -> K2() + S(I~P) kp
  P()  + S(I~P) -> P()  + S(I~U) ku

  K2() + S(J~U) -> K2() + S(J~P) kp
  P()  + S(J~P) -> P()  + S(J~U) ku

  S(dim) + S(dim) -> S(dim!1).S(dim!1) b
```

12

```
S(A~P,B~P,C~P,D~P,E~P,dim!1,stable~U).S(F~P,G~P,H~P,I~P,J~P,dim!1,stable~U)
->
S(A~P,B~P,C~P,D~P,E~P,dim!1,stable~U).S(F~P,G~P,H~P,I~P,J~P,dim!1,stable~P)
stb

   S(dim!1,stable~U).S(dim!1,stable~U) -> S(dim,stable~U) + S(dim,stable~U) d

   ++ K1() kadd  in region RgnL  since 1.0  until 3.0
   ++ K2() kadd  in region RgnR  since 5.0  until 7.0
 end


begin observables
   S_10u      S(A~U,B~U,C~U,D~U,E~U,F~U,G~U,H~U,I~U,J~U) color blue
   S_5pNterm  S(A~P,B~P,C~P,D~P,E~P,F~U,G~U,H~U,I~U,J~U) color gold
   S_5pCterm  S(A~U,B~U,C~U,D~U,E~U,F~P,G~P,H~P,I~P,J~P) color pink
   S_10p      S(A~P,B~P,C~P,D~P,E~P,F~P,G~P,H~P,I~P,J~P) color darkred
   SS_dim_stable S(dim!+,stable~P)  color red  # observing S-S dimer
   K1 K1() color black
   K2 K2() color dimgrey
   P  P()  color green
 end


begin simulation
   time end 500
   observer intervals 100
 end
```

Listing 5: Tutorial input file 5 (doc/examples/tutorial/05-rule_based_2.spatkin).

Tutorial μmodel 6: Gradient formation

This example (Listing 6) shows how a gradient of phosphorylated substrate can be formed between enzymes tethered to different "compartments" of the reactor.

```
begin parameters
  W  200    # Arithmetic expressions and previously defined parameters
  H  W/3    #  can be used to define parameters (evaluations are always
  A  8      #  performed in double floating-point precision).
  m  3
  p  100
  q  p
end


begin world
  topology planar size W H
end


begin regions
  reservoirK  rectangle W*(    1)/(2*A) H/2 W/A H  # in-place arithmetics
  reservoirP  rectangle W*(2*A-1)/(2*A) H/2 W/A H  #
end


begin molecule types   K() S(s) P()  (* kinase, substrate, phosphatase *)  end


begin seed species
  S(s~P)  occupancy 1/8    # not inserting: S(s~U), S(s~PP)
  K()      occupancy 1/32 in region reservoirK
  P()      occupancy 1/32 in region reservoirP
end


begin event rules
  >> S() m                 # K(), P() are immobile
  K() + S(s~U) -> K() + S(s~P)   2*p
  K() + S(s~P) -> K() + S(s~PP)    p
  P() + S(s~PP)-> P() + S(s~P)   2*q
  P() + S(s~P) -> P() + S(s~U)     q
end
```

14

```
begin observables
  K    K()       color darkmagenta
  S_u  S(s~U)   color yellow    group S  # Grouping observables may aid
  S_p  S(s~P)   color orange    group S  #  trajectory visualization;
  S_pp S(s~PP) color red        group S  #  group "all" is always created.
  P    P()       color green
end

begin simulation
  duration 10000
  observer intervals 100
end
```

Listing 6: Tutorial input file 6 (doc/examples/tutorial/06-gradient_formation.spatkin).

Tutorial µmodel 7: Steady state controlled by diffusion

In this example (Listing 7), lattice is divided into two regions; molecules located in one of them have significantly reduced diffusivity. By visual inspection of the trajectory it can be observed that diffusion controls the steady state (i.e., the fraction of phosphorylated S molecules – black). This case has been analyzed by Szymańska *et al.* [see Figure 2(b) in *Phys. Rev. E*, 2015, **91**, 022702].

```
begin parameters
  a      120       # -- geometric parameter
  rhoK    0.1      # \
  rhoP  rhoK/10    # -> parameters used to set up initial conditions
  rhoS    0.25     # /
end


begin world
  topology plane  size 2*a a  # width==2*height
end


begin regions
  Left  rectangle a/2 a/2 a a  diffusivity 0.01
end


begin molecule types
   K()  P()  S(s)   # kinase, phosphatase, and their substrate
end


begin seed species
  K()      occupancy rhoK
  P()      occupancy rhoP
  S(s~U)   occupancy rhoS
end


begin event rules
  >> K() m    >> P() m    >> S()  100
  K() + S(s~U) -> K() + S(s~P)     1
  P() + S(s~P) -> P() + S(s~U)   100
end
```

```
begin observables
  K K()        color yellow
  P P()        color red
  Su S(s~U)    color lightgrey
  Sp S(s~P)    color black
end

begin settings
  time end 20
  observer intervals 200
end
```

Listing 7: Tutorial input file 7 (doc/examples/tutorial/07-diffusion_controlled_steady_state.spatkin).

Tutorial μmodel 8: Ligand-induced receptor dimerization

This is an example (Listing 8) of excitable system where introduction of trivalent ligands that collocalize bivalent receptors facilitates their activatory autotransphosphorylation. This activity is further enhanced by recruitment and activation of autotransphosphorylating kinases and opposed by phosphatases which bind to and act on both activated receptors and kinases. This example is inspired by early events in B cell receptor signaling.

```
(*
 *  This is a stochastic simulation of an excitable system, which means
 *  that the system occasionally can get activated spontaneously (due to
 *  a fluctuation). In such case, one can change random generator seed(s)
 *  and re-run the simulation.
 *)


begin parameters
  m      10.
  occuR  0.03    # receptor occupancy
  occuK  0.1     # kinase ocupancy
  occuP  0.05    # phosphatase ocupancy
end


begin world
  topology plane  size 64 64
  random seed 12345  # This seed influences initial locations of molecules.
end


begin regions
  patch  circle 32 32 10
end


begin molecule types
  K(P,K,R,A)   # kinase
  P(R,K)       # phosphatase
  Ag[3]        # extracellular antigen, trivalent
  R(P,K,A)[2]  # bivalent receptor with 2 additional sites for binding K, P
end
```

```
begin seed species
  R(P,K,A~U)[@,@] occupancy occuR  # Molecules are inserted unbound.
  P(R,K)          occupancy occuP
  K(P,K,R,A~U)    occupancy occuK
end

begin event rules

  >> R() m     >> P() m     >> K() m

  # Immobile binders appear unbound in a lattice dual to the regular lattice.
  "Antigen appearance":
  ++ Ag[@,@,@]  0.01  in region patch  since 200  until 220

  "Receptor-ligand binding", "Receptor-ligand unbinding":
  +-!  R() &  Ag[]  10, 0.01

  # Receptors activation in trans:
  R()    + R(A~U) -> R()      + R(A~P)   0.01
  R()    + R(A~P) -> R()      + R(A~PP)  0.01
  R(A~P) + R(A~U) -> R(A~P)   + R(A~P)   0.02
  R(A~P) + R(A~P) -> R(A~P)   + R(A~PP)  0.02
  R(A~PP)+ R(A~U) -> R(A~PP)  + R(A~P)   0.05
  R(A~PP)+ R(A~P) -> R(A~PP)  + R(A~PP)  0.05

  R(P,K,A~PP) + K(P,K,R,A~U) -> R(P,K!1,A~PP).K(P,K,R!1,A~U)       1
  R(K!1,A~PP).K(P,K,R!1,A~U) -> R(K!1,A~PP).K(P,K,R!1,A~P)        10
  R(K!1).K(R!1) -> R(K) + K(R)                                     1

  K(P,K,R,A~P) + K(P,K,R,A~U)  -> K(P,K!1,R,A~P).K(P,K!1,R,A~U)  1
  K(P,K!1,R,A~P).K(P,K!1,R,A~U)-> K(P,K!1,R,A~P).K(P,K!1,R,A~P) 10
  K(K!1).K(K!1) -> K(K) + K(K)                                     1

  P(R,K) + R(P,K,A~PP) -> P(R!1,K).R(P!1,K,A~PP)                3
  P(R,K) + R(P,K,A~P)  -> P(R!1,K).R(P!1,K,A~P)                 3
  P(R!1,K).R(P!1,K,A~PP) -> P(R!1,K).R(P!1,K,A~P)              10
  P(R!1,K).R(P!1,K,A~P)  -> P(R!1,K).R(P!1,K,A~U)              10
  P(R!1).R(P!1) -> P(R) + R(P)                                  1
```

```
  P(R,K) + K(P,K,R,A~P)    -> P(R,K!1).K(P!1,K,R,A~P)              1
  P(R,K!1).K(P!1,K,R,A~P) -> P(R,K!1).K(P!1,K,R,A~U)             10
  P(K!1).K(P!1) -> P(K) + K(P)                                    1


end

begin observables
  Ag_tot          Ag[@!?,@!?,@!?]   color black
  Receptor_U      R(A~U)   color lightgrey
  Receptor_P      R(A~P)   color grey
  Receptor_PP     R(A~PP)  color brown
  Kinase_inactive K(A~U)   color gold
  Kinase_active   K(A~P)   color red
  Phosphatase     P()       color green
end

begin simulation
  time end 500
  observer intervals 1000
  snapshots on       # If you do not want snapshots, write: snapshots off
  random seed 12345  # This seed influences the order of events.
end
```

Listing 8: Tutorial input file 8 (doc/examples/tutorial/08-receptors_and_ligands.spatkin).

20

Tutorial μmodel 9: Crowding-facilitated switch in a bistable system

In this example (Listing 9), kinetics of a bistable system is simulated. In a defined instant, chemically inert molecules ("crowders") are introduced which leads to reduction of reactants' diffusivity. In this system, the presence of crowders favors processive rather than distributive phosphorylation, and in this way favors the steady state of a high amount of doubly phosphorylated kinases. Initially the system is in the steady state of a low amount of phosphorylated kinases; upon recruitment of crowders to the membrane, a transition to the other steady state is observed.

The effect of the presence of crowding molecules and their diffusivity on the effective diffusivity of (other) molecules on the lattice has been analyzed by Szymańska *et al.* [see Figure 9 in *Phys. Rev. E, 2015, **91**, 022702*].

```
(*
 *  This is a stochastic simulation of a bistable system, which means that
 *  the system may occasionally switch to another state (though it is very
 *  implausible). In such case, one can change random generator seed(s) and
 *  re-run the simulation.
 *)


begin parameters
  rhoK  0.4
  rhoP  0.1
  d     1    / (6 * rhoP)
  c1    0.02 / (6 * rhoK)
  c2    0.15 / (6 * rhoK)
  c3    4    / (6 * rhoK)
  m     300
end


begin world
  topology planar
  size 50 50
  random seed 123
end


begin regions
end
```

```
begin molecule types
  K(a)   # self-activating kinase
  P()    # phosphatase acting on the kinase
  C()    # crowder
end

begin seed species
  P()      occupancy rhoP
  K(a~U)   occupancy rhoK
end

begin event rules

  ## Rules for reactants:
  #
  >> K() m    >> P() m

  K(a~U) + K(a~U) -> K(a~U) + K(a~P)    2*c1
  K(a~U) + K(a~P) -> K(a~U) + K(a~PP)     c1

  K(a~P) + K(a~U) -> K(a~P) + K(a~P)    2*c2
  K(a~P) + K(a~P) -> K(a~P) + K(a~PP)     c2

  K(a~PP) + K(a~U) -> K(a~PP) + K(a~P) 2*c3
  K(a~PP) + K(a~P) -> K(a~PP) + K(a~PP)  c3

  P() + K(a~P)  -> P() + K(a~U)  d
  P() + K(a~PP) -> P() + K(a~P)  2*d

  ## Rules for crowders:
  #
  ++ C()  0.15  since 36  until 40
  >> C()  m/10
end

begin observables
  K    K(a~U)  color yellow
  K_p  K(a~P)  color orange
```

```
  K_pp K(a~PP) color red
  P    P()      color lime
  C    C()      color dimgray  # crowder
end


begin simulation
  duration 100
  observer intervals 1000
  random seed 123
  snapshots on
end
```

Listing 9: Tutorial input file 9 (doc/examples/tutorial/09-crowding_facilitated_switch.spatkin).

Tutorial μmodel 10: Traveling wave

The considered system contains phosphatases and auto-phosphorylating kinases reacting in a long cylindrical domain. This prototypical bistable system is the subject of the analysis described by Zuk *et al.* [*Phys. Biol.*, 2012, **5**, 055002] and Kochańczyk *et al.* [*J. R. Soc. Interface*, 2013, **10**, 20130151], where the concordance of particle-based simulations in SPATKIN and finite-element method-based simulations of a corresponding partial differential equation system is demonstrated.

```
(*
 *  Please note that the simulation can take about two hours. Occasionally,
 *  the stochastic traveling wave may fail to propagate or spontaneous self-
 *  activation may occur in another part of the lattice -- in such case one
 *  can change random number generator seed(s) and re-run the simulation.
 *)
begin parameters
  n_stat_K    183  # /
  n_stat_Kp   571  # > high-phospholevel steady state (calculated from ODEs)
  n_stat_Kpp  439  # /
  rhoK  0.4
  rhoP  0.1
  d    1    / (6 * rhoP)
  c1   0.02 / (6 * rhoK)
  c2   0.18 / (6 * rhoK)
  c3   4    / (6 * rhoK)
  m   1000
end


begin world
  topology planar  size 404 30  random seed 123456789
end


begin regions
  Barrier   rectangle  402  15    4 30  diffusivity 0  # reflective boundary
  Ignition  rectangle   50  15  100 30
  Rest      rectangle  250  15  300 30
end


begin molecule types   K(a)  P()    end
```

```
begin seed species
  P()       occupancy  rhoP    in region Ignition
  K(a~U)   n_stat_K             in region Ignition
  K(a~P)   n_stat_Kp            in region Ignition
  K(a~PP)  n_stat_Kpp           in region Ignition
  P()       occupancy  rhoP     in region Rest
  K(a~U)    occupancy  rhoK    in region Rest
end

begin event rules
  K(a~U)   + K(a~U)  -> K(a~U)   + K(a~P)    2*c1
  K(a~U)   + K(a~P)  -> K(a~U)   + K(a~PP)     c1
  K(a~P)   + K(a~U)  -> K(a~P)   + K(a~P)    2*c2
  K(a~P)   + K(a~P)  -> K(a~P)   + K(a~PP)     c2
  K(a~PP) + K(a~U)  -> K(a~PP) + K(a~P)    2*c3
  K(a~PP) + K(a~P)  -> K(a~PP) + K(a~PP)     c3
  P() + K(a~P)   -> P() + K(a~U)     d
  P() + K(a~PP) -> P() + K(a~P) 2*d
  >> K() m
  >> P() m
end

begin observables
  K    K(a~U)    color yellow
  K_p  K(a~P)    color orange
  K_pp K(a~PP)  color red
  P    P()        color lime
end

begin simulation
  description "Induced chemical travelling wave"
  duration 100    observer intervals 200
  random seed 987654321
end
```

Listing 10: Tutorial input file 10 (doc/examples/tutorial/10-traveling_wave.spatkin).

25

Spontaneous NF-κB Activation by Autocrine TNFα Signaling: A Computational Analysis

Jakub Pękalski[1,2], Pawel J. Zuk[1,3], Marek Kochańczyk[1], Michael Junkin[4], Ryan Kellogg[4], Savaş Tay[4], Tomasz Lipniacki[1,5]*

1 Institute of Fundamental Technological Research, Polish Academy of Sciences, Warsaw, Poland, 2 Institute of Physical Chemistry, Polish Academy of Sciences, Warsaw, Poland, 3 Institute of Theoretical Physics, Faculty of Physics, University of Warsaw, Warsaw, Poland, 4 Department of Biosystems Science and Engineering, ETH Zurich, Zurich, Switzerland, 5 Department of Statistics, Rice University, Houston, Texas, United States of America

Abstract

NF-κB is a key transcription factor that regulates innate immune response. Its activity is tightly controlled by numerous feedback loops, including two negative loops mediated by NF-κB inducible inhibitors, IκBα and A20, which assure oscillatory responses, and by positive feedback loops arising due to the paracrine and autocrine regulation via TNFα, IL-1 and other cytokines. We study the NF-κB system of interlinked negative and positive feedback loops, combining bifurcation analysis of the deterministic approximation with stochastic numerical modeling. Positive feedback assures the existence of limit cycle oscillations in unstimulated wild-type cells and introduces bistability in A20-deficient cells. We demonstrated that cells of significant autocrine potential, i.e., cells characterized by high secretion of TNFα and its receptor TNFR1, may exhibit sustained cytoplasmic–nuclear NF-κB oscillations which start spontaneously due to stochastic fluctuations. In A20-deficient cells even a small TNFα expression rate qualitatively influences system kinetics, leading to long-lasting NF-κB activation in response to a short-pulsed TNFα stimulation. As a consequence, cells with impaired A20 expression or increased TNFα secretion rate are expected to have elevated NF-κB activity even in the absence of stimulation. This may lead to chronic inflammation and promote cancer due to the persistent activation of antiapoptotic genes induced by NF-κB. There is growing evidence that A20 mutations correlate with several types of lymphomas and elevated TNFα secretion is characteristic of many cancers. Interestingly, A20 loss or dysfunction also leaves the organism vulnerable to septic shock and massive apoptosis triggered by the uncontrolled TNFα secretion, which at high levels overcomes the antiapoptotic action of NF-κB. It is thus tempting to speculate that some cancers of deregulated NF-κB signaling may be prone to the pathogen-induced apoptosis.

Introduction

NF-κB Regulatory System

Innate immunity forms the first line of defense against pathogens. In the first phase, cells detect pathogens with their membrane and cytoplasmic receptors. This leads to the activation of transcription factors from the NF-κB, IRF and AP-1 families. These factors jointly regulate the activity of several hundred genes responsible for inflammation, antiviral protection, proliferation and apoptosis. In particular, they induce the production of pro-inflammatory cytokines like IL-1, TNFα, as well as IFN-α and IFN-ß. Secretion of these cytokines leads to the second phase of the cellular innate immune response in cells that have not yet encountered the pathogen. The cytokine-activated cells may themselves produce and secrete the same cytokines leading to the spread of paracrine signaling [1,2] or to augmenting and stabilizing signaling in the secreting cells via autocrine regulation [3,4]. In the current study, the focus is on the analysis of TNFα autocrine regulation in the NF-κB pathway.

NF-κB regulates numerous genes important for pathogen- or cytokine-induced inflammation, immune response, cell prolifera-tion and survival (reviewed in [5,6]). Nuclear activity of NF-κB is tightly controlled by negative feedback loops mediated by NF-κB-responsive proteins: IκBα [7–9], IκBε [8,10,11] and A20 [12–14]. These negative feedback loops lead to oscillatory responses, in which NF-κB circulates between the cytoplasm and nucleus with the period of about 100 min [8]. The primary inhibitors, IκBα and IκB, directly bind to NF-κB, inhibit its transcriptional activity and transport it back to the cytoplasm. Interestingly, expression of IκBε is delayed with respect to IκBα [11], which increases desynchronization of cells and leads to damping of oscillations observed at the population level, resulting in robust tissue responses [15]. A20 mediates the outer negative feedback loop by attenuating the catalytic activity of the IKK complex (consisting of IKKγ, also called NEMO, IKKα and IKKß). In A20-deficient cells the IKK activity remains at a high level preventing the accumulation of inhibitors IκBα and IκBε [14]. This leads, in turn, to the elevated NF-κB transcriptional activity and causes chronic inflammation. There are at least two levels of A20-mediated

regulation of IKK complex activity: (1) A20 directly interacts with the IKK complex reducing its catalytic activity [16–18] and (2) A20 primes TNF receptor interacting protein (RIP) for degradation, and thus attenuates TNF receptor downstream signaling [19].

Regarding the direct regulation mode, A20 binds to IKKγ and speeds up further phosphorylation of active IKKß kinase into the inactive form [16,20]. (IKKß activation proceeds via phosphorylation at Ser-177 and Ser-181, but further phosphorylation at the C-terminal serine cluster inhibits its catalytic activity [20].) Later, it was found that A20 and ABIN-1 bind to the IKK complex, and A20 inhibits activation of NF-κB by de-ubiquitination of IKKγ [17], reviewed recently in [21]. (Lys-63-linked ubiquitination of IKKγ is an important step for the activation of IKK and NF-κB following various stimuli, including TNFα [22].) Interestingly, A20 itself is a putative substrate of IKKß, which phosphorylates A20 on Ser-381, thereby increasing its ability to downregulate NF-κB in response to multiple stimuli [23]. Recently, Skaug et al. reported a direct non-catalytic mechanism of IKK inhibition by A20 showing that overexpressed A20 impaired IKK activation without reducing RIP1 ubiquitination [18].

Regarding the indirect IKK regulation mode, A20 acts as a ubiquitin editing protein: it removes Lys-63-linked ubiquitin chains from RIP and then functions as a ubiquitin ligase by polyubiquitinating RIP with Lys-48-linked ubiquitin chains, thereby targeting RIP for proteasomal degradation, and thus attenuating TNFR1 receptor signaling [19], reviewed in [24,25]. The modeling studies showed distinctive roles of these two, direct and indirect, modes of regulation [26,27]. The direct mode allows for the termination (or strong reduction) of IKK activity after A20 is synthesized (which takes about 1 hour) [26], while the second mode renders cells less sensitive to subsequent pulses of TNFα, if these pulses are separated by a short timespan [27].

Later studies showed that the role of A20 goes beyond the control of NF-κB and that A20 is a general inhibitor in innate immune signaling; it protects cells from chronic inflammation, endotoxic shock and plays a role of tumor suppressor [28,29]. In particular, A20 inhibits IRF3/IRF7 signaling [30,31]. Similarly as for the NF-κB pathway, it acts upstream of the TBK1–IKKϵ–IKKγ complex regulating negatively retinoic acid-inducible gene I protein (RIG-I) [32], and potentially may act at the level of this complex by binding to IKKγ [31].

As said, the negative feedback loops involving IκBα and A20 lead to oscillatory responses. These oscillations appear damped when analyzed at the population level, but single cell experiments by Nelson et al. on SK-N-AS cells and Tay et al. on 3T3 cells demonstrated that oscillations persist at least up to 10 hours [33,34]. Discrepancy between population- and single cell-based observations can be explained by the progressing desynchronization of cells in the population [35,36], although the controversy about reconciling single cell and population data still exists [37]. The major objection towards single cell experiments is that the additional gene copies coding for fluorescently tagged NF-κB may alter dynamics of the whole system. However, both experimental [38] and modeling studies [39] show that the number of NF-κB gene copies or its expression level influences only the amplitude but not the period of oscillations. Moreover, in our recent experiment [34], the expression of NF-κB remained practically unchanged due to the knockout of endogenous RelA, yet the oscillatory pattern was still clearly visible for 10 ng/ml TNFα dose.

TNFα Autocrine and Paracrine Signaling

TNFα affects growth, differentiation and function of cells of many types, and is a major mediator of inflammatory immune responses [40,41]. It is considered as a key mediator of the septic shock syndrome induced by either LPS or bacterial superantigens [42,43]. The potent activating abilities of TNFα are transmitted by 2 distinct cell-surface receptors: TNFR1 and TNFR2; the first one binds TNFα molecules with higher affinity [44] and is considered responsible for the most of TNFα-induced signaling [45]. It is established that binding of TNFα initiates protein–protein interactions between TNFR1 and the TNFR-associated death domain protein (TRADD). TRADD in turn recruits receptor-interacting protein (RIP) and TRAF2 for NF-κB and survival signals [46,47].

The TNFα autocrine and paracrine signaling arises since TNFα-inducible NF-κB serve itself as a primary transcription factor for TNFα. Over twenty years ago Collart et al. showed that TNFα promoter contains four κB motifs that can bind constitutive and inducible forms of NF-κB [48]. Further analysis of κB motives in TNFα promoter revealed that two sites, κB2 and κB2a, play a primary role in TNFα regulation by NF-κB in response to LPS stimulation in human monocytes [49].

The autocrine regulation was observed in various cell lines and tissues: first, Wu et al. showed that TNFα functions as autocrine and paracrine growth factor in ovarian cancer [50]. Coward et al. and Guergnon et al. demonstrated that TNFα induces TNFα synthesis via NF-κB activation in human lung mast cells and B cells [51,52]; Nadeau and Rivest found that *in vivo* TNFα injection induced TNFα mRNA expression in microglia and astrocytes [53], and later Kuno et al. showed that the activation of microglia by LPS is partially mediated by microglia-derived TNFα, confirming the existence of a positive feedback loop [54]. Hu et al. demonstrated that autocrine TNFα signalling (via NF-κB) mediates endoplasmic reticulum stress-induced cell death [55]. Recently, Rushworth et al. reported the autocrine TNF signaling (via NF-κB) in monocytes: TNF stimulation leads to sustained production of TNF mRNA for 48 hours; the NF-κB inhibition suppresses the TNF autocrine regulation [56]. Although observed in many cell lines, strength of the autocrine and paracrine TNFα signaling is cell line-specific. Cells can be characterized by their autocrine potential based on their ability to secrete TNFα and by their sensitivity to TNFα stimulation controlled primarily by the TNFR1 level.

Autocrine TNFα signaling may start spontaneously or in response to numerous stimuli, including TNFα itself, other cytokines, or LPS. The spontaneous activation of the NF-κB signaling pathway was observed in isolated normal glomeruli [57]. The data suggested that NF-κB was spontaneously activated in explanted glomeruli via autocrine/paracrine factors including TNFα.

Although NF-κB serves itself as a primary transcription factor for TNFα, there are other factors and mechanisms which control TNFα mRNA synthesis, transcript stability, translation and TNFα protein secretion. TNFα gene regulation in activated T cells involves AP-1 transcription factors ATF-2 and c-Jun which cooperate with NFATp [58]. In macrophages, c-Jun and C/EBPß transcriptionally activate TNFα, however regulation by NF-κB was found stronger and independent of these factors [59]. Covert and colleagues [3,4] proposed that the LPS-induced TNFα secretion is mediated by TRIF-dependent activation of IRF3. Stability of TNFα mRNA is signal-dependent; Deleault et al. demonstrated that simultaneous activation of both ERK and p38 inhibit tristetraprolin and stabilize TNFα mRNA [60]. Massive TNFα protein production requires ERK and p38 atop of NF-κB in mice with constitutively active IKKß [61]. In LPS-stimulated murine dendritic cells, MK2, effector kinase of p38 promotes TNFα translation [62]. Interestingly, in articular chondrocytes and

skeletal muscles, TNFα stimulates the activation of three subclasses of MAPKs: ERKs, p38, and JNKs [63,64]. This opens the possibility that in some cells TNFα autocrine regulation involves both NF-κB-induced TNFα transcription and MAPK pathway-driven TNFα translation.

Majority of mechanisms which increase TNFα mRNA stability and translation, discussed above, are induced by the LPS stimulation, which strongly activates MAPK pathways as well as NF-κB via MyD88 (early phase) and TRIF-dependent pathways (late phase), reviewed in [65,66]. Xaus et al. showed that LPS induces apoptosis in macrophages via autocrine TNFα production, and this mechanism is suppressed in TNFR1-deficient mice [42]. Hao and Baltimore found that TNFα mRNA degradation is several-fold lower when TNFα is produced in response to LPS when compared to TNFα stimulation [67]. This explains why the LPS stimulation leads to the massive secretion of TNFα, which in turn may trigger autocrine signaling, leading to prolonged oscillations of NF-κB, observed recently in a fraction of LPS-stimulated cells [68].

Finally, we should mention that there exist other cytokines, in particular IL-1, which are NF-κB-responsive [69], and which in turn may activate NF-κB [70]. For the sake of simplicity and clarity, we neglect this positive feedback loop in the current study.

Methods

The modeling studies of NF-κB system started in 2002, by the study of oscillations of NF-κB–IκBα feedback loop (damped by the presence of IκBε and IκBß isoforms) by Hoffmann, Levchenko and colleagues [8], followed by Lipniacki et al. study introducing A20 regulatory loop [26], reviewed in [36,71]. The considered model is based on our earlier studies [27,34]. The key modification is the inclusion of autocrine regulation via TNFα which leads to the positive feedback loop and qualitatively changes dynamics of cells characterized by sizable TNFα synthesis. For completeness of the current study, we briefly review the structure of the model. The detailed description of the mathematical methods and the model, including the list of reactions and corresponding ordinary differential equations (ODEs), can be found in Text S1. The model involves seven proteins: NF-κB, its inducible inhibitors IκBα and A20, signal transduction kinases IKK and IKKK, cytokine TNFα and its receptor TNFR1 (Fig. 1). The model is two-compartmental and the translocations of NF-κB, IκBα and their complex between the cytoplasmic and nuclear compartments are considered. However, in contrast to recent studies by Terry and Chaplain [72], we do not account for spatial gradients (leading to the diffusion and transport terms) within these two compartments. Total levels of NF-κB, IKK and IKKK are assumed constant, without accounting for their production and degradation explicitly. In the case of IκBα, A20 and TNFα, the processes of mRNA transcription and protein translation are explicitly present in the model. The activation of corresponding genes follows NF-κB binding, while gene inactivation follows the NF-κB removal via IκBα binding.

A20 and IκBα Negative Feedback Loops

Nuclear NF-κB activity is controlled by two interlinked negative feedback loops, one mediated by IκB proteins: IκBα and IκBε, the other mediated by A20 (Fig. 1). The inhibitors IκBα and IκBε bind NF-κB and sequester it in the cytoplasm. Upon the signal mediated by the kinases IKKK and IKK, IκBα is phosphorylated and rapidly degraded. IκBε is also phosphorylated and degraded, although its degradation (and further resynthesis) is delayed by about 45 min with respect to IκBα. Free NF-κB translocates to the

nucleus and triggers transcription of its inhibitors, IκBα, IκBε and A20. Synthesized IκBα and IκBε translocate to the nucleus, bind NF-κB and convey it back to the cytoplasm. IκBε is several fold less abundant than the primary inhibitor IκBα, and as demonstrated by experimental and computational studies the main impact of IκBε on the system dynamic is in desynchronizing cells [15]. Although individual cell trajectories are very similar for IκBε-deficient and wild-type cells, the latter are less synchronized, and therefore oscillations appear damped when averaged over population [15,35]. In the current study, we focus on TNFα autocrine regulation and neglect the regulatory differences between IκBε and IκBα and replace these two proteins by a more abundant IκBα. The (NF-κB:IκBα) complexes may circulate between the nucleus and cytoplasm, however since they mostly accumulate in cytoplasm, which is visible in unstimulated cells (for which majority of NF-κB is bound to IκBα and other isoforms) [33,34,73], we neglect the nuclear import term for (NF-κB:IκBα). Accumulation of IκBα protein is enabled by A20 which attenuates the strength of the extracellular signal (discussed in Introduction). First, A20 attenuates the activity of TNFR1 receptors (which is the consequence of A20-induced degradation of RIP – the key component of the receptor complex). Second, it enhances conversion of catalytically active IKK (IKK_a), into catalytically inactive form (IKK_i). Inactive kinase IKK_i spontaneously converts back to the neutral form IKK_n through the intermediate form IKK_{ii}. It is worth noticing here, that Ashall et al. [73] in their model variant assumed that A20 inhibits conversion of IKK_i to neutral form IKK_n, rather than it enhances conversion of IKK_a to IKK_i.

Autocrine TNFα Regulation

TNFα is one of NF-κB-responsive genes, and its expression level is cell type-dependent. 3T3 cells, which we studied experimentally in this work, exhibit a relatively low TNFα expression, reaching 20 mRNA molecules (on average) per cell at the highest TNFα stimulation dose, Fig. 2A. However, expression levels calculated per activated cell were independent of the TNFα dose showing digital responses similar to that of early genes we analyzed earlier [34]. The dynamic gene expression measurements show that the TNFα synthesis has a distinct peak at $t = 1$ hour regardless of the TNFα dose, and shows a low plateau which extends to beyond 10 hours.

Interestingly, we found that a small fraction (about 3%) of 3T3 cells secrete TNFα without any stimulation as shown by ELISpot assay, Fig. 2B. The fraction of secreting cells was found to be larger (about 10%) for RAW 264.7 (mouse leukaemic monocyte macrophage) cells, Fig. 2C. These measurements add to the evidence that TNFα production and secretion can be triggered spontaneously, and that probability of such spontaneous activations is cell line-dependent. Motivated by this observation, and earlier experimental studies demonstrating that TNFα induces TNFα synthesis via NF-κB activation ([51,52] as discussed in Introduction), we expanded our earlier model to include the TNFα autocrine regulation. Accordingly, we consider NF-κB-inducible TNFα mRNA synthesis, followed by TNFα protein translation and secretion. We assume that some fraction of secreted TNFα molecules may bind to receptors on the same cell, and that the fraction of captured TNFα molecules increases with the number of TNFR1 receptors according to the Hill function. The fraction of secreted TNFα which is not bound by receptors of the secreting cell is neglected in the considerations, but could be accounted for by modifying the extracellular TNFα concentration.

We analyze the evolution of the NF-κB system in the absence of any stimulation as well as its responses to the imposed

Figure 1. Schematic of the NF-κB model. Solid arrow-headed lines denote transitions; dashed lines denote influence: positive for circle-headed lines, negative for hammer-headed lines.
doi:10.1371/journal.pone.0078887.g001

concentrations of TNFα, considering both tonic and pulsed stimulation. In the whole analysis we account for intracellular and extracellular TNFα degradation, with degradation half-time $\simeq$ 1 h (degradation rate of 2×10^{-4}/s), consistent with our earlier estimations [34].

Deterministic and Stochastic Modeling

We and others predicted and demonstrated that responses of the NF-κB system to low TNFα doses, as well as low LPS doses, are highly stochastic, and only a fraction of cells exhibit measurable NF-κB activation [27,34,74,75]. Our ELISpot data on 3T3 cells and macrophages show that only a small fraction of cells secrete TNFα. Therefore, in order to analyze the autocrine TNFα regulation we will combine deterministic and stochastic modeling. In the deterministic approximation, the system of 25 ODEs is derived from the list of chemical reactions. The equations are then solved using MATLAB and BIONETGEN (Materials S1 and S2). The deterministic approximation is used to analyze the dynamical
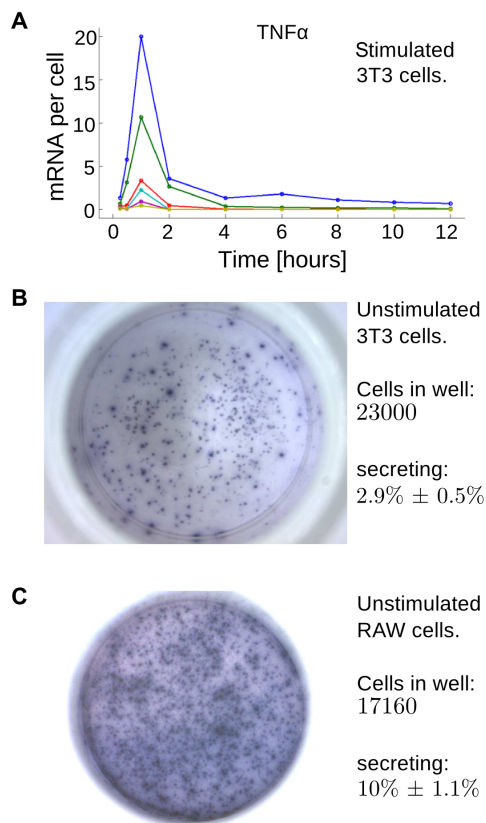
Figure 2. Evidence of TNFα synthesis and secretion in 3T3 cells and RAW cells. (**A**) Time-course of population averaged expression of TNFα mRNA in mouse 3T3 fibroblast cells stimulated with various doses of TNFα; color lines from dark blue to yellow correspond to TNFα doses of 10, 1, 0.1 0.05, 0.025 and 0.01 ng/ml. Cells were treated with different doses of TNFα, and TNFα mRNA was quantified at different times using microfluidic qPCR. Microfluidic digital-PCR was used to calibrate expression levels to mRNA counts. (**B**, **C**) Representative ELISpot assays showing TNFα secretion by (**B**) unstimulated 3T3 and (**C**) RAW cells.
doi:10.1371/journal.pone.0078887.g002

structure of the regulatory system, which is needed to properly interpret more complex stochastic trajectories. Based on the bifurcation analysis performed using MatCont continuation software (see Text S1 and Material S3), we will show that unstimulated wild-type (WT) cells may have, depending on the strength of the autocrine regulation, two stable recurrent solutions: steady state and limit cycle, the latter corresponding to the cytoplasmic–nuclear NF-κB oscillations. In contrast, A20-deficient cells may simultaneously have two stable steady state solutions, corresponding to the active and inactive cells.

In the stochastic approach, chemical reactions are simulated using the direct Stochastic Simulation Algorithm [76] implemented in BioNetGen. BioNetGen is a rule-based specification language and environment [77]. In BioNetGen language, models are constructed by specifying rules that describe allowed protein–protein interactions, processes, and covalent modifications. Based on the rules, the reaction network is automatically generated along with the system of ODEs. The advantage of this approach is that it allows for concise definitions of models with large numbers of interactions and protein states [78]. Here, the model is relatively small, and the BioNetGen software is used because of its very efficient implementation of the Stochastic Simulation Algorithm

(direct method). Trajectories obtained in stochastic simulations are interpreted as single cell trajectories. These trajectories, as we will see, may switch between the attractors of the deterministic approximation or may exhibit the excitatory behavior. Stochastic simulations will be used to determine the fraction of responding cells as a function of the TNFα dose. Averages over a large number of stochastic trajectories will be used to fit the model to the population data. As demonstrated before, in non-linear systems, the average over a large number of stochastic trajectories may qualitatively differ from the trajectory obtained in the deterministic approximation, and thus the deterministic approximation of the process may not satisfactorily reproduce population data [79]. In the stochastic model two types of noise are considered:

Extrinsic noise. The analysis performed in our previous study [34] indicated for a broad distribution of TNFR1 receptor number across the cell population. The heterogeneity of NF-κB expression is of smaller importance, and will be neglected here for the sake of simplicity. Following [34] we assume that the number of receptors is log-normally distributed with probability density $f(x,\mu,\sigma)$ (see also Fig. S1 in Text S1),

$$f(x,\mu,\sigma) = \frac{1}{x\sigma\sqrt{2\pi}} e^{-\frac{(\ln x - \mu)^2}{2\sigma^2}}, \quad x > 0 \qquad (1)$$

with $\mu = \ln 7000$ and $\sigma^2 = 0.7$. Such distribution is characterized by median $M_0 = 7 \times 10^3$, mean $\simeq 10^4$ and variance $\simeq 10^8$. In the deterministic approximation, if not otherwise specified, we assumed that the number of receptors R is equal to median M_0.

Intrinsic noise. Intrinsic noise in the system results mainly from the discrete regulation of TNFR1 receptors activity and activation of A20, IκBα, and TNFα genes, see [36,80]. We found, however, that at low or zero dose stimulation, when the number of A20, IκBα, and TNFα mRNA molecules is very low, the transcriptional noise is also important. Accordingly, in contrast to our earlier studies [27,34,35] that relied on Haseltine and Rawlings algorithm [81], in the current study we perform all stochastic simulations using the direct method of Gillespie [76].

Results

Analysis of the Deterministic Model

Wild-type cells. The presence of the negative feedback loop together with the delay introduced by the mRNA transcription, protein translation and cytoplasmic to nuclear transport induces oscillatory responses to tonic TNFα stimulation. One can thus expect that cells which produce and secrete TNFα can exhibit tonic oscillations even without any external stimulation, being constantly activated by TNFα they secrete. In the bifurcation analysis (Fig. 3; see also Text S1, Fig. S3 for a 3-D plot), we consider the system without any external stimulation, i.e. assuming that the extracellular TNFα concentration equals zero. As a bifurcation parameter we choose TNFα mRNA synthesis rate λ, i.e., mRNA synthesis from a single active TNFα gene copy. The analysis shows that until the TNFα synthesis rate remains low, $\lambda < \lambda_1$, the system may not exhibit persistent (limit cycle) oscillations. The only recurrent solution is the stable steady state in which the nuclear NF-κB fraction is low (below 0.01). At $\lambda = \lambda_1 \simeq 0.045$ mRNA/s, the stable limit cycle arises in the cyclic fold bifurcation, and for intermediate TNFα synthesis rates, $\lambda \in (\lambda_1, \lambda_2)$, the oscillatory solution coexist with the stable steady state solution. The further growth of the TNFα synthesis rate causes that the stable steady state solution loses its stability in bifurcation at $\lambda = \lambda_2 \simeq 0.093$ mRNA/s, and in a broad range of

$\lambda \in (\lambda_2, \lambda_3)$ the stable limit cycle is the only stable recurrent solution. A scrupulous analysis of the bifurcation at λ_2 showed that in the very close vicinity of λ_2 there are in fact two bifurcations: supercritical Hopf at $\lambda = 0.09281$ and cyclic fold at $\lambda = 0.09290$ (see Text S1, Fig. S2). These two bifurcations in coarse-grained view are equivalent to the single subcritical Hopf bifurcation and in further discussion will be considered as such. Finally, at $\lambda = \lambda_3 \simeq 0.34$ mRNA/s the limit cycle oscillations are replaced by a single stable steady state. We should notice, however, that $\lambda = \lambda_3 \simeq 0.34$ mRNA/s exceeds the physiological maximum transcriptional rate estimated as $\lambda_{phys} \simeq 0.1$ mRNA/s, assumed in the model for A20 and IκBα, known for very rapid mRNA synthesis (see [35]). In summary, we found that within the deterministic approximation, in the absence of stimulation, WT cells remain in the inactive state when TNFα synthesis rate is low ($\lambda < \lambda_1$), or exhibit limit cycle oscillations for the high TNFα synthesis rate ($\lambda > \lambda_2$). For intermediate TNFα synthesis rates $\lambda \in (\lambda_1, \lambda_2)$ cells may either remain in the inactive state or exhibit limit cycle oscillations. The values of bifurcation points, in particular λ_1 at which limit cycle oscillations arise, decrease (almost linearly for small TNFR1 numbers) with cell sensitivity which is proportional to the assumed level of TNFR1 receptors, Fig. 3F.

A20-deficient cells. In A20$^{-/-}$ cells the negative feedback is disturbed. Since A20 promotes transformation from active IKK (IKK$_a$) to inactive IKK (IKK$_i$), lack of A20 results in the prolonged IKK activity. This in turn prevents the accumulation of IκBα protein and results in the persistent nuclear NF-κB occupancy. As a result, in response to the tonic TNFα stimulation, A20-deficient cells do not exhibit limit cycle oscillation, but reach the active steady state, characterized by a high IKK activity, a high level of nuclear NF-κB and correspondingly high level of IκBα transcript, but low level of IκBα protein, which is constantly degraded due to the high IKK activity. One can thus expect that A20$^{-/-}$ cells which synthesize and secrete TNFα may remain in the active state, without external stimulation. In fact, the bifurcation analysis (Fig. 4) demonstrated that there exists a broad range of TNFα mRNA synthesis rate λ, $\lambda \in (\lambda_1, \lambda_2)$, in which the system is bistable, i.e., it can remain either in the active state (with high nuclear NF-κB level) or the inactive state (with low nuclear NF-κB level). The value of parameter $\lambda_1 \simeq 0.0037$ mRNA/s in which the active steady state appears (in saddle-node bifurcation) is very low, more than 10 times lower than the value of bifurcation parameter in which limit cycle oscillations arise in WT cells. The value of the second saddle-node bifurcation, λ_2, in which the inactive steady state vanishes, is much larger, $\lambda_2 \simeq 0.050$ mRNA/s. As a result, one may expect that A20-deficient cells will remain inactive without any stimulation, but even transient TNFα stimulation will drive them to the active state, in which they can remain for a long time (formally, infinitely long time).

The bifurcation analysis of the deterministic model demonstrated that due to the positive feedback regulation, even in the absence of any external stimulation, WT cells exhibit limit cycle oscillations while A20-deficient cells exhibit persistent activation, provided that TNFα mRNA synthesis rate is sufficiently large. The A20$^{-/-}$ cells were found to be much more sensitive, i.e., they can remain active for 10 times lower TNFα synthesis rate than needed for WT cells activation. In addition, we found that both A20$^{-/-}$ and WT cells exhibit bistability: in WT cells it is manifested by the coexistence of the stable limit cycle and the stable steady state. One can thus expect that real (noisy) cells will exhibit transitions between the basins of attraction of recurrent solutions found in the deterministic analysis.

Stochastic Switching in the Absence of TNFα Stimulation

In Fig. 5 we compare deterministic and stochastic trajectories projected onto the ('Nuclear NF-κB', 'Total IκBα') plane. For $\lambda = 0.050$ mRNA/s (Fig. 5A) the system in the deterministic approximation has the stable steady state and the stable limit cycle. As expected, the stochastic trajectory switches between limit cycle oscillations and small fluctuations in the vicinity of the inactive steady state. The large magnitude of noise causes large departures from the stable orbit of the deterministic approximation. For the twice smaller value of $\lambda = 0.025$ mRNA/s (Fig. 5B), the inactive steady state is the only recurrent solution of the deterministic system. The deterministic trajectory (red line), after the large departure from this unique stable steady state in response to the 5-min 1 ng/ml TNFα pulse, exhibits a series of four oscillations before returning to the close vicinity of the steady state. In contrast, a stochastic trajectory may exhibit longer series of semi-periodic oscillations, without any TNFα stimulation (black line). The phenomenon of noise-induced oscillations is quite common in dynamical systems; here, the oscillations are additionally stabilized by the "ghost" of the limit cycle.

In Fig. 6 we analyze stochastic switching of WT and A20$^{-/-}$ cells. WT cells are analyzed for two TNFα transcription coefficients $\lambda = 0.05$ mRNA/s (Fig. 6A) and $\lambda = 0.025$ mRNA/s (Fig. 6B). In the first case, 3000-hour-long simulation reveals irregular jumps between the inactive and the oscillatory phases (Fig. 6A). In the inactive phase (Fig. 6C), the nuclear NF-κB fluctuations are irregular and their amplitude is of order of 10^3 molecules. In contrast, in the oscillatory phase, the oscillations are semiperiodic with the average amplitude of 3×10^4 molecules (Fig. 6D), more than an order of magnitude larger than in the inactive phase. For $\lambda = 0.05$ the stochastic transitions between the inactive and the oscillatory phases occur on average every 70 h, and the fraction of time spent in each phase is almost equal. For smaller $\lambda = 0.025$ mRNA/s, for which the deterministic system is monostable, transitions to the oscillatory phase are still possible, but the characteristic number of oscillations in a series is smaller. As one could expect, the probability that a cell is in the oscillatory phase grows with λ (Fig. 6E). A bit surprisingly, even when the deterministic approximation is monostable ($\lambda < 0.045$ mRNA/s), the oscillatory phase probability is nonzero, and, similarly, when the deterministic systems has only limit cycle oscillations ($\lambda > 0.093$ mRNA/s), the oscillatory phase probability may still be smaller than 1.

As already said, A20-deficient cells are more sensitive to TNFα, and they are activated at a much smaller TNFα transcription coefficient λ. This property is even more evident when the stochastic system is analyzed. For $\lambda = 0.004$ the transitions to the active state are very infrequent (Fig. 6G), but for larger $\lambda = 0.006$ cells spend more than half of time in the active state. Despite the deterministic system is bistable for $\lambda \in (0.0037, 0.050)$, it appears that the stochastic system is persistently active for $\lambda > 0.01$ (Fig. 6E and Text S1, Fig. S4C).

Individual Cell Responses to Different TNFα Doses

Wild-type cells. Turner et al. [75] found that about 20% of unstimulated SK-N-AS cells exhibit NF-κB oscillations without any stimulation. In light of our model, this finding suggests that these cell express TNFα, and that the TNFα transcription coefficient, λ, is about 0.025 mRNA/s (or, more precisely, that effectiveness of TNFα transcription, translation and secretion process is such as in the model for $\lambda = 0.025$ mRNA/s). As shown in Fig. 6E for this λ, the probability to find a cell in the oscillatory phase is about 20%. More precisely, the fitted value of λ, as well as
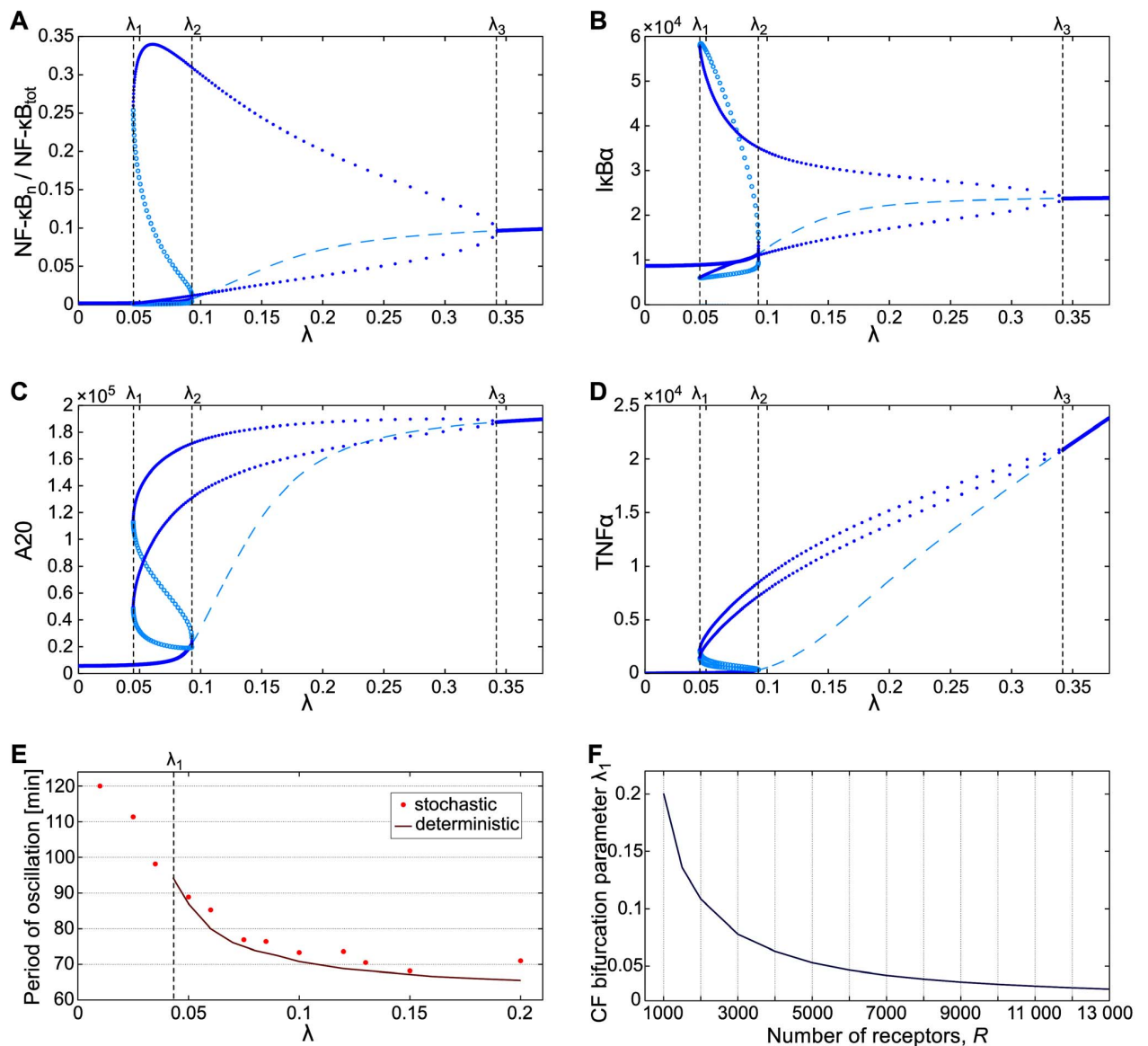
Figure 3. Bifurcation diagrams for WT cells. Recurrent solutions in a function of TNFα mRNA transcription coefficient λ. (**A–D**) Nuclear NF-κB, free cytoplasmic IκBα, A20, intracellular TNFα. There are three bifurcations: cyclic fold (CF) at λ_1, subcritical Hopf at λ_2 (see Text S1 and Fig. S3 therein for details) and supercritical Hopf at λ_3. (**E**) Oscillation period of stochastic and deterministic trajectories as a function of λ. (**F**) Cyclic fold bifurcation parameter λ_1 as a function of TNFR1 receptor number. Bifurcations diagrams shown in (**A–D**) where obtained for receptor number $R = 7000$ (equal to the median receptor number assumed for stochastic simulations).
doi:10.1371/journal.pone.0078887.g003

the cyclic fold bifurcation parameter λ_1, depend on the assumed level of TNFR1 receptors (Fig. 3F). Keeping the experiment of Turner et al. as a reference for SK-N-AS cells, we set $\lambda = 0.025$ mRNA/s [75]. As shown in Fig. 3E for $\lambda = 0.025$ the oscillation period (of spontaneous oscillation) is about 110 min in agreement with experimental data, and then decreases with the value of λ. Accordingly, for $\lambda = 0.025$ we simulate cell responses to four TNFα doses. In simulations the level of TNFα is increased abruptly in $t = 1$ h from 0 to respectively 1 ng/ml, 100 pg/ml, 30 pg/ml, 3 pg/ml, and then decreases exponentially with half-time of ∼1 h due to protein degradation (Fig. 7).

The single cell trajectories obtained in numerical simulations (Fig. 7) are in plausible agreement with the experiment of Turner

et al. [75]. In particular, both experiment and simulation showed that the amplitude of the first pulse decreases with dose, but the amplitudes of subsequent peaks are higher for the low than for the high dose.

The low dose (≤ 30 pg/ml) responses have a purely stochastic nature. They are not observed in the deterministic simulations (thick red line), and are invisible at the population level due to the asynchrony of individual cells. The average activation time and its variance increases with decreasing TNFα dose, which suggests that the first activation has a stochastic character. As predicted and demonstrated recently, massive NF-κB translocation may follow binding of single TNFα molecules to TNFR1 receptors [27,34]. However, even at low doses the first peak is frequently followed by
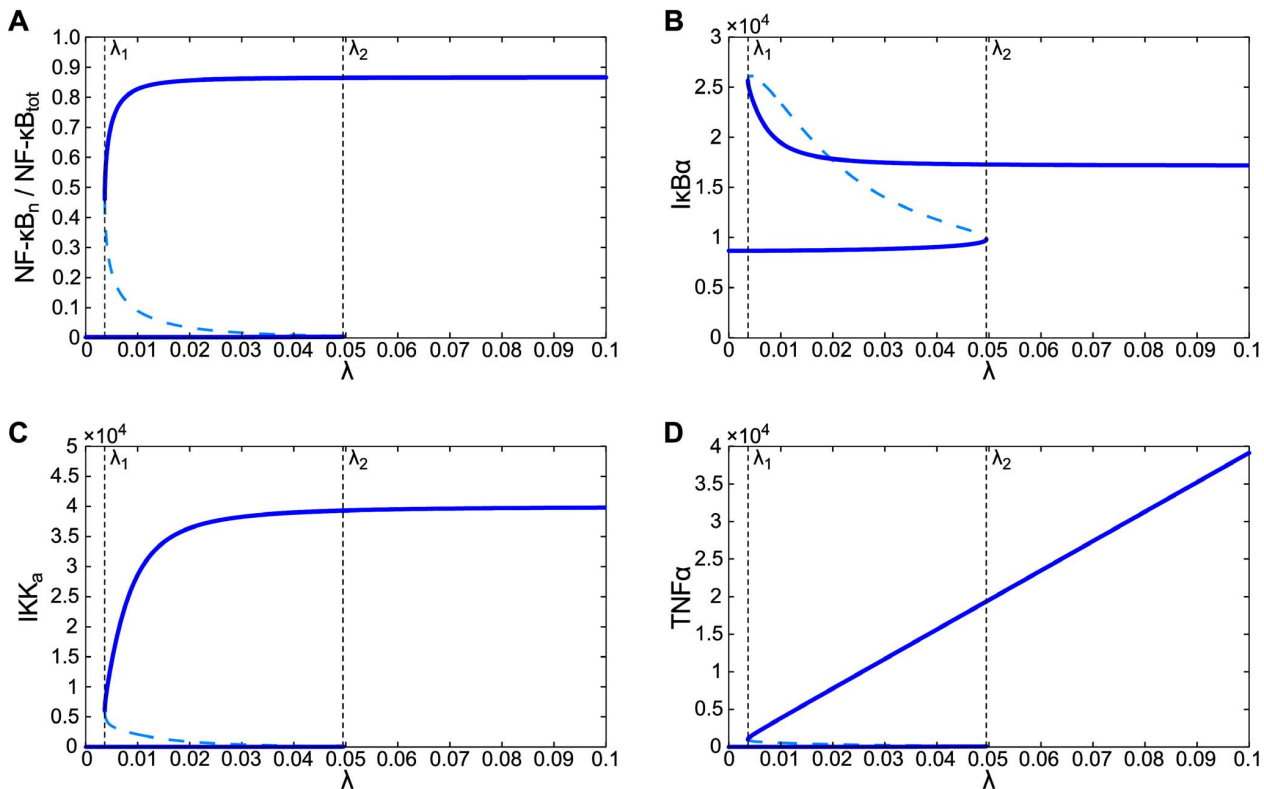
Figure 4. Bifurcation diagrams for A20-deficient cells. Stable recurrent solutions in a function of TNFα mRNA transcription coefficient λ. (**A–D**) Nuclear NF-κB, free cytoplasmic IκBα, active IKK, intracellular TNFα. There are two saddle-node bifurcations at λ_1 and λ_2.
doi:10.1371/journal.pone.0078887.g004

subsequent ones, which according to the model is due to (1) autoactivation via autocrine TNFα regulation and (2) broad distribution of the level of receptors. Responding cells likely have higher receptor number so they are more prone for subsequent activation [34].

As found by Turner et al., the fraction of activated cells in first 300 minutes decreases with TNFα dose, but even for zero doses the activated cell fraction is about 20% [75]. This phenomenon is clearly visible in our simulation (Fig. 8). Following Turner et al., we analyze two cases: tonic TNFα stimulation, and 5-min TNFα

pulse [75]. As expected, for the same dose, tonic stimulation yield higher fraction of responding cells. The model predictions are in reasonable agreement with experiment, with the main difference being observed for the tonic stimulation. For 3 pg/ml the model predicts lower fraction of responding cells than that observed experimentally. This can be attributed to the paracrine activation of neighboring cells, which is not taken into account in the model. Paracrine signaling can be also responsible for huge error bars for 3 pg/ml dose: one can imagine that the denser arrays of cells are more prone to activation.
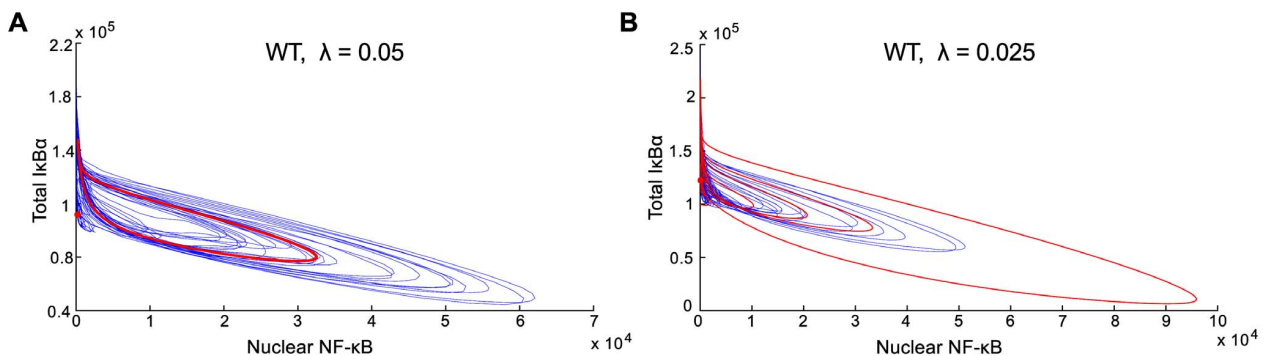

Figure 5. Stochastic versus deterministic solutions for WT cells. (**A**) $\lambda = 0.05$; thick red line and red dot – stable limit cycle and stable steady state for the deterministic approximation; blue line – example stochastic trajectory (total simulation time: 70 h). (**B**) $\lambda = 0.025$; red line – deterministic damped oscillations in response to 5-min pulsed 1 ng/ml TNFα; blue line – example stochastic trajectory (total simulation time: 70 h) in the absence of TNFα stimulation.
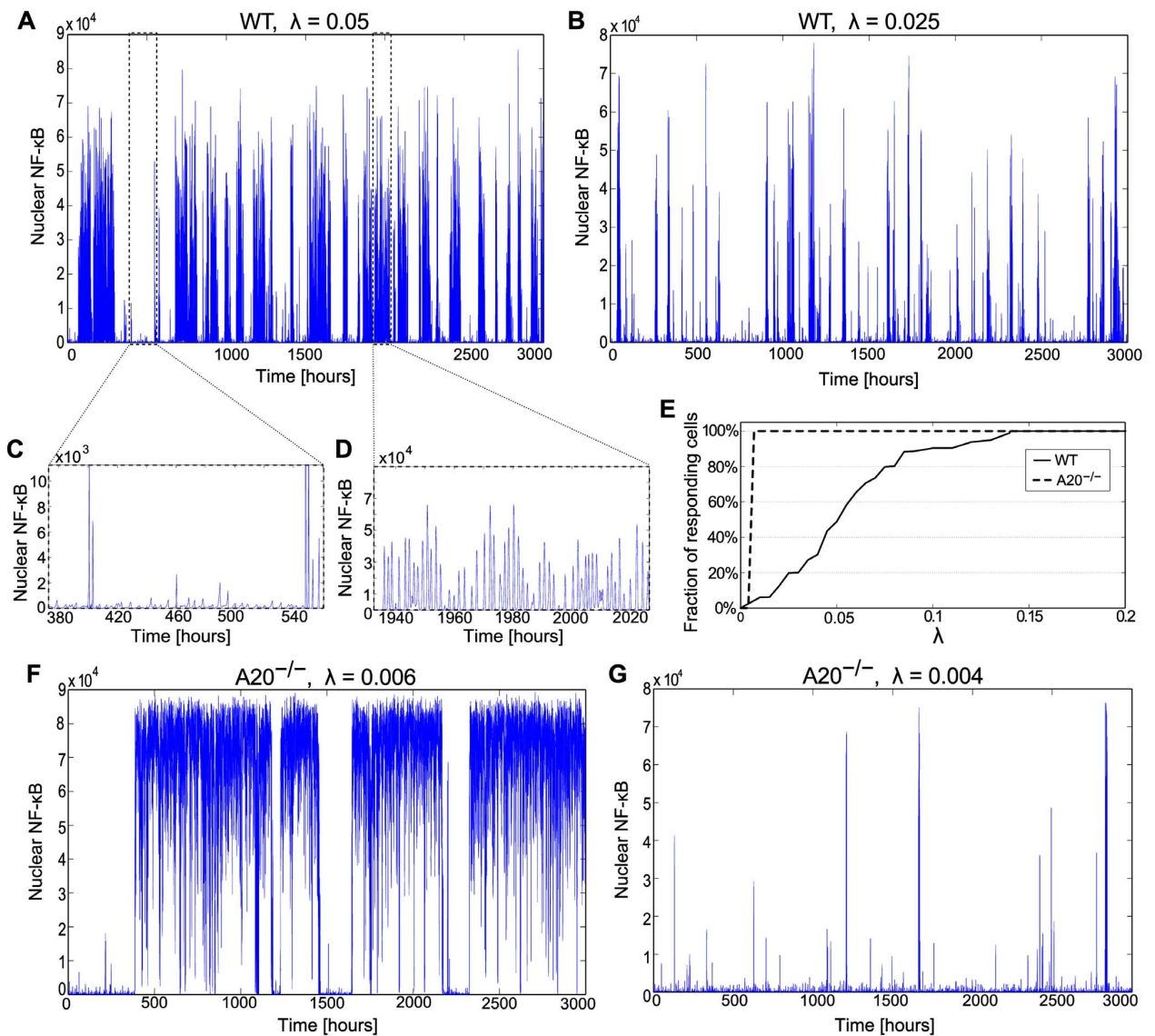doi:10.1371/journal.pone.0078887.g005

Figure 6. Long run stochastic trajectories in the absence of external stimulation. (**A**, **B**) WT cells for $\lambda = 0.05$ and $\lambda = 0.025$, respectively, and TNFR1 receptors number $R = 7000$. (**C**, **D**) Zoomed fragments of trajectory showing (**C**) small stochastic fluctuations in the vicinity of the stable steady state and (**D**) large amplitude oscillations in the basin of attraction of the stable limit cycle. (**E**) Fraction of oscillating WT and A20$^{-/-}$ cells as a function of λ. (**F**, **G**) A20$^{-/-}$ cells trajectories for $\lambda = 0.006$ and $\lambda = 0.004$.
doi:10.1371/journal.pone.0078887.g006

A20-deficient cells. In their seminal work, Lee et al. observed that A20$^{-/-}$ MEFs (in contrast to WT cells) do not exhibit oscillations to the tonic TNFα stimulation [14]. More surprisingly, Werner et al. (2005 and 2008) observed that in A20$^{-/-}$ MEFs even a short 5-min pulse of TNFα stimulation leads to at least 3-hour-long nuclear NF-κB activity [82,83]. As already found in the deterministic model analysis, A20$^{-/-}$ cells producing even small amounts of TNFα are bistable, and thus may be "persistently" activated by a short pulse of TNFα.

In Fig. 9 we compare WT and A20$^{-/-}$ cell responses to 5-, 15- and 45-min TNFα stimulation. We assume TNFα mRNA synthesis rate $\lambda = 0.004$, much smaller than the value for SK-N-AS cells. This is in accordance with the observation that 3T3 cells do not exhibit spontaneous activation. WT cells respond with a single pulse of IKK activity, which leads in most cases to a single pulse of nuclear NF-κB. In contrast, A20$^{-/-}$ cells show a high tail of IKK activity, which results in the prolonged nuclear NF-κB occupancy. In the deterministic model (thick red line), 5- and 15-min pulses are not sufficient to drive cells into the active state; only after the 45-min pulse cells became persistently activated. In contrast, most of single cell stochastic trajectories exhibit a high level of nuclear NF-κB even after the 5-min pulse. As a result, the population average trajectory shows single NF-κB pulse followed by a very high tail. The IKK and NF-κB activity profiles for WT and A20$^{-/-}$ are in plausible agreement with experiments of Werner et al. [82,83].
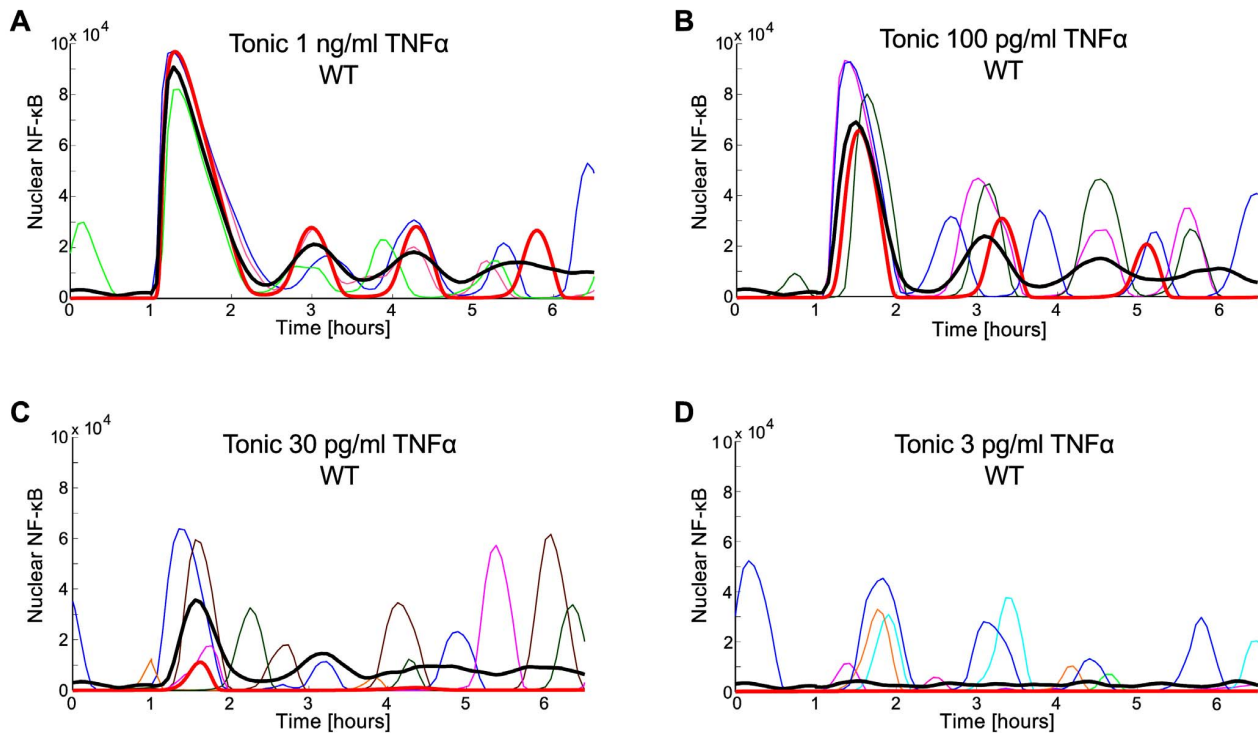
Figure 7. Simulated responses of WT cells (with l = 0.025) to tonic TNFα stimulation beginning at t = 1 h. (A–D): TNFα doses: 1 ng/ml, 100 pg/ml, 30 pg/ml, 3 pg/ml. Red thick line – deterministic simulation; thin colored lines – single cell stochastic simulations; black thick line – population average. In (A) and (B), 3 individual representative cells trajectories are shown (in each panel). In (C) and (D), respectively 5 and 10 individual cell trajectories are shown, but only 3 trajectories (in each panel) exhibit visible oscillations.
doi:10.1371/journal.pone.0078887.g007

Discussion

We investigated theoretically and computationally the effect of autocrine TNFα signaling on NF-κB regulation. NF-κB activity is regulated by two interlinked negative feedback loops. The first loop involves NF-κB responsive inhibitors: IκBα and IκBε, which directly bind to NF-κB and sequester it in the cytoplasm. The second loop is mediated by another NF-κB strongly responsive protein, A20, which attenuates the IKK activity. Without A20 expression, IKK retains its activity, which leads to the rapid degradation of the newly synthesized IκBα and destroys the NF-κB–IκBα feedback loop. The autocrine positive feedback loop arises in cell lines that are characterized by a sufficiently high TNFR1 expression and TNFα secretion. As demonstrated in this study, the positive feedback qualitatively changes the system dynamics. It may lead to long-lasting NF-κB oscillations in WT cells and persistent NF-κB activity in A20-deficient cells, which were found to be very prone to activation. The approach proposed in this study combined deterministic and stochastic modeling.

Bifurcation analysis was performed for WT and A20-deficient cells. In both cases, TNFα mRNA synthesis rate was chosen as a bifurcation parameter λ. Analysis of WT cells shown in Fig. 3

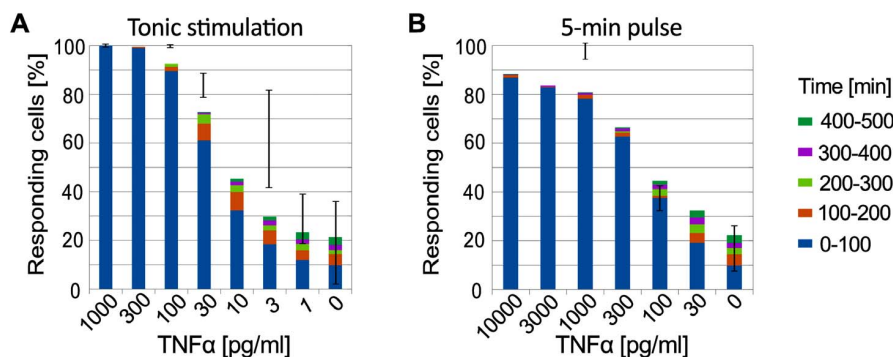**Figure 8. Fraction of responding cells versus TNFα dose.** (A) Tonic stimulation. (B) 5-min pulsed stimulation. Color bars: model prediction for $\lambda = 0.025$– fraction of cells responding within the given time period. Error bars show fractions of cells responding during the first 300-min in the experiment of Turner et al. [75] on SK-N-AS cells, see the main text.
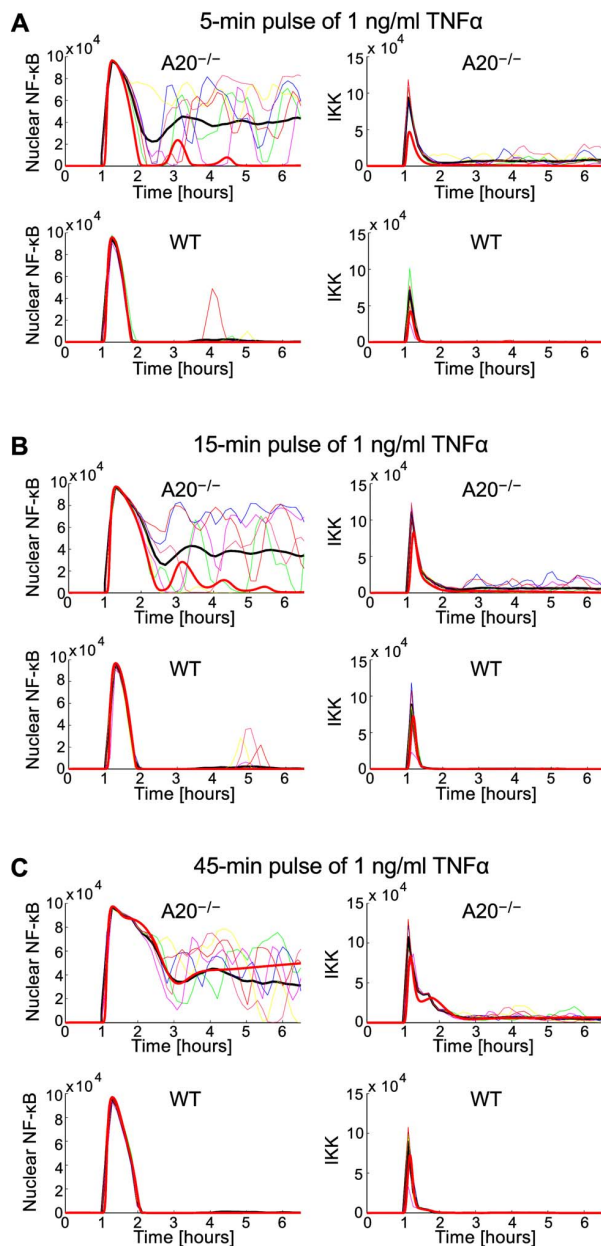doi:10.1371/journal.pone.0078887.g008

Figure 9. Simulated responses of WT and A20$^{-/-}$ cells to pulsed stimulation with 1 ng/ml TNFα for I = 0.004. (**A**) 5-min pulse. (**B**) 15-min pulse. (**C**) 45-min pulse. Red thick line – deterministic simulation; thin colored lines – single cell stochastic simulations; black thick line – population average.
doi:10.1371/journal.pone.0078887.g009

revealed that at some value of $\lambda = \lambda_1$ the limit cycle oscillations appear. These oscillations coexist with steady state (characterized by low level of nuclear NF-κB), which loses stability for $\lambda = \lambda_2 > \lambda_1$. That is, in range of bifurcation parameter $\lambda \in (\lambda_1, \lambda_2)$ the system has two stable recurrent solutions, steady state and limit cycle. In contrast to WT cells, A20-deficient cells (considered in the deterministic approximation) do not exhibit oscillations. Instead, in a broad range of bifurcation parameter they exhibit bistability characterized by the coexistence of states of the low and high level of nuclear NF-κB. The A20 deficiency dramatically increases cell

sensitivity: the critical value of TNFα synthesis at which cells may be activated due to autocrine signaling was found more than 10 times lower for A20$^{-/-}$ cells than for WT cells, ~0.0037 mRNA/ s (for A20$^{-/-}$) versus ~0.045 mRNA/s (for WT).

By analyzing the stochastic model we demonstrated that noise, arising mostly at the level of gene regulation, enables switching between the stable steady state and limit cycle in WT cells, and between inactive and active steady state in A20-deficient cells (Fig. 6). Interestingly, in WT cells the semiperiodic oscillations can be driven by noise even for $\lambda < \lambda_1$, i.e., in the absence of the limit cycle (Fig. 6E). This can be interpreted as *stochastic resonance*, which in the broad definition refers to the case when noise has a positive role in the signal-processing context [84]. The transition from the inactive to the oscillatory state can be also induced by an external TNFα stimulation, and the probability of such transition increases with the stimulation dose (Figs. 7 and 8). Based on our analysis, one should also expect that the LPS stimulation leading to the activation of NF-κB (which controls TNFα transcription) and MAPK pathways (effector kinases which stabilize TNFα transcript and enhance TNFα translation), which together results in massive secretion of TNFα, can also trigger long-lasting NF-κB oscillations in cells with high autocrine potential [4,68].

Introduction of positive feedback enabled us to reproduce the noise-triggered oscillations observed by Turner et al. in unstimulated cells, as well as earlier experiments by Werner et al. showing prolonged NF-κB activation in response to the pulsed TNFα stimulation in A20-deficient MEFs [75,82,83]. Since the sensitivity to the autocrine-driven activation of A20-deficient cells is much higher than that of WT cells, even a weak stimulus can drive these cells to the state of persistent NF-κB activation characterized by massive secretion of TNFα and other inflammatory cytokines such as IL-8 and IL-6. This explains why the loss of A20 or its dysfunction disturbs regulation of immune system and renders the organism vulnerable to the septic shock resulting from the uncontrolled secretion of inflammatory cytokines [85]. Mice lacking A20 are hypersensitive to the TNFα-induced cell death, which suggests that positive auto- and paracrine signaling upregulate the TNFα expression so strongly that it overcomes the antiapoptotic action of NF-κB [14]. Boone et al. demonstrated that A20 is critical for the regulation of macrophage responses in vivo and protects mice against the septic shock [28].

There is a bulk of evidence that the loss or dysfunction of A20 as well as the other inhibitory DUBase, named Cyld, promote inflammatory diseases and cancer (reviewed in [24,86]). It was found recently that A20 functions as a tumor suppressor in several subtypes of non-Hodgkin as well as Hodgkin lymphomas, and its silencing results in the constitutive activation of NF-κB [29,87]. Kato et al. found that when re-expressed in a lymphoma-derived cell line with no functional A20 alleles, wild-type A20, but not mutant A20, resulted in the suppression of cell growth and induction of apoptosis, accompanied by downregulation of NF-κB activation [87]. Somatic mutations of A20 are associated with constitutive activation of NF-κB and poor overall survival in diffuse large B-cell lymphoma [88]. Huang et al. observed that the loss of A20 expression accompanies the oncogenic transformation of MEFs [89]. The above findings indicate that constitutive NF-κB activation, resulting form A20 dysfunction or increased TNFα autocrine potential (due to elevated TNFα and/or TNFR1 expression), in general promote cancer [90,91]. In correspondence to our considerations, Bian et al. found that constitutively active NF-κB is required for the survival of S-type neuroblastic SH-EP1 and SK-N-AS cell lines [92].

As already said, particular cell lines are characterized by the high TNFα autocrine potential. Macrophages are generally considered as major TNFα producers, and are also highly TNFα-responsive. There is a growing evidence that macrophages require autocrine TNFα regulation for survival and differentiation [93–95]. In monocytes, sustained Nrf2 activation that protects cells from oxidative damage involves TNFα autocrine signaling [56].

In summary, the proposed model explains the mechanism of spontaneous or signal-dependent activation of NF-κB in cells with high autocrine potential. The cells prone to autocrine activation are characterized by high level of TNFα and TNFR1 synthesis or loss of functional A20. A20 dysfunction may promote inflammation and cancer, and also render the organism vulnerable to septic shock. In some cell lines, however, the self-sustained NF-κB activation can be required for performing their functions or undergo differentiation.

Supporting Information

Text S1 The supplementary text includes: list of reactions and parameters, list of differential equations, numerical simulation protocols, mathematical methods and experimental protocols, and four supplementary figures: Fig. S1– distribution of the number of receptors; Fig. S2– close-up on the bifurcation diagram near λ_2 for WT cells; Fig. S3—3-D bifurcation diagram for WT cells; Fig. S4– long run stochastic trajectories for WT cells for $\lambda = 0.1$ and $\lambda = 0.2$ and for $A20^{-/-}$ cells for $\lambda = 0.01$.
(PDF)

Material S1 MATLAB code of the model for performing deterministic simulations. (ZIP-archived directory containing MATLAB scripts and a ReadMe file).
(ZIP)

Material S2 BIONETGEN code of the model for performing both deterministic and stochastic simulations. (ZIP-archived directory containing a BNGL model file and a ReadMe file).
(ZIP)

Material S3 MATLAB/MATCONT code for performing bifurcation analysis. (ZIP-archived directory containing MATLAB scripts calling MATCONT functions, and a ReadMe file).
(ZIP)

Author Contributions

Conceived and designed the experiments: ST TL. Performed the experiments: MJ RK. Analyzed the data: JP MJ RK. Wrote the paper: TL. Designed study: TL. Performed mathematical and numerical analysis: JP MK. Wrote the numerical codes: PJZ MK JP.

References

1. Yde P, Mengel B, Jensen MH, Krishna S, Trusina A (2011) Modeling the NF-κB mediated inflammatory response predicts cytokine waves in tissue. BMC Syst Biol 5: 115.
2. Rand U, Rinas M, Schwerk J, Nöhren G, Linnes M, et al. (2012) Multi-layered stochasticity and paracrine signal propagation shape the type-I interferon response. Mol Syst Biol 8: 584.
3. Covert MW, Leung TH, Gaston JE, Baltimore D (2005) Achieving stability of lipopolysaccharideinduced NF-κB activation. Science 309: 1854–1857.
4. Lee TK, Denny EM, Sanghvi JC, Gaston JE, Maynard ND, et al. (2009) A noisy paracrine signal determines the cellular NF-κB response to lipopolysaccharide. Sci Signal 2: ra65.
5. Brasier AR (2006) The NF-κB regulatory network. Cardiovasc Toxicol 6: 111–130.
6. Hoffmann A, Baltimore D (2006) Circuitry of nuclear factor κB signaling. Immunol Rev 210: 171–186.
7. Brown K, Park S, Kanno T, Franzoso G, Siebenlist U (1993) Mutual regulation of the transcriptional activator NF-κB and its inhibitor, IκB-α. Proc Natl Acad Sci USA 90: 2532–2536.
8. Hoffmann A, Levchenko A, Scott ML, Baltimore D (2002) The IκB–NF-κB signaling module: temporal control and selective gene activation. Science 298: 1241–1245.
9. Cho KH, Shin SY, Lee HW, Wolkenhauer O (2003) Investigations into the analysis and modeling of the TNFα-mediated NF-κB-signaling pathway. Genome Res 13: 2413–2422.
10. Whiteside ST, Epinat JC, Rice NR, Isral A (1997) IκBε, a novel member of the IκB family, controls RelA and cRel NF-κB activity. EMBO J 16: 1413–1426.
11. Kearns JD, Basak S, Werner SL, Huang CS, Hoffmann A (2006) IκBε provides negative feedback to control NF-κB oscillations, signaling dynamics, and inflammatory gene expression. J Cell Biol 173: 659–664.
12. Krikos A, Laherty CD, Dixit VM (1992) Transcriptional activation of the tumor necrosis factor α-inducible zinc finger protein, a20, is mediated by κB elements. J Biol Chem 267: 17971–17976.
13. Jttel M, Mouritzen H, Elling F, Bastholm L (1996) A20 zinc finger protein inhibits TNF and IL-1 signaling. J Immunol 156: 1166–1173.
14. Lee EG, Boone DL, Chai S, Libby SL, Chien M, et al. (2000) Failure to regulate TNF-induced NF-κB and cell death responses in A20-deficient mice. Science 289: 2350–2354.
15. Paszek P, Ryan S, Ashall L, Sillitoe K, Harper CV, et al. (2010) Population robustness arising from cellular heterogeneity. Proc Natl Acad Sci USA 107: 11644–11649.
16. Zhang SQ, Kovalenko A, Cantarella G, Wallach D (2000) Recruitment of the IKK signalosome to the p55 TNF receptor: RIP and A20 bind to NEMO (IKKγ) upon receptor stimulation. Immunity 12: 301–311.
17. Mauro C, Pacifico F, Lavorgna A, Mellone S, Iannetti A, et al. (2006) ABIN-1 binds to NEMO/IKKγ and co-operates with A20 in inhibiting NF-κB. J Biol Chem 281: 18482–18488.
18. Skaug B, Chen J, Du F, He J, Ma A, et al. (2011) Direct, noncatalytic mechanism of IKK inhibition by A20. Mol Cell 44: 559–571.
19. Wertz IE, O'Rourke KM, Zhou H, Eby M, Aravind L, et al. (2004) Deubiquitination and ubiquitin ligase domains of A20 downregulate NF-κB signalling. Nature 430: 694–699.
20. Delhase M, Hayakawa M, Chen Y, Karin M (1999) Positive and negative regulation of IκB kinase activity through IKKβ subunit phosphorylation. Science 284: 309–313.
21. Chen ZJ (2012) Ubiquitination in signaling to and activation of IKK. Immunol Rev 246: 95–106.
22. Zhou H, Wertz I, O'Rourke K, Ultsch M, Seshagiri S, et al. (2004) Bcl10 activates the NF-κB pathway through ubiquitination of NEMO. Nature 427: 167–171.
23. Hutti JE, Turk BE, Asara JM, Ma A, Cantley LC, et al. (2007) IκB kinase β phosphorylates the K63 deubiquitinase A20 to cause feedback inhibition of the NF-κB pathway. Mol Cell Biol 27: 7451–7461.
24. Harhaj EW, Dixit VM (2011) Deubiquitinases in the regulation of NF-κB signaling. Cell Res 21: 22–39.
25. Harhaj EW, Dixit VM (2012) Regulation of NF-κB by deubiquitinases. Immunol Rev 246: 107–124.
26. Lipniacki T, Paszek P, Brasier ARAR, Luxon B, Kimmel M (2004) Mathematical model of NF-κB regulatory module. J Theor Biol 228: 195–215.
27. Lipniacki T, Puszynski K, Paszek P, Brasier AR, Kimmel M (2007) Single tnf α trimers mediating NF-κB activation: stochastic robustness of NF-κB signaling. BMC Bioinformatics 8: 376.
28. Boone DL, Turer EE, Lee EG, Ahmad RC, Wheeler MT, et al. (2004) The ubiquitin-modifying enzyme A20 is required for termination of Toll-like receptor responses. Nat Immunol 5: 1052–1060.
29. Honma K, Tsuzuki S, Nakagawa M, Tagawa H, Nakamura S, et al. (2009) TNFAIP3/A20 functions as a novel tumor suppressor gene in several subtypes of non-Hodgkin lymphomas. Blood 114: 2467–2475.
30. Lin R, Lacoste J, Nakhaei P, Sun Q, Yang L, et al. (2006) Dissociation of a MAVS/IPS- 1/VISA/Cardif-IKKε molecular complex from the mitochondrial outer membrane by hepatitis C virus NS3–4A proteolytic cleavage. J Virol 80: 6072–6083.
31. Zhao T, Yang L, Sun Q, Arguello M, Ballard DW, et al. (2007) The NEMO adaptor bridges the nuclear factor-κB and interferon regulatory factor signaling pathways. Nat Immunol 8: 592–600.
32. Lin R, Yang L, Nakhaei P, Sun Q, Sharif-Askari E, et al. (2006) Negative regulation of the retinoic acid-inducible gene I-induced antiviral state by the ubiquitin-editing protein A20. J Biol Chem 281: 2095–2103.
33. Nelson DE, Ihekwaba AEC, Elliott M, Johnson JR, Gibney CA, et al. (2004) Oscillations in NF-κB signaling control the dynamics of gene expression. Science 306: 704–708.
34. Tay S, Hughey JJ, Lee TK, Lipniacki T, Quake SR, et al. (2010) Single-cell NF-κB dynamics reveal digital activation and analogue information processing. Nature 466: 267–271.
35. Lipniacki T, Paszek P, Brasier AR, Luxon BA, Kimmel M (2006) Stochastic regulation in early immune response. Biophys J 90: 725–742.

36. Lipniacki T, Kimmel M (2007) Deterministic and stochastic models of NF-κB pathway. Cardiovasc Toxicol 7: 215–234.

37. Barken D, Wang CJ, Kearns J, Cheong R, Hoffmann A, et al. (2005) Comment on "Oscillations in NF-κB signaling control the dynamics of gene expression". Science 308: 52.

38. Nelson DE, Horton CA, See V, Johnson JR, Nelson G, et al. (2005) Response to comment on "Oscillations in NF-κB signaling control the dynamics of gene expression". Science 308: 52.

39. Hat B, Puszynski K, Lipniacki T (2009) Exploring mechanisms of oscillations in p53 and nuclear factor-κB systems. IET Syst Biol 3: 342–355.

40. Beutler B, Cerami A (1988) Tumor necrosis, cachexia, shock, and inflammation: a common mediator. Annu Rev Biochem 57: 505–518.

41. Aggarwal BB (2003) Signalling pathways of the TNF superfamily: a double-edged sword. Nat Rev Immunol 3: 745–756.

42. Xaus J, Comalada M, Valledor AF, Lloberas J, López-Soriano F, et al. (2000) LPS induces apoptosis in macrophages mostly through the autocrine production of TNF-α. Blood 95: 3823–3831.

43. Tracey KJ, Fong Y, Hesse DG, Manogue KR, Lee AT, et al. (1987) Anti-cachectin/TNF monoclonal antibodies prevent septic shock during lethal bacteraemia. Nature 330: 662–664.

44. Grell M, Wajant H, Zimmermann G, Scheurich P (1998) The type 1 receptor (CD120a) is the high-affinity receptor for soluble tumor necrosis factor. Proc Natl Acad Sci USA 95: 570–575.

45. Beg AA, Baltimore D (1996) An essential role for nf-κB in preventing TNF-α-induced cell death. Science 274: 782–784.

46. Kelliher MA, Grimm S, Ishida Y, Kuo F, Stanger BZ, et al. (1998) The death domain kinase RIP mediates the TNF-induced NF-κB signal. Immunity 8: 297–303.

47. Hsu H, Shu HB, Pan MG, Goeddel DV (1996) TRADD-TRAF2 and TRADD-FADD interactions define two distinct TNF receptor 1 signal transduction pathways. Cell 84: 299–308.

48. Collart MA, Baeuerle P, Vassalli P (1990) Regulation of tumor necrosis factor alpha transcription in macrophages: involvement of four κB-like motifs and of constitutive and inducible forms of NF-κB. Mol Cell Biol 10: 1498–1506.

49. Udalova IA, Knight JC, Vidal V, Nedospasov SA, Kwiatkowski D (1998) Complex NF-κB interactions at the distal tumor necrosis factor promoter region in human monocytes. J Biol Chem 273: 21178–21186.

50. Wu S, Boyer CM, Whitaker RS, Berchuck A, Wiener JR, et al. (1993) Tumor necrosis factor alpha as an autocrine and paracrine growth factor for ovarian cancer: monokine induction of tumor cell proliferation and tumor necrosis factor alpha expression. Cancer Res 53: 1939–1944.

51. Coward WR, Okayama Y, Sagara H, Wilson SJ, Holgate ST, et al. (2002) NF-κB and TNF-α: a positive autocrine loop in human lung mast cells? J Immunol 169: 5287–5293.

52. Guergnon J, Chaussepied M, Sopp P, Lizundia R, Moreau MF, et al. (2003) A tumour necrosis factor alpha autocrine loop contributes to proliferation and nuclear factor-κB activation of Theileria parva-transformed B cells. Cell Microbiol 5: 709–716.

53. Nadeau S, Rivest S (2000) Role of microglial-derived tumor necrosis factor in mediating CD14 transcription and nuclear factor κB activity in the brain during endotoxemia. J Neurosci 20: 3456–3468.

54. Kuno R, Wang J, Kawanokuchi J, Takeuchi H, Mizuno T, et al. (2005) Autocrine activation of microglia by tumor necrosis factor-α. J Neuroimmunol 162: 89–96.

55. Hu P, Han Z, Couvillon AD, Kaufman RJ, Exton JH (2006) Autocrine tumor necrosis factor alpha links endoplasmic reticulum stress to the membrane death receptor pathway through IRE1 α-mediated NF-κB activation and down-regulation of TRAF2 expression. Mol Cell Biol 26: 3071–3084.

56. Rushworth SA, Shah S, MacEwan DJ (2011) TNF mediates the sustained activation of Nrf2 in human monocytes. J Immunol 187: 702–707.

57. Hayakawa K, Meng Y, Hiramatsu N, Kasai A, Yao J, et al. (2006) Spontaneous activation of the NF-κB signaling pathway in isolated normal glomeruli. Am J Physiol Renal Physiol 291: F1169–F1176.

58. Tsai EY, Jain J, Pesavento PA, Rao A, Goldfeld AE (1996) Tumor necrosis factor α gene regulation in activated T cells involves ATF-2/Jun and NFATp. Mol Cell Biol 16: 459–467.

59. Liu H, Sidiropoulos P, Song G, Pagliari LJ, Birrer MJ, et al. (2000) TNF-α gene expression in macrophages: regulation by NF-κB is independent of c-Jun or C/EBP beta. J Immunol 164: 4277–4285.

60. Deleault KM, Skinner SJ, Brooks SA (2008) Tristetraprolin regulates TNF TNF-α mRNA stability via a proteasome dependent mechanism involving the combined action of the ERK and p38 pathways. Mol Immunol 45: 13–24.

61. Guma M, Stepniak D, Shaked H, Spehlmann ME, Shenouda S, et al. (2011) Constitutive intestinal NF-κB does not trigger destructive inflammation unless accompanied by MAPK activation. J Exp Med 208: 1889–1900.

62. Gais P, Tiedje C, Altmayr F, Gaestel M, Weighardt H, et al. (2010) TRIF signaling stimulates translation of TNF-α mRNA via prolonged activation of MK2. J Immunol 184: 5842–5848.

63. Liacini A, Sylvester J, Li WQ, Huang W, Dehnade F, et al. (2003) Induction of matrix metalloproteinase-13 gene expression by TNF-α is mediated by MAP

64. Li YP, Chen Y, John J, Moylan J, Jin B, et al. (2005) TNF-α acts via p38 MAPK to stimulate expression of the ubiquitin ligase atrogin1/MAFbx in skeletal muscle. FASEB J 19: 362–370.

65. Kawai T, Akira S (2007) Signaling to NF-κB by Toll-like receptors. Trends Mol Med 13: 460–469.

66. Kawai T, Akira S (2011) Toll-like receptors and their crosstalk with other innate receptors in infection and immunity. Immunity 34: 637–650.

67. Hao S, Baltimore D (2009) The stability of mRNA influences the temporal order of the induction of genes encoding inflammatory molecules. Nat Immunol 10: 281–288.

68. Gutschow MV, Hughey JJ, Ruggero NA, Bajar BT, Valle SD, et al. (2013) Single-cell and population NF-κB dynamic responses depend on lipopolysaccharide preparation. PLoS One 8: e53222.

69. Hiscott J, Marois J, Garoufalis J, D'Addario M, Roulston A, et al. (1993) Characterization of a functional NF-κB site in the human interleukin 1 β promoter: evidence for a positive autoregulatory loop. Molecular and Cellular Biology 13: 6231–6240.

70. Schooley K, Zhu P, Dower SK, Qwarnstrm EE (2003) Regulation of nuclear translocation of nuclear factor-κB relA: evidence for complex dynamics at the single-cell level. Biochem J 369: 331–339.

71. Cheong R, Hoffmann A, Levchenko A (2008) Understanding NF-κB signaling via mathematical modeling. Mol Syst Biol 4: 192.

72. Terry AJ, Chaplain MAJ (2011) Spatio-temporal modelling of the NF-κB intracellular signalling pathway: the roles of diffusion, active transport, and cell geometry. J Theor Biol 290: 7–26.

73. Ashall L, Horton CA, Nelson DE, Paszek P, Harper CV, et al. (2009) Pulsatile stimulation determines timing and specificity of NF-κB-dependent transcription. Science 324: 242–246.

74. James CD, Moorman MW, Carson BD, Branda CS, Lantz JW, et al. (2009) Nuclear translocation kinetics of NF-κB in macrophages challenged with pathogens in a microfluidic platform. Biomed Microdevices 11: 693–700.

75. Turner DA, Paszek P, Woodcock DJ, Nelson DE, Horton CA, et al. (2010) Physiological levels of TNF α stimulation induce stochastic dynamics of NF-κB responses in single living cells. J Cell Sci 123: 2834–2843.

76. Gillespie DT (1977) Exact stochastic simulation of coupled chemical reactions. J Phys Chem 81: 2340–2361.

77. Faeder JR, Blinov ML, Hlavacek WS (2009) Rule-based modeling of biochemical systems with BioNetGen. Methods Mol Biol 500: 113–167.

78. Barua D, Hlavacek WS, Lipniacki T (2012) A computational model for early events in B cell antigen receptor signaling: analysis of the roles of Lyn and Fyn. J Immunol 189: 646–658.

79. Lipniacki T, Hat B, Faeder JR, Hlavacek WS (2008) Stochastic effects and bistability in T cell receptor signaling. J Theor Biol 254: 110–122.

80. Raj A, Peskin CS, Tranchina D, Vargas DY, Tyagi S (2006) Stochastic mRNA synthesis in mammalian cells. PLoS Biol 4: e309.

81. Haseltine EL, Rawlings JB (2005) On the origins of approximations for stochastic chemical kinetics. J Chem Phys 123: 164115.

82. Werner SL, Barken D, Hoffmann A (2005) Stimulus specificity of gene expression programs determined by temporal control of IKK activity. Science 309: 1857–1861.

83. Werner SL, Kearns JD, Zadorozhnaya V, Lynch C, O'Dea E, et al. (2008) Encoding NF-κB temporal control in response to TNF: distinct roles for the negative regulators IκBα and A20. Genes Dev 22: 2093–2101.

84. McDonnell MD, Abbott D (2009) What is stochastic resonance? Definitions, misconceptions, debates, and its relevance to biology. PLoS Comput Biol 5: e1000348.

85. Vodovotz Y, Csete M, Bartels J, Chang S, An G (2008) Translational systems biology of inflammation. PLoS Comput Biol 4: e1000014.

86. Hymowitz SG, Wertz IE (2010) A20: from ubiquitin editing to tumour suppression. Nat Rev Cancer 10: 332–341.

87. Kato M, Sanada M, Kato I, Sato Y, Takita J, et al. (2009) Frequent inactivation of A20 in B-cell lymphomas. Nature 459: 712–716.

88. Dong G, Chanudet E, Zeng N, Appert A, Chen YW, et al. (2011) A20, ABIN-1/2, and CARD11 mutations and their prognostic value in gastrointestinal diffuse large B-cell lymphoma. Clin Cancer Res 17: 1440–1451.

89. Huang HL, Yeh WC, Lai MZ, Mirtsos C, Chau H, et al. (2009) Impaired TNFα-induced A20 expression in E1A/Ras-transformed cells. Br J Cancer 101: 1555–1564.

90. Jackson-Bernitsas DG, Ichikawa H, Takada Y, Myers JN, Lin XL, et al. (2007) Evidence that TNF-TNFR1-TRADD-TRAF2-RIP-TAK1-IKK pathway mediates constitutive NF-κB activation and proliferation in human head and neck squamous cell carcinoma. Oncogene 26: 1385–1397.

91. Lisby S, Faurschou A, Gniadecki R (2007) The autocrine TNFα signalling loop in keratinocytes requires atypical PKC species and NF-κB activation but is independent of cholesterol-enriched membrane microdomains. Biochem Pharmacol 73: 526–533.

92. Bian X, Opipari AW, Ratanaproeksa AB, Boitano AE, Lucas PC, et al. (2002) Constitutively active nfκB is required for the survival of S-type neuroblastoma. J Biol Chem 277: 42144–42150.

93. Lombardo E, Alvarez-Barrientos A, Maroto B, Bosc L, Knaus UG (2007) TLR4-mediated survival of macrophages is MyD88 dependent and requires TNF-α autocrine signalling. J Immunol 178: 3731–3739.

94. Witsell AL, Schook LB (1992) Tumor necrosis factor alpha is an autocrine growth regulator during macrophage differentiation. Proc Natl Acad Sci USA 89: 4754–4758.

95. Parameswaran N, Patial S (2010) Tumor necrosis factor-α signaling in macrophages. Crit Rev Eukaryot Gene Expr 20: 87–103.

Spontaneous NF-κB Activation by Autocrine TNFα Signaling: A Computational Analysis

Jakub Pękalski, Pawel J. Zuk, Marek Kochańczyk,
Michael Junkin, Ryan Kellogg, Savaş Tay,
and Tomasz Lipniacki

Supporting Information

Supplementary Text S1 with Figures S1–S4

1 Parameters and reactions

Table — Notation guide

Symbol	Description
$TNFR_i$	inactive TNFR1 receptors
$TNFR_a$	active TNFR1 receptors
$IKKK_n$	neutral form of IKKK
$IKKK_a$	active form of IKKK
IKK_i	inactive form of IKK
IKK_{ii}	inactive intermediate form of IKK
IKK_n	neutral form of IKK kinase
IKK_a	active form of IKK
$A20_{mRNA}$	A20 transcript
$A20$	cytoplasmic A20
$I\kappa B\alpha_{mRNA}$	IκBα transcript
$I\kappa B\alpha$	cytoplasmic IκBα
$I\kappa B\alpha_n$	nuclear IκBα
$I\kappa B\alpha_p$	phosphorylated cytoplasmic IκBα
$NF\kappa B$	cytoplasmic NF-κB
$NF\kappa B_n$	nuclear NF-κB
$(NF\kappa B : I\kappa B\alpha)$	cytoplasmic NF-κB:IκBα complexes
$(NF\kappa B_n : I\kappa B\alpha_n)$	nuclear NF-κB:IκBα complexes
$(NF\kappa B : I\kappa B\alpha_p)$	phosphorylated cytoplasmic IκBα complexed to NF-κB
TNF_{mRNA}	TNFα transcript
TNF	intracellular TNFα
TNF_{ext}	extracellular TNFα
$G^i_{I\kappa B}$	state of the ith IκBα gene copy, discrete random variable: $G^i_{I\kappa B} \in \{0,1\}$
G^i_{A20}	state of the ith A20 gene copy, discrete random variable: $G^i_{A20} \in \{0,1\}$
G^i_{TNF}	state of the ith TNFα gene copy, discrete random variable: $G^i_{TNF} \in \{0,1\}$
$G_{I\kappa B}$	$G_{I\kappa B} := \sum_i G^i_{I\kappa B}$
G_{A20}	$G_{A20} := \sum_i G^i_{A20}$
G_{TNF}	$G_{TNF} := \sum_i G^i_{TNF}$

Table — The cell parameters

Parameter	Symbol	Value	Remarks	References
$(\text{N:C ratio})^{-1} = \frac{\text{Volume of the cytoplasm}}{\text{Volume of the nucleus}}$	k_{v}	5	—	[2]
Number of IκBα gene copies	N_{I}	2	—	[1]
Number of A20 gene copies	N_{A}	2	—	[1]
Number of TNFα gene copies	N_{T}	2	—	this study
Median number of receptors	M_0	7×10^3	*(see also Figure S1, page 7)*	this study
Mean number of receptors	—	$\simeq 10^4$	mean $= M_0\,\mathrm{e}^{M_1^2/2}$, $M_1 = \sqrt{0.7}$	this study
Variance of the number of receptors	—	$\simeq 10^8$	variance $= M_0^2\,(\mathrm{e}^{M_1^2} - 1)\,\mathrm{e}^{M_1^2}$	this study
Number of receptors	R	M_0	$R = \mathit{TNFR}_{\mathrm{a}}(t) + \mathit{TNFR}_{\mathrm{i}}(t)$	this study
Number of IKKK molecules	K_{N}	10^5	$K_{\mathrm{N}} = \mathit{IKKK}_{\mathrm{n}}(t) + \mathit{IKKK}_{\mathrm{a}}(t)$	[1]
Number of IKK molecules	K_{NN}	2×10^5	$K_{\mathrm{NN}} = \mathit{IKK}_{\mathrm{n}}(t) + \mathit{IKK}_{\mathrm{a}}(t) +$ $\mathit{IKK}_{\mathrm{i}}(t) + \mathit{IKK}_{\mathrm{ii}}(t)$	[2]
Number of NF-κB molecules	$\mathit{NF\kappa B}_{\mathrm{tot}}$	10^5	$\mathit{NF\kappa B}_{\mathrm{tot}} = \mathit{NF\kappa B}(t) +$ $\mathit{NF\kappa B}_{\mathrm{n}}(t) + (\mathit{NF\kappa B}\!:\!\mathit{I\kappa B\alpha})(t) +$ $(\mathit{NF\kappa B}_{\mathrm{n}}\!:\!\mathit{I\kappa B\alpha}_{\mathrm{n}})(t) + (\mathit{NF\kappa B}\!:\!\mathit{I\kappa B\alpha}_{\mathrm{p}})(t)$	[2]

(For references, see page 6.)

Table — List of reactions

(See on the next page.)

Reaction	Rate	Coefficients	Value	References
TNFR1 activation and signal transduction cascade				
$TNF_{\mathrm{ext}} \to \varnothing$	c_{deg}	c_{deg}	$2 \times 10^{-4}\ \mathrm{s}^{-1}$	[1]
$TNFR_{\mathrm{i}} \to TNFR_{\mathrm{a}}$	$k_{\mathrm{b}} \cdot TNF_{\mathrm{ext}}$	k_{b}	$1.2 \times 10^{-5}\ \mathrm{s}^{-1}(\mathrm{ng/ml})^{-1}$	[1]
$TNFR_{\mathrm{i}} + TNF \to TNFR_{\mathrm{a}}$	$\dfrac{c_{\mathrm{sec}}}{TNFR_{\mathrm{i}} + c_{\mathrm{b}}}$	c_{sec} c_{b}	$10^{-5}\ \mathrm{s}^{-1}$ 10^{4}	this study this study
$TNFR_{\mathrm{a}} \to TNFR_{\mathrm{i}}$	k_{f}	k_{f}	$1.2 \times 10^{-3}\ \mathrm{s}^{-1}$	[1]
$IKKK_{\mathrm{n}} \to IKKK_{\mathrm{a}}$	$\dfrac{k_{\mathrm{a}} \cdot k_{\mathrm{A20}}}{k_{\mathrm{A20}} + A20} \cdot TNFR_{\mathrm{a}}$	k_{a} k_{A20}	$10^{-5}\ \mathrm{s}^{-1}$ 10^{5}	this study [1]
$IKKK_{\mathrm{a}} \to IKKK_{\mathrm{n}}$	k_{i}	k_{i}	$10^{-2}\ \mathrm{s}^{-1}$	[1]
$IKK_{\mathrm{n}} \to IKK_{\mathrm{a}}$	$k_{1} \cdot IKKK_{\mathrm{a}}^{2}$	k_{1}	$6 \times 10^{-10}\ \mathrm{s}^{-1}$	[1]
$IKK_{\mathrm{a}} \to IKK_{\mathrm{i}}$	$\dfrac{k_{3}}{k_{2}} \cdot (k_{2} + A20)$	k_{2} k_{3}	$10^{4}\ \mathrm{s}^{-1}$ $2 \times 10^{-3}\ \mathrm{s}^{-1}$	[2] [1]
$IKK_{\mathrm{i}} \to IKK_{\mathrm{ii}}\ ,\ \ IKK_{\mathrm{ii}} \to IKK_{\mathrm{n}}$	k_{4}	k_{4}	$10^{-3}\ \mathrm{s}^{-1}$	[1]
IκBα, A20 and TNFα gene expression				
$(G^{i}_{\mathrm{A20}} = 0) \to (G^{i}_{\mathrm{A20}} = 1)$ $(G^{i}_{\mathrm{I\kappa B\alpha}} = 0) \to (G^{i}_{\mathrm{I\kappa B\alpha}} = 1)$	$q_{1} \cdot NF\kappa B_{\mathrm{n}}$	q_{1}	$4 \times 10^{-7}\ \mathrm{s}^{-1}$	[1]
$(G^{i}_{\mathrm{A20}} = 1) \to (G^{i}_{\mathrm{A20}} = 0)$ $(G^{i}_{\mathrm{I\kappa B\alpha}} = 1) \to (G^{i}_{\mathrm{I\kappa B\alpha}} = 0)$	$q_{2} \cdot I\kappa B\alpha_{\mathrm{n}}$	q_{2}	$10^{-6}\ \mathrm{s}^{-1}$	[2]
$(G^{i}_{\mathrm{TNF}} = 0) \to (G^{i}_{\mathrm{TNF}} = 1)$	$q_{\mathrm{1t}} \cdot NF\kappa B_{\mathrm{n}}$	q_{1t}	$4 \times 10^{-8}\ \mathrm{s}^{-1}$	this study
$(G^{i}_{\mathrm{TNF}} = 1) \to (G^{i}_{\mathrm{TNF}} = 0)$	$q_{\mathrm{2t}} \cdot I\kappa B\alpha_{\mathrm{n}}$	q_{2t}	$10^{-6}\ \mathrm{s}^{-1}$	this study
$(G^{i}_{\mathrm{TNF}} = 1) \to (G^{i}_{\mathrm{TNF}} = 0)$	q_{2tt}	q_{2tt}	$2 \times 10^{-3}\ \mathrm{s}^{-1}$	this study
$\varnothing \to TNF_{\mathrm{mRNA}}$	$\lambda \cdot G^{i}_{\mathrm{TNF}}$	λ	*variable*	this study
$\varnothing \to A20_{\mathrm{mRNA}}$	$c_{1} \cdot G^{i}_{\mathrm{A20}}$	c_{1}	$0.1\ \mathrm{s}^{-1}$	[2]
$A20_{\mathrm{mRNA}} \to \varnothing$	c_{3}	c_{3}	$7.5 \times 10^{-4}\ \mathrm{s}^{-1}$	[2]
$\varnothing \to A20$	$c_{4} \cdot A20_{\mathrm{mRNA}}$	c_{4}	$0.5\ \mathrm{s}^{-1}$	[2]
$\varnothing \to I\kappa B\alpha_{\mathrm{mRNA}}$	$c_{1} \cdot G^{i}_{\mathrm{I\kappa B\alpha}}$	c_{1}	$0.1\ \mathrm{s}^{-1}$	[2]
$I\kappa B\alpha_{\mathrm{mRNA}} \to \varnothing$	c_{3}	c_{3}	$7.5 \times 10^{-4}\ \mathrm{s}^{-1}$	[2]
$\varnothing \to I\kappa B\alpha$	$c_{4} \cdot I\kappa B\alpha_{\mathrm{mRNA}}$	c_{4}	$0.5\ \mathrm{s}^{-1}$	[2]
$TNF_{\mathrm{mRNA}} \to \varnothing$	c_{3t}	c_{3t}	$7.5 \times 10^{-4}\ \mathrm{s}^{-1}$	this study
$\varnothing \to TNF$	$c_{\mathrm{4t}} \cdot TNF_{\mathrm{mRNA}}$	c_{4t}	$0.05\ \mathrm{s}^{-1}$	this study
Protein interactions and lifetime				
$NF\kappa B + I\kappa B\alpha \to (NF\kappa B : I\kappa B\alpha)$ $NF\kappa B_{\mathrm{n}} + I\kappa B\alpha_{\mathrm{n}} \to (NF\kappa B_{\mathrm{n}} : I\kappa B\alpha_{\mathrm{n}})$	a_{1} $a_{1} \cdot k_{\mathrm{v}}$	a_{1} k_{v}	$5 \times 10^{-7}\ \mathrm{s}^{-1}$ 5	[2] [2]
$I\kappa B\alpha \to I\kappa B\alpha_{\mathrm{p}}$	$a_{2} \cdot IKK_{\mathrm{a}}$	a_{2}	$10^{-7}\ \mathrm{s}^{-1}$	[2]
$(NF\kappa B : I\kappa B\alpha) \to (NF\kappa B : I\kappa B\alpha_{\mathrm{p}})$	$a_{3} \cdot IKK_{\mathrm{a}}$	a_{3}	$5 \times 10^{-7}\ \mathrm{s}^{-1}$	[2]
$A20 \to \varnothing$	c_{5}	c_{5}	$5 \times 10^{-4}\ \mathrm{s}^{-1}$	[2]
$I\kappa B\alpha_{\mathrm{p}} \to \varnothing$ $(NF\kappa B : I\kappa B\alpha_{\mathrm{p}}) \to NF\kappa B$	t_{p}	t_{p}	$10^{-2}\ \mathrm{s}^{-1}$	[2]
$I\kappa B\alpha \to \varnothing$	c_{5a}	c_{5a}	$10^{-4}\ \mathrm{s}^{-1}$	[2]
$TNF \to \varnothing$	$c_{\mathrm{sec}} + c_{\mathrm{5t}}$	c_{sec} c_{5t}	$10^{-5}\ \mathrm{s}^{-1}$ $2 \times 10^{-4}\ \mathrm{s}^{-1}$	this study this study
$(NF\kappa B : I\kappa B\alpha) \to NF\kappa B$	c_{6a}	c_{6a}	$2 \times 10^{-5}\ \mathrm{s}^{-1}$	[2]
Transport				
$NF\kappa B \to NF\kappa B_{\mathrm{n}}$	i_{1}	i_{1}	$10^{-2}\ \mathrm{s}^{-1}$	[2]
$(NF\kappa B_{\mathrm{n}} : I\kappa B\alpha_{\mathrm{n}}) \to (NF\kappa B : I\kappa B\alpha)$	e_{2a}	e_{2a}	$5 \times 10^{-2}\ \mathrm{s}^{-1}$	[2]
$I\kappa B\alpha \to I\kappa B\alpha_{\mathrm{n}}$	i_{1a}	i_{1a}	$2 \times 10^{-3}\ \mathrm{s}^{-1}$	[2]
$I\kappa B\alpha_{\mathrm{n}} \to I\kappa B\alpha$	e_{1a}	e_{1a}	$5 \times 10^{-3}\ \mathrm{s}^{-1}$	[2]

2 Differential equations

$$\frac{\mathrm{d}}{\mathrm{d}t}TNFR_\mathrm{a}(t) = TNF(t) \cdot c_\mathrm{sec} \frac{TNFR_\mathrm{i}(t)}{TNFR_\mathrm{i}(t) + c_\mathrm{b}} + k_\mathrm{b} \cdot TNF_\mathrm{ext}(t) \cdot TNFR_\mathrm{i}(t) - k_\mathrm{f} \cdot TNFR_\mathrm{a}(t) \tag{1}$$

$$\frac{\mathrm{d}}{\mathrm{d}t}IKKK_\mathrm{a}(t) = k_\mathrm{a} \cdot \frac{k_\mathrm{A20}}{k_\mathrm{A20} + A20(t)} \cdot TNFR_\mathrm{a}(t) \cdot IKKK_\mathrm{n}(t) - k_\mathrm{i} \cdot IKKK_\mathrm{a}(t) \tag{2}$$

$$\frac{\mathrm{d}}{\mathrm{d}t}IKK_\mathrm{a}(t) = k_1 \cdot IKKK_\mathrm{a}(t)^2 \cdot IKK_\mathrm{n}(t) - IKK_\mathrm{a}(t) \cdot \frac{k_3}{k_2}(k_2 + A20(t)) \tag{3}$$

$$\frac{\mathrm{d}}{\mathrm{d}t}IKK_\mathrm{n}(t) = -k_1 \cdot IKKK_\mathrm{a}(t)^2 \cdot IKK_\mathrm{n}(t) + k_4 \cdot IKK_\mathrm{ii}(t) \tag{4}$$

$$\frac{\mathrm{d}}{\mathrm{d}t}IKK_\mathrm{i}(t) = IKK_\mathrm{a}(t) \cdot \frac{k_3}{k_2}(k_2 + A20(t)) - k_4 \cdot IKK_\mathrm{i}(t) \tag{5}$$

$$\frac{\mathrm{d}}{\mathrm{d}t}A20_\mathrm{mRNA}(t) = c_1 \cdot G_\mathrm{A20}(t) - c_3 \cdot A20_\mathrm{mRNA}(t) \tag{6}$$

$$\frac{\mathrm{d}}{\mathrm{d}t}A20(t) = c_4 \cdot A20_\mathrm{mRNA}(t) - c_5 \cdot A20(t) \tag{7}$$

$$\frac{\mathrm{d}}{\mathrm{d}t}I\kappa B\alpha_\mathrm{mRNA}(t) = c_1 \cdot G_\mathrm{I\kappa B\alpha}(t) - c_3 \cdot I\kappa B\alpha_\mathrm{mRNA}(t) \tag{8}$$

$$\frac{\mathrm{d}}{\mathrm{d}t}I\kappa B\alpha(t) = -a_2 \cdot IKK_\mathrm{a}(t) \cdot I\kappa B\alpha(t) - a_1 \cdot I\kappa B\alpha(t) \cdot NF\kappa B(t) + c_4 \cdot I\kappa B\alpha_\mathrm{mRNA}(t) \\ -c_\mathrm{5a} \cdot I\kappa B\alpha(t) - i_\mathrm{1a} \cdot I\kappa B\alpha(t) + e_\mathrm{1a} \cdot I\kappa B\alpha_\mathrm{n}(t) \tag{9}$$

$$\frac{\mathrm{d}}{\mathrm{d}t}I\kappa B\alpha_\mathrm{n}(t) = -a_1 \cdot k_\mathrm{v} \cdot I\kappa B_\mathrm{n}(t) \cdot NF\kappa B_\mathrm{n}(t) + i_\mathrm{1a} \cdot I\kappa B\alpha(t) - e_\mathrm{1a} \cdot I\kappa B\alpha_\mathrm{n}(t) \tag{10}$$

$$\frac{\mathrm{d}}{\mathrm{d}t}I\kappa B\alpha_\mathrm{p}(t) = a_2 \cdot IKK_\mathrm{a}(t) \cdot I\kappa B\alpha(t) - t_\mathrm{p} \cdot I\kappa B\alpha_\mathrm{p}(t) \tag{11}$$

$$\frac{\mathrm{d}}{\mathrm{d}t}NF\kappa B(t) = c_\mathrm{6a} \cdot (NF\kappa B : I\kappa B\alpha)(t) - a_1 \cdot NF\kappa B(t) \cdot I\kappa B\alpha(t) \\ +t_\mathrm{p} \cdot (NF\kappa B : I\kappa B\alpha_\mathrm{p})(t) - i_1 \cdot NF\kappa B(t) \tag{12}$$

$$\frac{\mathrm{d}}{\mathrm{d}t}NF\kappa B_\mathrm{n}(t) = i_1 \cdot NF\kappa B(t) - a_1 \cdot k_\mathrm{v} \cdot I\kappa B\alpha_\mathrm{n}(t) \cdot NF\kappa B_\mathrm{n}(t) \tag{13}$$

$$\frac{\mathrm{d}}{\mathrm{d}t}(NF\kappa B : I\kappa B\alpha)(t) = a_1 \cdot I\kappa B\alpha(t) \cdot NF\kappa B(t) - c_\mathrm{6a} \cdot (NF\kappa B : I\kappa B\alpha)(t) \\ +e_\mathrm{2a} \cdot (NF\kappa B_\mathrm{n} : I\kappa B\alpha_\mathrm{n})(t) - a_3 \cdot IKK_\mathrm{a} \cdot (NF\kappa B : I\kappa B\alpha)(t) \tag{14}$$

$$\frac{\mathrm{d}}{\mathrm{d}t}(NF\kappa B : I\kappa B\alpha_\mathrm{p})(t) = a_3 \cdot IKK_\mathrm{a}(t) \cdot (NF\kappa B : I\kappa B\alpha)(t) - t_\mathrm{p} \cdot (NF\kappa B : I\kappa B\alpha_\mathrm{p})(t) \tag{15}$$

$$\frac{\mathrm{d}}{\mathrm{d}t}TNF_\mathrm{mRNA}(t) = \lambda \cdot G_\mathrm{TNF}(t) - c_\mathrm{3t} \cdot TNF_\mathrm{mRNA}(t) \tag{16}$$

$$\frac{\mathrm{d}}{\mathrm{d}t}TNF(t) = c_\mathrm{4t} \cdot TNF_\mathrm{mRNA}(t) - c_\mathrm{5t} \cdot TNF(t) - c_\mathrm{sec} \cdot TNF \tag{17}$$

$$\frac{\mathrm{d}}{\mathrm{d}t}TNF_\mathrm{ext}(t) = -c_\mathrm{deg} \cdot TNF_\mathrm{ext} \tag{18}$$

$$\frac{\mathrm{d}}{\mathrm{d}t}G_\mathrm{A20}(t) = q_1 \cdot NF\kappa B_\mathrm{n}(t) \cdot (N_\mathrm{A} - G_\mathrm{A20}(t)) - q_2 \cdot I\kappa B\alpha_\mathrm{n}(t) \cdot G_\mathrm{A20}(t) \tag{19}$$

$$\frac{\mathrm{d}}{\mathrm{d}t}G_\mathrm{I\kappa B\alpha}(t) = q_1 \cdot NF\kappa B_\mathrm{n}(t) \cdot (N_\mathrm{I} - G_\mathrm{I\kappa B\alpha}(t)) - q_2 \cdot I\kappa B\alpha_\mathrm{n}(t) \cdot G_\mathrm{I\kappa B\alpha}(t) \tag{20}$$

$$\frac{\mathrm{d}}{\mathrm{d}t}G_\mathrm{TNF}(t) = q_\mathrm{1t} \cdot NF\kappa B_\mathrm{n}(t) \cdot (N_\mathrm{T} - G_\mathrm{TNF}(t)) - (q_\mathrm{2tt} + q_\mathrm{2t} \cdot I\kappa B\alpha_\mathrm{n}(t)) \cdot G_\mathrm{TNF}(t) \tag{21}$$

. . . .

$$\frac{\mathrm{d}}{\mathrm{d}t}TNFR_\mathrm{i}(t) = -TNF(t) \cdot c_\mathrm{sec} \frac{TNFR_\mathrm{i}(t)}{TNFR_\mathrm{i}(t) + c_\mathrm{b}} - k_\mathrm{b} \cdot TNF_\mathrm{ext}(t) \cdot TNFR_\mathrm{i}(t) + k_\mathrm{f} \cdot TNFR_\mathrm{a}(t) \tag{22}$$

$$\frac{\mathrm{d}}{\mathrm{d}t}IKKK_\mathrm{n}(t) = -k_\mathrm{a} \cdot \frac{k_\mathrm{A20}}{k_\mathrm{A20} + A20(t)} \cdot TNFR_\mathrm{a}(t) \cdot IKKK_\mathrm{n}(t) + k_\mathrm{i} \cdot IKKK_\mathrm{a}(t) \tag{23}$$

$$\frac{\mathrm{d}}{\mathrm{d}t}IKK_\mathrm{ii}(t) = k_4 \cdot IKK_\mathrm{i}(t) - k_4 \cdot IKK_\mathrm{ii}(t) \tag{24}$$

$$\frac{\mathrm{d}}{\mathrm{d}t}(NF\kappa B_\mathrm{n} : I\kappa B\alpha_\mathrm{n})(t) = a_1 \cdot k_\mathrm{v} \cdot I\kappa B\alpha_\mathrm{n}(t) \cdot NF\kappa B_\mathrm{n}(t) - e_\mathrm{2a} \cdot (NF\kappa B_\mathrm{n} : I\kappa B\alpha_\mathrm{n})(t) \tag{25}$$

4

The last four variables from equations (22–25) can be determined equivalently by the following conservation laws:

$$TNFR_i(t) = R - TNFR_a(t) \tag{26}$$

$$IKKK_n(t) = K_N - IKKK_a(t) \tag{27}$$

$$IKK_{ii}(t) = K_{NN} - IKK_a(t) - IKK_i(t) - IKK_n(t) \tag{28}$$

$$(NF\kappa B_n : I\kappa B\alpha_n)(t) = NF\kappa B_{tot} - NF\kappa B(t) - NF\kappa B_n(t) - (NF\kappa B : I\kappa B\alpha)(t) - (NF\kappa B : I\kappa B\alpha_p)(t) \tag{29}$$

The complete system (1–25) is however more convenient for further development of the model.

3 Methods and protocols of numerical simulations

Deterministic model

The model was coded both in MATLAB and BIONETGEN. BIONETGEN is a language and software intended for defining and simulating regulatory networks of high combinatorial complexity [3], and is capable of performing deterministic as well as stochastic simulations. BIONETGEN allows for rule-based specification of the model; the rules are then used to build a list of reactions or ODEs which are solved by an integrated CVODE solver or simulated according to the Gillespie direct Stochastic Simulation Algorithm [4]. The model was originally written in MATLAB and then rewritten to BIONETGEN only to enable efficient stochastic simulations. Since the BIONETGEN code results from the exact translation of the original MATLAB code, the number of rules is equal to the number of reactions.

The bifurcation diagrams with TNFα transcription rate λ as the bifurcation parameter (Figs. 3 and 4 in the main text and Supplementary Figs. S2 and S3) were obtained using the MATCONT continuation software. In order to perform the analysis, we used ODEs (1–21) in which variables $TNFR_i$, $IKKK_n$, IKK_{ii} and $(NF\kappa B_n : I\kappa B\alpha_n)$ were defined by algebraic equations (26–29).

The simulations of WT and A20$^{-/-}$ cells showed in Figs. 5, 7 and 9 (in the main text) were started from the steady state corresponding to the extracellular TNFα concentration equal zero. A20$^{-/-}$ cells were modeled by setting the number of A20 gene copies equal to zero. Numerical integration was performed using the MATLAB's implementation of the TR-BDF2 method (solver `ode23tb`).

Stochastic model

The stochastic simulations were performed using the Gillespie direct Stochastic Simulation Algorithm [4]. The direct method of stochastic simulation as implemented in BIONETGEN allows for expressing reaction rates through functions of the system state, i.e. current number of molecules of given species. At every time step between consecutive reaction events, reaction propensities calculated using such functions remain constant. This enables exact simulation in accordance with the underlying Chemical Master Equation and at the same time allows for defining propensities not necessarily following the mass action kinetics.

To ensure random initial conditions at time $t = 0$, each stochastic simulation was started at time $t = -300$ h. The population average (Figs. 7 and 9 in the main text) was obtained based on 100 simulations. The fraction of responding cells (Fig. 6 in the main text) for each value of TNFα dose was obtained based on 500 simulations. For the purpose of analysis presented in Fig. 8 (in the main text), cells were considered activated when the fraction of nuclear NF-κB increased above 0.15, which allows for almost maximum expression of IκBα and A20 genes.

4   Experimental protocols

Gene expression analysis was performed on mouse 3T3 fibroblast cells using high-throughput microfluidic qPCR and digital-PCR. Cells grown on regular culture wells at equal density (80% confluence) were stimulated with various doses of TNFα at the beginning of experiments (10, 1, 0.1, 0.05, 0.025 and 0.01 ng/ml). At the end of each experiment ($t = 0.25$, 0.5, 2, 4, 6, 8, 10 and 12 hours), cells were lysed and cDNA was synthesized using standard protocols from Invitrogen (CellsDirect One-Step RT-PCR). Real-time qPCR was performed using the Invitrogen TaqMan probe for TNFα using the 48×48 Dynamic Array microfluidic chips and the Biomark System, both from Fluidigm. Each time and dose condition was repeated four times and the median value was used in Figure 2A (in the main text), resulting in a total of 192 qPCR measurements.

ELISpot experiments were carried out in a 96-well format according to manufacturer's instructions (R&D Systems ELISpot Kit EL410). NIH 3T3 fibroblast and 264.7 RAW macrophage cells were seeded onto plates at $\approx 2 \times 10^5$ cells/ml. The total number of cells added into each well was established via cell counting during seeding. After incubating cells for five hours, the assay was completed. Spots were manually counted from images taken with a Nikon SMZ 1500 microscope, without regard to intensity level of the spot. This allows for quantifying the percentage of cells which have secreted the cytokine over the course of the experiment.

Supplementary references

[1] Tay S, Hughey J, Lee T, Lipniacki T, Covert M, Quake M (2010) Single-cell NF-κB dynamics reveal digital activation and analogue information processing. *Nature* **466**:267–271.

[2] Lipniacki T, Puszynski T, Paszek P, Brasier AR, Kimmel M (2007) Single TNFα trimers mediating NF-κB activation: Stochastic robustness of NF-κB signaling. *BMC Bioinformatics* **8**:376.

[3] Faeder JR, Blinov ML, Hlavacek WS (2009) Rule-based modeling of biochemical systems with BioNet-Gen. *Methods Mol. Biol.* **500**:113–167.

[4] Gillespie DT (1977) Exact stochastic simulations of coupled chemical reactions. *J. Phys. Chem.* **81**:2340–2361.

5 Supplementary figures
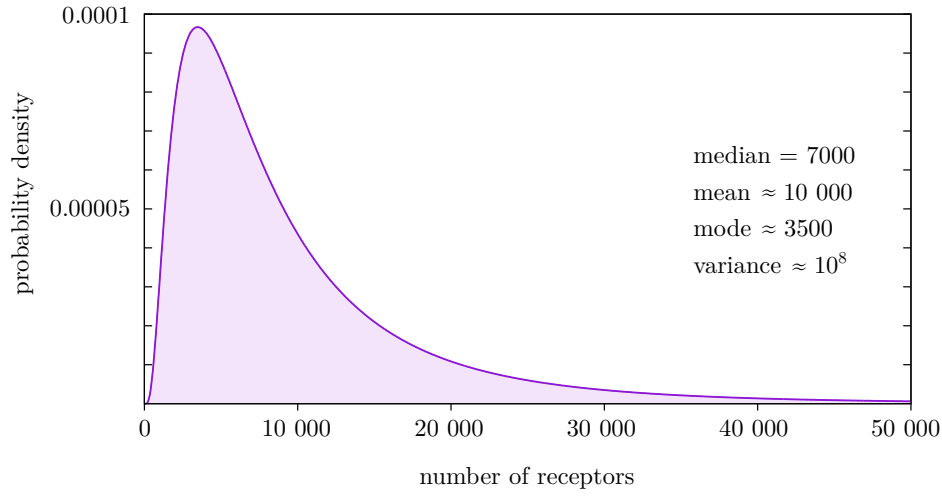
Supplementary Figure S1. The log-normal distribution of the number of TNFR1 receptors.
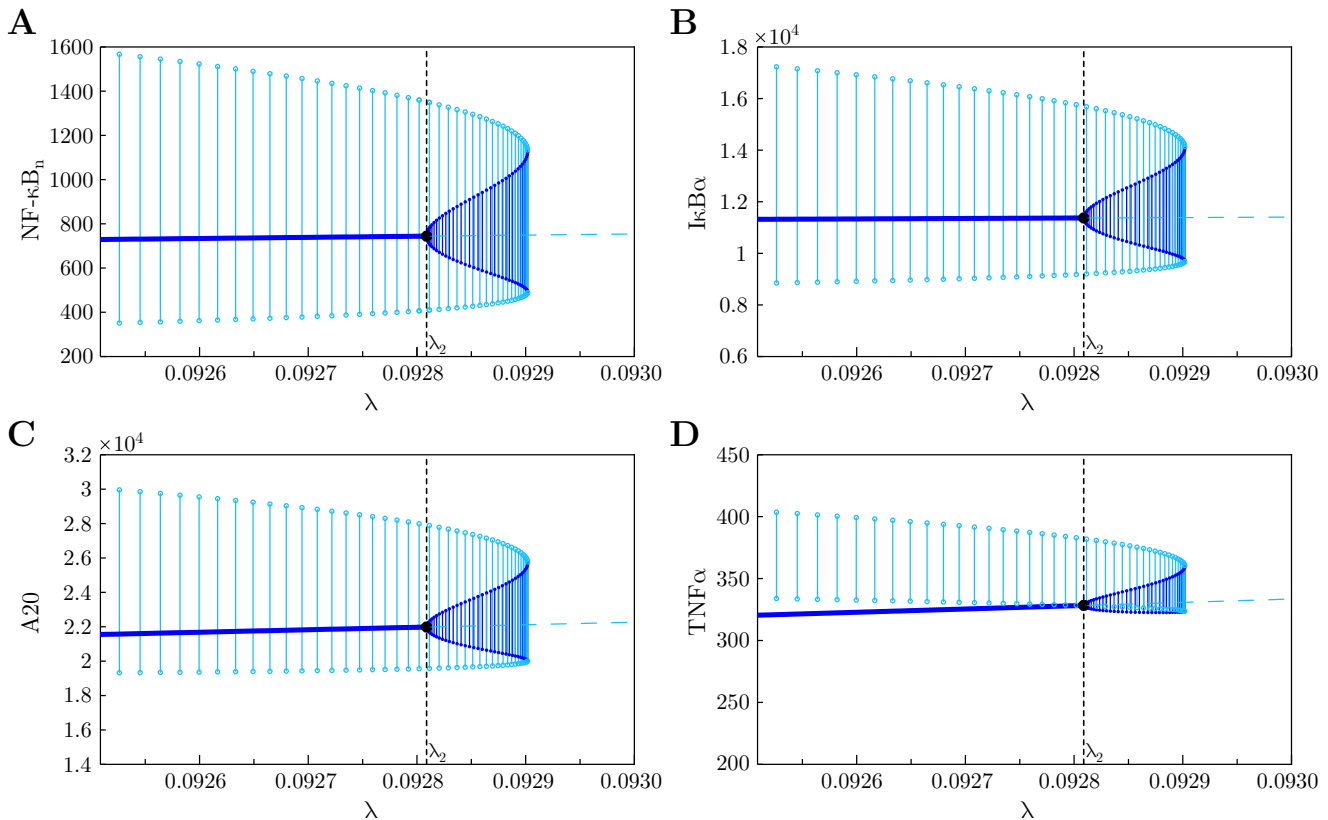
Supplementary Figure S2. Bifurcation diagrams: close-up of the Hopf bifurcation point in λ_2.
Stable steady state – thick dark blue line; unstable steady state – dashed light blue line;
stable limit cycle – filled dots connected by vertical dark blue lines;
unstable limit cycle – small circles connected by vertical light blue lines.

7
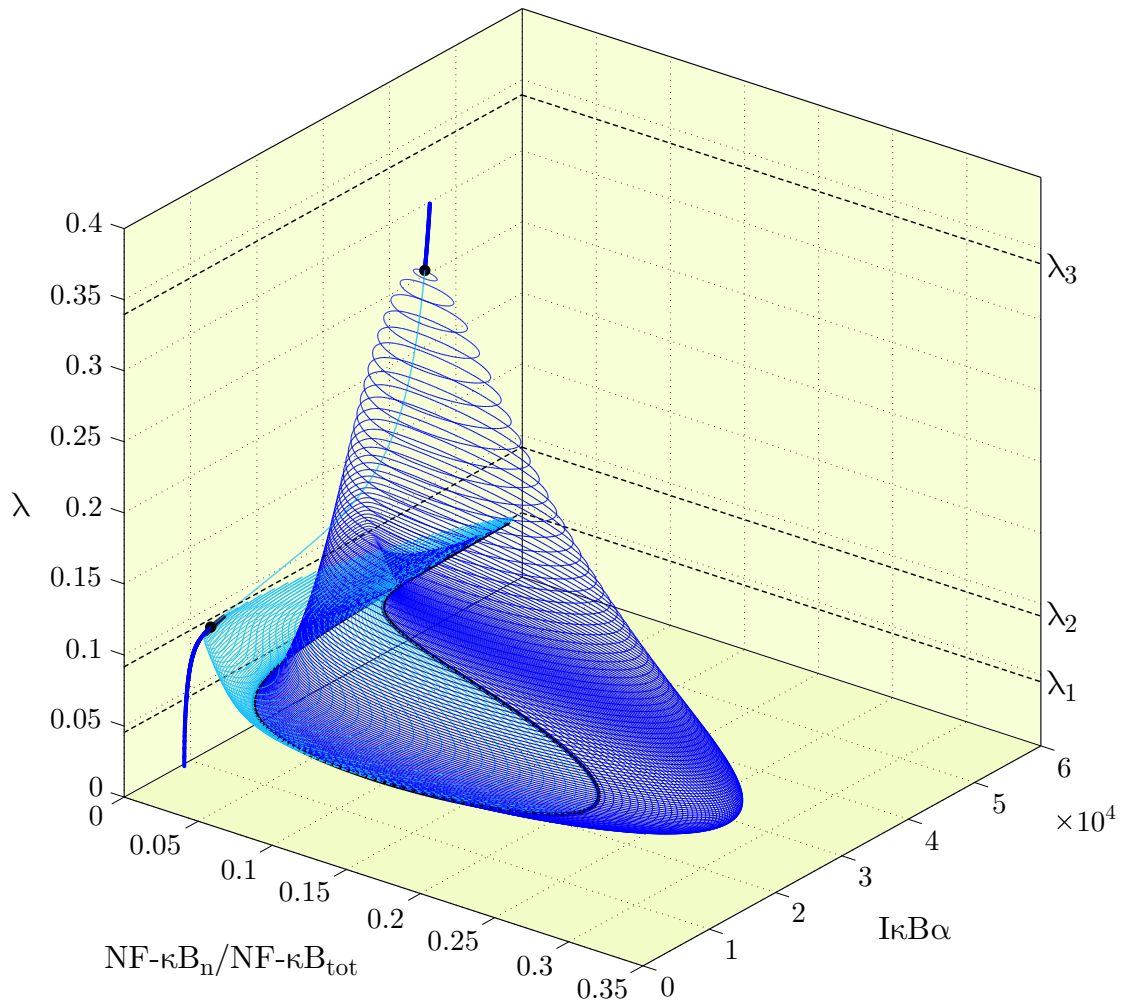
Supplementary Figure S3. Bifurcation diagram for wild-type cells.
Stable recurrent states – dark blue, unstable recurrent states – light blue.
Cyclic fold at λ_1 and bifurcation points at λ_2, λ_3 – black.

A

B

C
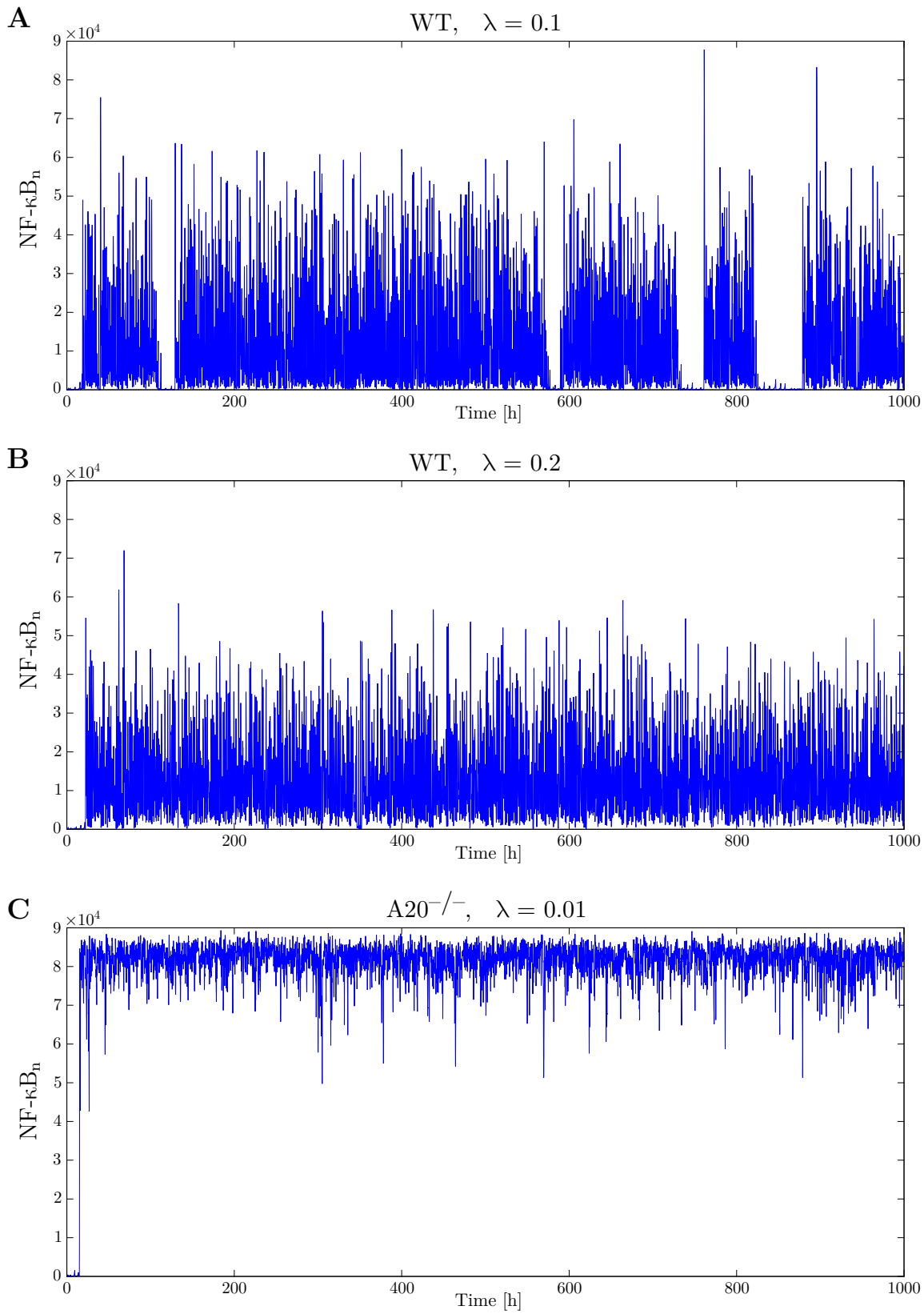
Supplementary Figure S4. Long run stochastic trajectories for wild type (WT) cells for (A) $\lambda = 0.1$, (B) $\lambda = 0.2$, and (C) for A20-deficient ($A20^{-/-}$) cells for $\lambda = 0.01$.

PLOS | COMPUTATIONAL BIOLOGY

RESEARCH ARTICLE

Feedbacks, Bifurcations, and Cell Fate Decision-Making in the p53 System

Beata Hat[1☯], Marek Kochańczyk[1☯], Marta N. Bogdał[1], Tomasz Lipniacki[1,2]*

1 Institute of Fundamental Technological Research, Polish Academy of Sciences, Warsaw, Poland,
2 Department of Statistics, Rice University, Houston, Texas, United States of America

☯ These authors contributed equally to this work.
* tlipnia@ippt.pan.pl

🔓 OPEN ACCESS

Abstract

The p53 transcription factor is a regulator of key cellular processes including DNA repair, cell cycle arrest, and apoptosis. In this theoretical study, we investigate how the complex circuitry of the p53 network allows for stochastic yet unambiguous cell fate decision-making. The proposed Markov chain model consists of the regulatory core and two subordinated bistable modules responsible for cell cycle arrest and apoptosis. The regulatory core is controlled by two negative feedback loops (regulated by Mdm2 and Wip1) responsible for oscillations, and two antagonistic positive feedback loops (regulated by phosphatases Wip1 and PTEN) responsible for bistability. By means of bifurcation analysis of the deterministic approximation we capture the recurrent solutions (i.e., steady states and limit cycles) that delineate temporal responses of the stochastic system. Direct switching from the limit-cycle oscillations to the "apoptotic" steady state is enabled by the existence of a subcritical Neimark—Sacker bifurcation in which the limit cycle loses its stability by merging with an unstable invariant torus. Our analysis provides an explanation why cancer cell lines known to have vastly diverse expression levels of Wip1 and PTEN exhibit a broad spectrum of responses to DNA damage: from a fast transition to a high level of p53 killer (a p53 phosphoform which promotes commitment to apoptosis) in cells characterized by high PTEN and low Wip1 levels to long-lasting p53 level oscillations in cells having PTEN promoter methylated (as in, e.g., MCF-7 cell line).

Author Summary

Cancers are diseases of signaling networks. Transcription factor p53 is a pivotal node of a network that integrates a variety of stress signals and governs critical processes of DNA repair, cell cycle arrest, and apoptosis. Somewhat paradoxically, despite the fact that carcinogenesis is prevalently caused by p53 network malfunction, most of our knowledge about p53 signaling is based on cancer or immortalized cell lines. In this paper, we construct a mathematical model of intact p53 network to understand dynamics of non-cancerous cells and then dynamics of cancerous cells by introducing perturbations to the regulatory system. Cell fate decisions are enabled by the presence of interlinked feedback loops which

give rise to a rich repertoire of behaviors. We explain and analyze by means of numerical simulations how the dynamical structure of the regulatory system allows for generating unambiguous single-cell fate decisions, also in the case when the cell population splits into an apoptotic and a surviving subpopulation. Perturbation analysis provides an explanation why cancer cell lines known to have vastly diverse expression levels of p53 regulators can exhibit a broad spectrum of responses to DNA damage.

Introduction

The tumor suppressor p53 plays a pivotal role in cell growth control, DNA repair, cell cycle suppression and eventually in the initiation of apoptosis [1–4]. It serves as a node of a complex and extensive gene regulatory network that integrates a variety of stress signals. One of the most important ways of p53 activation is through DNA damage, which can be caused by, i.a., ionizing radiation (IR), UV radiation, hypoxia, heat shock, viral infection, or nutrient deprivation [1,5,6]. Exposure to IR inflicts DNA double strand breaks (DSBs), the most critical DNA lesions, which when unrepaired can lead to genomic instability resulting in either cell death or DNA mutations that can propagate to subsequent cell generations [7–9]. The p53 regulatory network provides mechanisms that suppress cell cycle until DNA is repaired or trigger apoptosis when DNA damage is too extensive to be repaired [4,7,10].

Unsurprisingly, mutations of the p53 gene (*TP53*) turn out to be the most frequent genetic changes in human cancers [11]. About half of all human cancer cells carry a mutation in *TP53*. In many other cancers, the genes which encode components of the p53 regulatory pathway are mutated [12,13]. The lack of functional p53 protein decreases the efficiency of DNA repair and allows mutated cells to evade apoptosis leading to the propagation of mutations and eventually to cancer development and progression [13,14]. Various malfunctions of the p53 regulatory pathway are determinants of tumor aggressiveness and p53 pathway components have become targets in anticancer therapies [14,15].

The primary molecular function of p53 is the regulation of transcription [16,17]. It controls expression of numerous genes which encode proteins of contradictory roles: pro-survival, cell cycle-suppressing, or pro-apoptotic [17]. Its ability to regulate expression of distinct sets of genes is controlled by posttranslational modifications [5]. In particular, p53 can assume two different phosphorylation states: $p53_{ARRESTER}$ (when it is phosphorylated at Ser15 and Ser20 [5,18,19]) and $p53_{KILLER}$ (when it is additionally phosphorylated at Ser46 [20,21]). In the arrester state, p53 triggers transcription of its main inhibitor, E3 ubiquitin ligase Mdm2 [22], cell cycle-suppressing protein p21 [23], and pro-survival phosphatase Wip1 [24,25]. In the killer state, p53 triggers transcription of pro-apoptotic phosphatase PTEN [26] and another pro-apoptotic protein, Bax [27].

In unstressed cells p53 remains inactive and is kept at a low level through constant proteasome-mediated degradation, regulated by Mdm2 [28–30]. p53 is activated by kinase ATM, which is rapidly phosphorylated in response to DNA damage [31,32]. The DNA damage detection system is sensitive; a handful of DSBs is sufficient for ATM and p53 activation; 1 Gy of irradiation induces about 35–40 DSBs [8,33]. ATM phosphorylates p53 at several residues, including Ser15 and Ser20, leading to its stabilization and activation as a transcription factor [19,34,35]. ATM phosphorylates also p53 inhibitor, Mdm2, promoting its degradation [36]. As a result, p53 concentration increases 3–10-fold within an hour after DNA damage [34]. Activity of p53 can be suppressed by growth factor stimulation leading to the activation of PI3 kinase (PI3K), which phosphorylates phosphatidylinositol bisphosphate (PIP2) into trisphosphate

(PIP3) [37–40]. PIP3 allows for Akt recruitment to the plasma membrane where it can be activated via phosphorylation [41,42] by several kinases. Activated Akt phosphorylates Mdm2 at Ser166 and Ser186, allowing for its translocation to the nucleus where Mdm2 ubiquitinates p53 priming it for degradation [29,43].

The p53-regulated proteins comprise a complex regulatory network governed by multiple intertwined feedback loops spanning diverse time scales [44]. In addition to the primary p53 inhibitor, Mdm2, other key regulatory players in the network are two phosphatases: pro-survival Wip1 [24] and pro-apoptotic PTEN [26]. Wip1 attenuates signaling by dephosphorylating ATM [45] and inhibits apoptosis by facilitating dephosphorylation of p53$_{KILLER}$ to the p53$_{ARRESTER}$ form [46]. When DNA repair is accomplished, Wip1 enables the return to the pre-stress state [24,47]. PTEN mediates a positive feedback loop by inhibiting Akt and Mdm2, and by allowing p53$_{KILLER}$ to rise to a high level and initiate apoptosis [48].

Dysregulation of the p53 pathway can occur as a consequence of gene amplification, gene loss, promoter methylation, or mutations which alter protein function. Gene amplification or inhibition are the major mechanisms which enhance expression of genes involved in cancer development and progression [49]. In particular, Wip1 amplification and overexpression have been found in multiple human cancers, predominantly in those that retain functional p53 [50–53] such as breast, lung, pancreas, bladder, and liver cancer, and in neuroblastomas [50,52,54,55]. Conversely, Wip1-knockout mice are partially resistant to oncogene-induced cancer development, indicating that the inhibition of Wip1 activity may be potentially beneficial for cancer therapy [45,52,56,57]. Decreased PTEN expression has been found in prostate, kidney, breast, bladder cancers, and in glioblastoma [58–60]. Cell lines with defective PTEN have alterations in the cell cycle regulation and a defective apoptotic response, which places PTEN among the tumor suppressors most commonly lost in human cancers. In contrast, over-expression of wild-type PTEN in cancer cells induces apoptosis and blocks cell-cycle progression [61,62]. Another dysregulated protein observed in many cancers is PI3K. The amplification of PI3K gene have been found in colorectal, gastric, hepatocellular, thyroid, breast, lung, and ovarian cancer, and in glioblastoma and acute leukemia [63–70].

The clinical data shows that differences between cancer cells can be partially explained by different expression levels of PTEN, Wip1, and PI3K. The majority of breast cancers reveals amplification of Wip1 and reduced level of PTEN, which appear to correlate with poor prognosis as well as increased resistance to γ radiation-based therapy and apoptosis [55,58].

A number of computational models have been constructed to investigate the regulatory mechanisms of the p53 pathway. Earlier models were focused on explaining the origin of oscillations of p53 and Mdm2 levels in response to IR [71–76], which were first observed in the cell population experiment on MCF-7 cells by Bar-Or et al. [71] and later in single-cell experiments by Lahav et al. [77] and Geva-Zatorsky et al. [73]. Recently, the effort has been shifted to connecting p53 dynamics with cell fate decisions [75,78–85]. For the sake of conciseness of the Introduction, an overview of p53 modeling results cited in this paragraph is provided in S1 Text.

In this study, we focus on the p53 regulatory core to demonstrate that the structure of the p53 regulatory network is such that for a broad range of parameters at persistent DNA damage the limit cycle oscillations of p53$_{ARRESTER}$ (as well as p53$_{KILLER}$) coexist with the steady state characterized by a high level of p53$_{KILLER}$. The detailed bifurcation analysis shows that the direct switch between oscillations and high steady state is enabled by the existence of a Neimark—Sacker bifurcation. These two recurrent solutions delineate temporal responses of the system, which can be interpreted unambiguously by two slaved modules which control cell cycle arrest and apoptosis. This is confirmed by stochastic simulations of the model dynamics,

showing clear separation of cells into surviving and apoptotic subpopulations about 30 hours after DNA damage.

Results

Overview of the model structure

The proposed model consists of three modules: the core module, the cell cycle arrest module, and the apoptotic module. In Fig 1 we show a simplified scheme which summarizes the key feedback loops present in the core module. The detailed scheme with all model components is provided in S1 Fig. The regulatory pathway considered consists of 42 species (see Tables A and B in S1 Text), coupled by 74 reactions parametrized by 97 reaction rate coefficients (see Table C in S1 Text). The stochastic model is equivalent to a Markov process while its deterministic approximation is represented by ODEs. The levels of all substrates in stochastic as well as in deterministic simulations are expressed in the numbers of molecules per cell (mlcs/cell).

Core module. We consider the p53 system responses to DNA damage introduced by IR. DNA damage leads to the activation of ATM. Active ATM phosphorylates p53 inhibitor, Mdm2, priming it for faster degradation. It also stabilizes and activates p53 by phosphorylating it to one of its active phosphoforms, p53$_{ARRESTER}$. This phosphoform can be further phosphorylated (at Ser46) to the p53$_{KILLER}$ form. p53$_{ARRESTER}$ induces synthesis of Mdm2 and Wip1, a phosphatase which dephosphorylates ATM as well as p53$_{KILLER}$ to the p53$_{ARRESTER}$ form.

p53$_{KILLER}$ activates expression of another phosphatase, PTEN, which mediates the slow positive feedback loop which stabilizes the level of p53. PTEN indirectly suppresses Akt catalytic
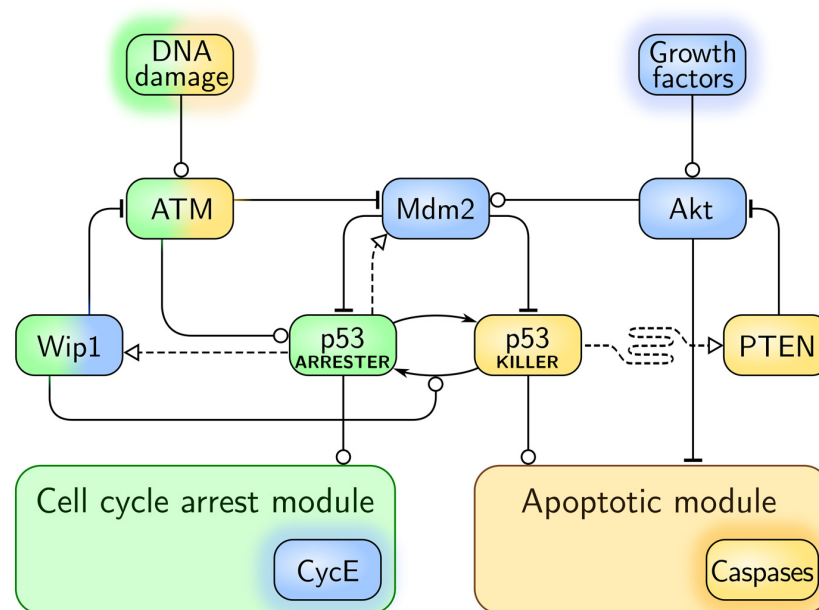
Fig 1. Simplified scheme of the model. Arrow-headed dashed lines indicate positive transcriptional regulation, arrow-headed solid lines—protein transformation, circle-headed solid lines—positive influence or activation, hammer-headed solid lines—inhibitory regulation. Pro-survival and cell cycle-promoting proteins are represented with blue boxes, pro-apoptotic proteins with yellow boxes, proteins involved in cell cycle arrest with green boxes. Details of the cell cycle arrest module and the apoptotic module are shown in Figs 2 and 3 respectively.

doi:10.1371/journal.pcbi.1004787.g001

activity, which is required to phosphorylate Mdm2 in order to enable its nuclear import. As a result, accumulation of PTEN leads to the accumulation of Mdm2 in cytoplasm and therefore physically disconnects nuclear p53 from its inhibitor, leading to the stabilization of $p53_{KILLER}$ and $p53_{ARRESTER}$ at high levels. PTEN action is opposed by the growth and survival factors which lead to Akt activation.

Cell cycle arrest module is controlled by $p53_{ARRESTER}$. This phosphoform activates transcription of p21 which suppresses cell cycle by inhibiting cyclin E (CycE). The apoptotic module is controlled by $p53_{KILLER}$, which activates transcription of pro-apoptotic protein Bax, and by Akt, which suppresses the apoptosis by phosphorylation of 14-3-3 protein.

Among more than ten feedbacks present in the system the following four are of key functional importance:

- **F1** Negative feedback $p53_{ARRESTER} \rightarrow$ Mdm2 –| p53: $p53_{ARRESTER}$ activates transcription of Mdm2 which ubiquitinates p53 inducing its rapid degradation. This feedback maintains homoeostasis in unstimulated cells and enables oscillations of p53 level upon DNA damage.

- **F2** Negative feedback ATM $\rightarrow p53_{ARRESTER} \rightarrow$ Wip1 –| ATM: ATM activates p53 to the $p53_{ARRESTER}$ form which activates transcription of Wip1, which in turn deactivates ATM. This feedback leads to recurrent ATM inhibition and initiation upon DNA damage enabling persistent oscillations of the p53 level.

- **F3** Positive feedback $p53_{ARRESTER} \rightarrow$ Wip1 $\rightarrow p53_{ARRESTER}$: $p53_{ARRESTER}$ activates transcription of Wip1, which dephosphorylates $p53_{KILLER}$ to $p53_{ARRESTER}$. This feedback stabilizes p53 in the arrester state and attenuates accumulation of $p53_{KILLER}$ preventing/postponing apoptosis.

- **F4** Positive feedback $p53_{KILLER} \rightarrow$ PTEN –| Akt $\rightarrow$ Mdm2 –| $p53_{KILLER}$: $p53_{KILLER}$ activates transcription of PTEN which (indirectly) deactivates Akt; Akt phosphorylates Mdm2 allowing for its import to the nucleus where Mdm2 ubiquitinates p53 inducing its rapid degradation. This feedback stabilizes the state of a high $p53_{KILLER}$ and low Akt activity, and thus induces apoptosis.

Two negative feedback loops, F1 and F2, associated with time delays introduced by the mRNA transcription, protein translation, and nuclear import, induce oscillatory responses upon DNA damage. As shown experimentally in [82] and demonstrated in analysis in S2 Fig the system without the negative feedback to ATM does not exhibit oscillations. The two positive feedbacks, F3 and F4, introduce bistability. These two feedbacks, mediated by Wip1 and PTEN phosphatases, act antagonistically. The Wip1-mediated loop (F3) prevents $p53_{KILLER}$ accumulation (by dephosphorylating $p53_{KILLER}$ to $p53_{ARRESTER}$) while the PTEN-mediated loop (F4) "supports" $p53_{KILLER}$ accumulation (by indirect inhibition of Mdm2). The PTEN loop results from double negation and involves several intermediates (PTEN, PIP2/PIP3, Akt, Mdm2), therefore its dynamics is slower. As a result, even in cells with extensive DNA damage, $p53_{KILLER}$ accumulation (and thus apoptosis) is postponed, granting the cell time which can be used for DNA repair. When DNA repair is accomplished before signal passes through the PTEN loop, the cell survives. However, when the DNA damage is severe so that its repair takes longer time, the PTEN-mediated feedback takes over and the cell commits to apoptosis.

Cell cycle arrest module. $p53_{ARRESTER}$ induces expression of p21, a protein which suppresses cell cycle progression to allow for DNA repair (Fig 2A). p21 directly binds and suppresses CycE which plays a critical role in the transition from G1 to S phase, and is considered a marker of cell cycle progression in the model [23]. CycE, synthesis of which is positively regulated by E2F1 (and several other transcription factors from the E2F family), can inactivate Rb1
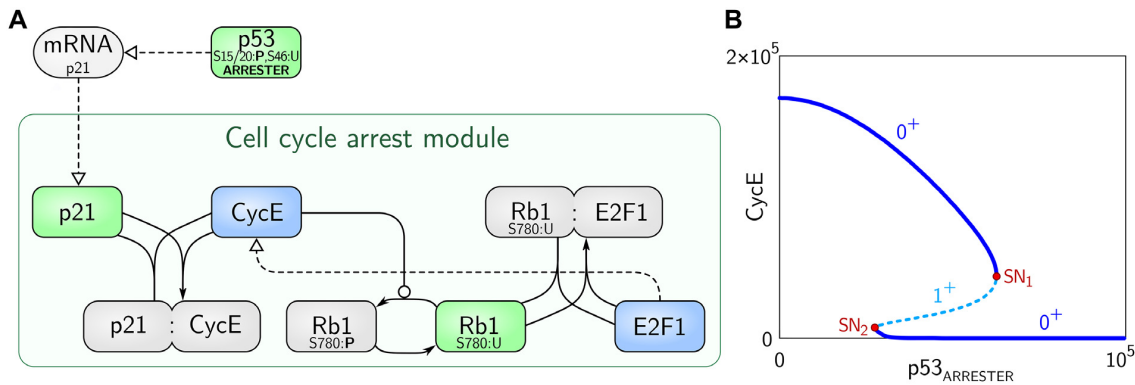
Fig 2. Scheme and the bifurcation diagram for the cell cycle arrest module. (A) Scheme: cell cycle-arresting proteins are represented with green boxes, proteins promoting cell cycle with blue boxes, other proteins or complexes with gray boxes. Bold 'P' denotes a phosphorylated protein residue. The arrow notation is same as in Fig 1. (B) Bifurcation diagram of CycE vs. $p53_{ARRESTER}$ (bifurcation parameter). The stable and unstable steady states are indicated by solid and dashed lines, respectively. SN_1 and SN_2 denote saddle-node bifurcations. The number of eigenvalues with positive real parts is either one (1^+) for the unstable steady state or zero (0^+) for stable steady states.

doi:10.1371/journal.pcbi.1004787.g002

protein by inducing its phosphorylation at Ser780. Phosphorylated Rb1 can no longer inhibit E2F1. This creates a positive feedback loop (based on double negation) in which CycE suppresses the inhibitor of its own transcription factor. This mode of regulation introduces bistability and allows for switch-like exit from and return to the cell cycle progression. Cell cycle progresses at a low level of p21 (i.e., when most of CycE is free). As p21 level increases the fraction of free CycE decreases, leading to dephosphorylation of Rb1 and inhibition of E2F1. At some level of p21 the system rapidly transits to the state in which most of E2F1 is inhibited and the level of CycE is close to zero (Fig 2B).

The analysis of the cell cycle arrest module shows that this subsystem exhibits bistability for a range of $p53_{ARRESTER}$ levels (Fig 2B). The low level of $p53_{ARRESTER}$ corresponds to a high level of CycE at which the cell cycle can progress. As the level of $p53_{ARRESTER}$ increases, the level of CycE decreases until the stable state loses its stability in the bifurcation point SN_1 and the system switches to the lower stable steady state in which the cell cycle is suppressed. When $p53_{ARRESTER}$ decreases from a high level, the system undergoes SN_2 bifurcation and the cell cycle may progress again.

Apoptotic module. The detailed description and analysis of the apoptotic module is contained in our recent paper by Bogdał et al. [86]. In this module (Fig 3A) we consider two inputs: pro-survival input, strength of which increases with the level of phosphorylated Akt (Akt_p), and pro-apoptotic, strength of which increases with the level of $p53_{KILLER}$. Non-apoptotic cells are characterized by a relatively high level of Akt_p and the lack or a very low level of $p53_{KILLER}$. The following two signals promote apoptosis: (1) suppression of pro-survival Akt, i.e., decrease of the Akt_p level, and (2) increase of the $p53_{KILLER}$ level.

In non-apoptotic cells the apoptosis is suppressed since the apoptotic effector, Bax, is neutralized through sequestration by pro-survival Bcl-x_L. This is possible because the other pro-apoptotic protein, Bad, that can bind Bcl-x_L, remains phosphorylated by Akt_p and sequestered by pro-survival protein 14-3-3. Dephosphorylation of Akt (which is considered here as pro-apoptotic signal) leads to the dephosphorylation of Bad and its release from the complex with 14-3-3. Subsequently, Bad binds to Bcl-x_L displacing Bax, which accumulates in the mitochondrial membrane, leading eventually to the release of cytochrome c, which initiates caspase activation (active both initiator and executioner caspases are collectively denoted as Casp). In the model, the step of cytochrome c release is omitted; instead, we assume that Bax activates Casp
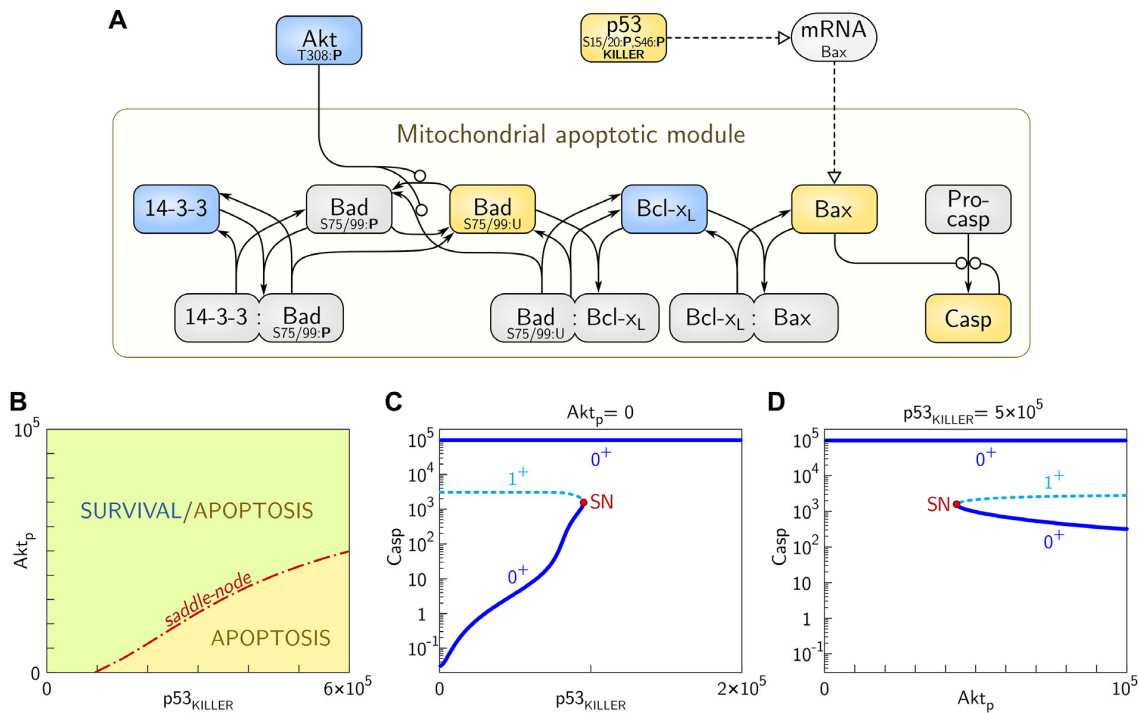
Fig 3. Scheme and the bifurcation diagrams for the apoptotic module. (A) Scheme: pro-survival proteins are in blue boxes, pro-apoptotic proteins are in yellow boxes, other proteins or protein complexes are in gray boxes. The arrow notation is same as in Fig 1. (B) Saddle—node bifurcations line in the $(p53_{KILLER}, Akt_p)$-plane (2-D bifurcation diagram) separates the region of parameters for which apoptotic and survival states coexist from the region for which only the apoptotic state exists. (C) Bifurcation diagram for Casp vs. $p53_{KILLER}$ (bifurcation parameter) for Akt_p; the saddle-node bifurcation point SN is $(p53_{KILLER}, Casp_{bif}) \cong (0.95 \times 10^5, 1.5 \times 10^3)$. (D) Bifurcation diagram for Casp vs. Akt_p (bifurcation parameter) for $p53_{KILLER} \cong 5 \times 10^5$; the saddle-node bifurcation point SN is $(Akt_p, Casp_{bif}) \cong (4.4 \times 10^4, 1.5 \times 10^3)$. The solid and dashed lines correspond respectively to the stable and unstable steady states. The number of eigenvalues with positive real parts is either one (1^+) for the unstable steady state or zero (0^+) for stable steady states. Notice the logarithmic scale on vertical axes in (C) and (D).

directly. The other pro-apoptotic signal comes from $p53_{KILLER}$, accumulation of which triggers Bax transcription and Bax protein accumulation.

In Fig 3B we analyze how cell fate decisions depend on the levels of $p53_{KILLER}$ and Akt_p. In the $(p53_{KILLER}, Akt_p)$-plane the saddle—node bifurcations line separates the region where survival coexists with apoptosis from the apoptotic region. The transition from survival to apoptosis requires crossing the saddle—node line, that is possible only when the level of $p53_{KILLER}$ increases and, simultaneously, a fraction of phosphorylated Akt (Akt_p) drops. Therefore, the apoptotic module integrates information about Akt_p and $p53_{KILLER}$ levels in the way similar to the AND logic gate (meaning that simultaneous dephosphorylation of Akt and build-up of $p53_{KILLER}$ are needed to trigger apoptosis). In our previous study [86], we demonstrated that the system can behave digitally, either as the logic gate AND, or as the logic gate OR, depending on the levels of Bad and Bcl-x_L. Gate AND arises for high levels of Bcl-x_L and low levels of Bad. The OR gate (when apoptosis may be initiated by one of the two apoptotic signals) arises for high Bad and low Bcl-x_L levels.

In Fig 3C and 3D we show bifurcation diagrams of the apoptotic switch with $p53_{KILLER}$ (Fig 3C) and Akt_p (Fig 3D) considered bifurcation parameters. The model predicts that for $Akt_p = 0$ and $p53_{KILLER} < 10^5$ the cell can exist either in the apoptotic or in surviving steady state,

characterized by a high and a low Casp levels, respectively ([Fig 3C](#)). At $p53_{KILLER} \approx 10^5$ the system undergoes the saddle—node bifurcation (in which $Casp \approx 1.5 \times 10^3$) in which the surviving state vanishes. In [Fig 3D](#) we show that for a high level of $p53_{KILLER}$ (i.e., $p53_{KILLER} \approx 5 \times 10^5$) the system exhibits bistability for $Akt_p > 4.5 \times 10^4$. At $Akt_p \approx 4.5 \times 10^4$ the system undergoes the saddle—node bifurcation, and for $Akt_p < 4.5 \times 10^4$ only the apoptotic state exists. The bifurcation diagrams shown in [Fig 3C and 3D](#) imply that the caspase activation switch (in contrast to the cell cycle arrest switch) is irreversible, i.e., there is no possibility to return from the apoptotic to the surviving state (even after $p53_{KILLER}$ drops to zero or Akt_p grows to its maximal value). The structure of the bifurcation diagram of Casp vs. $p53_{KILLER}$ resembles qualitatively the bifurcation diagram of Casp vs. Bax analyzed in our earlier work [86].

Bifurcation analysis of the p53 core module. In this section we focus on the discrimination of possible responses to DNA damage. In the bifurcation analysis we assume that the number of DSBs remains constant and equal to 100, which is considered as severe DNA damage. Bifurcation analysis allows us to determine the recurrent solutions (i.e., steady states and limit cycles) that delineate time-dependent responses to DNA damage. Since the two positive feedback loops are controlled by phosphatases Wip1 and PTEN, expression levels of which are varied substantially among cancer cells, we choose Wip1 and PTEN synthesis rates as bifurcation parameters. Additionally, PTEN has slow dynamics with respect to the other components and its gradual accumulation after DNA damage controls the behavior of the whole system. As a result, the system behavior can be predicted by bifurcation analysis in which PTEN is a bifurcation parameter.

In [Fig 4](#) we show the two-dimensional bifurcation diagram in the (s_1, s_2)-plane, where s_1 and s_2 are Wip1 and PTEN synthesis rates, respectively. As shown, the system involves three types of bifurcations: Hopf, saddle-node, and Neimark—Sacker. In the 2-D diagram, Neimark—Sacker bifurcations line arises at one zero—Hopf point $(s_1, s_2) \approx (0.1, 0.012)$ and vanishes at another zero—Hopf point $(s_1, s_2) \approx (0.3, 0.053)$. Between these points the Hopf bifurcations are supercritical, while outside them they are subcritical. The supercritical Hopfs line lies between the saddle—node line and the Neimark—Sacker bifurcations line. The saddle—node lines arise in a cusp point $(s_1, s_2) \approx (0.02, 0.001)$. The bifurcation lines divide the (s_1, s_2)-plane into subregions in which the system exhibits different behaviors. In short, the system is oscillatory in the parameter subdomain to the right of the Hopf bifurcations line, i.e., oscillations can arise due either increase of Wip1 synthesis or decrease of PTEN synthesis. The bistability (understood here as either the coexistence of two stable steady states or coexistence of one stable steady state and one stable limit cycle) can arise between two saddle—node lines.

The bifurcation lines divide the (s_1, s_2)-plane into seven subdomains characterized by different recurrent solutions:

D_1: monostability (one stable steady state),

D_2: oscillatory (stable limit cycle and one unstable steady state),

D_3: typical bistability (two stable steady states and one unstable steady state),

D_4: typical bistability (two stable steady states and one unstable steady state),

D_5: atypical bistability (the stable limit cycle coexists with one stable steady state and two unstable steady states),

D_6: monostability (one stable steady state, two unstable steady states and one unstable limit cycle),

D_7 (the tiny region between supercritical Hopf line and upper saddle—node line): monostability (one stable steady state and two unstable steady states).

We chose $(s_1, s_2) = (0.1, 0.03)$ as nominal model values for the Wip1 and PTEN mRNA synthesis rates. According to [Fig 4](#), $(s_1, s_2) = (0.1, 0.03)$ lies in domain D_1, in which the system with
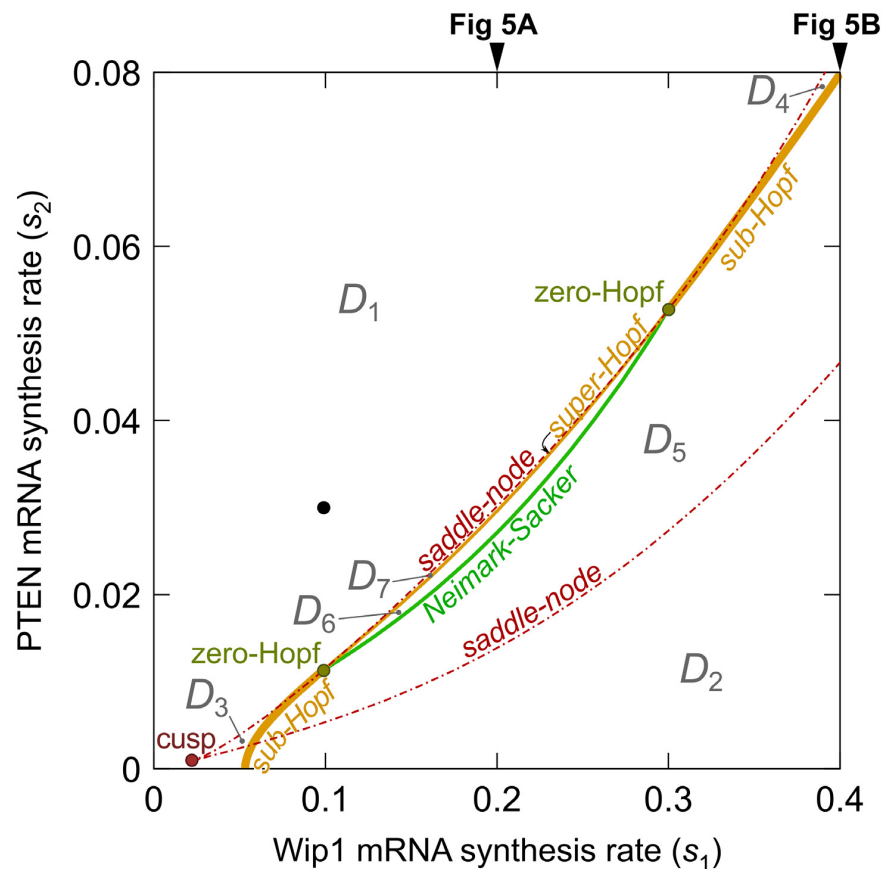
Fig 4. Two-dimensional bifurcation diagram showing various types of bifurcation lines and points in the (Wip1 synthesis rate, PTEN synthesis rate)-plane. The black dot indicates nominal values of parameters s_1 and s_2. The bifurcation lines divide the parameter domain into seven subdomains $D_1, \ldots, D_7$. The recurrent solutions in each of these domains are given in main text. Bifurcation diagrams in Fig 5A and 5B show the recurrent solutions obtained for $s_1 = 0.2$ and $s_1 = 0.4$, as indicated by black arrows, and varied s_2.

doi:10.1371/journal.pcbi.1004787.g004

persistent DNA damage has only one solution, the stable steady state. As we will see, this state is characterized by the level of p53$_{KILLER}$ high enough to trigger apoptosis.

In Fig 5 we show bifurcation diagrams of p53$_{KILLER}$ as a function of the PTEN synthesis rate, s_2. We consider two values of s_1, $s_1 = 0.2$ and $s_1 = 0.4$. The character of the bifurcation diagram for $s_1 = 0.2$ is qualitatively similar to that for nominal $s_1 = 0.1$, however it is visually clearer since the distance between Neimark—Sacker, Hopf, and saddle—node bifurcations is larger. For $s_1 = 0.4$ (Fig 5B) the bifurcation diagram is qualitatively different from that for $s_1 = 0.1$ and $s_1 = 0.2$ (Fig 5A).

As shown in Fig 4, with s_2 increasing (for fixed $s_1 = 0.2$) the system proceeds sequentially through five subdomains in the (s_1, s_2)-plane: D_2, D_5, D_6, D_7, and D_1. Fig 5A visualizes details of recurrent solutions along this line. In the description below we focus on stable steady states and limit cycles because these solutions shape time-dependent responses. For $s_2 < s_{SN1}$, i.e., in subdomain D_2, the system has a single stable limit cycle. This solution is characterized by oscillations of the levels of p53$_{KILLER}$ and p53$_{ARRESTER}$. Amplitude of p53$_{ARRESTER}$ oscillations is

Cell Fate Decisions in the p53 System
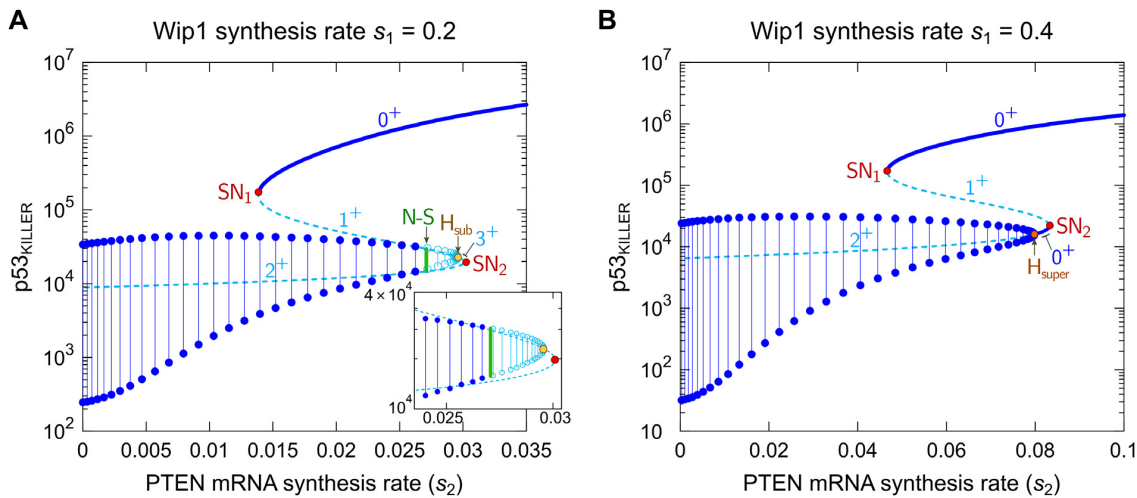
Fig 5. Bifurcation diagram of $p53_{KILLER}$ vs. PTEN mRNA synthesis rate (s_2). (A) Wip1 synthesis rate $s_1 = 0.2$, (B) $s_1 = 0.4$. The stable and unstable steady states are indicated by solid and dashed lines, respectively. Ranges of stable and unstable limit cycles are indicated by dark and light blue lines, respectively; dots and open circles are the maxima and minima of the stable and unstable limit cycles, respectively. Green vertical line in (A) shows Neimark—Sacker bifurcation (N—S). Red dots mark saddle-node bifurcations (SN_1, SN_2), orange dots mark supercritical Hopf (H_{super}) and subcritical Hopf (H_{sub}) bifurcations. The numbers in format n^+ adjacent to the steady state lines denote the number of eigenvalues with the positive real parts. Notice the logarithmic scale on vertical axes.

high enough to suppress the cell cycle, but the level of $p53_{KILLER}$ remains below the apoptotic threshold.

At $s_2 = s_{SN1}$ the first saddle—node bifurcation arises, and for $s_2 \in (s_{SN1}; s_{N-S})$, i.e., in D_5 subdomain, the system exhibits atypical bistability in which the stable limit cycle coexists with the stable steady state. This steady state is characterized by the $p53_{KILLER}$ level high enough to trigger apoptosis. Therefore, in this parameter range the apoptotic state and cell cycle arrest state coexist. At $s_2 = s_{N-S}$ the subcritical Neimark—Sacker bifurcation arises, in which the stable limit cycle loses its stability merging with an unstable invariant torus, and for $s_2 > s_{N-S}$ the only stable recurrent solution is the stable steady state associated with apoptosis. Therefore, as parameter s_2 increases (which is associated with the increase of the PTEN level), the cell with damaged DNA at $s_2 = s_{N-S}$ switches abruptly to apoptosis.

This biologically plausible behavior, allowing for unambiguous cell fate decisions, is associated with the specific bifurcation structure involving the subcritical Neimark—Sacker bifurcation. Then the cycle vanishes at $s_2 = s_{H_{super}}$ in the supercritical Hopf bifurcation (see the Fig 5A insert). Subsequently, two remaining unstable steady states (one with 3 eigenvalues of positive real parts), and the other (with 2 eigenvalues of positive real parts) "annihilate" in $s_2 = s_{SN2}$. Let us notice that unstable steady states in the analyzed diagram have at most 3 eigenvalues with positive real parts and the unstable cycle has 2 Floquet multipliers of moduli larger than 1. This implies that despite the system has complex structure which involves numerous feedback loops, its dynamics is essentially 3-dimensional, meaning that locally there exists a 3-dimensional attracting manifold.

A qualitatively different is the bifurcation diagram depicting the recurrent solutions along line $s_1 = 0.4$ with increasing s_2 (Fig 5B), i.e., when the system proceeds sequentially through D_2, D_5, D_4, and D_1 subdomains (shown in Fig 4). Similarly to the previous case for $s_2 < s_{SN1}$, the system has the stable limit cycle (cell cycle arrest state). Then, at $s_2 = s_{SN1}$, the first saddle—

node bifurcation arises, and for $s_2 \in (s_{SN1}; s_{H_{sub}})$ the stable limit cycle coexists with the stable steady state (apoptotic state). However, in contrast to bifurcation diagram shown in Fig 5A, the stable limit cycle does not lose its stability, but it is replaced by a steady state at $s_2 = s_{H_{sub}}$ through the subcritical Hopf bifurcation. In this steady state, p53$_{KILLER}$ does not exceed the apoptotic threshold. This steady state annihilates with an unstable steady state at $s_2 = s_{SN2}$ in the second saddle—node bifurcation. As in the previous case, for $s_2 > s_{SN2}$ the system has a single recurrent solution, the stable steady state associated with apoptosis.

We think that the bifurcation structure in Fig 5A reflects the experimental observations better than that of Fig 5B, suggesting that upon DNA damage the level of p53 either oscillates at a relatively low amplitude, or builds up to the high level in which apoptosis is triggered. Therefore, for further analysis we assume $s_1 = 0.1$, resulting in a bifurcation diagram as in Fig 5A. The bifurcation diagrams corresponding to $s_1 = 0.1$ (or qualitatively equivalent $s_1 = 0.2$) calculated with respect to Wip1, PI3K, and the number of DSBs are shown in S3 Fig. Qualitatively, diagrams with respect to Wip1 and PI3K are mirror images of the bifurcation diagram with respect to PTEN (Fig 5A), confirming the antagonistic action of Wip1 and PTEN. The antagonism of PI3K and PTEN is straightforward because PI3K phosphorylates PIP2 to PIP3, while PTEN dephosphorylated PIP3 to PIP2. The bifurcation diagram with respect to DNA damage (assumed, for this diagram, to be persistent) is similar to the bifurcation diagram with respect to PTEN, but the limit cycle oscillations start at a non-zero value of the bifurcation parameter.

Time-dependent dynamics

In this section we analyze time-dependent dynamics in response to DNA damage. First, we consider the case in which DNA repair is suppressed; then, we consider the nominal model in which DNA repair mechanism is active; finally, we analyze how cell fate depends on the expression levels of Wip1 and PTEN.

Dynamics of the system with suppressed DNA repair. In Fig 6 we analyze the system responses to the stimulation dose of 2 Gy, for nominal Wip1 and PTEN mRNA synthesis rates, i.e., $s_1 = 0.1$, $s_2 = 0.03$ (Fig 6A), as well as modified rates (Fig 6B and 6C). According to the bifurcation diagram (Fig 4) for the nominal parameters values, upon persistent DNA damage the system possesses the unique stable steady state. This state is reached after transient oscillations of p53$_{ARRESTER}$ and p53$_{KILLER}$ levels. Such response can be expected based on the bifurcation diagram shown in Fig 5A, indicating that the system generates oscillations for a sufficiently small PTEN synthesis rate, s_2; here, the PTEN rate is larger but due to the slow accumulation of PTEN the system initially exhibits oscillations. Shortly after DNA is damaged, in the oscillatory phase, the level of p53$_{ARRESTER}$ exceeds the cell cycle arrest threshold (see bifurcation point SN$_1$ in Fig 2) leading to a rapid decrease of the free CycE level and suppression of the cell cycle. During this phase the p53$_{ARRESTER}$ level remains below the apoptotic threshold (see the saddle—node bifurcations line in Fig 3B). After two oscillations the p53 killer grows to the high level, the apoptotic bifurcation line is surpassed and at about 25th hour since the DNA damage the cell is directed to apoptosis, a state characterized in the model by a high level of active caspases. Formally, within the model even in the apoptotic state the trajectory can still be calculated, but obviously initiation of apoptosis limits the validity of the model, and therefore after the apoptosis is initiated trajectories are drawn using faded lines.

In Fig 6B we analyze the response of the perturbed system in which PTEN synthesis rate, s_2, is equal 0.005, i.e., is 6-fold lower than the nominal value, while Wip1 synthesis rate is at its nominal value ($s_1 = 0.1$). For these parameters, as shown in the two-dimensional bifurcation diagram in Fig 4, the system possesses a unique stable recurrent solution, the limit cycle. Accordingly, as we see in Fig 6B, p53$_{ARRESTER}$ and p53$_{KILLER}$ exhibit sustained oscillations of

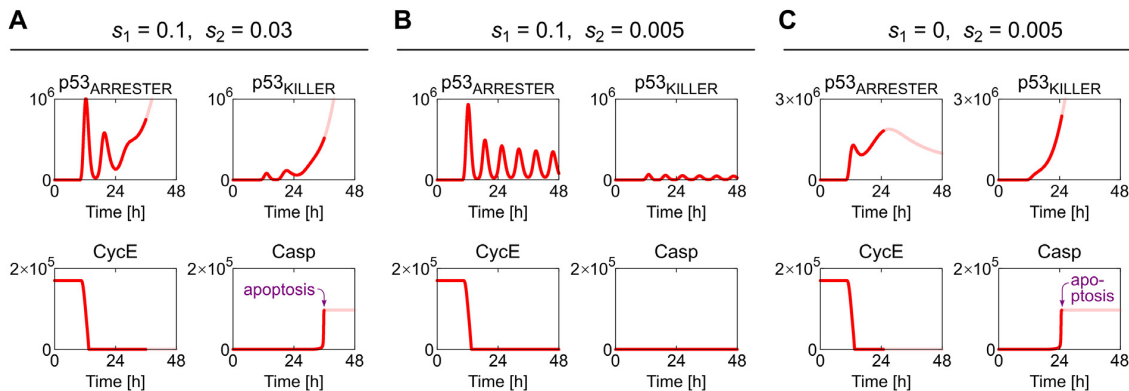Cell Fate Decisions in the p53 System

Fig 6. Deterministic simulation trajectories of the system with the suppressed DNA repair and either nominal or perturbed mRNA synthesis rates in response to 2-Gy irradiation. (A) Nominal Wip1 and PTEN mRNA synthesis rates (s_1 = 0.1, s_2 = 0.03). (B) Decreased PTEN mRNA synthesis rate (s_2 = 0.005). (C) Decreased PTEN mRNA synthesis rate (s_2 = 0.005) and zero Wip1 synthesis rate (s_1 = 0). The simulation started at Time = 0 h from the steady state corresponding to the resting (unstimulated) cell. At Time = 10 h the irradiation phase started and lasted for 10 min. The faded line visualizes the trajectory after the initiation of apoptosis, and thus must be interpreted with caution.

doi:10.1371/journal.pcbi.1004787.g006

period of about 6 hours. In these oscillations the level of p53$_{ARRESTER}$ is high enough to suppress the cell cycle, while the amplitude of p53$_{KILLER}$ oscillations does not exceed the apoptotic threshold. The observed behavior is similar to that exhibited by MCF-7 cells in the experiment of Geva-Zatorski et al. [73], in which irradiated cells showed quasiperiodic oscillation for 72 hours after irradiation. In these cells, the PTEN promoter is methylated and PTEN expression is not regulated by p53, and remains at a very low level.

In Fig 6C we analyze the response of the system with PTEN synthesis rate s_2 = 0.005 and no Wip1 synthesis (s_1 = 0). According to the two-dimensional bifurcation diagram in Fig 4 the system has the unique stable steady state. As shown in Fig 6C the level of p53$_{KILLER}$ switches to the high level triggering apoptosis. In contrast to the case of nominal parameter values, the oscillatory phase is absent and the apoptosis is initiated considerably faster, about 15 h after DNA damage. The direct passage to the apoptotic state can be also deduced from Fig 4 showing that oscillations are not possible for s_1 = 0, regardless of s_2.

Responses of the intact system—dependence on the irradiation dose. In Fig 7 we consider the model with nominal parameters and analyze the responses to two irradiation doses of 2 Gy and 10 Gy. As demonstrated in Fig 6A, in cells with suppressed DNA repair, the 2 Gy dose leads to apoptosis in about 25 hours since DNA damage. Here, the process is more complex as the repair of DNA may rescue cells from apoptosis. In this case the cell fate depends on the irradiation dose, and is decided through the competition between two processes: DNA repair and accumulation of PTEN which controls positive feedback-regulating levels of active Akt and p53$_{KILLER}$. As shown in Fig 7A, small DNA damage resulting from 2-Gy irradiation can be almost fully repaired in about 20 hours, thus the apoptosis is not initiated. In contrast, the repair of extensive damage resulting from 10-Gy irradiation can be not accomplished sufficiently fast and the cell undergoes apoptosis. The time delay associated with PTEN accumulation serves as a clock, giving about 24 hours for DNA repair, and then directing cells with unrepaired DNA to apoptosis.

In Fig 7A we show trajectories of key model components after 2-Gy irradiation. DNA damage leads to a rapid ATM phosphorylation and activation. Activated ATM phosphorylates p53 at Ser15 and Ser20 to the p53$_{ARRESTER}$ form, which accumulates and induces synthesis of p53 inhibitor, Mdm2, and phosphatase Wip1 which dephosphorylates ATM. These two negative
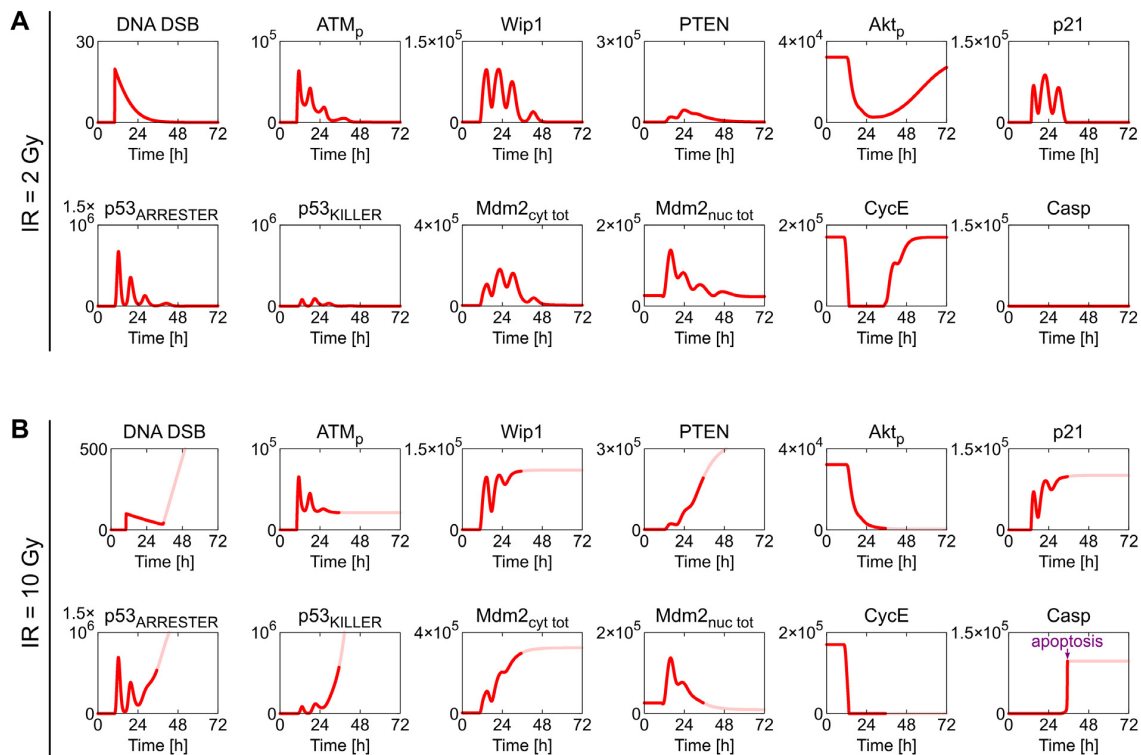
Fig 7. Deterministic simulation trajectories of the intact system in response to 2-Gy and 10-Gy irradiation. (A) 2-Gy irradiation is insufficient to trigger apoptosis and after several oscillations system recovers to the survival steady state. (B) 10-Gy irradiation is sufficient to trigger apoptosis: after two oscillations p53$_{KILLER}$ stabilizes at a high level triggering apoptosis.

doi:10.1371/journal.pcbi.1004787.g007

feedback loops (mediated by Mdm2 and Wip1) lead to oscillations of the level of p53$_{ARRESTER}$ and levels of p53$_{ARRESTER}$-regulated proteins, including p21. Increased level of p21 leads to the inhibition of CycE and transient cell cycle arrest, during which DNA can be repaired.

p53$_{ARRESTER}$ can be subsequently phosphorylated at Ser46 to the p53$_{KILLER}$ form by HIPK2 (a kinase which accumulates in response to DNA damage; see detailed scheme of the model in S1 Fig). This process is opposed by Wip1 which converts p53$_{KILLER}$ back to the p53$_{ARRESTER}$ form. As a result, the level of p53$_{KILLER}$ oscillates not surpassing the apoptotic threshold. After, about 20 h, when DNA repair is accomplished, ATM is deactivated and oscillations of p53$_{KILLER}$ and p53$_{ARRESTER}$ are terminated. Subsequently, the level of p21 drops below the threshold (bifurcation point SN$_2$, Fig 2B), CycE returns to its initial level, and cell cycle progression is resumed.

In the case of extensive DNA damage caused by 10-Gy irradiation (Fig 7B) DNA repair requires more time. Although initial regulatory events are similar to those at 2-Gy irradiation, prolonged p53$_{KILLER}$ activity induces accumulation of PTEN to a higher level, such that PTEN-mediated positive feedback loop terminates oscillations by sequestering Mdm2 in the cytoplasm, which separates it from its substrate, nuclear p53. Namely, accumulation of PTEN leads to dephosphorylation of Akt (see S1 Fig for details) and subsequent dephosphorylation of Mdm2 at Ser166 and Ser186, which blocks its nuclear entry and physically separates it from its target, p53. Of note, the positive feedback loop mediated by Wip1 (which stabilizes p53$_{ARRESTER}$) and the one mediated by PTEN (which stabilizes p53$_{KILLER}$) act antagonistically.

In the case of extensive DNA damage, the slow PTEN-mediated positive feedback can ultimately take over, causing the surge of the level of p53$_{KILLER}$ which ultimately surpasses the apoptosis-inducing threshold. Importantly, since early hours after DNA damage till (and throughout) apoptosis, the cell cycle remains suspended, preventing proliferation of cells which have lost their genomic integrity.

In summary, small DNA damage leads to a temporal cell cycle arrest during which DNA is repaired, while extensive DNA damage leads to the cell cycle arrest followed by apoptosis. Regulation of the core p53 module (see the bifurcation diagram in Fig 5) is such that in the oscillatory phase the level of p53$_{ARRESTER}$ is high enough to suppress cell cycle but the level of p53$_{KILLER}$ does not exceed the apoptotic threshold. Only in the "high" steady state levels of phosphorylated Akt and p53$_{KILLER}$ exceed the apoptotic threshold. This type of regulation assures that the cell fate decision is unanimous.

Impact of Wip1 and PTEN expression levels on the sensitivity to irradiation. As shown in the previous subsection, in response to irradiation the cell can either undergo apoptosis or repair its DNA and survive. Cell fate decision depends on the irradiation dose as well as expression levels of regulatory proteins in the p53 pathway. Here, we analyze how Wip1 and PTEN mRNA synthesis rates s_1 and s_2, and the level of active PI3K influence the critical irradiation dose. Level of active PI3K depends on the total level of PI3K which is cell line-dependent and can increase in response to various stimuli including growth factors. Gene copy amplification and overexpression of PI3K have been found in several types of cancer, including gastric (SNU1), prostate (LNCaP), head and neck squamous cell carcinoma (HNSCC), ovarian (OVCAR4) and breast (MCF-12A, MB157) [63,64,66–68]. Wip1 and PTEN mRNA synthesis rates are also cell line-specific. In the lung (NCI-H522), breast (MCF-7, BT474, KPL-1, MDA-MB361), prostate (DU-145), colon (HCT15) and ovarian (OVCAR4) cancers, and in melanoma (UACC-257) and lymphoma (MOLT4), Wip1 expression is frequently elevated due to gene copy amplification (32); PTEN expression is decreased due to gene loss in colon (HCT116) and lung (NCI-H1299) cancers [87,88] or due to methylation of PTEN promoter in breast (MCF-7, BT-549) and non-small cell lung (A549) cancers [87,89].

For nominal values of Wip1 and PTEN mRNA synthesis rates s_1 and s_2 assumed in the model and a nominal value of active PI3K the critical irradiation dose turns out to be 4.05 Gy. In Fig 8 we show the apoptotic and survival regions in the (s_1, s_2) parameter plane for four irradiation doses: 1 Gy, 2 Gy, 5 Gy, 10 Gy, as well as the persistent (irreparable) DNA damage (equal 100 DSBs). We consider three levels of active PI3K: nominal, twofold decreased, and twofold increased. For each level of active PI3K the apoptotic region (above separatrix) increases and the survival region (below separatrix) shrinks with the irradiation dose. Interestingly, even for irreparable DNA damage cells can survive provided that the ratio s_2/s_1 (PTEN to Wip1) is sufficiently low, as in the case analyzed in Fig 6B. The critical irradiation dose increases with increasing Wip1 and decreases with increasing PTEN. The ratio s_2/s_1 (PTEN to Wip1 mRNA synthesis rate) is roughly constant on each of survival/apoptosis separatrices (and increases with the irradiation dose) conforming the antagonistic relationship between Wip1 and PTEN.

One may notice that the ratio s_2/s_1 for each of the separatrices increases with the PI3K level (compare Fig 8A, 8B and 8C). This is, for a given Wip1 mRNA synthesis rate an increase of PTEN synthesis rate can be compensated by an increase of active PI3K. This relationship follows from the fact that PTEN and PI3K has directly opposing roles in the pathway.

Overall, our analysis indicates that cellular proclivity for irradiation-induced apoptosis increases with PTEN to Wip1 expression ratio, and decreases with the level of active PI3K. This confirms the pro-survival role of Wip1 and PI3K, and the pro-apoptotic role of PTEN. Since cancer cell lines have diverse expression levels of Wip1, PTEN and PI3K, they are
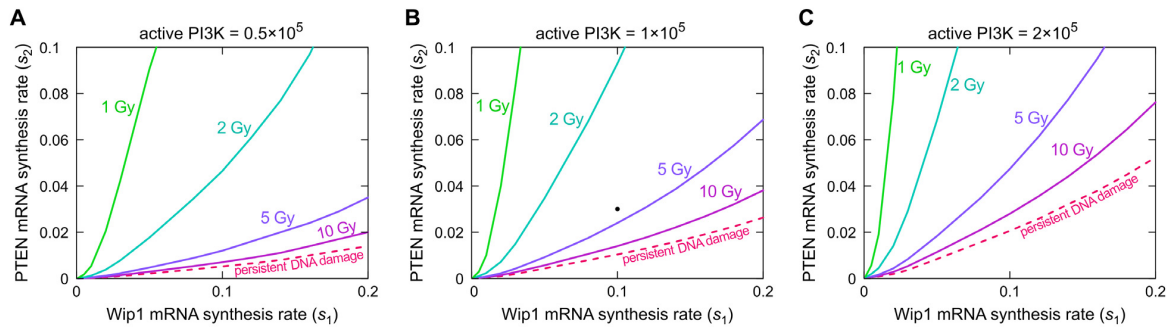
Fig 8. Critical irradiation doses as a function of Wip1 (s_1) and PTEN (s_2) mRNA synthesis rates. (A) Active PI3K level is decreased 2-fold from the nominal value. (B) The nominal value of active PI3K. (C) Active PI3K level is twice the nominal value. Color lines show the critical irradiation doses in the (s_1, s_2)-parameter space. Dashed line corresponds to the persistent (irreparable) DNA damage equal 100 DSBs. For each dose, the line separates the apoptotic region (above the line) and the survival region (below the line) in the (s_1, s_2)-parameter space. The black dot in (B) corresponds to nominal values of Wip1 and PTEN mRNA synthesis rates.

doi:10.1371/journal.pcbi.1004787.g008

expected to exhibit divergent responses to irradiation; therefore, different cancers may have widely varying sensitivity to radiotherapy. In particular, the performed analysis explains high survival rates of irradiated MCF-7 cells for which the expression of Wip1 is significantly increased while PTEN expression is reduced. This cell line (studied by Geva-Zatorski et al. [73]) respond to high irradiation dose by long-lasting oscillations, showing that even the persistent DNA damage does not induce apoptosis.

The role of stochasticity

In order to analyze the cell-to-cell variability we performed stochastic simulations according to the Gillespie algorithm [90] implemented in BioNetGen [91]. In Fig 9 we compare trajectories obtained in single-cell stochastic simulations with the deterministic trajectory as well as the population trajectory, i.e., trajectory obtained by averaging over 1000 single-cell stochastic trajectories. In the figure we show trajectories of p53$_{\text{ARRESTER}}$ and p53$_{\text{KILLER}}$ in response to three irradiation doses: small of 2 Gy, intermediate of 4 Gy (which is just below the critical dose for the deterministic approximation) and large of 8 Gy. As one can observe, the stochastic trajectories follow closely the deterministic trajectory for the low and high doses, and in these two cases the population trajectory almost matches the deterministic one. This is in contrast to the intermediate dose of 4 Gy, for which the deterministic trajectory after a few oscillations (during which DNA is repaired) returns to the initial state characterized by low levels of p53$_{\text{ARRESTER}}$ and p53$_{\text{KILLER}}$, while the stochastic trajectories separate into two groups corresponding to the apoptotic cells (of high p53 levels) and surviving cells (of low p53 levels). As a result, for 4 Gy the deterministic trajectory is much different from the population-averaged trajectory. Such discrepancy between deterministic and stochastic solutions has been demonstrated earlier for various, even very simple, nonlinear or multistable systems [92–97]. It is especially pronounced in the cases of bistable (or multistable) systems when the deterministic trajectory converges to one of steady states, while the stochastic trajectories split into two (or more) groups. In this case the population average (observed in population experiments by Western blotting or PCR) does not correspond to any single-cell trajectory.

The fraction of apoptotic cells increases with the irradiation dose (see Fig 10, where 5000 single-cell stochastic simulations were performed for each of 14 different doses from the 0–8 Gy range). For the critical (deterministic) dose equal 4.05 Gy, the fraction of apoptotic cells was found to be close to 50%. The fraction of apoptotic cells increases from about 10% to about
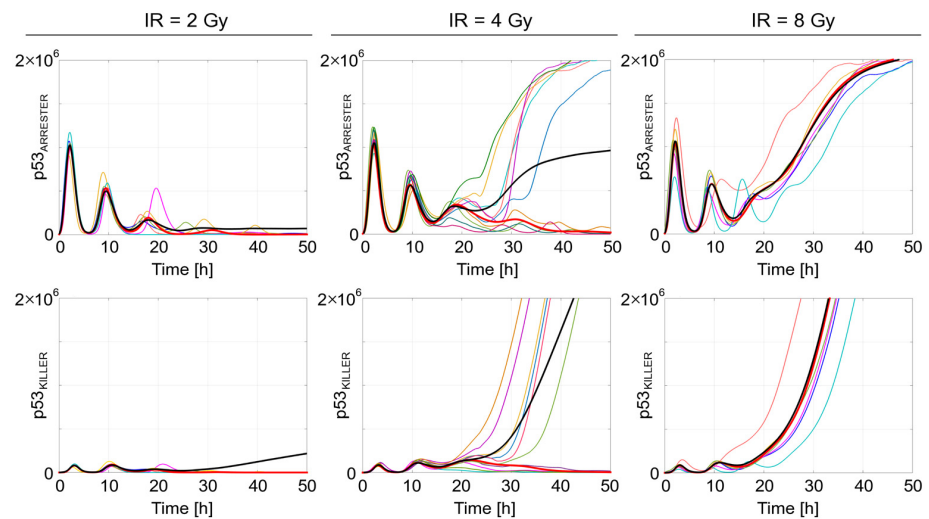
Fig 9. Stochastic vs. deterministic simulation trajectories in the response to low (2 Gy), intermediate (4 Gy) and high (8 Gy) irradiation doses. Single-cell stochastic trajectories—thin color lines; average over 1000 stochastic trajectories—bold black line; deterministic approximation—bold red line.

doi:10.1371/journal.pcbi.1004787.g009

90% as the irradiation dose increases from 2.5 Gy to 6 Gy. In order to determine how gene switching noise contributes to the heterogeneity in cell fate decisions we performed simulations in a model variant in which gene activity was assumed to be a deterministic function of the level of p53 (in a gene-specific phosphoform). As expected, after removing one source of stochasticity the individual cell responses has become less heterogeneous (see also S4 Fig), which is manifested by the steeper sigmoid of the fraction of apoptotic cells (violet vs. pink line). Surprisingly, the difference between these two cases is not very large, which indicates that transcriptional and translational noises significantly contribute to the overall stochasticity.
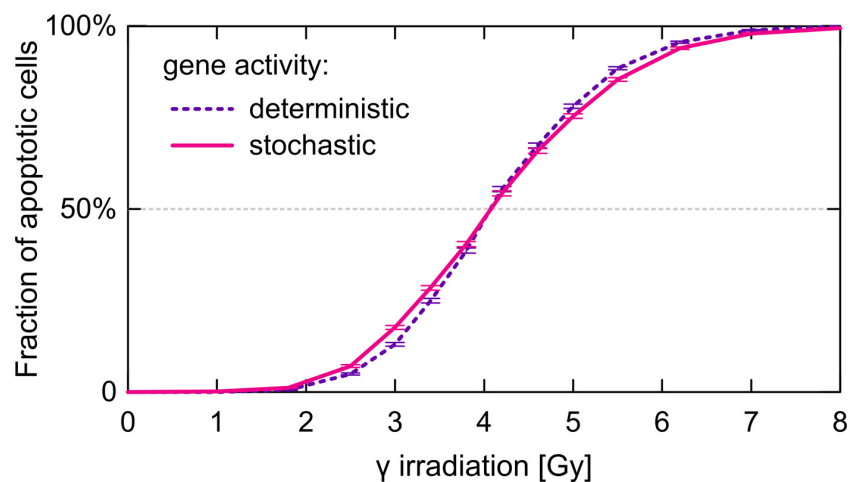
Fig 10. Fraction of apoptotic cells as a function of irradiation dose for two types of stochastic simulations. For each of analyzed doses the fraction and corresponding error was calculated based on 5000 stochastic single-cell simulations. The state of the cell was checked at 72. hour after irradiation which, as shown in Fig 11, is sufficient for unanimous cell fate decision.

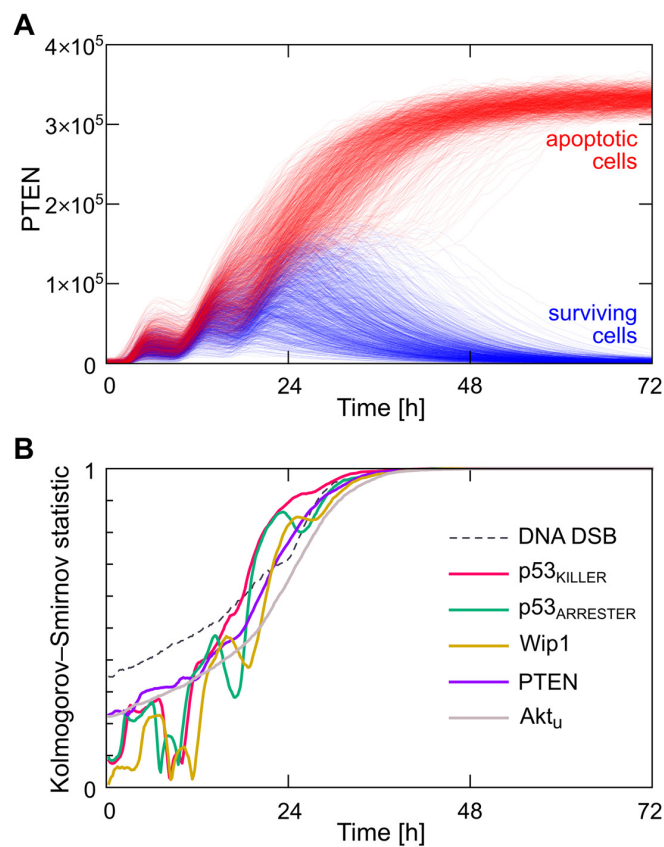doi:10.1371/journal.pcbi.1004787.g010

Fig 11. Analysis of the cell fate decision-making process. (A) PTEN levels in subpopulations of surviving (blue) and apoptotic (red) cells after 4-Gy irradiation. 10 000 cells are simulated in total. (B) Kolmogorov—Smirnov statistics between distributions of six variables which characterize surviving and apoptotic cells.

As showed above for the intermediate doses, the cell population splits into apoptotic and surviving subpopulations. In Fig 11 we analyze how the cell fate decision after 4-Gy irradiation is reached in time. In Fig 11A we show trajectories of PTEN, which is a key protein mediating slow positive feedback loop and thus its level was found to be a good predictor of the ultimate cell fate decision. As shown, the trajectories of surviving cells (blue) are almost fully separated from trajectories of apoptotic cells (red) after about 36 hours. The separation between apoptotic and surviving trajectories progresses in time, as shown in Fig 11B where temporal evolution of the Kolmogorov—Smirnov statistic between 6 distributions of different variables characterizing apoptotic and surviving cells is calculated. This figure confirms that the cell fate decision is reached after about 36 hours, as for this time Kolmogorov—Smirnov statistics (for all variables) reaches 1, which indicates that distributions corresponding to apoptotic and surviving cells fully separate. The number of DSBs that arise during the irradiation phase (which, due to the stochasticity, can be different for cells irradiated with the same dose) is the fastest predictor. PTEN and Akt_u (levels of which can be different prior to the irradiation due to stochastic fluctuations in resting cells) are also fast predictors and, moreover, the Kolmogorov—Smirnov statistics corresponding to their distributions grow monotonically. This is in contrast to $p53_{KILLER}$, $p53_{ARRESTER}$, and Wip1 levels, which exhibit pronounced oscillations after irradiation, and for which the Kolmogorov—Smirnov statistics reach 1 non-monotonously.

Discussion

p53 is thoroughly studied as a pivotal signaling node that integrates and transforms diverse stress signals into downstream responses including cell cycle arrest and apoptosis to limit proliferation of cells with the damaged genetic material. Based on the experimental knowledge about feedbacks and interactions within the p53 network, we proposed a modular model of p53 signaling pathway, in which the dynamics of the core p53 module controls downstream modules that govern cell cycle arrest and apoptosis. The model has the purposeful bifurcation structure that delineates plausible temporal responses and allows for, we think, the most unambiguous cell death, cycle arrest, or survival decisions.

The stochastic, yet unambiguous, processing of analog irradiation signals to reach a digital cell fate outcome is assured by the bistability of cell cycle arrest and apoptotic modules, but primarily by a specific-type bistability of the core p53 module. As demonstrated by the two-parameter bifurcation analysis of the core module, in a relatively broad range of parameters the limit cycle oscillations (of $p53_{ARRESTER}$ and $p53_{KILLER}$ levels) coexist with the stable steady state in which the $p53_{KILLER}$ level is very high, while the level of phosphorylated Akt is very low. The limit cycle oscillations of $p53_{ARRESTER}$ induce cell cycle arrest, while the high $p53_{KILLER}$ level and low level of phosphorylated Akt induce apoptosis. The key difference between dynamics of the cycle arrest module and the apoptotic module is that the former is based on reversible bistability and involves one input signal, $p53_{ARRESTER}$, which suppresses cell cycle when above the threshold and releases the cell cycle arrest when below the lower threshold. In turn, apoptosis induction requires two signals (increase of $p53_{KILLER}$ and decrease of phosphorylated Akt) simultaneously, and is an irreversible process.

The bifurcation structure delineates temporal responses to DNA damage. Small DNA damage results in temporal cell cycle arrest, followed by DNA repair and return to the resting cell state, while high DNA damage results in the cell cycle arrest and subsequent apoptosis (without returning to cell cycle). The direct jump between limit cycle oscillations and the stable steady state is enabled by the presence of a subcritical Neimark—Sacker bifurcation in which the limit cycle loses its stability merging with an unstable invariant torus. Interestingly, this type of bifurcation, rarely analyzed in the context of molecular regulatory networks, can exist in at least three-dimensional systems. Although the core module is 18-dimensional, the stability analysis of the steady state showed that at most three eigenvalues have positive real parts which implies that locally the system could be reduced to a three-dimensional one. It remains an open question whether such reduction is possible globally.

We propose that in the process of cell fate decision-making the p53 system can exhibit the most robust transitions when the only stable recurrent solutions are a stable limit cycle and a stable steady state (out of this limit cycle), provided there exists a parameter region for which these recurrent solutions coexist. Such structure allows cells to switch to the cell cycle arrest (associated in the model with limit-cycle oscillations of the levels of p53 phosphoforms) and then to direct transition to either apoptosis or recovery. Interestingly, there exists an even simpler bifurcation structure, shown in S5 Fig, that allows for such transitions. In this hypothetical case, as the bifurcation parameter s_2 increases the limit cycle simply vanishes in the saddle—loop bifurcation. The most pronounced dynamical difference between the modeled and the hypothetical scenario is that the period of oscillations diverges to infinity as the bifurcation parameter approaches the saddle—loop bifurcation point. This would imply that in a heterogeneous cellular population some cells would exhibit much longer oscillation periods, which is not observed in experiments [73]. As discussed by us earlier [76], we thus expect that oscillations in the p53 system (as well as in the NF-κB system) do not arise or vanish through a

saddle—loop bifurcation or a saddle—node on invariant cycle bifurcation (also called SNIPER) in which limit cycle arises from orbit homoclinic to the saddle.

Biochemical signal processing depends on the topology and time scales of feedback loops. Regulatory networks with negative feedback(s) can produce oscillatory or pulsed responses to tonic stimuli, and allow for adaptation to the change in the level of stimulation. The existence of positive feedbacks, in turn, can give rise to bistability [98] (or multistability [99]) that can be harnessed for cell fate decisions. Combinations of positive and negative feedbacks allow for more complex behaviors. At least three qualitatively different type of responses leading to distinct regulatory outcomes are possible. (1) In the case when a positive feedback loop acts on a short time scale and is embedded in a longer negative feedback loop, the system can switch periodically between two predefined states (e.g., the autophagy/translation switch [100]). (2) In the case when a positive feedback loops encompasses the negative one, the system can exhibit autonomous oscillations (e.g., oscillations in the TNF—NF-κB autocrine system [101]). (3) In the case when a slow positive feedback loop can turn off a negative feedback, the system can exhibit biphasic responses in which after an oscillatory phase it either returns to the initial state (more likely when the signal is short-lasting) or it switches to another steady state (more likely when the signal is persistent or lasts sufficiently long [102]). The last case (which is a simplification of the p53 regulatory core organization discussed in this study) seems to be a good candidate for the unbiased and proportionate process of cell fate decisions. The oscillatory phase provides a time interval to collect and integrate various signals, and estimate the severity of stress, before a (potentially irreversible) switch to another committed state is done.

Stochastic simulations of the model allowed to analyze how the death-or-life decision is achieved in time, and what are the best or earliest indicators of apoptosis. By calculating time-dependent Kolmogorov—Smirnov statistic between distributions of protein levels corresponding to two populations of cells with apoptotic and surviving fates, we found that the clear separation between these two populations is reached at about 30 hours after irradiation. PTEN, the p53-induced phosphatase that mediates slow positive feedback loop, was found to be the most robust and fast apoptosis predictor. Interestingly, the Kolmogorov—Smirnov statistics for Wip1, p53$_{ARRESTER}$ and p53$_{KILLER}$ are non-monotonous in time, what possibly follows from the pronounced oscillations of these components and indicates that at some time-points of the response the elevated or decreased levels of pro- or anti-apoptotic proteins may not correlate with the ultimate cell fate decision.

Most of experimental data were gathered for cancer (or immortalized) cell lines, which became cancerous as a result of malfunctions in the p53 network. Much less is known about regulation of normal, i.e., non-cancer, non-immortalized cells. Nevertheless, we expect that the plausible responses of normal cells should consist of the cell cycle suppression phase (which can be associated with p53 oscillations), followed by either apoptosis or recovery, depending on the extent of the DNA damage. Accordingly, in contrast to the majority of previous studies focused on modeling of cancer cell lines, we aimed at constructing the model that reflects behavior of normal cells after γ irradiation. Within this model, the responses of different cancer cell lines can be analyzed by adjusting the appropriate parameters such as mRNA synthesis rates or steady-state levels of proteins that are assumed to be not regulated in the model. In this way one can simulate cancer cell lines that are known to have elevated expression of Wip1 such as MCF-7, BT474 (breast cancers), OVCAR4 (ovarian cancer), MOLT4 (lymphoma), U2OS (osteosarcoma) [50–52,54,103], lines of decreased PTEN expression such as MCF-7 (breast cancer), H1299, H322, Calu1 (lung cancers) [58–60], or with amplification of PI3K gene, such as MKN1, SNU1 (gastric cancers), OVCAR4, A2780 (ovarian cancers) [63–70].

The life-or-death decision is reached in the interplay of two antagonistic phosphatases Wip1 and PTEN. Our analysis shows that sensitivity to apoptosis increases with PTEN expression

and decreases with Wip1 or PI3K expression, which confirms the pro-survival functions of Wip1 and PI3K, and pro-apoptotic functions of PTEN. The other key regulatory pro-apoptotic protein present in network is kinase HIPK2 that converts $p53_{ARRESTER}$ to the $p53_{KILLER}$ phosphoform [104]. The model shows that undamped oscillations of $p53_{ARRESTER}$ and $p53_{KILLER}$ levels observed in MCF-7 cells can result from the low expression of PTEN. Analogously, our analysis indicates that cell lines with Wip1 overexpression (resulting from, e.g., gene amplification) can exhibit persistent oscillations and resistance to apoptosis. Strong dependence of the critical irradiation dose on PTEN, Wip1, and PI3K expression may suggest that pretreatment of cancer cells (with intact p53) with drugs that act temporally to elevate the expression of PTEN or to repress the expression of Wip1 or PI3K can enhance the effectiveness of radiotherapy.

Very recently, Puszyński et al. [105] have modified his earlier model [80] to study the responses of the p53 network to nutlins, promising antitumor chemical agents which bind to a p53-binding pocket of Mdm2 and thus hinder Mdm2 from ubiquitinating p53. Puszyński et al. demonstrated *in silico* that dose-splitting can be ineffective at low doses but effective at high doses, which can be attributed to nonlinear behavior of the regulatory system, manifested by the fact that a certain p53 threshold has to be exceeded to induce apoptosis. We propose that the current model can be used to study combination therapies involving agents which reduce the expression or inhibit the activity of Wip1, Mdm2, PI3K, together with ionizing radiation. In Fig 12 we survey over agents known to inhibit the selected nodes of the p53 pathway as well as DNA-damaging compounds that can be used in place of irradiation [106,107]. The proposed model provides the opportunity to investigate responses of particular cancer types, for which the anomalies in expression of p53 inhibitors are characterized. The aim is to propose a treatment that would reduce the levels or activity of Wip1, Mdm2, PI3K in cancer cells to make them more sensitive to radiotherapy, and to devise optimal drug and irradiation protocols that would leverage the impact of inhibitors by synchronizing their administration with the induced DNA damage.

The regulatory proteins Wip1, PTEN, PI3K, and HIPK2 present in the model are themselves important nodes of a larger regulatory network thus their levels and activity can be modulated by numerous other proteins or stimuli. For example, Wip1 expression is upregulated by not only p53 but also c-Jun, nuclear factor κB (NF-κB), cyclic adenosine monophosphate response element-binding protein (CREB), E2F transcription factor 1 (E2F1), Estrogen Receptor-alpha (ERα) [108–112]. PTEN expression is upregulated by early growth-response protein 1 (EGR1), or downregulated by Proto-Oncogene Polycomb Ring Finger (BMI1), NF-κB, c-Jun, Snail Family Zinc Finger 1 (SNAI1), oncogenic factor inhibitor of DNA binding 1 (ID1), ecotropic virus integration site 1 protein (EVI1) [113–116]. Neurogenic locus notch homolog protein 1 (NOTCH1) can either upregulate PTEN through CBF1 (C-repeat binding factor 1) or downregulate it through V-Myc Avian Myelocytomatosis Viral Oncogene Homolog (Myc) [115]. PI3K is activated by various growth and survival factors, including fibroblast growth factor (FGF), vascular endothelial cell growth factor (VEGF), human growth factor (HGF), angiopoietin I (Ang1), insulin, receptor tyrosine kinases (RTKs), G-protein-coupled receptors (GPCRs) [40,117]. These and other existing connections allow to expand the *in silico* drug impact analysis onto a larger network, and dissect possible dynamical consequences of inhibition of proteins more distant from p53 in the network.

Materials and Methods

Stochastic and deterministic model representations

The ordinary differential equations were integrated numerically in MATLAB. Stochastic simulations were performed using the Gillespie algorithm implemented in BIONETGEN. Bifurcation

Fig 12. Chemotherapeutic agents targeting the p53 regulatory core. A selection of chemical compounds, both clinically approved chemotherapeutic drugs and newly discovered inhibitors, are shown. Some agents have pleiotropic effects (gemcitabine, 5-fluoroacil); several p53 inhibitors may be effective only towards a mutated, conformationally disrupted p53 (PRIMA-1 and similar not shown); tenovins have activating influence on p53 because they inhibit p53 inhibitor, sirtuin. Nutlins, MIs and RITA inhibit Mdm2 and p53 interaction.

doi:10.1371/journal.pcbi.1004787.g012

diagrams were obtained with MATCONT. The MATLAB code (full model, core module, cell cycle arrest module, apoptotic module), BIONETGEN code (full model) and MATLAB/MATCONT files (core module, cell cycle arrest module, apoptotic module) are provided as S1, S2 and S3 Codes.

Stochastic simulations

To account for initial heterogeneity in protein levels in cell population the 10-min long irradiation phase was preceded by a 100-hour long simulation of resting cells, except for S4 Fig, where the resting phase lasted for 300 hours. Average protein levels in Fig 9 were obtained by averaging over 1000 independent stochastic simulations; the fraction of apoptotic cells with respect to the dose was determined based on 5000 stochastic simulations; the (time-dependent) two-sample Kolmogorov—Smirnov statistic between apoptotic and surviving cell subpopulations was calculated based on 10 000 stochastic simulations, Fig 11.

The stratification into surviving and apoptotic cells was based on the level of active caspases at 72. hour after the irradiation phase; cells with the level of active caspases higher (lower) than the threshold defined as the value of active caspases at the saddle-node bifurcation point (SN in

[Fig 3C](#)) were considered apoptotic (surviving). The Kolmogorov—Smirnov statistic is defined as $D_{a,s}(t) = \sup_x |F_a(x,t) - F_s(x,t)|$ where F_a and F_s are time-dependent cumulative distributions for the surviving and apoptotic subpopulations, calculated numerically, and sup is the supremum function.

Supporting Information

S1 Text. This supplementary document includes: overview of mathematical models of the p53 system, detailed description of the model, three tables containing the notation guide, list of parameters, and list of reactions.
(PDF)

S1 Fig. Detailed representation of the full model. Arrow-headed dashed lines indicate transcriptional regulation, arrow-headed solid lines—protein transformation, circle-headed solid lines—positive influence, hammer-headed dotted lines—ubiquitination by Mdm2 leading to protein degradation. The subscripts n or c denote either nuclear or cytoplasmic localization of Mdm2. Bold 'P' and non-bold 'U' denote phosphorylated and unphosphorylated states of given residues, respectively. Pro-survival and cycle-promoting proteins are represented with blue boxes, pro-apoptotic proteins with yellow boxes, proteins involved in cell cycle arrest with green boxes, while the remaining proteins and protein complexes are left in grey boxes.
(PDF)

S2 Fig. The negative feedback mediated by Wip1 is required for generating oscillations. Trajectories for p53 and Mdm2 were simulated using the model variant in which there is no Wip1-mediated dephosphorylation of ATM. Simulations were performed for four different pairs of Wip1 (s_1) and PTEN (s_2) synthesis rates, with IR dose equal 3 Gy. Black line corresponds to nominal values of s_1 and s_2.
(PDF)

S3 Fig. Recurrent solutions for p53$_{KILLER}$ as a function of Wip1 synthesis rate, active PI3K level and DNA damage level. PTEN mRNA synthesis rate is equal to the nominal value $s_2 = 0.03$; Wip1 synthesis rate is equal $s_1 = 0.2$ in (B) and $s_1 = 0.1$ in (C). The number of DSBs is equal 100 for (A) and (B). The stable and unstable steady states are indicated by solid and dashed lines, respectively. Dots and open circles show the maxima and minima of the stable and unstable limit cycles, respectively. Green vertical line shows the Neimark—Sacker bifurcation (N—S). Red dots mark saddle—node bifurcations (SN$_1$, SN$_2$), yellow dots mark the supercritical Hopf (H$_{super}$) and the subcritical Hopf (H$_{sub}$) bifurcation. Note the log-scale on the vertical axis. The bifurcation diagrams with respect to Wip1 and PI3K resemble the mirror image of the bifurcation diagram with respect to PTEN (see main text [Fig 5A](#)). The bifurcation diagram with respect to DNA damage is similar to the bifurcation diagram with respect to PTEN, but the limit cycle oscillations start at non-zero value of the bifurcation parameter.
(PDF)

S4 Fig. Influence of the gene switching rates on the single-cell stochastic trajectories for p53$_{tot}$ and Mdm2$_{tot}$. (A) and (B): nominal gene switching rates. (C) and (D): 10-fold increased gene switching rates. The irradiation phase started at Time = 300 h and lasted for 10 min, the irradiation dose was 4 Gy. The dynamics of the p53$_{tot}$ and Mdm2$_{tot}$ weakly depends on the gene switching rate, although its increase leads to some decrease of the amplitude of fluctuations in unstimulated cells. Notice the logarithmic scale on vertical axes.
(PDF)

S5 Fig. A hypothetical alternative bifurcation structure for the core module. The stable limit cycle (of envelope marked by pairs of blue points) coexists with a high-level stable steady state and disappears through the saddle—loop bifurcation (SL). The stable and unstable steady states are indicated by solid and dashed lines, respectively; red dots labeled SN mark saddle—node bifurcations.
(PDF)

S1 Code. ZIP-archived directory containing Matlab scripts and a ReadMe file.
(ZIP)

S2 Code. ZIP-archived directory containing a BioNetGen model file and a ReadMe file.
(ZIP)

S3 Code. ZIP-archived directory containing Matlab scripts calling Matcont functions, and a ReadMe file.
(ZIP)

Acknowledgments

Author Contributions

References

1. Vousden KH, Prives C. Blinded by the Light: The Growing Complexity of p53. Cell. 2009; 137: 413–431. doi: 10.1016/j.cell.2009.04.037 PMID: 19410540

2. Levine AJ. p53, the cellular gatekeeper for growth and division. Cell. 1997; 88: 323–331. PMID: 9039259

3. Kastan MB, Onyekwere O, Sidransky D, Vogelstein B, Craig RW. Participation of p53 protein in the cellular response to DNA damage. Cancer Res. 1991; 51: 6304–6311. PMID: 1933891

4. Elmore S. Apoptosis: A Review of Programmed Cell Death. Toxicol Pathol. 2007; 35: 495–516. doi: 10.1080/01926230701320337 PMID: 17562483

5. Siliciano JD, Canman CE, Taya Y, Sakaguchi K, Appella E, Kastan MB. DNA damage induces phosphorylation of the amino terminus of p53. Genes Dev. 1997; 11: 3471–3481. PMID: 9407038

6. Vogelstein B, Lane D, Levine AJ. Surfing the p53 network. Nature. 2000; 408: 307–310.

7. Rothkamm K, Krüger I, Thompson LH, Löbrich M. Pathways of DNA Double-Strand Break Repair during the Mammalian Cell Cycle. Mol Cell Biol. 2003; 23: 5706–5715.

8. Iliakis G. The role of DNA double strand breaks in ionizing radiation-induced killing of eukaryotic cells. BioEssays. 1991; 13: 641–648. doi: 10.1002/bies.950131204 PMID: 1789781

9. Vilenchik MM, Knudson AG. Endogenous DNA double-strand breaks: Production, fidelity of repair, and induction of cancer. Proc Natl Acad Sci USA. 2003; 100: 12871–12876. doi: 10.1073/pnas.2135498100 PMID: 14566050

10. Alberts B, Johnson A, Lewis J, Raff M, Roberts K, Walter P. Molecular Biology of the Cell. 4th ed. Garland Science; 2002.

11. Soussi T, Dehouche K, Béroud C. p53 website and analysis of p53 gene mutations in human cancer: forging a link between epidemiology and carcinogenesis. Hum Mutat. 2000; 15: 105–113. doi: 10.1002/(SICI)1098-1004(200001)15:1<105::AID-HUMU19>3.0.CO;2-G PMID: 10612830

12. Hanahan D, Weinberg RA. The hallmarks of cancer. Cell. 2000; 100: 57–70. PMID: 10647931

13. Bode AM, Dong Z. Post-translational modification of p53 in tumorigenesis. Nat Rev Cancer. 2004; 4: 793–805. doi: 10.1038/nrc1455 PMID: 15510160

14. Reed JC. Dysregulation of apoptosis in cancer. J Clin Oncol. 1999; 17: 2941–2953. PMID: 10561374

15. Mirzayans R, Andrais B, Scott A, Murray D. New Insights into p53 Signaling and Cancer Cell Response to DNA Damage: Implications for Cancer Therapy. BioMed Res Int. 2012; 2012: e170325. doi: 10.1155/2012/170325

16. Vogelstein B, Lane D, Levine AJ. Surfing the p53 network. Nature. 2000; 408: 307–310. doi: 10.1038/35042675 PMID: 11099028

17. Wei C-L, Wu Q, Vega VB, Chiu KP, Ng P, Zhang T, et al. A global map of p53 transcription-factor binding sites in the human genome. Cell. 2006; 124: 207–219. doi: 10.1016/j.cell.2005.10.043 PMID: 16413492

18. Chehab NH, Malikzay A, Stavridi ES, Halazonetis TD. Phosphorylation of Ser-20 mediates stabilization of human p53 in response to DNA damage. Proc Natl Acad Sci USA. 1999; 96: 13777–13782. PMID: 10570149

19. Shieh SY, Taya Y, Prives C. DNA damage-inducible phosphorylation of p53 at N-terminal sites including a novel site, Ser20, requires tetramerization. EMBO J. 1999; 18: 1815–1823. doi: 10.1093/emboj/18.7.1815 PMID: 10202145

20. Shieh SY, Ikeda M, Taya Y, Prives C. DNA damage-induced phosphorylation of p53 alleviates inhibition by MDM2. Cell. 1997; 91: 325–334. PMID: 9363941

21. D'Orazi G, Cecchinelli B, Bruno T, Manni I, Higashimoto Y, Saito S 'ichi, et al. Homeodomain-interacting protein kinase-2 phosphorylates p53 at Ser 46 and mediates apoptosis. Nat Cell Biol. 2002; 4: 11–19. doi: 10.1038/ncb714 PMID: 11780126

22. Barak Y, Juven T, Haffner R, Oren M. mdm2 expression is induced by wild type p53 activity. EMBO J. 1993; 12: 461–468. PMID: 8440237

23. El-Deiry WS, Tokino T, Velculescu VE, Levy DB, Parsons R, Trent JM, et al. WAF1, a potential mediator of p53 tumor suppression. Cell. 1993; 75: 817–825. PMID: 8242752

24. Fiscella M, Zhang H, Fan S, Sakaguchi K, Shen S, Mercer WE, et al. Wip1, a novel human protein phosphatase that is induced in response to ionizing radiation in a p53-dependent manner. Proc Natl Acad Sci USA. 1997; 94: 6048–6053. PMID: 9177166

25. Choi J, Nannenga B, Demidov ON, Bulavin DV, Cooney A, Brayton C, et al. Mice deficient for the wild-type p53-induced phosphatase gene (Wip1) exhibit defects in reproductive organs, immune function, and cell cycle control. Mol Cell Biol. 2002; 22: 1094–1105. PMID: 11809801

26. Stambolic V, MacPherson D, Sas D, Lin Y, Snow B, Jang Y, et al. Regulation of PTEN transcription by p53. Mol Cell. 2001; 8: 317–325. PMID: 11545734

27. Miyashita T, Reed JC. Tumor suppressor p53 is a direct transcriptional activator of the human bax gene. Cell. 1995; 80: 293–299. PMID: 7834749

28. Haupt Y, Maya R, Kazaz A, Oren M. Mdm2 promotes the rapid degradation of p53. Nature. 1997; 387: 296–299. doi: 10.1038/387296a0 PMID: 9153395

29. Meek DW, Knippschild U. Posttranslational Modification of MDM2. Mol Cancer Res. 2003; 1: 1017–1026. PMID: 14707285

30. Brooks CL, Gu W. p53 Ubiquitination: Mdm2 and Beyond. Mol Cell. 2006; 21: 307–315. doi: 10.1016/j.molcel.2006.01.020 PMID: 16455486

31. Saito S 'ichi, Goodarzi AA, Higashimoto Y, Noda Y, Lees-Miller SP, Appella E, et al. ATM Mediates Phosphorylation at Multiple p53 Sites, Including Ser46, in Response to Ionizing Radiation. J Biol Chem. 2002; 277: 12491–12494. PMID: 11875057

32. Bakkenist CJ, Kastan MB. DNA damage activates ATM through intermolecular autophosphorylation and dimer dissociation. Nature. 2003; 421: 499–506. doi: 10.1038/nature01368 PMID: 12556884

33. Stenerlöw B, Karlsson KH, Cooper B, Rydberg B. Measurement of Prompt DNA Double-Strand Breaks in Mammalian Cells without Including Heat-Labile Sites: Results for Cells Deficient in Nonhomologous End Joining. Radiat Res. 2003; 159: 502–510. doi: 10.1667/0033-7587(2003)159[0502:MOPDDS]2.0.CO;2 PMID: 12643795

34. Banin S, Moyal L, Shieh S, Taya Y, Anderson CW, Chessa L, et al. Enhanced phosphorylation of p53 by ATM in response to DNA damage. Science. 1998; 281: 1674–1677. PMID: 9733514

35. Canman CE, Lim D-S, Cimprich KA, Taya Y, Tamai K, Sakaguchi K, et al. Activation of the ATM Kinase by Ionizing Radiation and Phosphorylation of p53. Science. 1998; 281: 1677–1679. doi: 10.1126/science.281.5383.1677 PMID: 9733515

36. Maya R, Balass M, Kim S-T, Shkedy D, Leal J-FM, Shifman O, et al. ATM-dependent phosphorylation of Mdm2 on serine 395: role in p53 activation by DNA damage. Genes Dev. 2001; 15: 1067–1077. doi: 10.1101/gad.886901 PMID: 11331603

37. Lawlor MA, Alessi DR. PKB/Akt: a key mediator of cell proliferation, survival and insulin responses? J Cell Sci. 2001; 114: 2903–2910. PMID: 11686294

38. Volinia S, Hiles I, Ormondroyd E, Nizetic D, Antonacci R, Rocchi M, et al. Molecular Cloning, cDNA Sequence, and Chromosomal Localization of the Human Phosphatidylinositol 3-Kinase p110α (PIK3CA) Gene. Genomics. 1994; 24: 472–477. doi: 10.1006/geno.1994.1655 PMID: 7713498

39. Vanhaesebroeck B, Leevers SJ, Panayotou G, Waterfield MD. Phosphoinositide 3-kinases: A conserved family of signal transducers. Trends Biochem Sci. 1997; 22: 267–272. doi: 10.1016/S0968-0004(97)01061-X PMID: 9255069

40. Cantley LC. The Phosphoinositide 3-Kinase Pathway. *Science*. 2002; 296: 1655–1657. doi: 10.1126/science.296.5573.1655 PMID: 12040186

41. Marte BM, Downward J. PKB/Akt: connecting phosphoinositide 3-kinase to cell survival and beyond. Trends Biochem Sci. 1997; 22: 355–358. doi: 10.1016/S0968-0004(97)01097-9 PMID: 9301337

42. Kandel ES, Hay N. The regulation and activities of the multifunctional serine/threonine kinase Akt/PKB. Exp Cell Res. 1999; 253: 210–229. doi: 10.1006/excr.1999.4690 PMID: 10579924

43. Ogawara Y, Kishishita S, Obata T, Isazawa Y, Suzuki T, Tanaka K, et al. Akt enhances Mdm2-mediated ubiquitination and degradation of p53. J Biol Chem. 2002; 277: 21843–21850. doi: 10.1074/jbc.M109745200 PMID: 11923280

44. Harris SL, Levine AJ. The p53 pathway: positive and negative feedback loops. Oncogene. 2005; 24: 2899–2908. doi: 10.1038/sj.onc.1208615 PMID: 15838523

45. Shreeram S, Hee WK, Demidov ON, Kek C, Yamaguchi H, Fornace AJ, et al. Regulation of ATM/p53-dependent suppression of myc-induced lymphomas by Wip1 phosphatase. J Exp Med. 2006; 203: 2793–2799. doi: 10.1084/jem.20061563 PMID: 17158963

46. Takekawa M, Adachi M, Nakahata A, Nakayama I, Itoh F, Tsukuda H, et al. p53-inducible Wip1 phosphatase mediates a negative feedback regulation of p38 MAPK-p53 signaling in response to UV radiation. EMBO J. 2000; 19: 6517–6526. doi: 10.1093/emboj/19.23.6517 PMID: 11101524

47. Lu X, Ma O, Nguyen T-A, Jones SN, Oren M, Donehower LA. The Wip1 Phosphatase Acts as a Gatekeeper in the p53-Mdm2 Autoregulatory Loop. Cancer Cell. 2007; 12: 342–354. doi: 10.1016/j.ccr.2007.08.033 PMID: 17936559

48. Hlobilkova A, Knillova J, Svachova M, Skypalova P, Krystof V, Kolar Z. Tumour suppressor PTEN regulates cell cycle and protein kinase B/Akt pathway in breast cancer cells. Anticancer Res. 2006; 26: 1015–1022. PMID: 16619501

49. Knuutila S, Björkqvist AM, Autio K, Tarkkanen M, Wolf M, Monni O, et al. DNA copy number amplifications in human neoplasms: review of comparative genomic hybridization studies. Am J Pathol. 1998; 152: 1107–1123. PMID: 9588877

50. Li J, Yang Y, Peng Y, Austin RJ, van Eyndhoven WG, Nguyen KCQ, et al. Oncogenic properties of PPM1D located within a breast cancer amplification epicenter at 17q23. Nat Genet. 2002; 31: 133–134. doi: 10.1038/ng888 PMID: 12021784

51. Saito-Ohara F, Imoto I, Inoue J, Hosoi H, Nakagawara A, Sugimoto T, et al. PPM1D is a potential target for 17q gain in neuroblastoma. Cancer Res. 2003; 63: 1876–1883. PMID: 12702577

52. Bulavin DV, Demidov ON, Saito S, Kauraniemi P, Phillips C, Amundson SA, et al. Amplification of PPM1D in human tumors abrogates p53 tumor-suppressor activity. Nat Genet. 2002; 31: 210–215. doi: 10.1038/ng894 PMID: 12021785

53. Castellino RC, Bortoli MD, Lu X, Moon S-H, Nguyen T-A, Shepard MA, et al. Medulloblastomas overexpress the p53-inactivating oncogene WIP1/PPM1D. J Neurooncol. 2007; 86: 245–256. doi: 10.1007/s11060-007-9470-8 PMID: 17932621

54. Hirasawa A, Saito-Ohara F, Inoue J, Aoki D, Susumu N, Yokoyama T, et al. Association of 17q21-q24 Gain in Ovarian Clear Cell Adenocarcinomas with Poor Prognosis and Identification of PPM1D and APPBP2 as Likely Amplification Targets. Clin Cancer Res. 2003; 9: 1995–2004. PMID: 12796361

55. Rauta J, Alarmo E-L, Kauraniemi P, Karhu R, Kuukasjärvi T, Kallioniemi A. The serine-threonine protein phosphatase PPM1D is frequently activated through amplification in aggressive primary breast tumours. Breast Cancer Res Treat. 2006; 95: 257–263. doi: 10.1007/s10549-005-9017-7 PMID: 16254685

56. Harrison M, Li J, Degenhardt Y, Hoey T, Powers S. Wip1-deficient mice are resistant to common cancer genes. Trends Mol Med. 2004; 10: 359–361. doi: 10.1016/j.molmed.2004.06.010 PMID: 15310454

57. Belova GI, Demidov ON, Fornace AJ, Bulavin DV. Chemical inhibition of Wip1 phosphatase contributes to suppression of tumorigenesis. Cancer Biol Ther. 2005; 4: 1154–1158. PMID: 16258255

58. Garcia JM, Silva JM, Dominguez G, Gonzalez R, Navarro A, Carretero L, et al. Allelic loss of the PTEN region (10q23) in breast carcinomas of poor pathophenotype. Breast Cancer Res Treat. 1999; 57: 237–243.

59. Li J, Yen C, Liaw D, Podsypanina K, Bose S, Wang SI, et al. PTEN, a Putative Protein Tyrosine Phosphatase Gene Mutated in Human Brain, Breast, and Prostate Cancer. Science. 1997; 275: 1943–1947. doi: 10.1126/science.275.5308.1943 PMID: 9072974

60. Steck PA, Pershouse MA, Jasser SA, Yung WKA, Lin H, Ligon AH, et al. Identification of a candidate tumour suppressor gene, MMAC1, at chromosome 10q23.3 that is mutated in multiple advanced cancers. Nat Genet. 1997; 15: 356–362. doi: 10.1038/ng0497-356 PMID: 9090379

61. Li J, Simpson L, Takahashi M, Miliaresis C, Myers MP, Tonks N, et al. The PTEN/MMAC1 tumor suppressor induces cell death that is rescued by the AKT/protein kinase B oncogene. Cancer Res. 1998; 58: 5667–5672. PMID: 9865719

62. Weng L-P, Brown JL, Eng C. PTEN induces apoptosis and cell cycle arrest through phosphoinositol-3-kinase/Akt-dependent and -independent pathways. Hum Mol Genet. 2001; 10: 237–242.

63. Astanehe A, Arenillas D, Wasserman WW, Leung PCK, Dunn SE, Davies BR, et al. Mechanisms underlying p53 regulation of PIK3CA transcription in ovarian surface epithelium and in ovarian cancer. J Cell Sci. 2008; 121: 664–674. doi: 10.1242/jcs.013029 PMID: 18270270

64. Campbell IG, Russell SE, Choong DYH, Montgomery KG, Ciavarella ML, Hooi CSF, et al. Mutation of the PIK3CA gene in ovarian and breast cancer. Cancer Res. 2004; 64: 7678–7681. doi: 10.1158/0008-5472.CAN-04-2933 PMID: 15520168

65. Oda K, Stokoe D, Taketani Y, McCormick F. High frequency of coexistent mutations of PIK3CA and PTEN genes in endometrial carcinoma. Cancer Res. 2005; 65: 10669–10673. doi: 10.1158/0008-5472.CAN-05-2620 PMID: 16322209

66. Byun D-S, Cho K, Ryu B-K, Lee M-G, Park J-I, Chae K-S, et al. Frequent monoallelic deletion of PTEN and its reciprocal associatioin with PIK3CA amplification in gastric carcinoma. J Int Cancer. 2003; 104: 318–327. doi: 10.1002/ijc.10962

67. Pedrero JMG, Carracedo DG, Pinto CM, Zapatero AH, Rodrigo JP, Nieto CS, et al. Frequent genetic and biochemical alterations of the PI 3-K/AKT/PTEN pathway in head and neck squamous cell carcinoma. J Int Cancer. 2005; 114: 242–248. doi: 10.1002/ijc.20711

68. Wu G, Xing M, Mambo E, Huang X, Liu J, Guo Z, et al. Somatic mutation and gain of copy number of PIK3CA in human breast cancer. Breast Cancer Res. 2005; 7: R609–R616.

69. Samuels Y, Wang Z, Bardelli A, Silliman N, Ptak J, Szabo S, et al. High Frequency of Mutations of the PIK3CA Gene in Human Cancers. Science. 2004; 304: 554–554. doi: 10.1126/science.1096502 PMID: 15016963

70. Ollikainen M, Gylling A, Puputti M, Nupponen NN, Abdel-Rahman WM, Butzow R, et al. Patterns of PIK3CA alterations in familial colorectal and endometrial carcinoma. Int J Cancer. 2007; 121: 915–920. doi: 10.1002/ijc.22768 PMID: 17471559

71. Bar-Or RL, Maya R, Segel LA, Alon U, Levine AJ, Oren M. Generation of oscillations by the p53-Mdm2 feedback loop: A theoretical and experimental study. Proc Natl Acad Sci USA. 2000; 97: 11250–11255. doi: 10.1073/pnas.210171597 PMID: 11016968

72. Lahav G, Rosenfeld N, Sigal A, Geva-Zatorsky N, Levine AJ, Elowitz MB, et al. Dynamics of the p53-Mdm2 feedback loop in individual cells. Nat Genet. 2004; 36: 147–150. doi: 10.1038/ng1293 PMID: 14730303

73. Geva-Zatorsky N, Rosenfeld N, Itzkovitz S, Milo R, Sigal A, Dekel E, et al. Oscillations and variability in the p53 system. Mol Syst Biol. 2006; 2: 2006.0033. doi: 10.1038/msb4100068 PMID: 16773083

74. Ma L, Wagner J, Rice JJ, Hu W, Levine AJ, Stolovitzky GA. A plausible model for the digital response of p53 to DNA damage. Proc Natl Acad Sci USA. 2005; 102: 14266–14271. doi: 10.1073/pnas.0501352102 PMID: 16186499

75. Ciliberto A, Novak B, Tyson JJ. Steady states and oscillations in the p53/Mdm2 network. Cell Cycle. 2005; 4: 488–493. PMID: 15725723

76. Hat B, Puszynski K, Lipniacki T. Exploring mechanisms of oscillations in p53 and nuclear factor-κB systems. IET Syst Biol. 2009; 3: 342–355. doi: 10.1049/iet-syb.2008.0156 PMID: 21028925

77. Lahav G, Rosenfeld N, Sigal A, Geva-Zatorsky N, Levine AJ, Elowitz MB, et al. Dynamics of the p53-Mdm2 feedback loop in individual cells. Nat Genet. 2004; 36: 147–150. doi: 10.1038/ng1293 PMID: 14730303

78. Wee KB, Aguda BD. Akt versus p53 in a Network of Oncogenes and Tumor Suppressor Genes Regulating Cell Survival and Death. Biophys J. 2006; 91: 857–865. doi: 10.1529/biophysj.105.077693 PMID: 16648169

79. Zhang T, Brazhnik P, Tyson JJ. Exploring mechanisms of the DNA-damage response: p53 pulses and their possible relevance to apoptosis. Cell Cycle. 2007; 6: 85–94. PMID: 17245126

80. Puszyński K, Hat B, Lipniacki T. Oscillations and bistability in the stochastic model of p53 regulation. J Theor Biol. 2008; 254: 452–465. doi: 10.1016/j.jtbi.2008.05.039 PMID: 18577387

81. Wee KB, Surana U, Aguda BD. Oscillations of the p53-Akt Network: Implications on Cell Survival and Death. PLoS ONE. 2009; 4: e4407. doi: 10.1371/journal.pone.0004407 PMID: 19197384

82. Batchelor E, Mock CS, Bhan I, Loewer A, Lahav G. Recurrent initiation: a mechanism for triggering p53 pulses in response to DNA damage. Mol Cell. 2008; 30: 277–289. doi: 10.1016/j.molcel.2008.03.016 PMID: 18471974

83. Zhang X-P, Liu F, Wang W. Two-phase dynamics of p53 in the DNA damage response. Proc Natl Acad Sci USA. 2011; 108: 8990–8995. doi: 10.1073/pnas.1100600108 PMID: 21576488

84. Zhang X-P, Liu F, Cheng Z, Wang W. Cell fate decision mediated by p53 pulses. Proc Natl Acad Sci USA. 2009; 106: 12245–12250. doi: 10.1073/pnas.0813088106 PMID: 19617533

85. Zhang X-P, Liu F, Wang W. Coordination between Cell Cycle Progression and Cell Fate Decision by the p53 and E2F1 Pathways in Response to DNA Damage. J Biol Chem. 2010; 285: 31571–31580. doi: 10.1074/jbc.M110.134650 PMID: 20685653

86. Bogdał MN, Hat B, Kochańczyk M, Lipniacki T. Levels of pro-apoptotic regulator Bad and anti-apoptotic regulator Bcl-xL determine the type of the apoptotic logic gate. BMC Syst Biol. 2013; 7: 67. doi: 10.1186/1752-0509-7-67 PMID: 23883471

87. Soria J-C, Lee H-Y, Lee JI, Wang L, Issa J-P, Kemp BL, et al. Lack of PTEN expression in non-small cell lung cancer could be related to promoter methylation. Clin Cancer Res. 2002; 8: 1178–1184. PMID: 12006535

88. Langlois M-J, Bergeron S, Bernatchez G, Boudreau F, Saucier C, Perreault N, et al. The PTEN Phosphatase Controls Intestinal Epithelial Cell Polarity and Barrier Function: Role in Colorectal Cancer Progression. PLoS ONE. 2010; 5: e15742. doi: 10.1371/journal.pone.0015742 PMID: 21203412

89. Khan S, Kumagai T, Vora J, Bose N, Sehgal I, Koeffler PH, et al. PTEN promoter is methylated in a proportion of invasive breast cancers. Int J Cancer. 2004; 112: 407–410. doi: 10.1002/ijc.20447 PMID: 15382065

90. Gillespie DT. Exact stochastic simulation of coupled chemical reactions. J Phys Chem. 1977; 81: 2340–2361. doi: 10.1021/j100540a008

91. Faeder JR, Blinov ML, Hlavacek WS. Rule-Based Modeling of Biochemical Systems with BioNetGen. In: Maly IV, editor. Systems Biology. Totowa, NJ: Humana Press; 2009. pp. 113–167. Available: http://link.springer.com/10.1007/978-1-59745-525-1_5

92. Keizer J. Statistical Thermodynamics of Nonequilibrium Processes. 1st ed. Springer-Verlag New York; 1987.

93. Paulsson J, Berg OG, Ehrenberg M. Stochastic focusing: Fluctuation-enhanced sensitivity of intracellular regulation. Proc Natl Acad Sci USA. 2000; 97: 7148–7153. doi: 10.1073/pnas.110057697 PMID: 10852944

94. Barkai N, Leibler S. Biological rhythms: Circadian clocks limited by noise. Nature. 2000; 403: 267–268.

95. Togashi Y, Kaneko K. Molecular discreteness in reaction-diffusion systems yields steady states not seen in the continuum limit. Phys Rev E. 2004; 70: 020901.

96. Samoilov M, Plyasunov S, Arkin AP. Stochastic amplification and signaling in enzymatic futile cycles through noise-induced bistability with oscillations. Proc Natl Acad Sci USA. 2005; 102: 2310–2315. doi: 10.1073/pnas.0406841102 PMID: 15701703

97. Sneppen K, Mitarai N. Multistability with a Metastable Mixed State. Phys Rev Lett. 2012; 109: 100602. PMID: 23005273

98. Xiong W, Ferrell JE. A positive-feedback-based bistable "memory module" that governs a cell fate decision. Nature. 2003; 426: 460–465. doi: 10.1038/nature02089 PMID: 14647386

99. Lu M, Jolly MK, Levine H, Onuchic JN, Ben-Jacob E. MicroRNA-based regulation of epithelial—hybrid—mesenchymal fate determination. Proc Natl Acad Sci USA. 2013; 110: 18144–18149. doi: 10.1073/pnas.1318192110 PMID: 24154725

100. Szymańska P, Martin KR, MacKeigan JP, Hlavacek WS, Lipniacki T. Computational analysis of an autophagy/translation switch based on mutual inhibition of MTORC1 and ULK1. PLOS One. 2015; 10: e0116550. doi: 10.1371/journal.pone.0116550 PMID: 25761126

101. Pękalski J, Zuk PJ, Kochańczyk M, Junkin M, Kellogg R, Tay S, et al. Spontaneous NF-κB activation by autocrine TNFα signaling: a computational analysis. PLOS One. 2013; 8: e78887. doi: 10.1371/journal.pone.0078887 PMID: 24324544

102. Schultz D, Lu M, Stavropoulos T, Onuchic J, Ben-Jacob E. Turning Oscillations Into Opportunities: Lessons from a Bacterial Decision Gate. Sci Rep. 2013; 3. doi: 10.1038/srep01668

103. Saito-Ohara F, Imoto I, Inoue J, Hosoi H, Nakagawara A, Sugimoto T, et al. PPM1D is a potential target for 17q gain in neuroblastoma. Cancer Res. 2003; 63: 1876–1883. PMID: 12702577

PLOS | COMPUTATIONAL BIOLOGY

104. Puca R, Nardinocchi L, Sacchi A, Rechavi G, Givol D, D'Orazi G. HIPK2 modulates p53 activity towards pro-apoptotic transcription. Mol Cancer. 2009; 8: 85. doi: 10.1186/1476-4598-8-85 PMID: 19828042

105. Puszynski K, Gandolfi A, d'Onofrio A. The Pharmacodynamics of the p53-Mdm2 Targeting Drug Nutlin: The Role of Gene-Switching Noise. PLOS Comput Biol. 2014; 10: e1003991. doi: 10.1371/journal.pcbi.1003991 PMID: 25504419

106. Wade M, Li Y-C, Wahl GM. MDM2, MDMX and p53 in oncogenesis and cancer therapy. Nat Rev Cancer. 2013; 13: 83–96.

107. Zawacka-Pankau J, Selivanova G. Pharmacological reactivation of p53 as a strategy to treat cancer. J Intern Med. 2015; 277: 248–259. doi: 10.1111/joim.12336 PMID: 25495071

108. Han H-S, Yu E, Song J-Y, Park J-Y, Jang SJ, Choi J. The Estrogen Receptor α Pathway Induces Oncogenic Wip1 Phosphatase Gene Expression. Mol Cancer Res. 2009; 7: 713–723. doi: 10.1158/1541-7786.MCR-08-0247 PMID: 19435816

109. Song J, Han H-S, Sabapathy K, Lee B-M, Yu E, Choi J. Expression of a Homeostatic Regulator, Wip1 (Wild-type p53-induced Phosphatase), Is Temporally Induced by c-Jun and p53 in Response to UV Irradiation. J Biol Chem. 2010; 285: 9067–9076. doi: 10.1074/jbc.M109.070003 PMID: 20093361

110. Lowe JM, Cha H, Yang Q, Fornace AJ. Nuclear Factor-κB (NF-κB) Is a Novel Positive Transcriptional Regulator of the Oncogenic Wip1 Phosphatase. J Biol Chem. 2010; 285: 5249–5257.

111. Rossi M, Demidov ON, Anderson CW, Appella E, Mazur SJ. Induction of PPM1D following DNA-damaging treatments through a conserved p53 response element coincides with a shift in the use of transcription initiation sites. Nucl Acids Res. 2008; 36: 7168–7180. doi: 10.1093/nar/gkn888 PMID: 19015127

112. Hershko T, Korotayev K, Polager S, Ginsberg D. E2F1 Modulates p38 MAPK Phosphorylation via Transcriptional Regulation of ASK1 and Wip1. J Biol Chem. 2006; 281: 31309–31316. doi: 10.1074/jbc.M601758200 PMID: 16912047

113. Whelan JT, Forbes SL, Bertrand FE. CBF-1 (RBP-J kappa) binds to the PTEN promoter and regulates PTEN gene expression. Cell Cycle. 2007; 6: 80–84. PMID: 17245125

114. Yoshimi A, Goyama S, Watanabe-Okochi N, Yoshiki Y, Nannya Y, Nitta E, et al. Evi1 represses PTEN expression and activates PI3K/AKT/mTOR via interactions with polycomb proteins. Blood. 2011; 117: 3617–3628. doi: 10.1182/blood-2009-12-261602 PMID: 21289308

115. Song MS, Salmena L, Pandolfi PP. The functions and regulation of the PTEN tumour suppressor. Nat Rev Mol Cell Biol. 2012; 13: 283–296. doi: 10.1038/nrm3330 PMID: 22473468

116. Liu S, Ma X, Ai Q, Huang Q, Shi T, Zhu M, et al. NOTCH1 functions as an oncogene by regulating the PTEN/PI3K/AKT pathway in clear cell renal cell carcinoma. Urol Oncol. 2013; 31: 938–948. doi: 10.1016/j.urolonc.2011.07.006 PMID: 21993533

117. Morita Y, Manganaro TF, Tao X-J, Martimbeau S, Donahoe PK, Tilly JL. Requirement for Phosphati-dylinositol-3′-Kinase in Cytokine-Mediated Germ Cell Survival during Fetal Oogenesis in the Mouse. Endocrinology. 1999; 140: 941–949. doi: 10.1210/endo.140.2.6539 PMID: 9927327

Supporting Information – S1 Text
(with Tables A, B, C)

featuring the article

Feedbacks, Bifurcations, and Cell Fate Decision-Making in the p53 System

by Beata Hat, Marek Kochańczyk, Marta N. Bogdał, and Tomasz Lipniacki

PLOS Computational Biology 2016

Overview of mathematical models of the p53 system

Generation of oscillations

Bar-Or et al. [S1] found that oscillations arise due to the existence of the negative feedback loop coupling p53 with its inhibitor Mdm2 and proposed a three-component model with a hypothetical intermediate which introduces time delay between accumulation of p53 and accumulation of its inhibitor Mdm2, explaining the observed damped oscillations. Later, when Lahav et al. [S2] and Geva-Zatorski et al. [S3] demonstrated experimentally that single cells can exhibit undamped oscillations of p53 and Mdm2 levels, Ma et al. [S4] attributed time delays to the processes of Mdm2 transcription and translation, which resulted in the model featuring limit cycle oscillations. Later, Batchelor et al. [S5] demonstrated experimentally that oscillations require recurrent initiation of ATM pulses by Wip1 and proposed a model based on two negative feedback loops: one coupling p53 with Mdm2, the other involving p53, ATM, Chk2, and Wip1.

In the theoretical study from Tyson group, Ciliberto et al. [S6] introduced a positive feedback (in which p53 inhibits indirectly nuclear translocation of Mdm2, while Mdm2 degrades p53 in the nucleus) and demonstrated that it leads to more robust oscillations arising with non-zero amplitude either in the saddle–node–loop (SNL, also known as saddle node on invariant circle, SNIC) or in the cyclic fold bifurcation accompanying the subcritical Hopf bifurcation. However, the problem with SNL bifurcation is that in this bifurcation oscillations arise with infinite period while the period of oscillations in cells seems to be similar and roughly conserved, see Hat et al. [S7] for discussion.

p53 and cell fate decisions

Wee and Aguda (2006) [S8] demonstrated that the presence of the positive feedback following the scheme p53 → PTEN –| Pip3 → Akt → Mdm2 –| p53 introduces bistability that can be harnessed to control cell fate decisions.

Tyson group, extending their previous work [S6], proposed a small three-component model in which the positive feedback arises from the assumption that p53 synthesis is positively regulated by cytoplasmic Mdm2 [S9]. This model exhibits limit cycle oscillation between two cyclic fold bifurcations associated with subcritical Hopf bifurcations. The model was combined with the apoptotic/cell cycle arrest model in which three forms of p53 where introduced: p53-killer (that activates apoptotic genes like PUMA, p53DINP1 and p53AIP1), p53-helper (that induces p21 and Wip1 production, blocks CDK activity) and p53-lurker (that induces p21 production). In the resulting model, pulses of p53 lead to cell cycle arrest and, if sustained, to cell death.

Later, we (Puszynski et al. 2008 [S10]) proposed a more complex model of p53 regulation, exhibiting both oscillations and bistability. We found that the intact p53 system can exhibit oscillations in response to DNA damage, which can be either terminated when DNA is repaired, or the system may switch to the apoptotic state of a high p53 level when DNA repair is not accomplished in sufficiently short time. The positive feedback loop considered earlier by Wee and Aguda (2006) [S8] allows for switching to the apoptotic state and works as a clock. The cell can return to homeostasis if DNA repair is accomplished before the signal is relayed through the PTEN-controlled loop which inhibits Mdm2. We demonstrated that PTEN-deficient cells (such as MCF-7 line cells) exhibit sustained oscillations without triggering apoptosis. The idea was explored later by Wee et al. (2009) [S11], who augmented the p53 regulatory core with an apoptotic module involving Bax, Bad, Bcl-2, and Bcl-x$_L$.

Dynamics very similar to that of [S10] was achieved in an elaborate model proposed by Zhang et al. (2011) [S12]. The important modification introduced by the group of Zhang (see also Zhang et al. (2009) [S13] and Zhang et al. (2010) [S14]) was the inclusion of distinct phosphorylation states of p53: p53$_{ARRESTER}$ and p53$_{KILLER}$ which regulate different groups of genes. The model of Zhang et al. [S12] encompasses also the negative feedback loop mediated by Wip1, introduced earlier by Batchelor et al. [S5]. This allowed to analyze the competition between the p53/PTEN/Akt/Mdm2 and the ATM/p53/Wip1 feedbacks during DNA repair, and attribute pro- and anti-apoptotic roles to PTEN and Wip1, respectively.

2

The model

The proposed model of the p53 regulatory network consists of three modules: p53 core, cell cycle arrest module and apoptotic module. The cell cycle arrest and apoptotic modules have been described in detail in the main text. The detailed scheme of the core module is presented in Figure S1. Here, we describe briefly considered interactions and provide references to the literature.

DNA damage leads to the activation of ATM by phosphorylation at Ser1981 [S15,S16]. Activated ATM phosphorylates p53 at Ser15 and Ser20 to the $p53_{ARRESTER}$ form leading to its transcriptional activation and stabilization (reduction of the degradation rate) [S17–S23]. Simultaneously, ATM phosphorylates p53 inhibitor Mdm2 at Ser395 leading to its inactivation and destabilization (increase of the degradation rate) [S24]. Additionally, ATM phosphorylates SIAH1 at Ser19 leading to disruption of the HIPK2–SIAH1 complex resulting in HIPK2 accumulation [S25]. Kinase HIPK2 phosphorylates $p53_{ARRESTER}$ at Ser46 to the $p53_{KILLER}$ form [S26–S29]. $p53_{ARRESTER}$ and $p53_{KILLER}$ have different target genes. $p53_{ARRESTER}$ induces synthesis of p53 inhibitor Mdm2 [S30,S31], anti-apoptotic phosphatase Wip1 [S32] and cell cycle suppressor p21 [S33]. In turn, $p53_{KILLER}$ induces synthesis of pro-apoptotic protein Bax [S34] and pro-apoptotic phosphatase PTEN [S35].

Wip1 has 3 targets in the model; It dephosphorylates: ATM at Ser1981 [S36], Mdm2 at Ser395 (leading to its stabilization) [S37], and $p53_{KILLER}$ at Ser46 to $p53_{ARRESTER}$. PTEN mediates long positive feedback loop that stabilizes p53: it dephosphorylates PIP3 to PIP2 while PIP3 enables membrane localization of pro-survival kinase Akt, allowing its activation via phosphorylation at Thr308 [S38–S40]. Activated Akt phosphorylates Mdm2 at Ser166 and Ser186 enabling its translocation to the nucleus [S41], where it ubiquitinates all forms of p53 promoting their degradation by the proteasome [S42,S43]. This way PTEN accumulation leads to inhibition of Akt [S39], which itself is the activator of p53 inhibitor Mdm2 [S43]. Action of PTEN is opposed by growth factor stimulation leading to activation of kinase PI3K that phosphorylates PIP2 to PIP3 [S44,S45].

There are three outcomes from the core module, p21, Bax, and phosphorylated Akt. p21 regulates cell cycle arrest module in such a way that increase of p21 above some threshold leads suppression of cell cycle, while decrease of p21 below some lower threshold allows cell to return to the cycle. Bax and Akt regulate apoptotic module, in such a way that simultaneous increase of Bax level and decrease of phosphorylated Akt level lead to the irreversible apoptosis.

Supporting Tables

Table A. Notation guide.

Symbol	Description
Core module	
DNA_{DSB}	DNA damage due to IR: double strand breaks (DSBs)
ATM	kinase ATM
ATM_p	ATM phosphorylated at Ser1981 (upon DNA DSBs)
$Wip1_{gene}$	state of the Wip1 gene: active/inactive
$Wip1_{mRNA}$	Wip1 transcript
Wip1	phosphatase Wip1
$SIAH1_u$	unphosphorylated SIAH1
$SIAH1_p$	SIAH1 phosphorylated at Ser19
HIPK2	kinase HIPK2
$p53_{0p}$	unphosphorylated p53
$p53_{ARRESTER}$	p53 phosphorylated at Ser15, Ser20
$p53_{KILLER}$	p53 phosphorylated at Ser15, Ser20 and additionally at Ser46
$p53_{s46}$	p53 phosphorylated at Ser46 only
$Mdm2_{gene}$	state of the Mdm2 gene: active/inactive
$Mdm2_{mRNA}$	Mdm2 transcript
$Mdm2_{cyt\_0p}$	cytoplasmic, unphosphorylated Mdm2
$Mdm2_{cyt\_2p}$	cytoplasmic Mdm2 phosphorylated at Ser166 and Ser186
$Mdm2_{nuc\_2p}$	nuclear Mdm2 phosphorylated at Ser166 and Ser186
$Mdm2_{nuc\_3p}$	nuclear Mdm2 phosphorylated at Ser166, 186 and additionally at Ser395
PI3K	kinase PI3K
$PTEN_{gene}$	state of the PTEN gene: active/inactive
$PTEN_{mRNA}$	PTEN transcript
PIP2	bi-phosphatidylinositol
PIP3	tri-phosphatidylinositol
Akt_u	unphosphorylated AKT
Akt_p	Akt phosphorylated at Thr308
Apoptotic module	
Bax_{gene}	state of the Bax gene: active/inactive
Bax_{mRNA}	Bax transcript
Bax	unbound form of Bax
$Bclx_L$	unbound form of Bcl-x_L
Bax : $Bclx_L$	complex of Bax and Bcl-x_L
Bad_u	unbound, unphosphorylated Bad
Bad_p	Bad: unbound, phosphorylated at Ser75 and Ser99
$Bclx_L$: Bad_u	complex of Bcl-x_L and Bad_u
14-3-3	unbound adapter protein 14-3-3
Bad_p : 14-3-3	complex of Bad_p and 14-3-3
proCasp	inactive caspase
Casp	active caspase
Cell cycle arrest module	
$p21_{gene}$	state of the p21 gene: active/inactive
$p21_{mRNA}$	p21 transcript
p21	unbound p21
CycE	unbound Cyclin E
p21: CycE	complex of p21 and Cyclin E
$Rb1_u$	Rb1: unbound, unphosphorylated at Ser780
$Rb1_p$	Rb1: unbound, phosphorylated at Ser780
$Rb1_u$: E2F1	complex of unphosphorylated Rb1 and E2F1

4

Table B. List of parameters.

Parameter	Symbol	Value	Remarks	Ref.
Duration of the IR phase	IR_T	600 [s]	—	this study
IR dose	IR_{Gy}	1,2,3,4,10 [Gy]	—	this study
Number of DSBs per 1Gy of IR	DSB_{Gy}	10	—	[S4]*
Maximal number of DSBs	DSB_{max}	10^6	—	[S4]
Number of repair complexes	DSB_{rep}	20	—	[S4]
Total amount of Rb1	$Rb1_{tot}$	3×10^5 [mlcs/cell]	$Rb1_{tot} = Rb1_p(t) + Rb1_u(t)$ $+ Rb1_u{:}E2F1(t)$	this study
Total amount of E2F1	$E2F1_{tot}$	2×10^5 [mlcs/cell]	$E2F1_{tot} = E2F1(t)$ $+ Rb1_u{:}E2F1(t)$	this study
Total amount of Akt	Akt_{tot}	10^5 [mlcs/cell]	$Akt_{tot} = Akt_u(t) + Akt_p(t)$	this study
Total amount of PIP3 and PIP2	PIP_{tot}	10^5 [mlcs/cell]	$PIP_{tot} = PIP2(t) + PIP3(t)$	this study

*We consider only DSBs that undergo slow repair.

Table C. List of reactions.

Reaction	Rate	Coeff(s)	Value
Core module			
$\varnothing \xrightarrow{\text{IR}} DNA_{DSB}$	$h_1 \cdot \dfrac{DSB_{Gy} \cdot IR_{Gy}}{IR_T} \cdot (DSB_{max} - DNA_{DSB})$	h_1 DSB_{Gy} IR_{Gy}	10^{-6} 10 $1, 2, 3, 4, 10$
$\varnothing \xrightarrow{\text{Casp}} DNA_{DSB}$	$h_2 \cdot Casp \cdot (DSB_{max} - DNA_{DSB})$	IR_T DSB_{max} h_2	600 10^6 10^{-13}
$DNA_{DSB} \rightarrow \varnothing$	$\dfrac{rep}{DNA_{DSB} + DSB_{rep}}$	rep DSB_{rep}	10^{-3} 20
$ATM \xrightarrow{DNA_{DSB}} ATM_p$	$p_1 \cdot \dfrac{DNA_{DSB}^h}{M_1^h + DNA_{DSB}^h}$	p_1 h M_1	3×10^{-4} 2 5
$ATM \xleftarrow{\text{Wip1}} ATM_p$	$d_1 \cdot Wip1$	d_1	10^{-8}
$SIAH\text{-}1 \xrightarrow{ATM_p} SIAH\text{-}1_p$	$p_2 \cdot ATM_p$	p_2	10^{-8}
$SIAH\text{-}1 \leftarrow SIAH\text{-}1_p$	d_2	d_2	3×10^{-5}

Reaction	Rate	Parameter	Value
$\emptyset \rightarrow \text{HIPK2}$	s_8	s_8	3×10^{-5}
$\text{HIPK2} \xrightarrow{\text{Mdm2}_{\text{nuc\_2p}},\ \text{SIAH1}} \emptyset$	$g_7 \cdot (SIAH1_u + Mdm2_{\text{nuc\_2p}})^2$	g_7	3×10^{-5}
$\emptyset \xrightarrow{\text{p53}_{\text{KILLER}}} \text{Wip1}_{\text{mRNA}}$	$s_1 \cdot \dfrac{q_{0\_\text{Wip1}} + q_{1\_\text{Wip1}} \cdot p53_{\text{KILLER}}^h}{q_2 + q_{0\_\text{Wip1}} + q_{1\_\text{Wip1}} \cdot p53_{\text{KILLER}}^h}$	s_1 q_{0_Wip1} q_{1_Wip1} h q_2	0.1 10^{-5} 3×10^{-13} 2 3×10^{-3}
$\text{Wip1}_{\text{mRNA}} \rightarrow \emptyset$	g_1	g_1	3×10^{-4}
$\emptyset \rightarrow \text{Wip1}$	$t_1 \cdot Wip1_{\text{mRNA}}$	t_1	3×10^{-5}
$\text{Wip1} \rightarrow \emptyset$	g_8	g_8	3×10^{-13}
$\emptyset \rightarrow \text{p53}_{0p}$	s_6	s_6	300
$\text{p53}_{0p} \rightarrow \emptyset$	g_{101}	g_{101}	0.1×10^{-13}
$\text{p53}_{0p} \xrightarrow{\text{Mdm2}_{\text{nuc\_2p}}} \emptyset$	$g_{11} \cdot Mdm2_{\text{nuc\_2p}}^2$	g_{11}	100×10^{-13}
$\text{p53}_{\text{ARRESTER}} \xrightarrow{\text{Mdm2}_{\text{nuc\_2p}}} \emptyset$ $\text{p53}_{\text{KILLER}} \xrightarrow{\text{Mdm2}_{\text{nuc\_2p}}} \emptyset$ $\text{p53}_{s46} \xrightarrow{\text{Mdm2}_{\text{nuc\_2p}}} \emptyset$	$g_{12} \cdot Mdm2_{\text{nuc\_2p}}^2$	g_{12}	10^{-13}
$\text{p53}_{0p} \xrightarrow{\text{ATM}_p} \text{p53}_{\text{ARRESTER}}$	$p_3 \cdot ATM_p$	p_3	3×10^{-8}
$\text{p53}_{0p} \leftarrow \text{p53}_{\text{ARRESTER}}$	d_3	d_3	10^{-4}
$\text{p53}_{0p} \xrightarrow{\text{HIPK2}} \text{p53}_{s46}$	$p_4 \cdot HIPK2$	p_4	10^{-10}
$\text{p53}_{0p} \leftarrow \text{p53}_{s46}$	$d_4 \cdot Wip1$	d_4	10^{-10}
$\emptyset \xrightarrow{\text{p53}_{\text{ARRESTER}}} \text{Mdm2}_{\text{mRNA}}$	$s_3 \cdot \dfrac{q_{0\_\text{Mdm2}} + q_{1\_\text{Mdm2}} \cdot p53_{\text{ARRESTER}}^h}{q_2 + q_{0\_\text{Mdm2}} + q_{1\_\text{Mdm2}} \cdot p53_{\text{ARRESTER}}^h}$	s_3 q_{0_Mdm2} q_{1_Mdm2} h q_2	0.1 10^{-4} 3×10^{-13} 2 3×10^{-3}
$\text{Mdm2}_{\text{mRNA}} \rightarrow \emptyset$	g_1	g_1	3×10^{-4}
$\text{Mdm2}_{\text{mRNA}} \rightarrow \text{Mdm2}_{\text{cyt\_0p}}$	$t_3 \cdot Mdm2_{\text{mRNA}}$	t_3	0.1
$\text{Mdm2}_{\text{cyt\_0p}} \xrightarrow{\text{AKT}_p} \text{Mdm2}_{\text{cyt\_2p}}$	$p_5 \cdot Akt_p$	p_5	10^{-8}
$\text{Mdm2}_{\text{cyt\_0p}} \leftarrow \text{Mdm2}_{\text{cyt\_2p}}$	d_5	d_5	10^{-4}
$\text{Mdm2}_{\text{cyt\_2p}} \rightarrow \text{Mdm2}_{\text{nuc\_2p}}$	i_1	i_1	10^{-3}
$\text{Mdm2}_{\text{nuc\_2p}} \xrightarrow{\text{ATM}_p} \text{Mdm2}_{\text{nuc\_3p}}$	$p_6 \cdot ATM_p$	p_6	10^{-8}
$\text{Mdm2}_{\text{nuc\_2p}} \xleftarrow{\text{Wip1}} \text{Mdm2}_{\text{nuc\_3p}}$	$d_6 \cdot Wip1$	d_6	10^{-10}
$\text{Mdm2}_{\text{cyt\_0p}} \rightarrow \emptyset$	g_{14}	g_{14}	10^{-13}
$\text{Mdm2}_{\text{cyt\_2p}} \rightarrow \emptyset$ $\text{Mdm2}_{\text{nuc\_2p}} \rightarrow \emptyset$	g_{15}	g_{15}	3×10^{-14}
$\text{Mdm2}_{\text{nuc\_3p}} \rightarrow \emptyset$	g_{16}	g_{16}	10^{-13}
$\emptyset \xrightarrow{\text{p53}_{\text{KILLER}}} \text{PTEN}_{\text{mRNA}}$	$s_2 \cdot \dfrac{q_{0\_\text{PTEN}} + q_{1\_\text{PTEN}} \cdot p53_{\text{KILLER}}^h}{q_2 + q_{0\_\text{PTEN}} + q_{1\_\text{PTEN}} \cdot p53_{\text{KILLER}}^h}$	s_2 q_{0_PTEN} q_{1_PTEN} h q_2	0.03 10^{-5} 3×10^{-13} 2 3×10^{-3}
$\text{PTEN}_{\text{mRNA}} \rightarrow \emptyset$	g_2	g_2	3×10^{-4}
$\emptyset \rightarrow \text{PTEN}$	$t_2 \cdot PTEN_{\text{mRNA}}$	t_2	0.1
$\text{PTEN} \rightarrow \emptyset$	g_6	g_6	10^{-13}
$\text{PIP2} \xrightarrow{\text{PI3K}} \text{PIP3}$	$p_8 \cdot PI3K$	p_8	3×10^{-9}
$\text{PIP2} \xleftarrow{\text{PTEN}} \text{PIP3}$	$d_7 \cdot PTEN$	d_7	3×10^{-7}
$\text{Akt} \xrightarrow{\text{PIP3}} \text{Akt}_p$	$p_{12} \cdot PIP3$	p_{12}	10^{-9}
$\text{Akt} \leftarrow \text{Akt}_p$	d_8	d_8	10^{-4}

Apoptotic module			
$\emptyset \xrightarrow{\text{p53}_{\text{KILLER}}} \text{Bax}_{\text{mRNA}}$	$s_4 \cdot \dfrac{q_{0\_\text{Bax}} + q_{1\_\text{Bax}} \cdot p53_{\text{KILLER}}^h}{q_2 + q_{0\_\text{Bax}} + q_{1\_\text{Bax}} \cdot p53_{\text{KILLLER}}^h}$	s_4 q_{0_Bax} q_{1_Bax} h q_2	0.03 10^{-5} 3×10^{-13} 2 3×10^{-3}
$\text{Bax}_{\text{mRNA}} \to \emptyset$	g_4	g_4	3×10^{-4}
$\emptyset \to \text{Bax}$	$t_4 \cdot Bax_{\text{mRNA}}$	t_4	0.1
$\text{Bax} \to \emptyset$	g_9	g_9	10^{-13}
$\text{Bax} \to \text{Bclx}_{\text{L}}$	b_1	b_1	3×10^{-5}
$\text{Bax} \leftarrow \text{Bclx}_{\text{L}}$	u_1	u_1	10^{-3}
$\text{Bax}: \text{Bclx}_{\text{L}} \to \text{Bclx}_{\text{L}}$	g_{16}	g_{16}	10^{-13}
$\text{Bclx}_{\text{L}} + \text{Bad}_{\text{u}} \to \text{Bclx}_{\text{L}}: \text{Bad}_{\text{u}}$	b_2	b_2	3×10^{-3}
$\text{Bclx}_{\text{L}} + \text{Bad}_{\text{u}} \leftarrow \text{Bclx}_{\text{L}}: \text{Bad}_{\text{u}}$	u_2	u_2	10^{-3}
$\text{Bclx}_{\text{L}}: \text{Bad}_{\text{u}} \xrightarrow{\text{Akt}_{\text{p}}} \text{Bclx}_{\text{L}}$	$p_7 \cdot Akt_{\text{p}}$	p_7	3×10^{-9}
$\text{Bad}_{\text{u}} \xrightarrow{\text{AKT}_{\text{p}}} \text{Bad}_{\text{p}}$	$p_7 \cdot Akt_{\text{p}}$	p_7	3×10^{-9}
$\text{Bad}_{\text{u}} \leftarrow \text{Bad}_{\text{p}}$	d_9	d_9	3×10^{-5}
$\text{Bad}_{\text{p}} + \text{14-3-3} \to \text{Bad}_{\text{p}}: \text{14-3-3}$	b_3	b_3	3×10^{-3}
$\text{Bad}_{\text{p}} + \text{14-3-3} \leftarrow \text{Bad}_{\text{p}}: \text{14-3-3}$	u_3	u_3	10^{-3}
$\text{Bad}_{\text{p}}: \text{14-3-3} \to \text{Bad}_{\text{u}} + \text{14-3-3}$	d_9	d_9	3×10^{-5}
$\emptyset \to \text{proCasp}$	s_7	s_7	30
$\text{proCasp} \xrightarrow{\text{Bax, Casp}} \text{Casp}$	$a_1 \cdot Bax + a_2 \cdot Casp^2$	a_1 a_2	3×10^{-10} 10^{-12}
$\text{proCasp} \to \emptyset$ $\text{Casp} \to \emptyset$	g_{17}	g_{17}	3×10^{-13}
Cell cycle arrest module			
$\emptyset \xrightarrow{\text{p53}_{\text{ARRESTER}}} \text{p21}_{\text{mRNA}}$	$s_5 \cdot \dfrac{q_{0\_p21} + q_{1\_p21} \cdot p53_{\text{ARRESTER}}^h}{q_2 + q_{0\_p21} + q_{1\_p21} \cdot p53_{\text{ARRESTER}}^h}$	s_5 q_{0_p21} q_{1_p21} h q_2	0.1 10^{-5} 10^{-13} 2 3×10^{-3}
$\text{p21}_{\text{mRNA}} \to \emptyset$	g_5	g_5	3×10^{-4}
$\emptyset \to \text{p21}$	$t_5 \cdot p21_{\text{mRNA}}$	t_5	0.1
$\text{p21} \to \emptyset$	g_{19}	g_{19}	3×10^{-13}
$\text{p21} + \text{CycE} \to \text{p21}: \text{CycE}$	b_5	b_5	10^{-5}
$\text{p21} + \text{CycE} \leftarrow \text{p21}: \text{CycE}$	u_6	u_6	10^{-14}
$\text{p21}: \text{CycE} \to \emptyset$	g_{20}	g_{20}	10^{-13}
$\text{Rb1} \xrightarrow{\text{CycE}} \text{Rb1}_{\text{p}}$	$p_9 \cdot CycE$	p_9	3×10^{-6}
$\text{Rb1} \leftarrow \text{Rb1}_{\text{p}}$	$\dfrac{d_{12}}{M_2 + Rb1_{\text{p}}}$	d_{12} M_2	10^4 10^5
$\text{Rb1}_{\text{u}} + \text{E2F1} \to \text{Rb1}_{\text{u}}: \text{E2F1}$	b_4	b_4	10^{-5}
$\text{Rb1}_{\text{u}} + \text{E2F1} \leftarrow \text{Rb1}_{\text{u}}: \text{E2F1}$	u_5	u_5	10^{-14}
$\text{Rb1}_{\text{u}}: \text{E2F1} \xrightarrow{\text{CycE}} \text{Rb1}_{\text{p}} + \text{E2F1}$	$p_{10} \cdot CycE$	p_{10}	3×10^{-6}

Supplementary references

S1. Bar-Or RL, Maya R, Segel LA, Alon U, Levine AJ, Oren M. Generation of oscillations by the p53-Mdm2 feedback loop: A theoretical and experimental study. *Proc Natl Acad Sci USA*. 2000;97: 11250–11255. doi:10.1073/pnas.210171597

S2. Lahav G, Rosenfeld N, Sigal A, Geva-Zatorsky N, Levine AJ, Elowitz MB, et al. Dynamics of the p53-Mdm2 feedback loop in individual cells. *Nat Genet*. 2004;36: 147–150. doi:10.1038/ng1293

S3. Geva-Zatorsky N, Rosenfeld N, Itzkovitz S, Milo R, Sigal A, Dekel E, et al. Oscillations and variability in the p53 system. *Mol Syst Biol.* 2006;2: 2006.0033. doi:10.1038/msb4100068

S4. Ma L, Wagner J, Rice JJ, Hu W, Levine AJ, Stolovitzky GA. A plausible model for the digital response of p53 to DNA damage. *Proc Natl Acad Sci USA*. 2005;102: 14266–14271. doi:10.1073/pnas.0501352102

S5. Batchelor E, Mock CS, Bhan I, Loewer A, Lahav G. Recurrent initiation: a mechanism for triggering p53 pulses in response to DNA damage. *Mol Cell.* 2008;30: 277–289. doi:10.1016/j.molcel.2008.03.016

S6. Ciliberto A, Novak B, Tyson JJ. Steady states and oscillations in the p53/Mdm2 network. *Cell Cycle*. 2005;4: 488–493.

S7. Hat B, Puszynski K, Lipniacki T. Exploring mechanisms of oscillations in p53 and nuclear factor-B systems. *IET Syst Biol*. 2009;3: 342–355. doi:10.1049/iet-syb.2008.0156

S8. Wee KB, Aguda BD. Akt versus p53 in a Network of Oncogenes and Tumor Suppressor Genes Regulating Cell Survival and Death. *Biophys J*. 2006;91: 857–865. doi:10.1529/biophysj.105.077693

S9. Zhang T, Brazhnik P, Tyson JJ. Exploring mechanisms of the DNA-damage response: p53 pulses and their possible relevance to apoptosis. *Cell Cycle*. 2007;6: 85–94.

S10. Puszyński K, Hat B, Lipniacki T. Oscillations and bistability in the stochastic model of p53 regulation. *J Theor Biol*. 2008;254: 452–465. doi:10.1016/j.jtbi.2008.05.039

S11. Wee KB, Surana U, Aguda BD. Oscillations of the p53-Akt Network: Implications on Cell Survival and Death. *PLoS ONE*. 2009;4: e4407. doi:10.1371/journal.pone.0004407

S12. Zhang X-P, Liu F, Wang W. Two-phase dynamics of p53 in the DNA damage response. *Proc Natl Acad Sci USA*. 2011;108: 8990–8995. doi:10.1073/pnas.1100600108

S13. Zhang X-P, Liu F, Cheng Z, Wang W. Cell fate decision mediated by p53 pulses. *Proc Natl Acad Sci USA*. 2009;106: 12245–12250. doi:10.1073/pnas.0813088106

S14. Zhang X-P, Liu F, Wang W. Coordination between Cell Cycle Progression and Cell Fate Decision by the p53 and E2F1 Pathways in Response to DNA Damage. *J Biol Chem*. 2010;285: 31571–31580. doi:10.1074/jbc.M110.134650

S15. So S, Davis AJ, Chen DJ. Autophosphorylation at serine 1981 stabilizes ATM at DNA damage sites. *J Cell Biol*. 2009;187: 977–990. doi:10.1083/jcb.200906064

S16. Bakkenist CJ, Kastan MB. DNA damage activates ATM through intermolecular autophosphorylation and dimer dissociation. *Nature*. 2003;421: 499–506. doi:10.1038/nature01368

S17. Banin S, Moyal L, Shieh S-Y, Taya Y, Anderson CW, Chessa L, et al. Enhanced Phosphorylation of p53 by ATM in Response to DNA Damage. *Science*. 1998;281: 1674–1677. doi:10.1126/science.281.5383.1674

S18. Canman CE, Lim D-S, Cimprich KA, Taya Y, Tamai K, Sakaguchi K, et al. Activation of the ATM Kinase by Ionizing Radiation and Phosphorylation of p53. *Science*. 1998;281: 1677–1679. doi:10.1126/science.281.5383.1677

S19. Chehab NH, Malikzay A, Stavridi ES, Halazonetis TD. Phosphorylation of Ser-20 mediates stabilization of human p53 in response to DNA damage. *Proc Natl Acad Sci USA*. 1999;96: 13777–13782.

S20. Shieh SY, Taya Y, Prives C. DNA damage-inducible phosphorylation of p53 at N-terminal sites including a novel site, Ser20, requires tetramerization. *EMBO J*. 1999;18: 1815–1823. doi:10.1093/emboj/18.7.1815

S21. Wei C-L, Wu Q, Vega VB, Chiu KP, Ng P, Zhang T, et al. A global map of p53 transcription-factor binding sites in the human genome. *Cell*. 2006;124: 207–219. doi:10.1016/j.cell.2005.10.043

S22. Shieh SY, Ikeda M, Taya Y, Prives C. DNA damage-induced phosphorylation of p53 alleviates inhibition by MDM2. *Cell*. 1997;91: 325–334.

S23. Siliciano JD, Canman CE, Taya Y, Sakaguchi K, Appella E, Kastan MB. DNA damage induces phosphorylation of the amino terminus of p53. *Genes Dev*. 1997;11: 3471–3481.

S24. Maya R, Balass M, Kim S-T, Shkedy D, Leal J-FM, Shifman O, et al. ATM-dependent phosphorylation of Mdm2 on serine 395: role in p53 activation by DNA damage. *Genes Dev*. 2001;15: 1067–1077. doi:10.1101/gad.886901

S25. Winter M, Sombroek D, Dauth I, Moehlenbrink J, Scheuermann K, Crone J, et al. Control of HIPK2 stability by ubiquitin ligase Siah-1 and checkpoint kinases ATM and ATR. *Nat Cell Biol*. 2008;10: 812–824. doi:10.1038/ncb1743

S26. D'Orazi G, Cecchinelli B, Bruno T, Manni I, Higashimoto Y, Saito S, et al. Homeodomain-interacting protein kinase-2 phosphorylates p53 at Ser 46 and mediates apoptosis. *Nat Cell Biol*. 2002;4: 11–19. doi:10.1038/ncb714

S27. Dauth I, Krüger J, Hofmann TG. Homeodomain-interacting protein kinase 2 is the ionizing radiation-activated p53 serine 46 kinase and is regulated by ATM. *Cancer Res*. 2007;67: 2274–2279. doi:10.1158/0008-5472.CAN-06-2884

S28. Hofmann TG, Möller A, Sirma H, Zentgraf H, Taya Y, Dröge W, et al. Regulation of p53 activity by its interaction with homeodomain-interacting protein kinase-2. *Nat Cell Biol*. 2002;4: 1–10. doi:10.1038/ncb715

S29. Tomasini R, Samir AA, Carrier A, Isnardon D, Cecchinelli B, Soddu S, et al. TP53INP1s and Homeodomain-interacting Protein Kinase-2 (HIPK2) Are Partners in Regulating p53 Activity. *J Biol Chem*. 2003;278: 37722–37729. doi:10.1074/jbc.M301979200

S30. Barak Y, Juven T, Haffner R, Oren M. mdm2 expression is induced by wild type p53 activity. *EMBO J*. 1993;12: 461–468.

S31. Kubbutat MHG, Jones SN, Vousden KH. Regulation of p53 stability by Mdm2. *Nature*. 1997;387: 299–303. doi:10.1038/387299a0

S32. Fiscella M, Zhang H, Fan S, Sakaguchi K, Shen S, Mercer WE, et al. Wip1, a novel human protein phosphatase that is induced in response to ionizing radiation in a p53-dependent manner. *Proc Natl Acad Sci USA*. 1997;94: 6048–6053.

S33. el-Deiry WS, Tokino T, Velculescu VE, Levy DB, Parsons R, Trent JM, et al. WAF1, a potential mediator of p53 tumor suppression. *Cell*. 1993;75: 817–825.

S34. Miyashita T, Reed JC. Tumor suppressor p53 is a direct transcriptional activator of the human bax gene. *Cell*. 1995;80: 293–299.

S35. Stambolic V, MacPherson D, Sas D, Lin Y, Snow B, Jang Y, et al. Regulation of PTEN transcription by p53. *Mol Cell*. 2001;8: 317–325.

S36. Shreeram S, Demidov ON, Hee WK, Yamaguchi H, Onishi N, Kek C, et al. Wip1 Phosphatase Modulates ATM-Dependent Signaling Pathways. *Mol Cell*. 2006;23: 757–764. doi:10.1016/j.molcel.2006.07.010

S37. Lu X, Nguyen T-A, Zhang X, Donehower LA. The Wip1 phosphatase and Mdm2: cracking the "Wip" on p53 stability. *Cell Cycle*. 2008;7: 164–168.

S38. Marte BM, Downward J. PKB/Akt: connecting phosphoinositide 3-kinase to cell survival and beyond. *Trends Biochem Sci*. 1997;22: 355–358. doi:10.1016/S0968-0004(97)01097-9

S39. Kandel ES, Hay N. The regulation and activities of the multifunctional serine/threonine kinase Akt/PKB. *Exp Cell Res*. 1999;253: 210–229. doi:10.1006/excr.1999.4690

S40. Franke TF, Yang S-I, Chan TO, Datta K, Kazlauskas A, Morrison DK, et al. The protein kinase encoded by the Akt proto-oncogene is a target of the PDGF-activated phosphatidylinositol 3-kinase. *Cell*. 1995;81: 727–736. doi:10.1016/0092-8674(95)90534-0

S41. Mayo LD, Donner DB. A phosphatidylinositol 3-kinase/Akt pathway promotes translocation of Mdm2 from the cytoplasm to the nucleus. *Proc Natl Acad Sci USA*. 2001;98: 11598–11603. doi:10.1073/pnas.181181198

S42. Haupt Y, Maya R, Kazaz A, Oren M. Mdm2 promotes the rapid degradation of p53. *Nature*. 1997;387: 296–299. doi:10.1038/387296a0

S43. Ogawara Y, Kishishita S, Obata T, Isazawa Y, Suzuki T, Tanaka K, et al. Akt Enhances Mdm2-mediated Ubiquitination and Degradation of p53. *J Biol Chem*. 2002;277: 21843–21850. doi:10.1074/jbc.M109745200

S44. Carracedo A, Pandolfi PP. The PTEN–PI3K pathway: of feedbacks and cross-talks. *Oncogene*. 2008;27: 5527–5541. doi:10.1038/onc.2008.247

S45. Cantley LC. The Phosphoinositide 3-Kinase Pathway. *Science*. 2002;296: 1655–1657. doi:10.1126/science.296.5573.1655

SCIENTIFIC REPORTS

Relaxation oscillations and hierarchy of feedbacks in MAPK signaling

Marek Kochańczyk[1], Paweł Kocieniewski[1], Emilia Kozłowska[2,†], Joanna Jaruszewicz-Błońska[1], Breanne Sparta[3], Michael Pargett[3], John G. Albeck[3], William S. Hlavacek[4] & Tomasz Lipniacki[1]

We formulated a computational model for a MAPK signaling cascade downstream of the EGF receptor to investigate how interlinked positive and negative feedback loops process EGF signals into ERK pulses of constant amplitude but dose-dependent duration and frequency. A positive feedback loop involving RAS and SOS, which leads to bistability and allows for switch-like responses to inputs, is nested within a negative feedback loop that encompasses RAS and RAF, MEK, and ERK that inhibits SOS via phosphorylation. This negative feedback, operating on a longer time scale, changes switch-like behavior into oscillations having a period of 1 hour or longer. Two auxiliary negative feedback loops, from ERK to MEK and RAF, placed downstream of the positive feedback, shape the temporal ERK activity profile but are dispensable for oscillations. Thus, the positive feedback introduces a hierarchy among negative feedback loops, such that the effect of a negative feedback depends on its position with respect to the positive feedback loop. Furthermore, a combination of the fast positive feedback involving slow-diffusing membrane components with slower negative feedbacks involving faster diffusing cytoplasmic components leads to local excitation/global inhibition dynamics, which allows the MAPK cascade to transmit paracrine EGF signals into spatially non-uniform ERK activity pulses.

A canonical mitogen-activated protein kinase (MAPK) pathway responsible for transducing signals from growth factors consists of three tiers of sequentially activated protein kinases: RAF, MEK, and ERK[1]. Activated ERK, considered the output of the cascade, phosphorylates more than 100 substrates including several transcription factors[2] and elicits a variety of cellular responses including growth, proliferation, and differentiation[3,4]. Unsurprisingly, dysregulated MAPK signaling underlies many cancers[5]. There is growing evidence that the cell fate decisions are regulated by temporal[6–8] or even spatiotemporal profiles of ERK and RAF[9–15]. It is thus important to understand how information about the level and gradient of an extracellular stimulus is encoded and transmitted to intracellular downstream effectors.

In the last two decades, numerous positive and negative feedback loops regulating the MAPK network have been discovered and characterized[16,17]. A positive feedback from RAS to SOS allows for signal amplification in the vicinity of the receptor and has been proposed to introduce bistability[18], which enables the system to respond to inputs in a switch-like (digital) fashion[19]. Negative feedbacks emanating from ERK have been associated mainly with response attenuation[20], but negative feedbacks in general may be harnessed to ensure perfect adaptation[21,22] or give rise to oscillations[23–26]. System-level mechanisms of controlling information processing in MAPK are still not fully understood, partially due to the fact that systems involving interlocked positive and negative feedback loops may exhibit rich nonlinear dynamical behavior. Dynamics assumed by such complex systems depends on the characteristic time scales involved and network connectivity/topology, i.e., where the feedbacks act and how they relate to each other. For example, sustained oscillations may arise when a negative feedback loop is embedded within a relatively slow positive feedback loop[27] or when a positive feedback loop is embedded within a relatively slow negative feedback loop[28]. In the latter case, the time profiles may be similar to those produced by

[1]Institute of Fundamental Technological Research, Polish Academy of Sciences, Warsaw, Poland. [2]Institute of Automatic Control, Silesian University of Technology, Gliwice, Poland. [3]Department of Molecular and Cellular Biology, University of California, Davis, California, United States of America. [4]Theoretical Biology and Biophysics Group, Theoretical Division, Los Alamos National Laboratory, Los Alamos, New Mexico, United States of America. [†]Present address: Research Programs Unit, Genome-Scale Biology, Faculty of Medicine, University of Helsinki, Helsinki, Finland. Correspondence and requests for materials should be addressed to M.K. (email: mkochan@ippt.pan.pl) or T.L. (email: tlipnia@ippt.pan.pl)
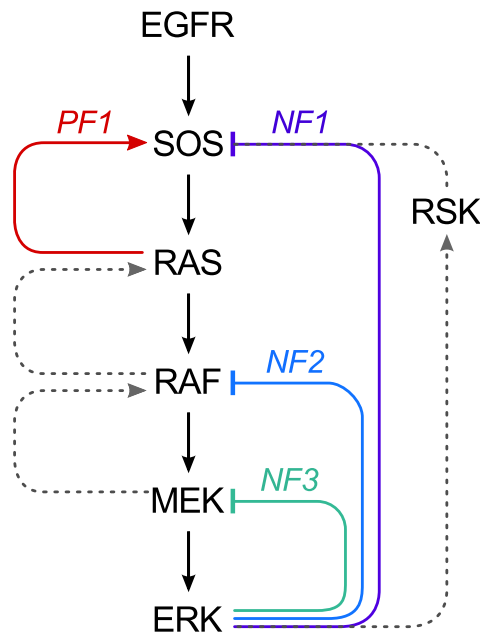
Figure 1. Feedback loops in the MAPK/ERK pathway. Loops captured in the model are shown with solid lines. The arrow labeled PF1 represents positive feedback. This feedback loop has been implicated in mediating bistable switching. The arrows labeled NF1–NF3 represent negative feedbacks. The NF1 feedback loop encompasses the positive feedback loop. The NF2 and NF3 feedback loops are placed out of the positive feedback loop. Dotted lines indicate feedbacks not included in the model.

a relaxation oscillator, i.e., consisting of a fast activation phase and a phase of (usually slow) relaxation to a state in which subsequent activation is possible[29]. In recent work[30], we observed similar pulses using a sensor based on phosphorylation-regulated Förster resonance energy transfer (FRET) to monitor EGF-stimulated ERK activity in single MCF10A cells. These pulses differ from constant-frequency quasisinusoidal oscillations in ERK nuclear translocation observed in other studies[26] and are characterized by an EGF dose-independent amplitude and an EGF dose-dependent period.

In this study, we construct a computational model for MAPK/ERK signaling downstream of EGFR with three aims: (i) to verify whether the combination of the positive and negative feedbacks considered in the model leads to observed relaxation oscillations, (ii) to characterize the functional roles of the different feedback loops depending on their position in the network, and (iii) to analyze the consequences of proteins participating in the feedback loops being localized to distinct subcellular compartments (the plasma membrane or the cytosol) for spatiotemporal profiles of the response. We restrict our analysis to four feedbacks: one positive and three negative (shown in Fig. 1 and discussed in Supplementary Text S1). The proposed model is corroborated by experimental analysis of single-cell responses to a broad range of EGF doses using a fast sensor of ERK activity based on phosphorylation-dependent regulation of nucleocytoplasmic shuttling[31,32].

Results

Model. We constructed a model for EGFR-mediated activation of ERK that captures the feedback loops illustrated in Fig. 1. In addition to well-known negative feedbacks from ERK to its upstream signaling partners, MEK, RAF, and SOS, which have been considered in earlier experimental and modeling studies, our model includes a positive feedback loop involving SOS and RAS. This relatively recently discovered feedback loop, labeled PF1 in Fig. 1, is upstream of negative feedback from ERK to RAF (labeled NF2 in Fig. 1), as well as negative feedback from ERK to MEK (labeled NF3 in Fig. 1), and it is encompassed within the negative feedback loop involving ERK and SOS (labeled NF1 in Fig. 1). It is known that interlocked positive and negative feedback loops can give rise to excitatory behavior, which we have observed in a recent study of single-cell ERK dynamics[30]. Our model was built and analyzed to determine whether positive feedback between plasma membrane-associated signaling proteins could potentially be responsible for the observed behavior, which includes apparent relaxation oscillations in ERK activity.

We formulated the model as a system of coupled ordinary differential equations (ODEs) for the mass-action kinetics of the reaction scheme shown in Fig. 2. Although this scheme provides a simplified representation of the MAPK signaling network downstream of EGFR, it preserves the dynamical structure of the network, meaning that it includes the essential processes responsible for the feedbacks connecting the main signaling proteins of the network (cf. Figs 1 and 2). Importantly, with this model, we can assign values to parameters that determine the relative time scales of activating and inhibiting processes. As we will discuss later, we considered two extensions of the model. One is a Markov chain that includes the same processes as those considered in the ODE model but adds stochastic processes that affect the level of EGFR expression on the surface of a single cell. This model
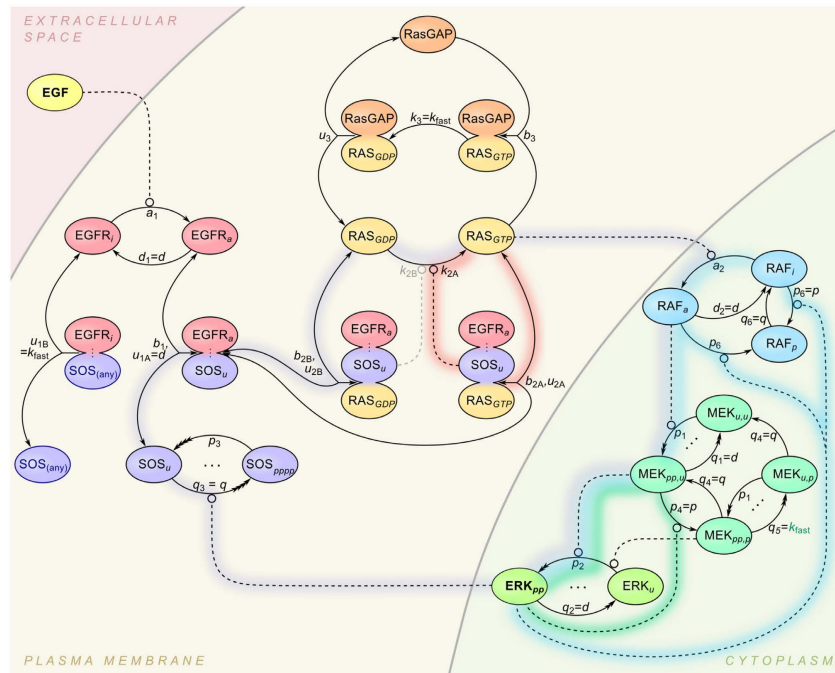
Figure 2. Model for MAPK signaling. Reactions considered in the model are represented by lines with arrowheads. Multiple arrowheads denote reactions with multiple steps (e.g., multi-site phosphorylation of SOS by ERK). Positive influences (e.g., ERK-catalyzed phosphorylation of SOS) are indicated by lines attached to small circles, with the circles identifying the reactions affected. The reactions and influences responsible for various feedback mechanisms are highlighted with shading: RAS-to-SOS positive feedback (red shading), ERK-to-SOS negative feedback (purple shading), ERK-to-MEK negative feedback (green shading), and ERK-to-RAF negative feedback (blue shading). Tripartite arrows, labeled with both binding and unbinding rate constants, are used to represent association and dissociation reactions.

extension is intended to account for extrinsic noise and the heterogeneity of cell populations (see Materials and Methods). The second extended model consists of a set of partial differential equations (PDEs). These equations incorporate the right-hand side terms of the ODE model. Reaction–diffusion processes in the extracellular space, on the plasma membrane, and in the cytosol are coupled through Robin-type boundary conditions. This model extension was formulated to study the subcellular spatial heterogeneity of responses to paracrine signaling, modeled as secretion of EGF at random times and random extracellular locations (see Materials and Methods).

An executable specification of the ODE model and the extended stochastic version of the model are provided in Supplementary Data 1. Default parameter settings for the ODE model are summarized in Supplementary Table S1. Supplementary Text S2 and Supplementary Table S2 contain non-dimensional model equations and parameters, respectively. Code for bifurcation analysis are provided in Supplementary Data 2. The stochastic extension of the ODE model has unique parameters that describe the dynamics of EGFR surface expression (Supplementary Table S3) and is provided in Supplementary Data 3. An executable specification of the PDE model is provided in Supplementary Data 4. This model has unique parameters that describe diffusion processes and paracrine signaling (Supplementary Table S4). Parameters were assigned default values as described in Materials and Methods. Simulations and bifurcation analyses were performed as described in Materials and Methods.

Positive feedback and bistability. According to the model with the default parameter settings of Supplementary Table S1, in the absence of negative feedbacks, the system exhibits bistability, i.e., bistable switching behavior (also known as hysteretic switching). As illustrated in Fig. 3, bistability depends on parameters governing positive feedback between SOS and RAS (Fig. 3A), as well as parameters governing saturation of RasGAP (Fig. 3B).

The results of Fig. 3A are consistent with earlier work, which has implicated positive feedback from SOS to RAS in hysteretic switching[33]. Positive feedback arises because the product of SOS's GEF activity, which is RAS-GTP, binds to SOS at SOS's REM domain, which is non-overlapping with SOS's GEF domain (also known as the Cdc25 homology domain). The outcome of RAS-GTP binding to SOS is an increase in the GEF activity of SOS. RAS-GDP binding to SOS also increases SOS's GEF activity, but to a lesser extent. The parameter values of Supplementary Table S1 were selected so that positive feedback from SOS to RAS generates hysteretic switching in the absence of negative feedbacks. The parameter values characterizing SOS GEF activity (k_{2C}, k_{2B}, and k_{2A}) are such that SOS's GEF activity is zero when its REM domain is not bound to RAS (i.e., $k_{2C} = 0$), and its GEF activity when SOS's REM domain is bound to RAS-GDP is an order of magnitude lower than when SOS's REM domain
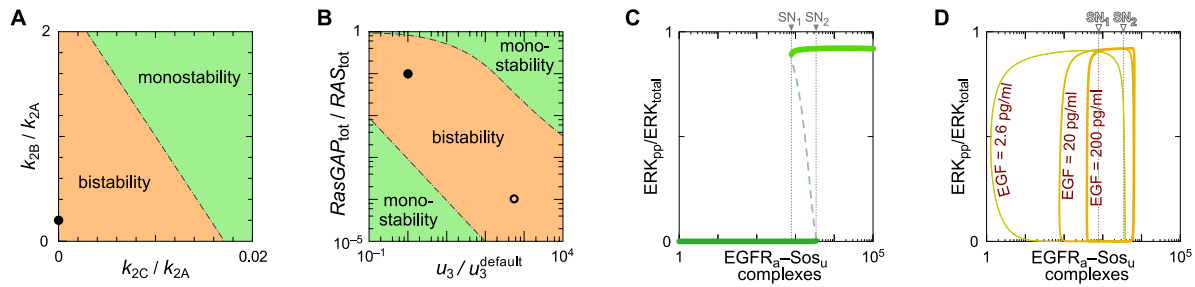
Figure 3. Conditions for bistability and the emergence of relaxation oscillations. With all negative feedbacks removed, the system exhibits either bistable switching or graded responses to EGF stimulation depending on parameter values. (**A**) Range of parameters governing positive feedback for which the system exhibits bistability (for some EGF concentrations higher than 0.1 pg/ml). The parameters are ratios of rate constants, which characterize the relative nucleotide exchange activity of SOS when the REM domain in SOS is not bound to RAS or bound to RAS-GDP compared to the activity when the REM domain is bound to RAS-GTP (k_{2C}/k_{2A} and k_{2B}/k_{2A}). We vary these ratios with k_{2A} fixed at the value given in Supplementary Table S1. (**B**) Range of parameters governing saturation of RasGAP for which the system exhibits bistability (for some EGF concentrations higher than 0.1 pg/ml). The parameters considered in this diagram characterize RasGAP activity: the ratio of enzyme (RasGAP$_{tot}$) to substrate (RAS$_{tot}$) and the rate constant for dissociation of the enzyme-product complex (u_3). We vary the ratio RasGAP$_{tot}$/RAS$_{tot}$ by varying RasGAP$_{tot}$ while keeping the value of the product $b_3 \times$ RasGAP$_{tot}$ constant. This product governs the rate of formation of the enzyme-substrate complex. For more information about parameters, see Supplementary Table S1. In both panels, a solid dot marks the location in parameter space that corresponds to the values of parameters given in Supplementary Table S1. In panel B, an open dot marks the location in parameter space that corresponds to the values of parameters in the model of Stites *et al.* (Ref. 34). (**C**) Bifurcation diagram showing the active ERK fraction vs. the level of EGFR$_a$–SOS$_u$ complexes in the system without all three negative feedbacks. Solid lines show two stable steady states; dashed line shows unstable steady state. (**D**) Analysis of the system with the negative feedback from ERK to SOS present and other two negative feedbacks absent. Parametric plot shows a projection of the limit cycle on the (active ERK fraction)—(EGFR$_a$–SOS$_u$ complexes) plane.

is bound to RAS-GTP (i.e., $k_{2B} = 0.1 \times k_{2A}$). As shown in Fig. 3A, bistability requires both parameters, k_{2B} and k_{2C}, to be sufficiently small with respect to k_{2A}.

Bistability is enabled by constraints on parameters related to SOS's GEF activity (mentioned above) or by saturability of RasGAP (Fig. 3B). Saturation of RasGAP may occur during a response to EGF if the abundance of RasGAP is sufficiently lower than that of RAS, or if RasGAP-RAS complexes are sufficiently long lived. We have set parameter values such that RasGAP is saturable (Supplementary Table S1). Different parameter settings used in an independent modeling study[34] are also consistent with saturability of RasGAP (Fig. 3B). In the steady state, the outcome of the pathway depends on the level of EGF-activated and SOS-bound receptors. In the bifurcation diagram of Fig. 3C, the level of EGFR$_a$–SOS$_u$ complexes serves as a bifurcation parameter. Here, we use the notation "EGFR$_a$–SOS$_u$" to refer to activated EGFR in complex with SOS, which can bind EGFR only when not phosphorylated. Bistability arises for a certain range of EGFR$_a$–SOS$_u$ abundance; below this range the system is monostable inactive (i.e., a low fraction of ERK is active), whereas above it, the system is monostable active (i.e., a high fraction of ERK is active).

Negative feedbacks and oscillations. Analysis of the bifurcation diagram in Fig. 3C suggests that the slow negative feedback mediated by ERK, which reduces the number of EGFR$_a$–SOS$_u$ complexes (by phosphorylation of SOS to the state in which it cannot bind EGFR), may lead to relaxation oscillations. The mechanism may be explained as follows. In unstimulated cells the level of EGFR$_a$–SOS$_u$ complexes is below the level corresponding to the saddle node bifurcation point SN$_1$ in Fig. 3C, and thus ERK is inactive. EGF stimulation activates receptors, with formation of EGFR$_a$–SOS$_u$ complexes. When the level of EGFR$_a$–SOS$_u$ exceeds the level corresponding to the saddle node bifurcation point SN$_2$, ERK is activated. Subsequently, ERK phosphorylates SOS, reducing the level of EGFR$_a$–SOS$_u$ complexes. When this level drops below SN$_1$, ERK activity is terminated. After ERK activity is terminated, SOS is dephosphorylated and the system resets; therefore, with persistent EGF stimulation, ERK activity pulses can be recurrent. The cycle is shown in parametric plot in Fig. 3D.

The full system (with all three negative feedbacks illustrated in Fig. 1 and parameterization according to Supplementary Table S1) can exhibit oscillations (Fig. 4). The amplitude of these oscillations very weakly depends on the strength of EGF stimulation, in contrast to the period and pulse width. These properties, indicating that the system switches between on and off states corresponding to the steady states of the system when only the positive feedback is present (Fig. 3C), are characteristic of relaxation oscillations. At a low level of EGF stimulation, ERK activity is pulsatile (Fig. 4A). In contrast, at a high level of EGF stimulation, pulse width is wide and off time is short, such that ERK activity is high most of the time (Fig. 4C). As a consequence, the ERK activity integrated over a population of (unsynchronized) cells would be expected to increase gradually with the EGF dose.

In the analyzed MAPK relaxation oscillator, period of oscillations is controlled by the speed of the inhibition and relaxation processes: inhibition relies on the phosphorylation of SOS by phosphorylated ERK (ERK$_{pp}$),
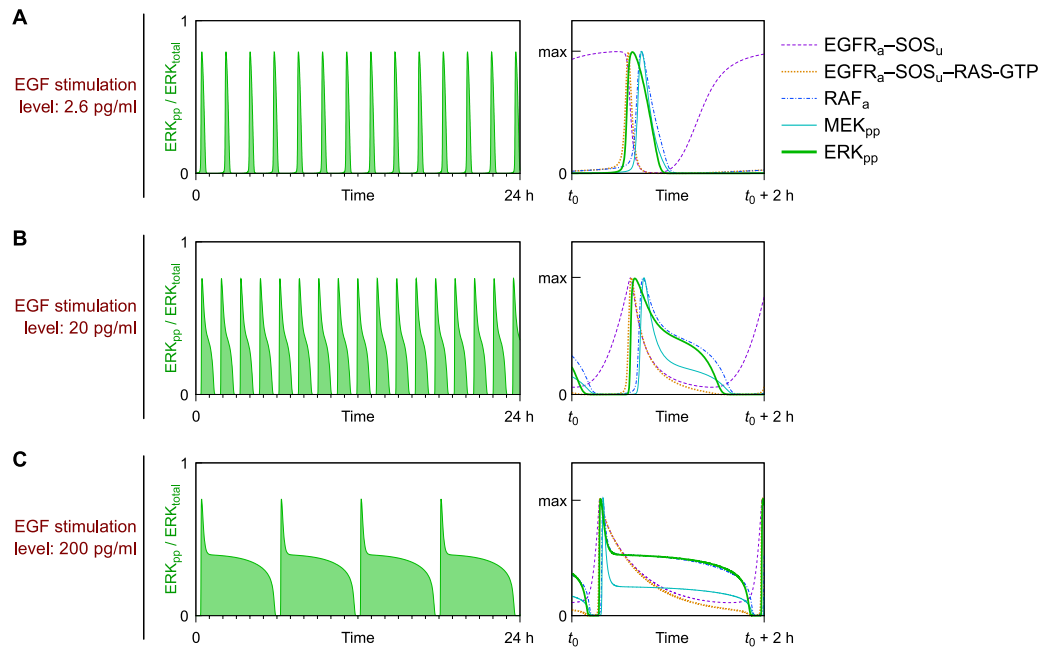
Figure 4. Simulated trajectories for three EGF stimulation doses. The active ERK fraction (left column) together with levels of $EGFR_a$–SOS_u complexes, $EGFR_a$–SOS_u–RAS-GTP complexes, RAF_a and MEK_{pp} normalized to their maxima (right column) are shown as a function of time after stimulation by (**A**) low, (**B**) intermediate, and (**C**) high doses of EGF.

whereas relaxation relies on the resurgence of dephosphorylated SOS (SOS_u) that can form complex with active EGFR ($EGFR_a$) – see Fig. 4, violet dashed line. In the model we assume that SOS phosphorylation and dephosphorylation are possible only when SOS is not bound to EGFR. At a low stimulation dose (Fig. 4a) the resurgence phase is long, because SOS_u has to recover to a high level (higher than in the case of a high stimulation dose) in order initiate a next pulse; at a high stimulation dose (Fig. 4c) the inhibition phase is long because SOS_u has to drop to a low level (lower than for low stimulation dose) in order to terminate pathway activation.

The prediction of relaxation oscillations (Fig. 4) is consistent with observations of periodic ERK activity made using two different ERK activity reporters, EKAR3 and ERKTR[32]. The ERKTR reporter indicates bursts of ERK activity separated by distinct periods of essentially no activity. The EKAR3 reporter indicates similar oscillatory dynamics, but the off periods are less pronounced (see Fig. 5B in ref. 32). To determine if these features can be explained by the different kinetics of ERK interaction with the two reporters on the top of the model of Fig. 2 we explicitly included ERK activity reporters (see Materials and Methods). As shown in Supplementary Figure S3, the shape of predicted oscillations in the level of reporter phosphorylation depends on the kinetics of ERK-reporter interaction. With slower interaction kinetics, the off periods become shorter.

To investigate the parameter dependence of oscillatory behavior, we performed a bifurcation analysis (Fig. 5). Two-dimensional bifurcation diagrams (Fig. 5A and B) illustrate how qualitative behavior depends on the strength of EGF stimulation and the strengths of three negative feedbacks. As indicated in Fig. 5B, four regimes of behavior are possible: monostable on and off states, bistability (wherein the steady state occupied depends on history), and oscillations. These regimes are separated by bifurcations of different types, which are indicated by the labeling of boundaries. Figure 5C–E are one-dimensional bifurcation diagrams (with the strength of EGF stimulation chosen as a bifurcation parameter) corresponding to different cross-sections of the parameter space of Fig. 5B. The cross-section in Fig. 5D corresponds to the default parameter values of Supplementary Table S1. This diagram shows that the system is off (on) at low (high) levels of EGF stimulation and exhibits oscillations over a ~100-fold intermediate range of EGF stimulation strength. Over this range, the period of oscillations in ERK activity first decreases and then increases with EGF dose. The default parameters, which were chosen for consistency with observed system behaviors[30], allow for a rich repertoire of behaviors. Moreover, the relatively modest modification of these parameters can change the system behavior from bistable to oscillatory, which is in line with the conjecture that complex systems are poised at criticality[35].

Oscillatory behavior depends on feedback strengths (Fig. 5A–D), and bistability is only realized when negative feedback from ERK to SOS is weak or absent (Fig. 5B and E). As can be seen by inspecting Fig. 5B and also by comparing Fig. 5C and D, the range of oscillatory behavior increases with the strength of negative feedback from ERK to SOS. Conversely, the range of oscillatory behavior shrinks with stronger feedbacks from ERK to MEK and RAF (Fig. 5A). Generally, for a system with a single negative feedback, increasing the strength of negative feedback tends to switch off the response of the system to a signal. Here, somewhat paradoxically, increasing the strength of the negative feedbacks from ERK to MEK and from ERK to RAF can push the system from oscillatory behavior to a persistent on state if EGF stimulation is sufficiently strong (Fig. 5A). This behavior arises because
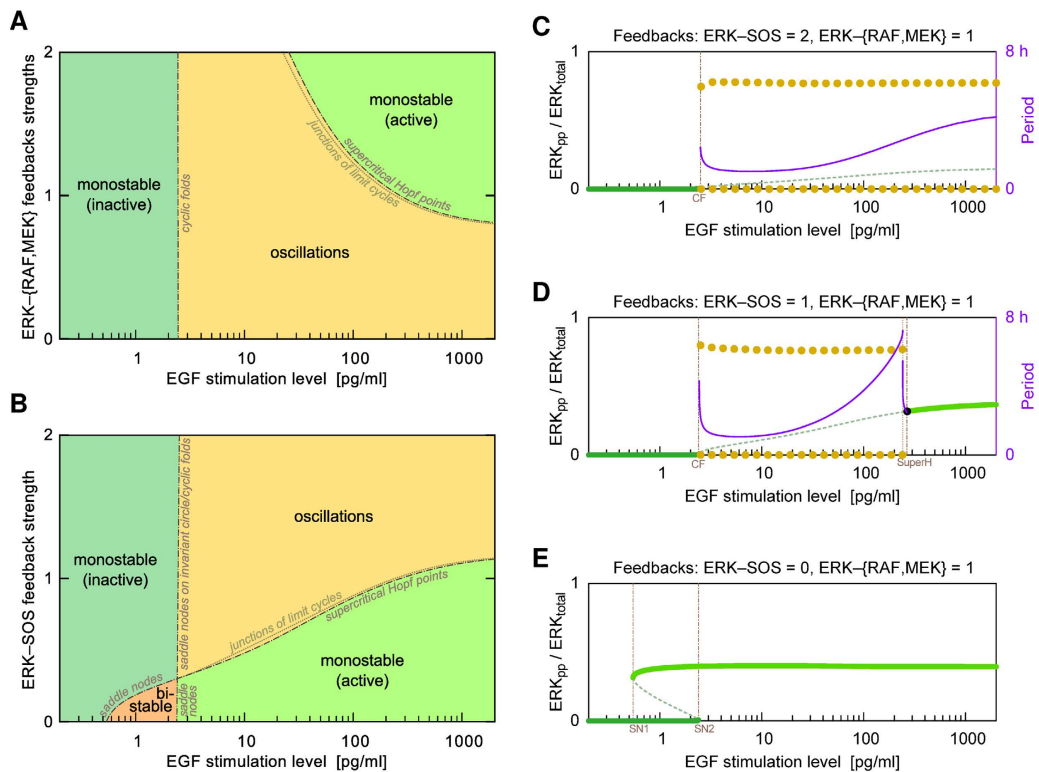
Figure 5. Bifurcation diagrams. Each plot indicates the recurrent solutions for the fraction of activated ERK (ERK_{pp}/ERK_{total}) as a function of either one or two bifurcation parameters. EGF dose (or stimulation level) is a bifurcation parameter in each plot. In the two-dimensional bifurcation diagrams, the second bifurcation parameter characterizes the strength of the negative feedbacks from ERK to RAF and MEK (**A**) and the strength of the negative feedback from ERK to SOS (B). Areas are colored to indicate distinct qualitative behaviors: oscillatory, monostable with low or high ERK activity, and bistable. The boundaries are labeled to indicate the bifurcation types that separate the different regimes of behavior. The one-dimensional bifurcation diagrams correspond to different strengths of the negative feedback from ERK to SOS (i.e., they correspond to different cross-sections of the parameter space of panel **B**): twice the default strength (**C**), the default strength (**D**), and absent (**E**). Solid green lines indicate stable steady states; dashed green lines indicate unstable steady states. Yellow dots indicate the upper and lower envelopes of stable limit cycles. Purple lines indicate the periods of oscillations. Cyclic fold (CF) bifurcations in panels C and D are accompanied by subcritical Hopf bifurcation points (not marked). In a tiny parameter region between the two bifurcation points there coexist a stable limit cycle, an unstable limit cycle, and a stable steady state. In panel D, supercritical Hopf bifurcation lies close to a series of complex bifurcations (seen as the period discontinuity) which effects in a junction of limit cycles.

negative feedbacks from ERK to MEK and from ERK to RAF weaken ERK activity, such that the ERK-to-SOS negative feedback cannot be engaged to induce oscillations.

We note that oscillatory behavior requires not only a sufficiently strong negative feedback from ERK to SOS (Fig. 5) but also multi-site phosphorylation of SOS (Supplementary Figure S2). In the model, the effect of (distributive) multi-site phosphorylation is to introduce a delay in reactivation of SOS after deactivation of ERK. The delay arises from the time required for phosphatases to act and an assumption that phosphorylation of a single site in SOS by ERK is sufficient to suppress SOS activity. The model accounts for four SOS residues that can be phosphorylated by ERK. If the number of such residues is reduced to three, oscillatory behavior is observed over a much narrower range of EGF concentrations and oscillations are not observed for less than three phosphorylatable residues in SOS (Supplementary Figure S2).

The shape of ERK activity pulses is controlled by the strengths of negative feedbacks from ERK to MEK and from ERK to RAF (Fig. 6). As illustrated in Fig. 6A and B, for a given strength of negative feedback from ERK to SOS, increasing the strengths of negative feedbacks from ERK to MEK and from ERK to RAF changes the waveform of system response from a square wave to a long-tail pulse. Although the ERK-to-MEK and ERK-to-RAF feedbacks are somewhat redundant, both being downstream of positive feedback from RAS to SOS, the ERK-to-RAF feedback is more far ranged and therefore more strongly impacts pulse shape (Fig. 6C and D). Note that we have taken the ERK-to-MEK and ERK-to-RAF feedbacks to be equally strong (Supplementary Table S1). Additional phase space analysis in Supplementary Figure S4 shows in parametric plots that cycle trajectories with two feedback strengths in common group together in tight clusters whereas trajectories with only one feedback strength in common group together in looser clusters.
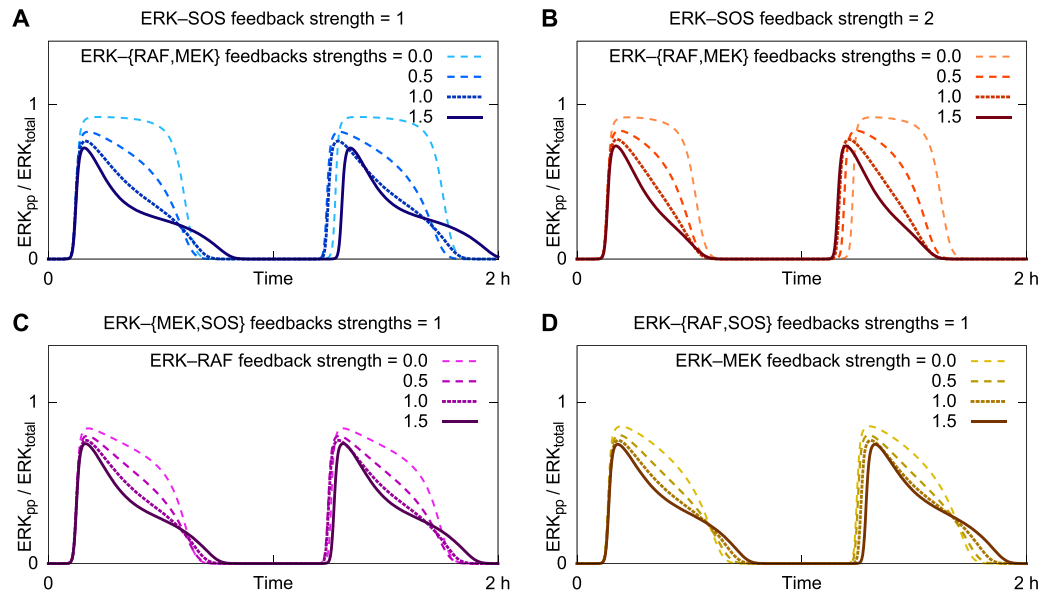
Figure 6. Negative feedback from ERK to MEK and RAF shape the time profile of response to EGF stimulation at 10 pg/ml. Each time course illustrates an oscillatory response to EGF stimulation. In the top panels, the strength of ERK-to-SOS negative feedback is set at the default level (**A**) or twice the default level (**B**). In these panels, different dash patterns correspond to different strengths of feedback from ERK to MEK and RAF, as indicated in the legends. The ERK-to-MEK and ERK-to-RAF feedback strengths are taken to be equal. In the bottom panels, the ERK-to-MEK and ERK-to-RAF feedback strengths are varied separately, as indicated in the legends.

Noisy oscillatory excitation of ERK. In earlier work[30], using the EKAR-EV reporter, we observed bursts of ERK activity at low EGF doses, regular pulses of ERK activity at intermediate EGF doses, and sustained ERK activity with short, intermittent off periods at high EGF doses. These behaviors have been confirmed using the ERKTR reporter (Ref. 32, Fig. 7), which because of its faster kinetics is able to better resolve oscillatory dynamics (Supplementary Figure S3).

As discussed above, the model of Fig. 2 predicts that oscillations, when they appear, will have an EGF dose-dependent frequency and dose-independent amplitude (Fig. 4). These features of predicted oscillatory behavior in single cells are similar to the oscillations in ERK activity that we observe in single cells (Ref. 30 and Fig. 7). However, the experimentally observed oscillations are noisy, with irregularity both within individual cells and across cells in the population monitored in experiments. To investigate how these irregularities could potentially arise (and whether they are consistent with the model), we extended the model of Fig. 2 to account for extrinsic noise. For simplicity, we considered only a single extrinsic noise source, which we took to be stochastic, time-varying cell-specific surface expression of EGFR. This extension is consistent with heterogeneity in protein expression levels across cell populations, which has been extensively studied and linked to bursts of gene expression[36,37].

Thus, the extended model was obtained by recasting the original model as a Markov chain and by adding processes for stochastic generation and clearance of EGFR. Parameters introduced with these extensions are summarized in Supplementary Table S3. Parameter values are such that EGFR surface expression changes on a time scale of hours (Fig. 8A). The influence of extrinsic noise characteristics on active ERK dynamics is analyzed in Supplementary Figure S5. Separate influences of the intrinsic and extrinsic noise on ERK dynamics are demonstrated in Supplementary Figure S6 and Supplementary Figure S7.

Figure 8 shows time courses obtained from the extended, stochastic model for a collection of 20 individual cells responding to different doses of EGF. As can be seen, the extended model predicts irregular EGF dose-dependent excitations of ERK, suggesting that the similar irregularities observed in experiments (Fig. 7) can be attributed to extrinsic noise, which may arise partly from cell-specific time-varying stochastic EGFR surface expression. For the lowest dose considered, 2 pg/ml, ERK is excited in bursts, which tend to be separated by relatively long periods of inactivity (Fig. 8B). According to the deterministic model, this dose lies outside the oscillatory range (Fig. 5D). Indeed, this dose places the system's steady state in the monostable, inactive regime. The stochastic model predicts bursts of ERK activity arising due to fluctuations of EGFR that allow the level of activated EGFR to exceed a threshold required for ERK activation. We note that inhibition of EGFR (with the kinase inhibitor gefitinib) immediately eliminates pulsatile ERK activity (Fig. 7), indicating that ERK activity pulses require uninhibited EGFR level being above a threshold. Additional analyses of 10-day-long trajectories is provided in Supplementary Figure S8.

Excitation of ERK by transient EGFR signaling. Positive feedback mediated by SOS influences system behavior, such that transient EGF stimulation is expected to produce responses having certain experimentally
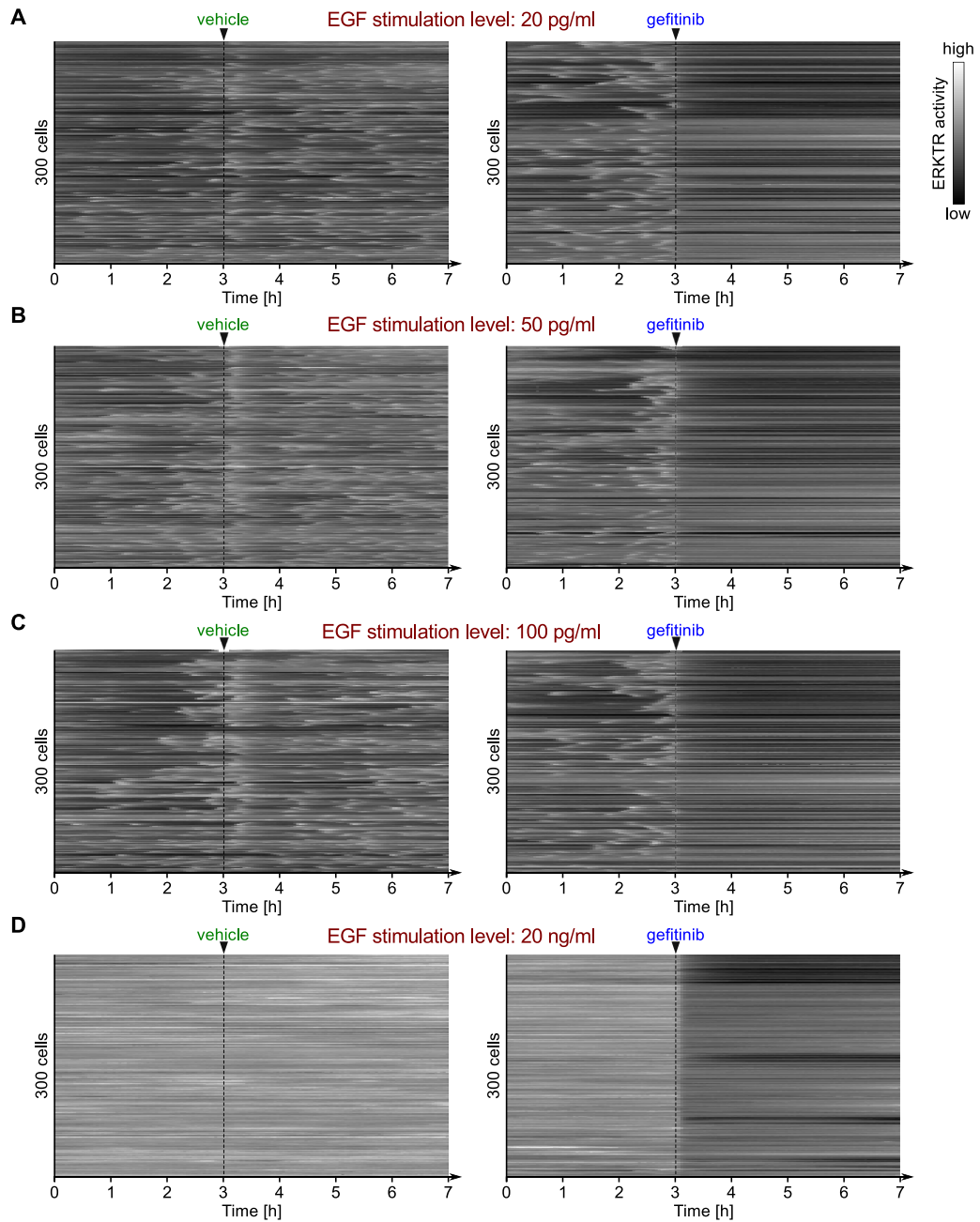
Figure 7. Kinetics of ERK activity as reported by ERKTR at four different doses of EGF. EGFR inhibition by gefitinib is sufficient for elimination of ERK pulses. The time points are spaced by 3 minutes. A smaller set of data from the same experiment was published previously[32].

detectable features. In Fig. 9, we consider predicted responses of the system to different transient doses of EGF. The smallest dose considered, 3 pg/ml, induces a pulse of high ERK activity only for the longest period of EGF stimulation, 20 min (Fig. 9A). In contrast, for a relatively high EGF dose of 60 pg/ml, even the shortest period of EGF stimulation, 30s, induces a pulse of high ERK activity (Fig. 9D). The stimulation time required to induce high ERK activity decreases with increasing EGF dose, which follows from the fact that there exists a threshold level of EGFR that must be activated to trigger downstream signaling. For short EGF stimulation times, active EGFR level increases linearly with time, with a rate proportional to the EGF stimulation dose. Therefore, in this regime, ERK is activated when the product of stimulation time and EGF dose exceeds some threshold. For longer stimulation times, the level of active EGFR saturates; in this limit, the critical dose for long stimulation converges to the critical dose for sustained stimulation, 2.5 pg/ml (cf. Figs 5D and 9E). Figure 9B–D show that for short, transient EGF stimulation periods, ERK activity starts to rise after EGF stimulation stops, which shows that after the level of active EGFR exceeds a threshold, signal propagates independently of further EGF stimulation.
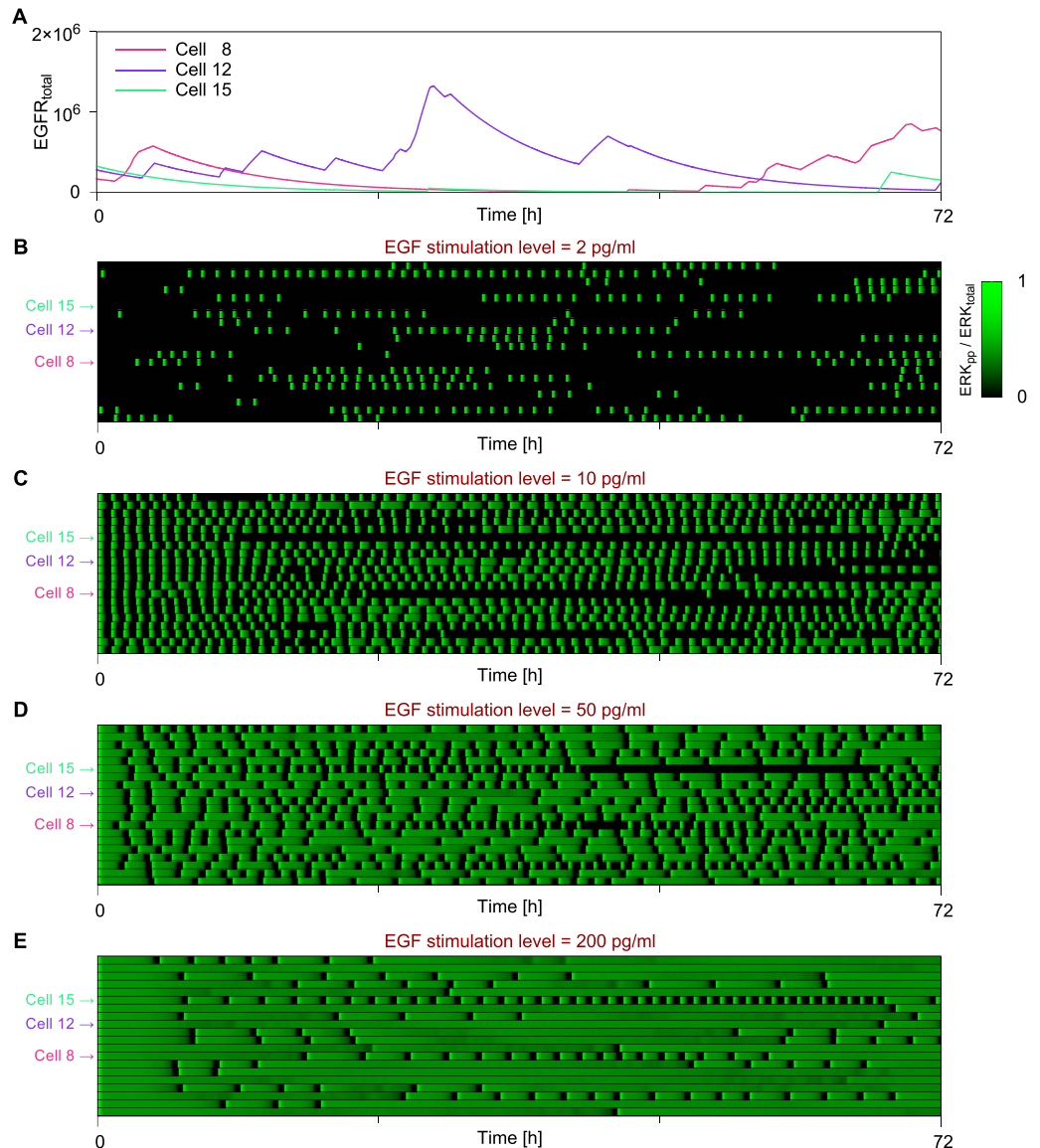
Figure 8. Single-cell temporal EGFR surface expression and ERK activity profiles obtained from stochastic simulations with fluctuating EGFR levels. We considered the effect of extrinsic noise on oscillations in ERK activity. As illustrated in panel (**A**), which shows representative single-cell simulations, we took EGFR surface expression dynamics to be stochastic and marked by bursts of synthesis/expression of variable size (total amount of EGFR added to the plasma membrane) and duration, with bursts being separated by intervals of variable duration. The bottom four panels show heat maps that indicate single-cell responses (ERK activity as a function of time) to different levels of EGF stimulation: (**B**) 2 pg/ml, (**C**) 10 pg/ml, (**D**) 50 pg/ml, and 200 pg/ml (**E**). Each row in a heat map corresponds to an individual cell characterized by a unique set of parameters for EGFR surface expression dynamics. The cells considered are otherwise identical. To demonstrate and isolate the effect of EGF dose, we have taken the temporal EGFR expression profile to be the same across panels for each cell (i.e., each row in each heat map corresponds to a common profile). Supplementary Table S3 provides information about the parameters that are unique for the stochastic simulations shown here.

Recently, we observed a similar effect in which the integral of stimulus (i.e., time × amplitude) determines the fraction of activated cells in a population in the case of LPS stimulation[38]. As in the case of growth factor signaling, the immunogenic signal is integrated at the membrane and after surpassing a threshold activates a downstream pathway. This property results from ultrasensitivity or positive feedback operating at the membrane level.

ERK responses to localized secretion of EGF. A notable feature of the feedback mechanisms involved in MAPK signaling is their ability to propagate signals through space. Positive feedback requires interactions on the plasma membrane (Fig. 2). In contrast, negative feedback signals are relayed by faster diffusing cytosolic proteins (Fig. 2). Such a combination of feedbacks can potentially give rise to local excitation/global inhibition (LEGI)
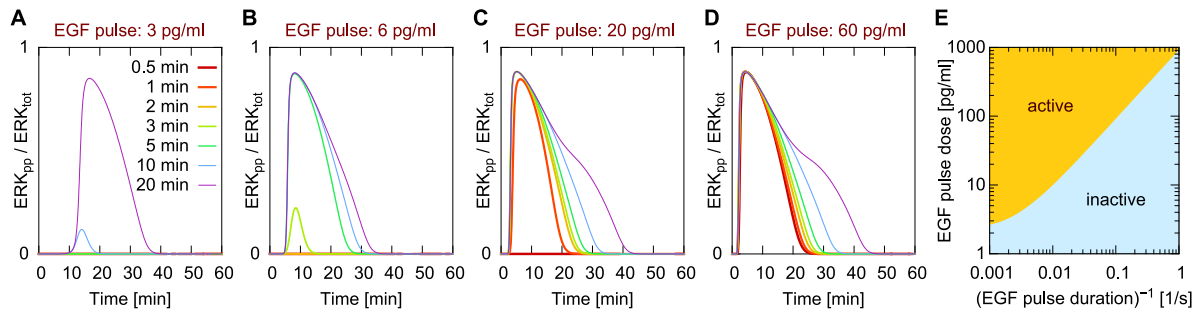
Figure 9. Predicted responses to pulsed EGF stimulations of various doses and durations. Each curve is obtained from a simulation of an experiment wherein EGFR signaling is stimulated by a low (**A**), intermediate (**B,C**) or high (**D**) dose of ligand (EGF) for the duration indicated in the legend. EGF stimulation pulse starts at time = 0. After this pulse of stimulation free ligand is removed. (**E**) Dependence of critical EGF stimulation dose on stimulation duration.
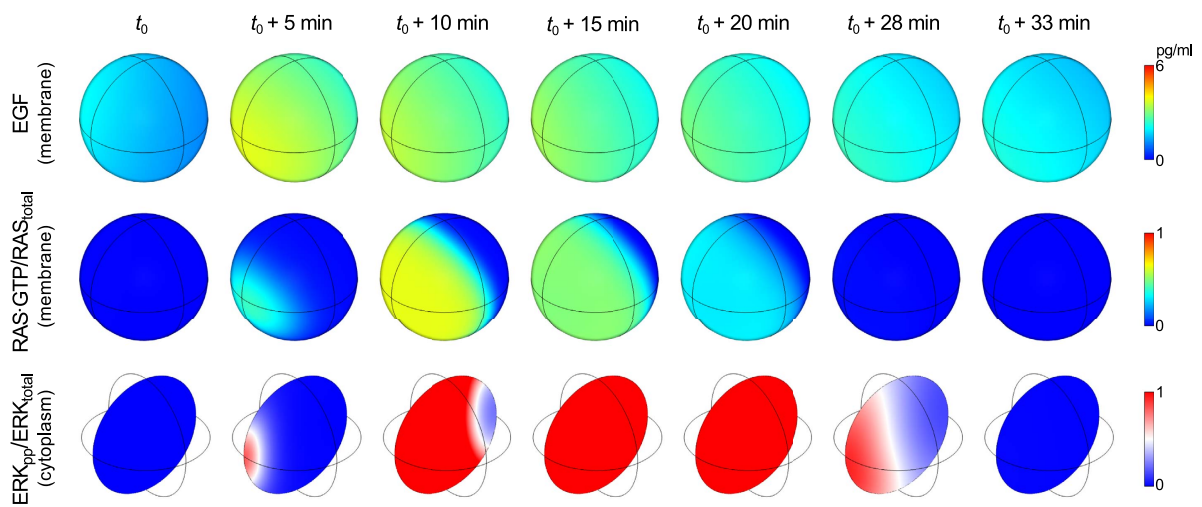

Figure 10. Spatiotemporal dynamics of EGF, RAS activity (RAS·GTP/RAS$_{total}$), and ERK activity (ERK$_{pp}$/ERK$_{total}$) for a cell responding to localized EGF secretion. Shown are sequential snapshots taken from Supplementary Video 1 in the Supporting Information that illustrate the response of a cell to a wave of EGF, which is produced by point sources releasing EGF at random times and locations in a shell surrounding the cell. At each time point, the spatial distribution of EGF at the cell surface is shown in the top row, fraction of activated RAS is shown in the middle row, and the spatial distribution of activated ERK inside the cell is shown in the bottom row (on a cross-section passing through the cell center). Supplementary Table S4 provides information about the parameters that are unique for the spatiotemporal simulations shown here.

dynamics. In LEGI-type regulation, the membrane components are activated due to propagation of a heteroclinic traveling wave (enabled by bistability introduced by a positive feedback). Activation of membrane components is followed by more uniform activation of cytoplasmic components and then global inhibition of membrane components via negative feedback. LEGI can generate spatial essential for proper cellular responses to directional cues, such as chemotactic movement of ameboid cells toward a higher concentration of a chemokine[39–42]. Detection of directional cues may be an important function of the EGFR signaling network. EGF gradient sensing or ERK heterogeneities have been implicated in mechanotransduction, cell polarization, and motility[12–14].

To investigate spatial heterogeneities in MAPK signaling, we extended the ODE model of Fig. 2 to obtain a reaction–diffusion PDE-based model. This extended model accounts for both the spatiotemporal kinetics of the signaling network components within the cell and extracellular randomized release of (paracrine) EGF. A more detailed description of this model extension is provided in the Materials and Methods section; parameters introduced with this extension are summarized in Supplementary Table S4. We used the PDE model to predict responses to localized (paracrine) EGF stimulation (Fig. 10). A sequence of simulation snapshots is shown in Fig. 10, which are taken from Supplementary Video 1. This sequence illustrates how non-uniform EGF stimulation, which is visualized in the top row of images, can trigger a traveling wave of activated RAS that spreads over the plasma membrane (Supplementary Video 1) and that produces a transient gradient of ERK activity within the cell, which is visualized in the bottom row of images. This spatiotemporal behavior is in accordance with LEGI dynamics.

Interestingly, ERK may be activated even when the average surface concentration of EGF is below the threshold concentration required for activation in the well-mixed limit (i.e., below the level corresponding to the saddle node bifurcation point SN_2 in Fig. 5E). This behavior, which can be seen at approximately 20 hr in Supplementary Video 1, occurs because the local concentration of EGF exceeds the average concentration, as well as SN_2, the threshold required to trigger a traveling wave of RAS activation. Once the heteroclinic wave is initiated on the membrane, its propagation requires only that the concentration of EGF remains above the lower limit of the bistability range, i.e., above the level of EGF corresponding to the saddle node bifurcation point SN_1 in Fig. 5E.

Discussion

The MAPK signaling cascade transmits signals that control diverse cell functions such as proliferation, differentiation, motility, and apoptosis[3]. The mechanisms allowing the pathway to achieve specificity are still elusive. There is growing evidence that diverse cellular functions are coordinated through multiple posttranslational modifications of RAF. These modifications allow RAF isoforms to propagate signals into diverse downstream pathways[43,44]. Another mode of cell fate control is associated with the temporal profiles of RAF, MEK, and ERK activity. Recently, Ryu *et al.* demonstrated in PC-12 cells that the choice between proliferation and differentiation depends on the frequency of ERK activity oscillations[8]. Here, we constructed and analyzed a computational model of MAPK signaling to clarify how such oscillations can be generated in response to persistent stimuli, and how their frequency and time profile (i.e., pulse shape) are controlled.

Within the MAPK/ERK signaling cascade, ERK mediates apparently redundant negative feedback loops that inhibit signal propagation at multiple upstream points. In our modeling study, we focused on the positive feedback loop that involves the small GTPase RAS and its guanine nucleotide exchange factor SOS. In the absence of negative feedbacks, this positive feedback loop leads to bistable switching. However, when this loop is nested within the negative feedback loop from ERK to SOS, the system produces relaxation oscillations, which match experimental time courses. The two other negative feedbacks, from ERK to MEK and RAF, play only auxiliary roles in the generation of oscillations, principally modulating the shape of ERK activity pulses. The presence of these two loops, however, allow for controlling activity of RAF, which has numerous targets in addition to MEK[45]. The positive feedback introduces a hierarchy between negative feedbacks, such that the ERK to SOS feedback is responsible for generating oscillations and the other two feedbacks considered in our analysis are responsible for shaping the waveform of oscillations.

In addition to the feedbacks discussed above, there are at least two other positive feedbacks that are nested within the ERK–SOS negative feedback loop: the ERK/MEK hidden feedback, in which bistability may arise in the double phosphorylation/dephosphorylation cycle due to distributive phosphorylation and saturability in dephosphorylation reaction[46], and the RAS–GAB1–PI3K feedback[47]. Both feedbacks fit into the discussed topology that can give rise to relaxation oscillations, but, importantly, only the RAS–GAB–PI3K feedback (in addition to the RAS–SOS feedback) can act as an initial signal amplifier, because it is upstream of the RAF/MEK/ERK cascade.

Overall, the feedbacks considered here encode a graded input into constant-amplitude pulses, such that the level of a stimulus is translated to the frequency of oscillation and pulse duration. We speculate that, in comparison with amplitude-to-amplitude coding, amplitude-to-frequency coding may decrease ambiguity in signal interpretation by downstream effectors and increase information channel capacity. The NF-κB signaling system, which is characterized by a constant period of oscillations and thus appears to employ the former scheme[48], was found to transmit only ~1 bit of information[49,50]. Interestingly, in the MAPK pathway, Aoki *et al.* found that frequency, but not amplitude, of ERK activity pulses is correlated with cell proliferation rates[51].

The ERK pathway can modulate cell adhesion and promote cell migration by activation of actin polymerization[52] or vimentin filament remodeling[53]. To respond properly to extracellular, directional cues[14,54], the pathway should be organized spatially[55]. By analyzing the MAPK/ERK network as a reaction–diffusion system we found that when a cell is exposed to localized bursts of EGF, ERK activation exhibits local excitation/global inhibition (LEGI) dynamics[56]. LEGI dynamics arise because of the existence of a fast positive feedback involving slowly diffusing membrane-bound proteins. Under these conditions, localized EGFR excitation can trigger RAS activation that spreads over the membrane as a traveling wave, which induces a non-uniform surge of RAF, MEK and ERK activity in the cytosol. Ultimately, ERK-mediated phosphorylation of SOS globally inhibits pathway activity because cytosolic proteins diffuse faster than membrane proteins, by at least one order of magnitude. Such a mechanism allows cells to encode information about concentration gradients of extracellular ligand into spatially structured pulses of cytosolic proteins activity. It has been suggested that ERK-controlled EGF shedding can maintain an intrinsic cell spatial polarity[15] which may be exploited to induce directed cell migration.

In our spatial model, RAS kinetics is simplified: we consider only a membrane pool of RAS and we neglect the existence of membrane microdomains that can be enriched in RAS. We are however aware that the heterogeneity in RAS distribution combined with the positive feedback between RAS and SOS can substantially influence signaling. In our earlier modelling efforts on B-cell activation[57] we demonstrate that clusterization of membrane components can itself lead to a local activation, which can then spread over the membrane by means of a traveling wave. Also, EGFR and RAS trafficking between plasma membrane and subcellular compartments, and trafficking-dependent signaling from inside the cell (in addition to signaling from the plasma membrane) would influence spatiotemporal activity profiles of downstream components, RAF, MEK, and ERK.

In summary, we have shown that the presence of the short positive feedback coupling RAS and SOS introduces bistability into the system and that this bistability, when frustrated by the negative feedback loop from ERK to SOS, introduces relaxation oscillations which can explain pulsatile time courses of active ERK observed in experiments. This regulatory circuitry allows for translation of graded inputs into constant-amplitude oscillations that have a period and pulse duration determined by signal strength. Because the positive feedback operates on a short time scale and involves slow-diffusing membrane components while the negative feedback operates on a longer

time scale but involves faster-diffusing cytoplasmic components, in response to localized EGF stimulation, the system exhibits local activation/global inhibition dynamics. This allows for translation of spatially-graded stimuli to spatially oriented pulses of RAF, MEK and ERK activity, which could be used to direct cell migration or induce polarity.

Materials and Methods

Setting parameters.   It is challenging to identify parameter values even when abundant experimental data are available to guide parameter estimation[58]. Here, we selected parameter values so as to obtain certain qualitative system behaviors and to allow for qualitative behavior to change in response to variation in the strength of EGF stimulation. This approach is consistent with the hypothesis that cellular regulatory systems operate close to bifurcation points[35,59]. First, we considered the system with only the positive feedback loop from RAS to SOS. We set parameter values so that there is a regime of bistability at low EGF stimulation levels. We then adjusted parameter values so that the time required for information to flow from RAS to ERK yields ERK activation kinetics in accord with experimental observations. Then, we considered negative feedback from ERK to SOS. We set parameters influencing this feedback such that SOS inhibition lasts long enough to allow for nearly complete deactivation of RAF, MEK and ERK. Finally, we considered negative feedbacks from ERK to MEK and RAF and set parameter values governing these feedbacks such that the time profiles of ERK activity are sensitive to the feedback strengths.

Active ERK reporters.   The ODE-based model was supplemented with two ERK activity reporters, EKAR3 and ERKTR. Their activation and deactivation reaction rate constants (Supplementary Table S1) have been tuned to be reproduce experimentally measured reporter kinetics[32].

Numerical integration of ODEs.   The deterministic model is based on an assumption of well-mixed reaction compartments. It was written in terms of reaction rules using the BioNetGen language (BNGL)[60]. The rules, which are provided in Supplementary Data 1, can be processed by BioNetGen[60] to obtain a reaction network and a corresponding system of coupled ordinary differential equations (ODEs) for the mass-action kinetics of the reaction network. The ODEs were numerically integrated using CVODE[61], which is an integral component of BioNetGen. We used BioNetGen's default settings for CVODE parameters, which are appropriate for stiff systems.

Construction of bifurcation diagrams.   Bifurcation diagrams were obtained using Matlab/Matcont[62]. Supplementary Data 2 contains scripts which can be used to obtain the bifurcation diagrams shown in Supplementary Figure S1.

Modeling stochastic EGFR surface expression dynamics.   To investigate how ERK response dynamics are influenced by stochasticity, we introduced a source of extrinsic noise by allowing the EGFR level to change over time and in this way to modulate cellular sensitivity to EGF stimulation. In the stochastic model, EGFR is expressed in bursts and has a predefined half-life, τ_{EGFR} (Supplementary Table S3). Bursts occur at random time points, distributed exponentially with a mean waiting time of $\lambda_{interburst}^{-1}$, and have durations that are drawn from an exponential distribution with mean burst duration of λ_{burst}^{-1}. The rate of EGFR production in each burst is cell-dependent and is computed as the product of a common intensity factor, A_{burst}, and a cell-specific factor, α_{cell}, which is drawn from a log-normal distribution having mean of 1. The simulations are performed using an efficient variation of Gillespie's direct method[63] as implemented in BioNetGen[60]. A BioNetGen input file corresponding to the simulations shown for cell 8 in Fig. 8B is provided in Supplementary Data 3.

PDE simulations.   A single cell is considered. It is represented as a sphere of radius R_{cell} with volume V_{cell}. Values of these and others parameters specific to this model extension are summarized in Supplementary Table S4. Membrane and cytosolic proteins diffuse with diffusivities D_{mem} and D_{cyt}, respectively, with $D_{cyt} = 10 \times D_{mem}$. Reaction–diffusion equations on the membrane and in the cytosol are coupled via Robin-type boundary conditions[64]. We assume that the flux Φ of active RAF at the membrane results from its phosphorylation by membrane-tethered RAS-GTP:

$$\Phi = a_2 RAS_{GTP} RAF_i = D_{cyt} \hat{n} \nabla RAF_a \big|_{r=R_{cell}},$$
(1)

where $\hat{n}$ is an outer unit vector normal to the cell surface. The rate of SOS phosphorylation is taken to be proportional to the boundary value of active cytoplasmic ERK. The point sources of EGF appear at random positions in the cell-concentric shell of outer radius $R_{EGF\_shell\_out}$ at random time points throughout the simulation, on average every $f_{EGF\_sources}^{-1}$. EGF releases each have a duration drawn from an exponential distribution with mean duration of $\lambda_{EGF\_source}^{-1}$, and a time-independent intensity A_{EGF}, which is drawn from a log-normal distribution. Released EGF diffuses with diffusivity D_{EGF} in the extracellular 3-D space, which is assumed to be unbounded and devoid of obstacles. EGF undergoes degradation with rate constant γ_{EGF} according to the diffusion–degradation equation:

$$\frac{\partial}{\partial t} EGF(r, t) = \frac{1}{r^2} \frac{\partial}{\partial r} \left(r^2 D_{EGF} \frac{\partial}{\partial r} EGF(r, t) \right) - \gamma_{EGF} EGF(r, t) + s(r, t)$$
(2)

where r is the distance from the point source localized at $r = 0$.

$$s(r, t) = \begin{cases} A_{\text{EGF}}\delta(r), & t \in [t_1, t_2] \\ 0, & t \notin [t_1, t_2] \end{cases} \tag{3}$$

$EGF(r, t)$ can be calculated using a Green's function (specific for the diffusion-degradation problem in 3D):

$$G(r, t) = (4\pi Dt)^{-3/2} e^{-r^2/4Dt} e^{-\gamma_{\text{EGF}}t} \tag{4}$$

as

$$EGF(r, t) = \int_{-\infty}^{t} s(r, t') G(r, t - t') \, dt'. \tag{5}$$

Because

$$\int G(r, t) \, dt = \frac{1}{8\pi D_{\text{EGF}} r} \left[e^{-\beta r} \operatorname{erfc}\left(\frac{r - 2\beta D_{\text{EGF}} t}{2\sqrt{D_{\text{EGF}} t}} \right) + e^{\beta r} \operatorname{erfc}\left(\frac{r + 2\beta D_{\text{EGF}} t}{2\sqrt{D_{\text{EGF}} t}} \right) - 2e^{-\beta r} \right] \tag{6}$$

where $\beta = \sqrt{\gamma_{\text{EGF}}/D_{\text{EGF}}}$ and erfc is the complementary error function, the contribution from a single EGF source $s(r, t)$ equals:

$$EGF(r, t) = A_{\text{EGF}} \times \begin{cases} 0, & t < t_1 \\ \int_{t_1}^{t} G(r, t') \, dt', & t_1 \leq t \leq t_2 \\ \int_{t_1}^{t_2} G(r, t - t') \, dt', & t_2 < t \end{cases} \tag{7}$$

PDE-based simulations were performed using COMSOL MULTIPHYSICS (see Supplementary Data 4). The spatio-temporal evolution of EGF concentration was evaluated as described above, while reaction–diffusion equations for the cell surface and within the cytosol were solved numerically using a finite element method. For simplicity, a nuclear compartment or other intracellular obstacles were not considered.

Materials and experimental protocols. Time-lapse imaging of ERK reporter activity was performed as previously described[32]. Briefly, MCF-10A cells stably expressing EKAR3-nes (containing a nuclear export sequence to maintain cytosolic localization) and ERKTR-mCherry were plated on #1.5 glass-bottom multi-well plates coated with type I collagen (BD Biosciences). During imaging, cells were cultured in customized low-fluorescence DMEM/F-12 medium in absence of serum and insulin and the presence of the indicated concentrations of recombinant EGF (PeproTech). At the indicated times, 1 μM gefitinib (Selleck) was added to the medium. Images were collected at 6-minute intervals, and custom MATLAB-based algorithms were used to segment images based on the cytosolic localization of EKAR3 in the YFP channel and extract fluorescence intensities; u-track[65] was used for cell tracking. ERKTR activity is shown as the ratio of cytosolic to nuclear fluorescence in the mCherry channel.

References

1. Chang, F. et al. Signal transduction mediated by the Ras/Raf/MEK/ERK pathway from cytokine receptors to transcription factors: potential targeting for therapeutic intervention. *Leukemia* **17**, 1263–1293 (2003).
2. Roskoski Jr., R. ERK1/2 MAP kinases: Structure, function, and regulation. *Pharmacol. Res.* **66**, 105–143 (2012).
3. Schaeffer, H. J. & Weber, M. J. Mitogen-Activated Protein Kinases: Specific Messages from Ubiquitous Messengers. *Mol. Cell. Biol.* **19**, 2435–2444 (1999).
4. Shaul, Y. D. & Seger, R. The MEK/ERK cascade: From signaling specificity to diverse functions. *Mitogen-Act. Protein Kinases New Insights Regul. Funct. Role Hum. Dis.* **1773**, 1213–1226 (2007).
5. Samatar, A. A. & Poulikakos, P. I. Targeting RAS-ERK signalling in cancer: promises and challenges. *Nat Rev Drug Discov* **13**, 928–942 (2014).
6. Murphy, L. O., Smith, S., Chen, R.-H., Fingar, D. C. & Blenis, J. Molecular interpretation of ERK signal duration by immediate early gene products. *Nat Cell Biol* **4**, 556–564 (2002).
7. Von Kriegsheim, A. et al. Cell fate decisions are specified by the dynamic ERK interactome. *Nat Cell Biol* **11**, 1458–1464 (2009).
8. Ryu, H. et al. Frequency modulation of ERK activation dynamics rewires cell fate. *Mol. Syst. Biol.* **11**, 838 (2015).
9. Brown, G. C. & Kholodenko, B. N. Spatial gradients of cellular phospho-proteins. *FEBS Lett.* **457**, 452–454 (1999).
10. Kholodenko, B. N. Spatially distributed cell signalling. *FEBS Lett.* **583**, 4006–4012 (2009).
11. Zhao, Q., Yi, M. & Liu, Y. Spatial distribution and dose–response relationship for different operation modes in a reaction–diffusion model of the MAPK cascade. *Phys. Biol.* **8**, 55004 (2011).
12. Mendoza, M. C. et al. ERK-MAPK Drives Lamellipodia Protrusion by Activating the WAVE2 Regulatory Complex. *Mol. Cell* **41**, 661–671 (2011).
13. Mendoza, M. C., Vilela, M., Juarez, J. E., Blenis, J. & Danuser, G. ERK reinforces actin polymerization to power persistent edge protrusion during motility. *Sci. Signal.* **8**, ra47 (2015).
14. Tschumperlin, D. J. et al. Mechanotransduction through growth-factor shedding into the extracellular space. *Nature* **429**, 83–86 (2004).
15. Maly, I. V., Steven Wiley, H. & Lauffenburger, D. A. Self-Organization of Polarized Cell Signaling via Autocrine Circuits: Computational Model Analysis. *Biophys. J.* **86**, 10–22 (2004).
16. Shin, S.-Y. et al. Positive- and negative-feedback regulations coordinate the dynamic behavior of the Ras-Raf-MEK-ERK signal transduction pathway. *J. Cell Sci.* **122**, 425–435 (2009).
17. Avraham, R. & Yarden, Y. Feedback regulation of EGFR signalling: decision making by early and delayed loops. *Nat Rev Mol Cell Biol* **12**, 104–117 (2011).

18. Das, J., Kardar, M. & Chakraborty, A. K. Positive feedback regulation results in spatial clustering and fast spreading of active signaling molecules on a cell membrane. *J. Chem. Phys.* **130** (2009).

19. Xiong, W. & Ferrell, J. E. A positive-feedback-based bistable 'memory module' that governs a cell fate decision. *Nature* **426,** 460–465 (2003).

20. Cirit, M., Wang, C.-C. & Haugh, J. M. Systematic Quantification of Negative Feedback Mechanisms in the Extracellular Signal-regulated Kinase (ERK) Signaling Network. *J. Biol. Chem.* **285,** 36736–36744 (2010).

21. Barkai, N. & Leibler, S. Robustness in simple biochemical networks. *Nature* **387,** 913–917 (1997).

22. Alon, U., Surette, M. G., Barkai, N. & Leibler, S. Robustness in bacterial chemotaxis. *Nature* **397,** 168–171 (1999).

23. Nelson, D. E. *et al.* Oscillations in NF-κB Signaling Control the Dynamics of Gene Expression. *Science* **306,** 704–708 (2004).

24. Geva-Zatorsky, N. *et al.* Oscillations and variability in the p53 system. *Mol. Syst. Biol.* **2,** 2006.0033 (2006).

25. Kholodenko, B. N. Negative feedback and ultrasensitivity can bring about oscillations in the mitogen-activated protein kinase cascades. *Eur. J. Biochem.* **267,** 1583–1588 (2000).

26. Shankaran, H. *et al.* Rapid and sustained nuclear–cytoplasmic ERK oscillations induced by epidermal growth factor. *Mol. Syst. Biol.* **5** (2009).

27. Pękalski, J. *et al.* Spontaneous NF-κB activation by autocrine TNFα signaling: a computational analysis. *PLOS One* **8,** e78887 (2013).

28. Szymańska, P., Martin, K. R., MacKeigan, J. P., Hlavacek, W. S. & Lipniacki, T. Computational analysis of an autophagy/translation switch based on mutual inhibition of MTORC1 and ULK1. *PLOS One* **10,** e0116550 (2015).

29. Krishna, S., Semsey, S. & Jensen, M. H. Frustrated bistability as a means to engineer oscillations in biological systems. *Phys. Biol.* **6,** 36009 (2009).

30. Albeck, J. G., Mills, G. B. & Brugge, J. S. Frequency-Modulated Pulses of ERK Activity Transmit Quantitative Proliferation Signals. *Mol. Cell* **49,** 249–261 (2013).

31. Regot, S., Hughey, J. J., Bajar, B. T., Carrasco, S. & Covert, M. W. High-Sensitivity Measurements of Multiple Kinase Activities in Live Single Cells. *Cell* **157,** 1724–1734 (2014).

32. Sparta, B. *et al.* Receptor Level Mechanisms Are Required for Epidermal Growth Factor (EGF)-stimulated Extracellular Signal-regulated Kinase (ERK) Activity Pulses. *J. Biol. Chem.* **290,** 24784–24792 (2015).

33. Das, J. *et al.* Digital Signaling and Hysteresis Characterize Ras Activation in Lymphoid Cells. *Cell* **136,** 337–351 (2009).

34. Stites, E. C., Trampont, P. C., Ma, Z. & Ravichandran, K. S. Network Analysis of Oncogenic Ras Activation in Cancer. *Science* **318,** 463–467 (2007).

35. Mora, T. & Bialek, W. Are Biological Systems Poised at Criticality? *J. Stat. Phys.* **144,** 268–302 (2011).

36. Raj, A., Peskin, C. S., Tranchina, D., Vargas, D. Y. & Tyagi, S. Stochastic mRNA Synthesis in Mammalian Cells. *PLoS Biol* **4,** e309 (2006).

37. Dey, S. S., Foley, J. E., Limsirichai, P., Schaffer, D. V. & Arkin, A. P. Orthogonal control of expression mean and variance by epigenetic features at different genomic loci. *Mol. Syst. Biol.* **11,** 806 (2015).

38. Kellogg, R. A., Tian, C., Lipniacki, T., Quake, S. R. & Tay, S. Digital signaling decouples activation probability and population heterogeneity. *eLife* **4,** e08931 (2015).

39. Parent, C. A. & Devreotes, P. N. A Cell's Sense of Direction. *Science* **284,** 765–770 (1999).

40. Xiong, Y., Huang, C.-H., Iglesias, P. A. & Devreotes, P. N. Cells navigate with a local-excitation, global-inhibition-biased excitable network. *Proc. Natl. Acad. Sci. USA* **107,** 17079–17086 (2010).

41. Shi, C., Huang, C.-H., Devreotes, P. N. & Iglesias, P. A. Interaction of Motility, Directional Sensing, and Polarity Modules Recreates the Behaviors of Chemotaxing Cells. *PLoS Comput Biol* **9,** e1003122 (2013).

42. Bhowmik, A., Rappel, W.-J. & Levine, H. Excitable waves and direction-sensing in Dictyostelium discoideum : steps towards a chemotaxis model. *Phys. Biol.* **13,** 16002 (2016).

43. Romano, D. *et al.* Protein interaction switches coordinate Raf-1 and MST2/Hippo signalling. *Nat Cell Biol* **16,** 673–684 (2014).

44. Cseh, B., Doma, E. & Baccarini, M. 'RAF' neighborhood: Protein–protein interaction in the Raf/Mek/Erk pathway. *FEBS Lett.* **588,** 2398–2406 (2014).

45. Roskoski Jr., R. RAF protein-serine/threonine kinases: Structure and regulation. *Biochem. Biophys. Res. Commun.* **399,** 313–317 (2010).

46. Markevich, N. I., Hoek, J. B. & Kholodenko, B. N. Signaling switches and bistability arising from multisite phosphorylation in protein kinase cascades. *J. Cell Biol.* **164,** 353–359 (2004).

47. Kiyatkin, A. *et al.* Scaffolding Protein Grb2-associated Binder 1 Sustains Epidermal Growth Factor-induced Mitogenic and Survival Signaling by Multiple Positive Feedback Loops. *J. Biol. Chem.* **281,** 19925–19938 (2006).

48. Hat, B., Puszynski, K. & Lipniacki, T. Exploring mechanisms of oscillations in p53 and nuclear factor-κB systems. *IET Syst. Biol.* **3,** 342–355 (2009).

49. Cheong, R., Rhee, A., Wang, C. J., Nemenman, I. & Levchenko, A. Information Transduction Capacity of Noisy Biochemical Signaling Networks. *Science* **334,** 354–358 (2011).

50. Selimkhanov, J. *et al.* Accurate information transmission through dynamic biochemical signaling networks. *Science* **346,** 1370–1373 (2014).

51. Aoki, K. *et al.* Stochastic ERK Activation Induced by Noise and Cell-to-Cell Propagation Regulates Cell Density-Dependent Proliferation. *Mol. Cell* **52,** 529–540 (2013).

52. Kempiak, S. J., Yip, S.-C., Backer, J. M. & Segall, J. E. Local signaling by the EGF receptor. *J. Cell Biol.* **162,** 781–788 (2003).

53. Ehrenreiter, K. *et al.* Raf-1 regulates Rho signaling and cell migration. *J. Cell Biol.* **168,** 955–964 (2005).

54. Joslin, E. J., Opresko, L. K., Wells, A., Wiley, H. S. & Lauffenburger, D. A. EGF-receptor-mediated mammary epithelial cell migration is driven by sustained ERK signaling from autocrine stimulation. *J. Cell Sci.* **120,** 3688–3699 (2007).

55. Kholodenko, B. N., Hancock, J. F. & Kolch, W. Signalling ballet in space and time. *Nat. Rev. Mol. Cell Biol.* **11,** 414–426 (2010).

56. Mori, Y., Jilkine, A. & Edelstein-Keshet, L. Wave-Pinning and Cell Polarity from a Bistable Reaction-Diffusion System. *Biophys. J.* **94,** 3684–3697 (2008).

57. Hat, B., Kazmierczak, B. & Lipniacki, T. B Cell Activation Triggered by the Formation of the Small Receptor Cluster: A Computational Study. *PLoS Comput Biol* **7,** e1002197 (2011).

58. Nienałtowski, K., Włodarczyk, M., Lipniacki, T. & Komorowski, M. Clustering reveals limits of parameter identifiability in multi-parameter models of biochemical dynamics. *BMC Syst. Biol.* **9,** 1–9 (2015).

59. Camalet, S., Duke, T., Jülicher, F. & Prost, J. Auditory sensitivity provided by self-tuned critical oscillations of hair cells. *Proc. Natl. Acad. Sci. USA* **97,** 3183–3188 (2000).

60. Faeder, J. R., Blinov, M. L. & Hlavacek, W. S. In *Systems Biology* (ed. Maly, I. V.) 500, 113–167 (Humana Press, 2009).

61. Hindmarsh, A. C. *et al.* SUNDIALS: Suite of Nonlinear and Differential/Algebraic Equation Solvers. *ACM Trans Math Softw* **31,** 363–396 (2005).

62. Dhooge, A., Govaerts, W. & Kuznetsov, Y. A. MATCONT: A MATLAB Package for Numerical Bifurcation Analysis of ODEs. *ACM Trans Math Softw* **29,** 141–164 (2003).

63. Gillespie, D. T. Stochastic Simulation of Chemical Kinetics. *Annu. Rev. Phys. Chem.* **58,** 35–55 (2007).

64. Kazmierczak, B. & Lipniacki, T. Regulation of kinase activity by diffusion and feedback. *J. Theor. Biol.* **259,** 291–296 (2009).

65. Jaqaman, K. *et al.* Robust single-particle tracking in live-cell time-lapse sequences. *Nat Meth* **5,** 695–702 (2008).

Acknowledgements

Author Contributions

Conceived and designed the study: W.S.H., M.K., T.L. Built and analyzed the mathematical models: J.J.-B., M.K., P.K., E.K., T.L. Performed the experiments: J.G.A., B.S. Interpreted the results: J.G.A., W.S.H., M.K., T.L., M.P., B.S., Wrote the manuscript: J.G.A., W.S.H., M.K., T.L.

Additional Information

Relaxation oscillations and hierarchy of feedbacks in MAPK signaling

M. Kochańczyk, P. Kocieniewski, E. Kozłowska, J. Jaruszewicz-Błońska, B. Sparta, M. Pargett, J.G. Albeck, W.S. Hlavacek, and T. Lipniacki

Supporting Information

- **Supplementary Text S1.** Molecular basis of feedbacks relevant to the model.
- **Supplementary Text S2.** Non-dimensional model equations.
- **Supplementary Table S1.** Parameter values.
- **Supplementary Table S2.** Non-dimensional parameter values.
- **Supplementary Table S3.** Parameters of the stochastic model accounting for cell-to-cell variability in EGFR expression dynamics.
- **Supplementary Table S4**. Parameters of the spatial model accounting for extracellular, localized stochastic releases of EGF.
- **Supplementary Figure S1.** Two-dimensional bifurcation diagrams.
- **Supplementary Figure S2.** Effect of multi-site phosphorylation of SOS on oscillatory behavior.
- **Supplementary Figure S3.** Time profiles of active ERK and its two reporters, EKAR3 and ERKTR.
- **Supplementary Figure S4.** Phase space analysis of sensitivity of oscillatory behavior to negative feedback strengths.
- **Supplementary Figure S5.** Influence of extrinsic noise features on the oscillatory behavior.
- **Supplementary Figure S6.** Effect of intrinsic noise on system trajectories.
- **Supplementary Figure S7.** Effect of extrinsic noise on system trajectories.
- **Supplementary Figure S8.** Distributions of active ERK and its frequency spectrum.

*Note: Executable model implementations are provided in <u>separate</u> **Supplementary Data files 1–4**.*
*Animation of COMSOL output is provided as a <u>separate</u> **Video** file.*

Supplementary Text S1. Molecular basis of feedbacks relevant to the model.

Positive feedbacks. SOS1, and presumably SOS2 as well, is a target of positive feedback from RAS [1–3]. Somewhat like a classical effector of RAS, such as RAF, SOS1 contains a binding site that preferentially recognizes GTP-loaded (vs. GDP-loaded) RAS. This site, which has been called the allosteric site, is a pocket formed partly by the Ras exchange motif (REM) domain in SOS [1]. It is distinct from the RAS binding site in SOS1's RasGEF domain, which is involved in promoting GDP/GTP exchange [4]. When the allosteric site is occupied by GTP-loaded RAS, SOS1's GEF activity is enhanced relative to the case where the allosteric site is empty or occupied by GDP-loaded RAS [5]. This allosteric enhancement of SOS1's GEF activity represents a positive feedback because GTP-loaded (active) RAS is the product of SOS1's GEF activity. Active RAS and SOS can also participate in a positive feedback mediated by PI3K which promotes membrane recruitment of GAB1, a scaffold for SOS1 and RAS [6]. Another positive feedback arises from the interplay between the CRAF isoform and its substrate MEK. A physical interaction with MEK has been reported to allosterically enhance the kinase activity of CRAF [7]. Furthermore, MEK can increase RAF catalytic activity by contributing to phosphorylation of the N-terminal acidic region of CRAF enabling it to function as an activator in RAF dimers [8]. RAF dimerization may also represent a positive feedback mechanism when RAF dimers stabilize RAS dimers, higher-order oligomers, or RAS nanoclusters [9]. Importantly, all positive feedbacks are of short range: each involves only two proteins, which likely interact with each other at the plasma membrane. Of note, in the ERK/MEK module, a "hidden" positive feedback may arise in the double phosphorylation/dephosphorylation cycle due to distributive phosphorylation and saturability in the dephosphorylation reaction [10].

The vast majority of negative feedbacks in the MAPK/ERK cascade emanate from activated ERK [11], which may be important for ensuring that signals reach ERK before becoming inhibited. These negative feedback loops can be grouped into two categories depending on their position with respect to the positive feedback loops discussed above.

Negative feedback loops downstream of positive feedback loops. There are two well-characterized negative feedback loops that involve ERK-mediated inhibition of MEK and RAF. ERK-mediated phosphorylation of the MEK1 isoform of MEK leads to inhibition of the kinase activities of both MEK1 and MEK2, provided that MEK2 is in complex with MEK1 [18]. As far as RAF is concerned, all its isoforms are hyperphosphorylated by ERK, which has the effect of inhibiting RAF dimerization and disrupting its interaction with RAS, which is an important step in RAF inactivation [19,20].

Negative feedbacks encompassing positive feedbacks. There are two, largely overlapping, feedback loops that involve inhibitory phosphorylation of SOS, mediated either directly by ERK or indirectly by ERK-activated kinase RSK [12]. Phosphorylation of SOS in a C-terminal proline-rich region containing one or more binding sites for Src homology 3 (SH3) domains prevents SOS from interacting with SH3 domain-containing adaptor

proteins, such as GRB2, a binding partner of EGFR [13]. GRB2 also interacts with phosphorylated SHC1 [14], another binding partner of EGFR, and thus GRB2 associates with EGFR both directly and indirectly. Disruption of SOS–GRB2 interaction prevents recruitment of SOS to EGFR via direct and indirect interaction of GRB2 with EGFR. SOS1 contains at least four residues phosphorylated by ERK [15], whereas SOS2 contains only one [16]. This difference suggests that the two isoforms may have different sensitivities to ERK-mediated negative feedbacks. The specificities of ERK and RSK with respect to SOS overlap. Thus, negative feedback to SOS is mediated by a network motif of a feed-forward loop (FFL), a coherent type 3 FFL in the classification scheme of Mangan and Alon [17]. Based on their analysis [17], this FFL can be expected to generate a delay in relief of SOS inhibition upon deactivation of ERK.

Supplementary Text S1 References

1. Margarit SM, Sondermann H, Hall BE, Nagar B, Hoelz A, Pirruccello M, et al. Structural Evidence for Feedback Activation by Ras·GTP of the Ras-Specific Nucleotide Exchange Factor SOS. Cell. 2003;112: 685–695. doi:10.1016/S0092-8674(03)00149-1

2. Boykevisch S, Zhao C, Sondermann H, Philippidou P, Halegoua S, Kuriyan J, et al. Regulation of Ras Signaling Dynamics by Sos-Mediated Positive Feedback. Curr Biol. 2006;16: 2173–2179. doi:10.1016/j.cub.2006.09.033

3. Vo U, Vajpai N, Flavell L, Bobby R, Breeze AL, Embrey KJ, et al. Monitoring Ras Interactions with the Nucleotide Exchange Factor Son of Sevenless (Sos) Using Site-specific NMR Reporter Signals and Intrinsic Fluorescence. J Biol Chem. 2016;291: 1703–1718. doi:10.1074/jbc.M115.691238

4. Boriack-Sjodin PA, Margarit SM, Bar-Sagi D, Kuriyan J. The structural basis of the activation of Ras by Sos. Nature. 1998;394: 337–343. doi:10.1038/28548

5. Iversen L, Tu H-L, Lin W-C, Christensen SM, Abel SM, Iwig J, et al. Ras activation by SOS: Allosteric regulation by altered fluctuation dynamics. Science. 2014;345: 50–54. doi:10.1126/science.1250373

6. Kiyatkin A, Aksamitiene E, Markevich NI, Borisov NM, Hoek JB, Kholodenko BN. Scaffolding Protein Grb2-associated Binder 1 Sustains Epidermal Growth Factor-induced Mitogenic and Survival Signaling by Multiple Positive Feedback Loops. J Biol Chem. 2006;281: 19925–19938. doi:10.1074/jbc.M600482200

7. Leicht DT, Balan V, Zhu J, Kaplun A, Bronisz A, Rana A, et al. MEK-1 activates C-Raf through a Ras-independent mechanism. Biochim Biophys Acta - Mol Cell Res. 2013;1833: 976–986. doi:10.1016/j.bbamcr.2013.01.015

8. Hu J, Stites EC, Yu H, Germino EA, Meharena HS, Stork PJS, et al. Allosteric Activation of Functionally Asymmetric RAF Kinase Dimers. Cell. 2013;154: 1036–1046. doi:10.1016/j.cell.2013.07.046

9. Cho K, Kasai RS, Park J-H, Chigurupati S, Heidorn SJ, van der Hoeven D, et al. Raf Inhibitors Target Ras Spatiotemporal Dynamics. Curr Biol. 2012;22: 945–955. doi:10.1016/j.cub.2012.03.067

10. Markevich NI, Hoek JB, Kholodenko BN. Signaling switches and bistability arising from multisite phosphorylation in protein kinase cascades. J Cell Biol. 2004;164: 353–359. doi:10.1083/jcb.200308060

11. Anderson NG, Maller JL, Tonks NK, Sturgill TW. Requirement for integration of signals from two distinct phosphorylation pathways for activation of MAP kinase. Nature. 1990;343: 651–653. doi:10.1038/343651a0

12. Douville E, Downward J. EGF induced SOS phosphorylation in PC12 cells involves P90 RSK-2. Oncogene. 1997;15: 373–383.

Kochańczyk *et al.*: Relaxation oscillations and hierarchy of feedbacks in MAPK signaling – SUPPORTING INFORMATION

13. Wang Z, Moran MF. Requirement for the Adapter Protein GRB2 in EGF Receptor Endocytosis. Science. 1996;272: 1935–1938. doi:10.1126/science.272.5270.1935

14. Zheng Y, Zhang C, Croucher DR, Soliman MA, St-Denis N, Pasculescu A, et al. Temporal regulation of EGF signalling networks by the scaffold protein Shc1. Nature. 2013;499: 166–171.

15. Kamioka Y, Yasuda S, Fujita Y, Aoki K, Matsuda M. Multiple Decisive Phosphorylation Sites for the Negative Feedback Regulation of SOS1 via ERK. J Biol Chem. 2010;285: 33540–33548. doi:10.1074/jbc.M110.135517

16. Corbalan-Garcia S, Yang SS, Degenhardt KR, Bar-Sagi D. Identification of the mitogen-activated protein kinase phosphorylation sites on human Sos1 that regulate interaction with Grb2. Mol Cell Biol. 1996;16: 5674–5682. doi:10.1128/MCB.16.10.5674

17. Mangan S, Alon U. Structure and function of the feed-forward loop network motif. Proc Natl Acad Sci USA. 2003;100: 11980–11985. doi:10.1073/pnas.2133841100

18. Catalanotti F, Reyes G, Jesenberger V, Galabova-Kovacs G, de Matos Simoes R, Carugo O, et al. A Mek1-Mek2 heterodimer determines the strength and duration of the Erk signal. Nat Struct Mol Biol. 2009;16: 294–303. doi:10.1038/nsmb.1564

19. Kubicek M, Pacher M, Abraham D, Podar K, Eulitz M, Baccarini M. Dephosphorylation of Ser-259 Regulates Raf-1 Membrane Association. J Biol Chem. 2002;277: 7913–7919. doi:10.1074/jbc.M108733200

20. Freeman AK, Ritt DA, Morrison DK. Effects of Raf Dimerization and Its Inhibition on Normal and Disease-Associated Raf Signaling. Mol Cell. 2013;49: 751–758. doi:10.1016/j.molcel.2012.12.018

21. Ciardiello F, McGeady ML, Kim N, Basolo F, Hynes N, Langton BC, et al. Transforming growth factor-alpha expression is enhanced in human mammary epithelial cells transformed by an activated c-Ha-ras protooncogene but not by the c-neu protooncogene, and overexpression of the transforming growth factor-alpha complementary DNA l. Cell Growth Differ. 1990;1: 407–420.

22. Beerli RR, Graus-Porta D, Woods-Cook K, Chen X, Yarden Y, Hynes NE. Neu differentiation factor activation of ErbB-3 and ErbB-4 is cell specific and displays a differential requirement for ErbB-2. Mol Cell Biol. 1995;15: 6496–6505.

Supplementary Text S2. Non-dimensional model equations

Model equations can be non-dimensionalized by expressing reaction rates in units in which dephosphorylation rate of inhibitory phosphosites in SOS, q, equals 1. There are two general types of equations in the model:

- *Association–dissociation processes*:

$$\frac{\mathrm{d}}{\mathrm{d}t}XY = b \times X \times Y - u \times XY$$

  where b is binding rate, u is unbinding rate, and multiplication is denoted by cross ($\times$). Let $\bar{\bar{X}}$ be a total number of X molecules per cell. We can convert amounts X, Y, XY to, respectively, $x = X/\bar{\bar{X}}$, $y = Y/\bar{\bar{X}}$, $xy = XY/\bar{\bar{X}}$ and rates b and u to, respectively, $\beta = b \times \bar{\bar{X}}/q$ and $v = u/q$. If the above equation for $(\mathrm{d}/\mathrm{d}t)XY$ is satisfied, then the following equation is satisfied as well:

$$\frac{\mathrm{d}}{\mathrm{d}t}xy = \beta \times x \times y - v \times xy$$

- *Activation–deactivation processes*:

$$\frac{\mathrm{d}}{\mathrm{d}t}S_{\mathrm{act}} = a \times R \times S_{\mathrm{inact}} - d \times S_{\mathrm{act}}$$

Let $\bar{\bar{R}}$ and $\bar{\bar{S}}$ be total numbers of R ("activator") and S molecules per cell, respectively. We convert molecule numbers $r = R/\bar{\bar{R}}$, $s_{\mathrm{act}} = S_{\mathrm{act}}/\bar{\bar{S}}$, $s_{\mathrm{inact}} = S_{\mathrm{inact}}/\bar{\bar{S}}$, and rates $\alpha = a \times \bar{\bar{R}}/q$, $\delta = d/q$ to obtain a non-dimensionalized equation:

$$\frac{\mathrm{d}}{\mathrm{d}t}s_{\mathrm{act}} = \alpha \times r \times s_{\mathrm{inact}} - \delta \times s_{\mathrm{act}}$$

Therefore, our chemical equations are converted into non-dimensional ones by dividing all reaction rate coefficients by q and by introducing new variables:

- $\mathrm{erk}_x = \mathrm{ERK}_x/\mathrm{ERK}_{\mathrm{tot}}$ where ERK_x stands for any ERK specie,

- $\mathrm{mek}_x = \mathrm{MEK}_x/\mathrm{MEK}_{\mathrm{tot}}$ where MEK_x stands for any MEK specie,

- $\mathrm{raf}_x = \mathrm{RAF}_x/\mathrm{RAF}_{\mathrm{tot}}$ where RAF_x stands for any RAF specie,

- $var = VAR/\mathrm{SOS}_{\mathrm{tot}}$ where VAR stands for any other variable (i.e., EGFR, RAS, SOS, RasGAP, and their phosphoforms and complexes); molecules represented by these variables can form complexes and therefore should be rescaled by a common factor, $\mathrm{SOS}_{\mathrm{tot}}$.

Supplementary Table S2 contains numerical values of rescaled molecule numbers and rate parameters.

Kochańczyk *et al.*: Relaxation oscillations and hierarchy of feedbacks in MAPK signaling – SUPPORTING INFORMATION

- $A{\cdot}B$ denotes the amount of complex of A and B (multiplication is written using $\times$).

- Parameters named $f_{A \mapsto B}$ denote the strength of a feedback from A to B.

Equations:

$$\frac{\mathrm{d}}{\mathrm{d}t}egfr_a = \alpha_1 \times EGF \times \big(egfr_{tot} - (egfr_a + egfr_i{\cdot}sos_u + egfr_a{\cdot}sos_u + egfr_i{\cdot}sos_u{\cdot}ras_{GTP}$$
$$+ egfr_i{\cdot}sos_u{\cdot}ras_{GDP} + egfr_a{\cdot}sos_u{\cdot}ras_{GTP} + egfr_a{\cdot}sos_u{\cdot}ras_{GDP})\big) - \delta_1 \times egfr_a$$
$$- \beta_1 \times egfr_a \times \big(sos_{tot} - (sos_p + sos_{pp} + sos_{ppp} + sos_{pppp} + egfr_i{\cdot}sos_u$$
$$+ egfr_a{\cdot}sos_u + egfr_i{\cdot}sos_u{\cdot}ras_{GDP} + egfr_i{\cdot}sos_u{\cdot}ras_{GTP} + egfr_a{\cdot}sos_u{\cdot}ras_{GDP}$$
$$+ egfr_a{\cdot}sos_u{\cdot}ras_{GTP})\big) + \upsilon_{1A} \times egfr_a{\cdot}sos_u$$

$$\frac{\mathrm{d}}{\mathrm{d}t}sos_p = -3 \times \rho_3 \times f_{ERK_{pp} \mapsto SOS1} \times erk_{pp} \times sos_p + 4 \times \rho_3 \times f_{ERK_{pp} \mapsto SOS1} \times erk_{pp} \times \big(sos_{tot}$$
$$- (sos_p + sos_{pp} + sos_{ppp} + sos_{pppp} + egfr_i{\cdot}sos_u + egfr_a{\cdot}sos_u + egfr_i{\cdot}sos_u{\cdot}ras_{GDP}$$
$$+ egfr_i{\cdot}sos_u{\cdot}ras_{GTP} + egfr_a{\cdot}sos_u{\cdot}ras_{GDP} + egfr_a{\cdot}sos_u{\cdot}ras_{GTP})\big) - sos_p + 2 \times sos_{pp}$$

$$\frac{\mathrm{d}}{\mathrm{d}t}sos_{pp} = 3 \times \rho_3 \times f_{ERK_{pp} \mapsto SOS1} \times erk_{pp} \times sos_p + 3 \times sos_{ppp} - 2 \times sos_{pp}$$
$$- 2 \times \rho_3 \times f_{ERK_{pp} \mapsto SOS1} \times erk_{pp} \times sos_{pp}$$

$$\frac{\mathrm{d}}{\mathrm{d}t}sos_{ppp} = 2 \times \rho_3 \times f_{ERK_{pp} \mapsto SOS1} \times erk_{pp} \times sos_{pp} + 4 \times sos_{pppp} - 3 \times sos_{ppp}$$
$$- \rho_3 \times f_{ERK_{pp} \mapsto SOS1} \times erk_{pp} \times sos_{ppp}$$

$$\frac{\mathrm{d}}{\mathrm{d}t}sos_{pppp} = \rho_3 \times f_{ERK_{pp} \mapsto SOS1} \times erk_{pp} \times sos_{ppp} - 4 \times sos_{pppp}$$

$$\frac{\mathrm{d}}{\mathrm{d}t}egfr_i{\cdot}sos_u = \upsilon_{2B} \times egfr_i{\cdot}sos_u{\cdot}ras_{GDP} - \alpha_1 \times EGF \times egfr_i{\cdot}sos_u - \upsilon_{1B} \times egfr_i{\cdot}sos_u$$
$$+ \delta_1 \times egfr_a{\cdot}sos_u - \beta_{2B} \times egfr_i{\cdot}sos_u \times \big(ras_{tot} - (ras_{GTP} + ras_{GTP}{\cdot}rasgap$$
$$+ ras_{GDP}{\cdot}rasfap + egfr_i{\cdot}sos_u{\cdot}ras_{GDP} + egfr_i{\cdot}sos_u{\cdot}ras_{GTP} + egfr_a{\cdot}sos_u{\cdot}ras_{GDP}$$
$$+ egfr_a{\cdot}sos_u{\cdot}ras_{GTP})\big) + \upsilon_{2A} \times egfr_i{\cdot}sos_u{\cdot}ras_{GTP} - \beta_{2A} \times egfr_i{\cdot}sos_u \times ras_{GTP}$$

$$\frac{\mathrm{d}}{\mathrm{d}t}egfr_a{\cdot}sos_u = \beta_1 \times egfr_a \times \big(sos_{tot} - (sos_p + sos_{pp} + sos_{ppp} + sos_{pppp}$$
$$+ egfr_i{\cdot}sos_u + egfr_a{\cdot}sos_u + egfr_i{\cdot}sos_u{\cdot}ras_{GDP}$$
$$+ egfr_i{\cdot}sos_u{\cdot}ras_{GTP} + egfr_a{\cdot}sos_u{\cdot}ras_{GDP} + egfr_a{\cdot}sos_u{\cdot}ras_{GTP})\big)$$
$$- \beta_{2B} \times egfr_a{\cdot}sos_u \times \big(ras_{tot} - (ras_{GTP} + ras_{GTP}{\cdot}rassgap + ras_{GDP}{\cdot}rasgap$$
$$+ egfr_i{\cdot}sos_u{\cdot}ras_{GDP} + egfr_i{\cdot}sos_u{\cdot}ras_{GTP} + egfr_a{\cdot}sos_u{\cdot}ras_{GDP}$$
$$+ egfr_a{\cdot}sos_u{\cdot}ras_{GTP})\big) - \upsilon_{1A} \times egfr_a{\cdot}sos_u + \upsilon_{2A} \times egfr_a{\cdot}sos_u{\cdot}ras_{GTP}$$
$$+ \upsilon_{2B} \times egfr_a{\cdot}sos_u{\cdot}ras_{GDP} + \alpha_1 \times EGF \times egfr_i{\cdot}sos_u$$
$$- \beta_{2A} \times egfr_a{\cdot}sos_u \times ras_{GTP} - \delta_1 \times egfr_a{\cdot}sos_u$$

$$
\begin{aligned}
\tfrac{\mathrm{d}}{\mathrm{d}t} ras_{\mathrm{GTP}} = {}& \kappa_{2B} \times egfr_i{\cdot}sos_u{\cdot}ras_{\mathrm{GDP}} \times \big(ras_{\mathrm{tot}} - (ras_{\mathrm{GTP}} + ras_{\mathrm{GTP}}{\cdot}rasgap + ras_{\mathrm{GDP}}{\cdot}rasgap \\
& + egfr_i{\cdot}sos_u{\cdot}ras_{\mathrm{GDP}} + egfr_i{\cdot}sos_u{\cdot}ras_{\mathrm{GTP}} + egfr_a{\cdot}sos_u{\cdot}ras_{\mathrm{GDP}} \\
& + egfr_a{\cdot}sos_u{\cdot}ras_{\mathrm{GTP}}) \big) + \upsilon_{2A} \times egfr_i{\cdot}sos_u{\cdot}ras_{\mathrm{GTP}} - \beta_{2A} \times egfr_a{\cdot}sos_u \times ras_{\mathrm{GTP}} \\
& + \kappa_{2B} \times egfr_a{\cdot}sos_u{\cdot}ras_{\mathrm{GDP}} \times \big(ras_{\mathrm{tot}} - (ras_{\mathrm{GTP}} + ras_{\mathrm{GTP}}{\cdot}rasgap + ras_{\mathrm{GDP}}{\cdot}rasgap \\
& + egfr_i{\cdot}sos_u{\cdot}ras_{\mathrm{GDP}} + egfr_i{\cdot}sos_u{\cdot}ras_{\mathrm{GTP}} + egfr_a{\cdot}sos_u{\cdot}rasS_{\mathrm{GDP}} \\
& + egfr_a{\cdot}sos_u{\cdot}ras_{\mathrm{GTP}}) \big) + \kappa_{2A} \times egfr_i{\cdot}sos_u{\cdot}ras_{\mathrm{GTP}} \times \big(ras_{\mathrm{tot}} - (ras_{\mathrm{GTP}} \\
& + ras_{\mathrm{GTP}}{\cdot}rasgap + ras_{\mathrm{GDP}}{\cdot}rasgap + egfr_i{\cdot}sos_u{\cdot}ras_{\mathrm{GDP}} + egfr_i{\cdot}sos_u{\cdot}ras_{\mathrm{GTP}} \\
& + egfr_a{\cdot}sos_u{\cdot}ras_{\mathrm{GDP}} + egfr_a{\cdot}sos_u{\cdot}ras_{\mathrm{GTP}}) \big) + \upsilon_{2A} \times egfr_a{\cdot}sos_u{\cdot}ras_{\mathrm{GTP}} \\
& - \beta_{2A} \times egfr_i{\cdot}sos_u \times ras_{\mathrm{GTP}}) + \kappa_{2A} \times egfr_a{\cdot}sos_u{\cdot}ras_{\mathrm{GTP}} \times \big(ras_{\mathrm{tot}} - (ras_{\mathrm{GTP}} \\
& + ras_{\mathrm{GTP}}{\cdot}rasgap + ras_{\mathrm{GDP}}{\cdot}rasfap + egfr_i{\cdot}sos_u{\cdot}ras_{\mathrm{GDP}} + egfr_i{\cdot}sos_u{\cdot}ras_{\mathrm{GTP}} \\
& + egfr_a{\cdot}sos_u{\cdot}ras_{\mathrm{GDP}} + egfr_a{\cdot}sos_u{\cdot}ras_{\mathrm{GTP}}) \big) - \beta_3 \times \big(rasgap_{\mathrm{tot}} - (ras_{\mathrm{GTP}}{\cdot}rasgap \\
& + ras_{\mathrm{GDP}}{\cdot}rasgap) \big) \times ras_{\mathrm{GTP}}
\end{aligned}
$$

$$
\begin{aligned}
\tfrac{\mathrm{d}}{\mathrm{d}t} egfr_i{\cdot}sos_u{\cdot}ras_{\mathrm{GDP}} = {}& -\upsilon_{2B} \times egfr_i{\cdot}sos_u{\cdot}ras_{\mathrm{GDP}} + \delta_1 \times egfr_a{\cdot}sos_u{\cdot}ras_{\mathrm{GDP}} \\
& - \alpha_1 \times EGF \times egfr_i{\cdot}sos_u{\cdot}ras_{\mathrm{GDP}} + \beta_{2B} \times egfr_i{\cdot}sos_u \\
& \times \big(ras_{\mathrm{tot}} - (ras_{\mathrm{GTP}} + ras_{\mathrm{GTP}}{\cdot}rasgap + ras_{\mathrm{GDP}}{\cdot}rasgap + egfr_i{\cdot}sos_u{\cdot}ras_{\mathrm{GDP}} \\
& + egfr_i{\cdot}sos_u{\cdot}ras_{\mathrm{GTP}} + egfr_a{\cdot}sos_u{\cdot}ras_{\mathrm{GDP}} + egfr_a{\cdot}sos_u{\cdot}ras_{\mathrm{GTP}}) \big)
\end{aligned}
$$

$$
\begin{aligned}
\tfrac{\mathrm{d}}{\mathrm{d}t} egfr_i{\cdot}sos_u{\cdot}ras_{\mathrm{GTP}} = {}& \beta_{2A} \times egfr_i{\cdot}sos_u \times ras_{\mathrm{GTP}} - \alpha_1 \times EGF \times egfr_i{\cdot}sos_u{\cdot}ras_{\mathrm{GTP}} \\
& - \upsilon_{2A} \times egfr_i{\cdot}sos_u{\cdot}ras_{\mathrm{GTP}} + \delta_1 \times egfr_a{\cdot}sos_u{\cdot}ras_{\mathrm{GTP}}
\end{aligned}
$$

$$
\begin{aligned}
\tfrac{\mathrm{d}}{\mathrm{d}t} egfr_a{\cdot}sos_u{\cdot}ras_{\mathrm{GDP}} = {}& \beta_{2B} \times egfr_a{\cdot}sos_u \times \big(ras_{\mathrm{tot}} - (ras_{\mathrm{GTP}} + ras_{\mathrm{GTP}}{\cdot}rasgap + ras_{\mathrm{GDP}}{\cdot}rasgap \\
& + egfr_i{\cdot}sos_u{\cdot}ras_{\mathrm{GDP}} + egfr_i{\cdot}sos_u{\cdot}ras_{\mathrm{GTP}} + egfr_a{\cdot}sos_u{\cdot}ras_{\mathrm{GDP}} \\
& + egfr_a{\cdot}sos_u{\cdot}ras_{\mathrm{GTP}}) \big) - \delta_1 \times egfr_a{\cdot}sos_u{\cdot}ras_{\mathrm{GDP}} \\
& + \alpha_1 \times EGF \times egfr_i{\cdot}sos_u{\cdot}ras_{\mathrm{GDP}} - \upsilon_{2B} \times egfr_a{\cdot}sos_u{\cdot}ras_{\mathrm{GDP}}
\end{aligned}
$$

$$
\begin{aligned}
\tfrac{\mathrm{d}}{\mathrm{d}t} egfr_a{\cdot}sos_u{\cdot}ras_{\mathrm{GTP}} = {}& \alpha_1 \times EGF \times egfr_i{\cdot}sos_u{\cdot}ras_{\mathrm{GTP}} + \beta_{2A} \times egfr_a{\cdot}sos_u \times ras_{\mathrm{GTP}} \\
& - \upsilon_{2A} \times egfr_a{\cdot}sos_u{\cdot}ras_{\mathrm{GTP}} - \delta_1 \times egfr_a{\cdot}sos_u \times ras_{\mathrm{GTP}}
\end{aligned}
$$

$$
\tfrac{\mathrm{d}}{\mathrm{d}t} ras_{\mathrm{GDP}}{\cdot}rasgap = -\upsilon_3 \times ras_{\mathrm{GDP}}{\cdot}rasgap + \kappa_3 \times ras_{\mathrm{GTP}}{\cdot}rasgap
$$

$$
\tfrac{\mathrm{d}}{\mathrm{d}t} ras_{\mathrm{GTP}}{\cdot}rasgap = -\kappa_3 \times ras_{\mathrm{GTP}}{\cdot}rasgap + \beta_3 \times \big(rasgap_{\mathrm{tot}} - (ras_{\mathrm{GTP}}{\cdot}rasgap + ras_{\mathrm{GDP}}{\cdot}rasgap) \big) \times ras_{\mathrm{GTP}}
$$

Kochańczyk *et al.*: Relaxation oscillations and hierarchy of feedbacks in MAPK signaling – SUPPORTING INFORMATION

$$\frac{\mathrm{d}}{\mathrm{d}t}raf_{\mathrm{a}} = -\rho_6 \times f_{\mathrm{ERK_{pp} \mapsto RAF}} \times erk_{\mathrm{pp}} \times raf_{\mathrm{a}} - \delta_2 \times raf_{\mathrm{a}} + \alpha_2 \times ras_{\mathrm{GTP}} \times \left(raf_{\mathrm{tot}} - (raf_{\mathrm{a}} + raf_{\mathrm{p}})\right)$$

$$\frac{\mathrm{d}}{\mathrm{d}t}raf_{\mathrm{p}} = \rho_6 \times f_{\mathrm{ERK_{pp} \mapsto RAF}} \times erk_{\mathrm{pp}} \times raf_{\mathrm{a}} + \rho_6 \times f_{\mathrm{ERK_{pp} \mapsto RAF}} \times erk_{\mathrm{pp}} \times \left(raf_{\mathrm{tot}} - (raf_{\mathrm{a}} + raf_{\mathrm{p}})\right) - raf_{\mathrm{p}}$$

$$\begin{aligned}\frac{\mathrm{d}}{\mathrm{d}t}mek_{\mathrm{u,T292p}} = &-mek_{\mathrm{u,T292p}} + \rho_4 \times f_{\mathrm{ERK_{pp} \mapsto MEK1}} \times erk_{\mathrm{pp}} \times \big(mek_{\mathrm{tot}} - (mek_{\mathrm{u,T292p}} + mek_{\mathrm{p,T292u}} \\ &+mek_{\mathrm{p,T292p}} + mek_{\mathrm{pp,T292u}} + mek_{\mathrm{pp,T292p}})\big) + \sigma_1 \times mek_{\mathrm{p,T292p}} + \sigma_5 \times mek_{\mathrm{p,T292p}} \\ &-2 \times \rho_1 \times mek_{\mathrm{p,T292p}} \times raf_{\mathrm{a}}\end{aligned}$$

$$\begin{aligned}\frac{\mathrm{d}}{\mathrm{d}t}mek_{\mathrm{p,T292u}} = &\,mek_{\mathrm{p,T292p}} - \sigma_1 \times mek_{\mathrm{p,T292u}} + 2 \times q_1 \times mek_{\mathrm{pp,T292u}} - \sigma_1 \times mek_{\mathrm{p,T292u}} \times raf_{\mathrm{a}} \\ &+2 \times \rho_1 \times \big(mek_{\mathrm{tot}} - (mek_{\mathrm{u,T292p}} + mek_{\mathrm{p,T292u}} + mek_{\mathrm{p,T292p}} + mek_{\mathrm{pp,T292u}} \\ &+mek_{\mathrm{pp,T292p}})\big) \times raf_{\mathrm{a}} - \rho_4 \times f_{\mathrm{ERK_{pp} \mapsto MEK1}} \times erk_{\mathrm{pp}} \times mek_{\mathrm{p,T292u}}\end{aligned}$$

$$\begin{aligned}\frac{\mathrm{d}}{\mathrm{d}t}mek_{\mathrm{p,T292p}} = &\,\rho_4 \times f_{\mathrm{ERK_{pp} \mapsto MEK1}} \times erk_{\mathrm{pp}} \times mek_{\mathrm{p,T292u}} - \sigma_1 \times mek_{\mathrm{p,T292p}} - \rho_1 \times mek_{\mathrm{p,T292p}} \times raf_{\mathrm{a}} \\ &-mek_{\mathrm{p,T292p}} - \sigma_5 \times mek_{\mathrm{p,T292p}} + 2 \times \sigma_5 \times mek_{\mathrm{pp,T292p}} + 2 \times \sigma_1 \times mek_{\mathrm{pp,T292p}} \\ &+2 \times \rho_1 \times mek_{\mathrm{u,T292p}} \times raf_{\mathrm{a}}\end{aligned}$$

$$\begin{aligned}\frac{\mathrm{d}}{\mathrm{d}t}mek_{\mathrm{pp,T292u}} = &-\rho_4 \times f_{\mathrm{ERK_{pp} \mapsto MEK1}} \times erk_{\mathrm{pp}} \times mek_{\mathrm{pp,T292u}} - 2 \times \sigma_1 \times mek_{\mathrm{pp,T292u}} + \rho_1 \times mek_{\mathrm{p,T292u}} \times raf_{\mathrm{a}} \\ &+mek_{\mathrm{pp,T292p}}\end{aligned}$$

$$\begin{aligned}\frac{\mathrm{d}}{\mathrm{d}t}mek_{\mathrm{pp,T292p}} = &\,\rho_1 \times mek_{\mathrm{p,T292p}} \times raf_{\mathrm{a}} + \rho_4 \times f_{\mathrm{ERK_{pp} \mapsto MEK1}} \times erk_{\mathrm{pp}} \times mek_{\mathrm{pp,T292u}} - mek_{\mathrm{pp,T292p}} \\ &-2 \times \sigma_1 \times mek_{\mathrm{pp,T292p}} - 2 \times \sigma_5 \times mek_{\mathrm{pp,T292p}}\end{aligned}$$

$$\begin{aligned}\frac{\mathrm{d}}{\mathrm{d}t}erk_{\mathrm{p}} = &\,2 \times \sigma_2 \times erk_{\mathrm{pp}} + 2 \times \rho_2 \times mek_{\mathrm{pp,T292u}} \times \left(erk_{\mathrm{tot}} - (erk_{\mathrm{p}} + erk_{\mathrm{pp}})\right) - \sigma_2 \times erk_{\mathrm{p}} \\ &-\rho_2 \times mek_{\mathrm{pp,T292u}} \times erk_{\mathrm{p}} + 2 \times \rho_2 \times mek_{\mathrm{pp,T292p}} \times \left(erk_{\mathrm{tot}} - (erk_{\mathrm{p}} + erk_{\mathrm{pp}})\right) \\ &-\rho_2 \times mek_{\mathrm{pp,T292p}} \times erk_{\mathrm{p}}\end{aligned}$$

$$\frac{\mathrm{d}}{\mathrm{d}t}erk_{\mathrm{pp}} = \rho_2 \times mek_{\mathrm{pp,T292p}} \times erk_{\mathrm{p}} - 2 \times \sigma_2 \times erk_{\mathrm{pp}} + \rho_2 \times mek_{\mathrm{pp,T292u}} \times erk_{\mathrm{p}}$$

Kochańczyk *et al.*: Relaxation oscillations and hierarchy of feedbacks in MAPK signaling – SUPPORTING INFORMATION

Supplementary Tables

Supplementary Table S1. Parameter values.

Parameter	Description (see also Fig. 2 in the main text)
Concentrations (protein copy number per cell)	
$EGFR_{tot} = 3\times10^5$	Total number of EGFR molecules (as reported for MCF10A cells [21,22])
$RAS_{tot} = 6\times10^4$	Total number of RAS molecules
$SOS_{tot} = 10^5$	Total number of SOS molecules
$RasGAP_{tot} = 6\times10^3$	Total number of RasGAP molecules
$RAF_{tot} = 5\times10^5$	Total number of RAF molecules
$MEK_{tot} = 2\times10^5$	Total number of MEK molecules
$ERK_{tot} = 3\times10^6$	Total number of ERK molecules
Rate constant for fast processes (s^{-1})	
$k_{fast} = 100$	As a simplification, three (pseudo) first-order processes considered in the model are assumed to be fast.
Rate constants for activation processes $[(\text{molecules/cell})^{-1}\,\mathrm{s}^{-1}$ except $(\text{pg/ml})^{-1}\,\mathrm{s}^{-1}$ for $a_1]$	
$a_1 = 5\times10^{-5}$	EGF-mediated activation of EGFR
$a_2 = 10^{-7}$	Activation of RAF by RAS-GTP
$b_1 = 10^{-5}$	Binding of EGF-activated EGFR and dephosphorylated SOS
$p_1 = 10^{-7}$	Phosphorylation of MEK's activation sites by RAF
$p_2 = 3\times10^{-6}$	Phosphorylation of ERK's activation sites by MEK
Rate constants for deactivation processes (s^{-1})	
$d_1 = d = 0.01$	Deactivation of EGFR
$d_2 = d$	Deactivation of RAF (spontaneous)
$u_{1A} = d$	Dissociation of active EGFR–SOS complex

$q_1 = d$	Dephosphorylation of MEK's activation sites
$q_2 = d$	Dephosphorylation of ERK's activation sites
Rate constants for SOS association reactions $[(\text{molecules/cell})^{-1}\,\text{s}^{-1}]$ *and dissociation reactions* (s^{-1})	
$b_{2A} = 10^{-6}$	Association of SOS and RAS-GTP
$b_{2B} = 0.1 \times b_{2A}$	Association of SOS and RAS-GDP
$u_{1B} = k_{fast}$	Dissociation of inactive EGFR–SOS complex
$u_{2A} = u_{2B} = 1$	Dissociation of SOS–RAS-GTP complex and SOS–RAS-GDP complex
Rate constants associated with SOS-to-RAS positive feedback $[(\text{molecules/cell})^{-1}\,\text{s}^{-1}$ *except* s^{-1} *for* k_3 *and* $u_3]$	
$k_{2A} = 10^{-4}$	SOS's nucleotide-exchange activity when RAS-GTP is bound to its REM domain
$k_{2B} = 0.1 \times k_{2A}$	SOS's nucleotide-exchange activity when RAS-GDP is bound to its REM domain
$k_{2C} = 0$	SOS's nucleotide-exchange activity when no RAS is bound to its REM domain
$b_3 = 10^{-5}$	Association of RasGAP and RAS-GTP
$k_3 = k_{fast}$	RasGAP-facilitated RAS-GTP→RAS-GDP hydrolysis
$u_3 = 0.01$	Dissociation of RasGAP from RAS-GDP after hydrolysis of GTP
Rate constants associated with ERK-mediated negative feedbacks $[(\text{molecules/cell})^{-1}\,\text{s}^{-1}]$	
$p_3 = 3\times10^{-9}$	Phosphorylation of unbound SOS by active ERK
$p_4 = p_6 = p = 6\times10^{-10}$	Phosphorylation of MEK (T292 in MEK1) and RAF by active ERK
Rate constants for (spontaneous) dephosphorylation reactions (s^{-1})	
$q_3 = q_4 = q_6 = q = 3\times10^{-4}$	Dephosphorylation of inhibitory phosphosites in SOS, MEK (T292 in MEK1), RAF
$q_5 = k_{fast}$	Dephosphorylation of MEK's activation sites when T292 (in MEK1) is phosphorylated

ERK activity reporters – concentrations (protein copy number per cell)	
$EKAR3_{tot} = ERKTR_{tot} = 10^6$	Total number of EKAR3 and ERKTR molecules
ERK activity reporters – rate constants for activation reactions $[(\text{molecules/cell})^{-1}\,s^{-1}]$	
$a_{EKAR3} = 3 \times 10^{-9}$	EKAR3 activation rate by active ERK
$a_{ERKTR} = 10^{-9}$	ERKTR activation rate by active ERK
ERK activity reporters – rate constants for deactivation reactions (s^{-1})	
$d_{EKAR3} = 10^{-3}$	EKAR3 deactivation rate
$d_{ERKTR} = 2 \times 10^{-3}$	ERKTR deactivation rate

Supplementary Table S2. Non-dimensional parameter values.

Non-dimensional parameter	Description
Concentrations	
$egfr_{tot} = 3$	Total number of EGFR molecules
$ras_{tot} = 0.6$	Total number of RAS molecules
$sos_{tot} = 1$	Total number of SOS molecules
$rasgap_{tot} = 0.06$	Total number of RasGAP molecules
$raf_{tot} = 1$	Total number of RAF molecules
$mek_{tot} = 1$	Total number of MEK molecules
$erk_{tot} = 1$	Total number of ERK molecules
Rate constant for fast processes	
$\kappa_{fast} = \frac{1}{3} \times 10^6$	As a simplification, three (pseudo) first-order processes considered in the model are assumed to be fast.
Rate constants for activation processes	
$\alpha_1 = \frac{1}{6}$	EGF-mediated activation of EGFR
$\alpha_2 = \frac{1}{3} \times 10^2$	Activation of RAF by RAS-GTP
$\beta_1 = \frac{1}{3} \times 10^4$	Binding of EGF-activated EGFR and dephosphorylated SOS
$\rho_1 = 166\frac{2}{3}$	Phosphorylation of MEK's activation sites by RAF
$\rho_2 = 2 \times 10^3$	Phosphorylation of ERK's activation sites by MEK
Rate constants for deactivation processes	
$\delta_1 = \delta = \frac{1}{3} \times 10^2$	Deactivation of EGFR
$\delta_2 = \delta$	Deactivation of RAF (spontaneous)
$\upsilon_{1A} = \delta$	Dissociation of active EGFR–SOS complex

$\sigma_1 = \delta$	Dephosphorylation of MEK's activation sites
$\sigma_2 = \delta$	Dephosphorylation of ERK's activation sites
Rate constants for SOS association reactions	
$\beta_{2A} = \frac{1}{3} \times 10^3$	Association of SOS and RAS-GTP
$\beta_{2B} = 0.1 \times \beta_{2A}$	Association of SOS and RAS-GDP
$\upsilon_{1B} = \kappa_{\text{fast}}$	Dissociation of inactive EGFR–SOS complex
$\upsilon_{2A} = \upsilon_{2B} = \frac{1}{3} \times 10^4$	Dissociation of SOS–RAS-GTP complex and SOS–RAS-GDP complex
Rate constants associated with SOS-to-RAS positive feedback	
$\kappa_{2A} = \frac{1}{3} \times 10^5$	SOS's nucleotide-exchange activity when RAS-GTP is bound to its REM domain
$\kappa_{2B} = 0.1 \times \kappa_{2A}$	SOS's nucleotide-exchange activity when RAS-GDP is bound to its REM domain
$\kappa_{2C} = 0$	SOS's nucleotide-exchange activity when no RAS is bound to its REM domain
$\beta_3 = \frac{1}{3} \times 10^4$	Association of RasGAP and RAS-GTP
$\kappa_3 = \kappa_{\text{fast}}$	RasGAP-facilitated RAS-GTP→RAS-GDP hydrolysis
$\upsilon_3 = \frac{1}{3} \times 10^2$	Dissociation of RasGAP from RAS-GDP after hydrolysis of GTP
Rate constants associated with ERK-mediated negative feedbacks	
$\rho_3 = 30$	Phosphorylation of unbound SOS by active ERK
$\rho_4 = \rho_6 = \rho = 6$	Phosphorylation of MEK (T292 in MEK1) and RAF by active ERK
Rate constants for (spontaneous) dephosphorylation reactions	
1 (time scale)	Dephosphorylation of inhibitory phosphosites in SOS, MEK (T292 in MEK1), RAF
$\sigma_5 = \kappa_{\text{fast}}$	Dephosphorylation of MEK's activation sites when T292 (in MEK1) is phosphorylated

Supplementary Table S3. Parameters of the stochastic model accounting for cell-to-cell variability in EGFR expression dynamics. These parameters, together with parameters in Supplementary Table S1, were used to perform simulations shown in Fig. 8 in the main text.

Parameter	Description
$\mu_{EGFR} = -0.03125$, $\sigma_{EGFR} = 0.25$ $A_{burst} = 60\ s^{-1}$	Intensity of EGFR production within each burst in a cell is computed as $A_{burst} \times \alpha_{cell}$, where α_{cell} has the log-normal distribution $\ln N(\mu_{EGFR}, \sigma_{EGFR})$ with mean of 1.0 and variance of about 0.0645.
$\lambda_{interburst} = 1/6\ h^{-1}$	Waiting times between EGFR bursts are distributed exponentially with a mean waiting time of $\lambda_{interburst}^{-1}$.
$\lambda_{burst} = 1\ h^{-1}$	Durations of EGFR bursts are distributed exponentially with mean burst duration of λ_{burst}^{-1}.
$\tau_{EGFR} = 12\ h$	EGFR half-life.

Supplementary Table S4. Parameters of the spatial model accounting for extracellular, localized stochastic releases of EGF. These parameters, together with parameters in Supplementary Table S1, were used to perform simulations shown in Fig. 10 and Supplementary Video 1.

Parameter	Description
$V_{cell} = 2000 \ \mu m^3$ $R_{cell} \approx 7.8 \ \mu m$	Volume and radius of the (spherical) cell
$D_{mem} = 10^{-2} \ \mu m^2/s$	Diffusion coefficient of membrane proteins: EGFR, SOS, RAS, and RasGAP, and their complexes
$D_{cyt} = 10 \times D_{mem} = 10^{-1} \ \mu m^2/s$	Diffusion coefficient of cytosolic proteins: RAF, MEK, ERK
$R_{EGF\_shell\_in} = R_{cell} \approx 7.8 \ \mu m$ $R_{EGF\_shell\_out} = 10 \times R_{cell} \approx 78 \ \mu m$	Inner and outer radii: point sources of EGF randomly appear uniformly within a concentric shell around a cell
$\mu_{EGF} = -1.25$, $\sigma_{EGF} = 0.5$	EGF source intensity, A_{EGF}, is drawn from a log-normal distribution $\ln N(\mu_{EGF}, \sigma_{EGF})$ with mean 3.25×10^{-1} and variance 2.99×10^{-2}
$D_{EGF} = 10 \times D_{cyt} = 1 \ \mu m^2/s$	Diffusion coefficient of EGF
$\gamma_{EGF} = 8.33 \times 10^{-4} \ s^{-1}$	EGF degradation rate constant
$\lambda_{EGF\_source} = 8.33 \times 10^{-4} \ s^{-1}$	EGF-releasing point source durations are drawn from an exponential distribution with mean $\lambda_{EGF\_source}^{-1} = 20$ min
$f_{EGF\_sources} = 1.11 \times 10^{-3} \ s^{-1}$	EGF sources appear at random time points during the simulation, on average every 15 min

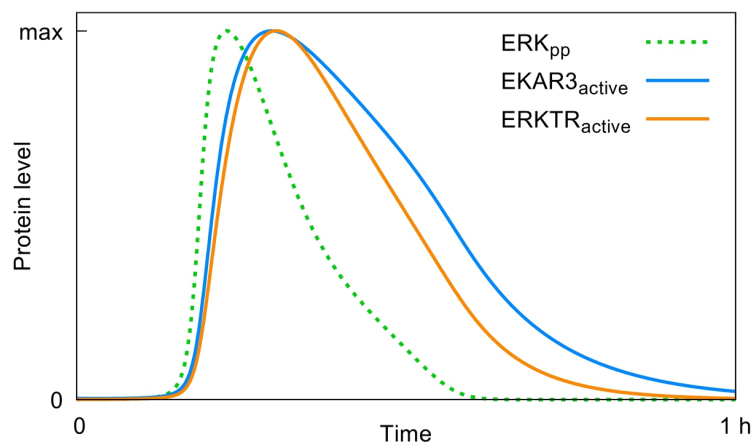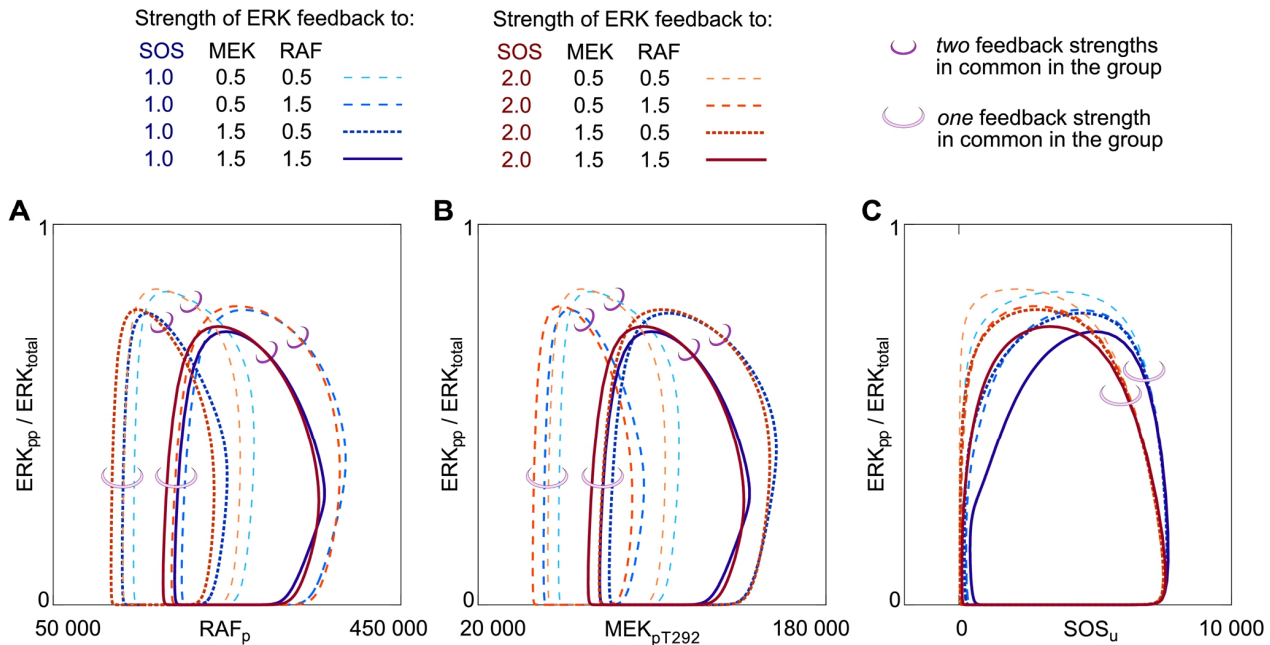## Supplementary Figures
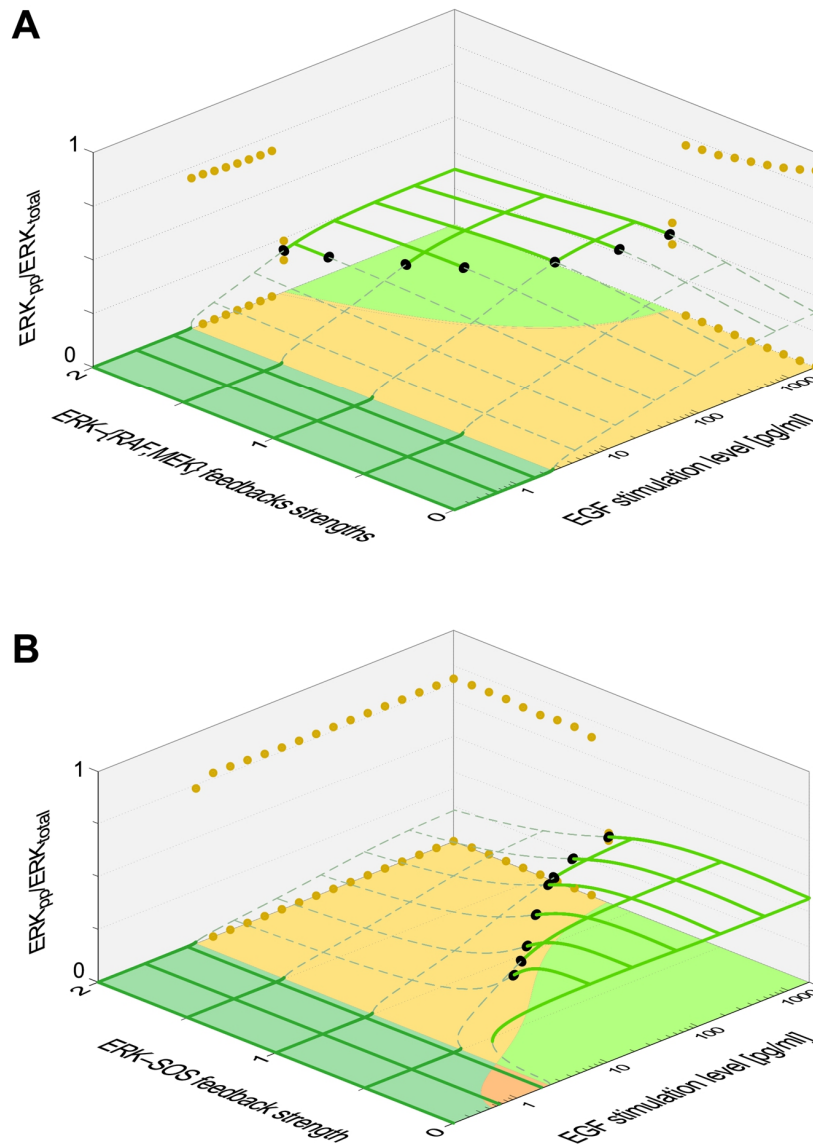
Supplementary Figure S1. Two-dimensional bifurcation diagrams. These diagrams complement Figs. 3A (**A**) and 3B (**B**) in the main text. In each panel, the *x*- and *y*-axes indicate the values of bifurcation parameters, as in Figs. 3A and 3B. The *z*-axis indicates the values of recurrent solutions (i.e., steady states and limit cycles) for activated ERK. Yellow dots mark the envelopes (i.e., the upper and lower bounds) of limit cycles. As in Fig. 5, black dots indicate supercritical Hopf bifurcation points.
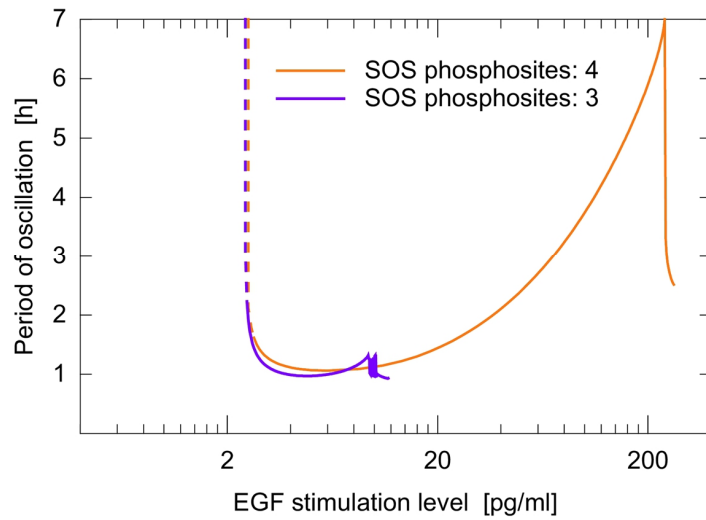
Kochańczyk *et al.*: Relaxation oscillations and hierarchy of feedbacks in MAPK signaling – SUPPORTING INFORMATION

Supplementary Figure S2. Effect of multi-site phosphorylation of SOS on oscillatory behavior. Ablation of a single ERK substrate in SOS decreases the range of EGF stimulation for which oscillations in ERK activity are observed. When SOS contains only one or two ERK substrates, the oscillatory regime vanishes.

Supplementary Figure S3. Time profiles of active ERK (ERK$_{pp}$) and its two reporters, EKAR3 and ERKTR. Trajectories were obtained for an EGF dose of 5 pg/ml. Activation and deactivation rates of both reporters are given in Table 1 in the main text.

17

Supplementary Figure S4. Phase space analysis of sensitivity of oscillatory behavior to negative feedback strengths. Each diagram illustrates eight limit cycles in a different planar projection of phase space. As indicated in the legend at top by line style, each trajectory is associated with a unique set of strengths for the ERK-to-SOS, ERK-to-MEK, and ERK-to-RAF feedbacks. Blue curves indicate trajectories corresponding to the default strength of negative feedback from ERK to SOS; red curves indicate trajectories corresponding to a 2-fold higher strength. (**A**) Trajectories in the ERK_{pp}/ERK_{total}–RAF_p projection plane. (**B**) Trajectories in the ERK_{pp}/ERK_{total}–MEK_{pT292} projection plane. (**C**) Trajectories in the ERK_{pp}/ERK_{total}–SOS_u projection plane. These parametric plots indicate that trajectories cluster together depending on their associated feedback strengths. Tight clusters (involving trajectories having two feedback strengths in common) are decorated with small rings. Looser clusters (involving trajectories having a single feedback strength in common) are decorated with large rings. Importantly, clustering depends on projection plane.
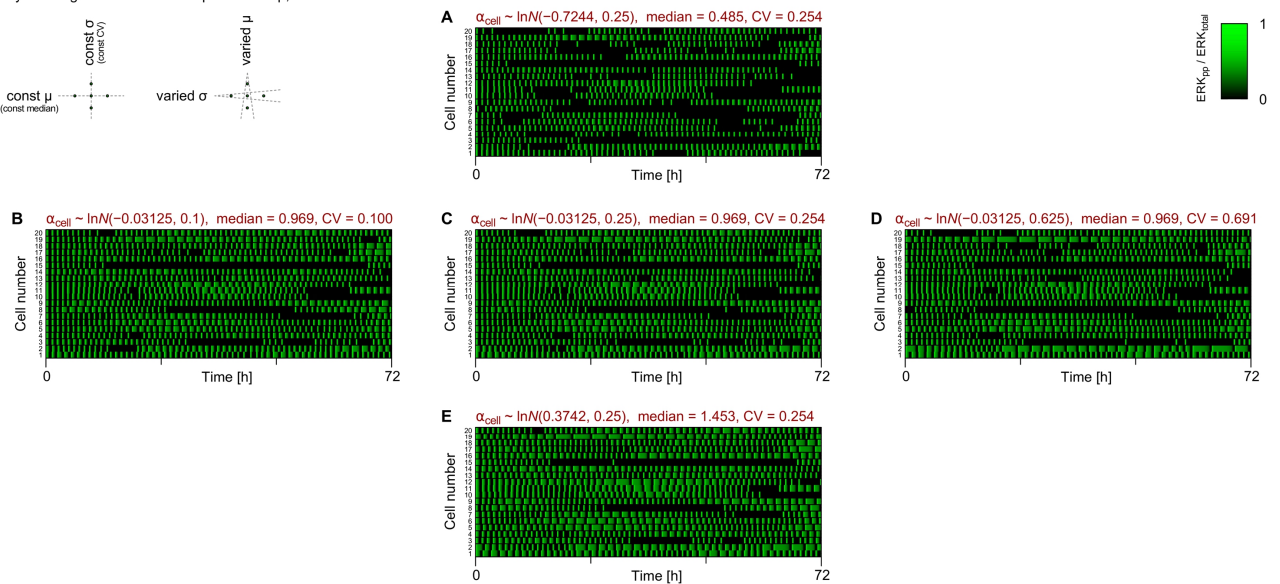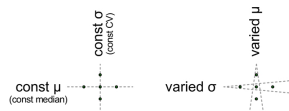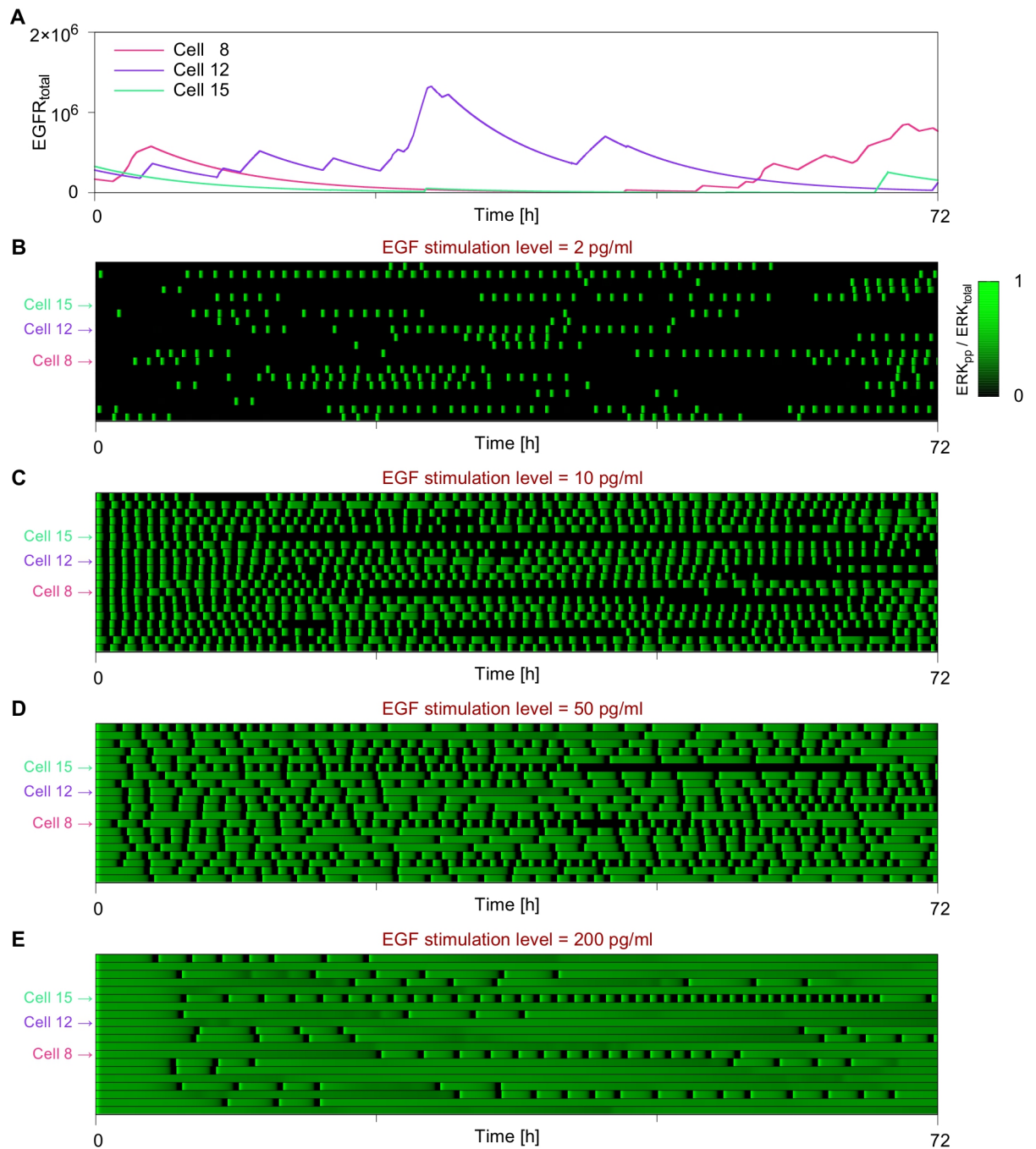
Supplementary Figure S5. Influence of extrinsic noise features on the oscillatory behavior. Each panel shows the results of 20 stochastic simulations of single-cell behavior for different values of two extrinsic noise parameters, which control the median and coefficient of variation (CV) of the EGFR surface expression burst size. Frequency of ERK activity pulses varies with the level of EGFR. In all simulations, oscillatory behavior is induced by an EGF dose of 10 pg/ml. Note that the central panel is for the same parameters as Fig. 8C (in the main text).
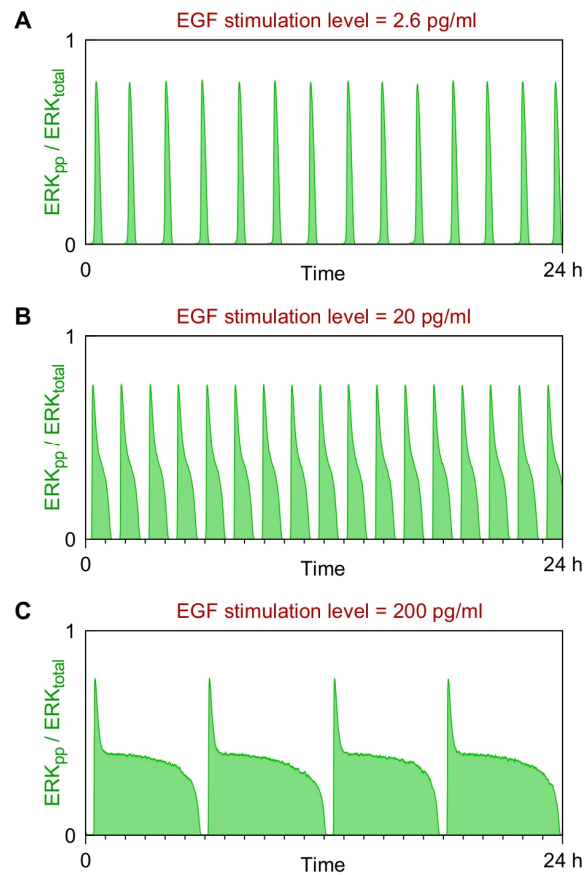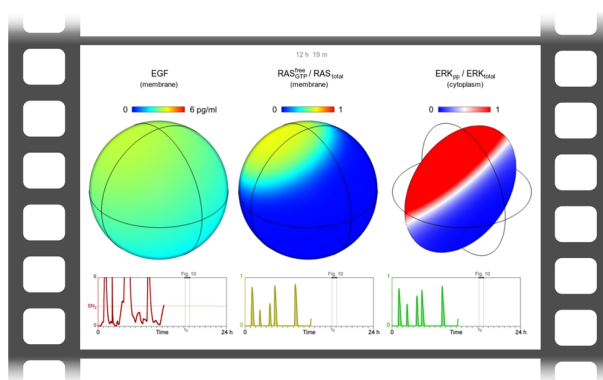
Supplementary Figure S6. Effect of intrinsic noise on system trajectories. At the assumed protein copy numbers per cell, the influence of intrinsic noise on system behavior is very weak; in panel C it can be visible as fine ripples. The simulations were performed using the Gillespie algorithm for default system parameters (Supplementary Table S1). This figure corresponds to Fig. 4 in the main text.

Supplementary Figure S7. Effect of extrinsic noise on system trajectories. The trajectories were obtained by piece-wise ODE integration. As can be seen by comparing this figure with Fig. 8 in the main text, the visible variability in cellular trajectories is predominantly due to the extrinsic noise.
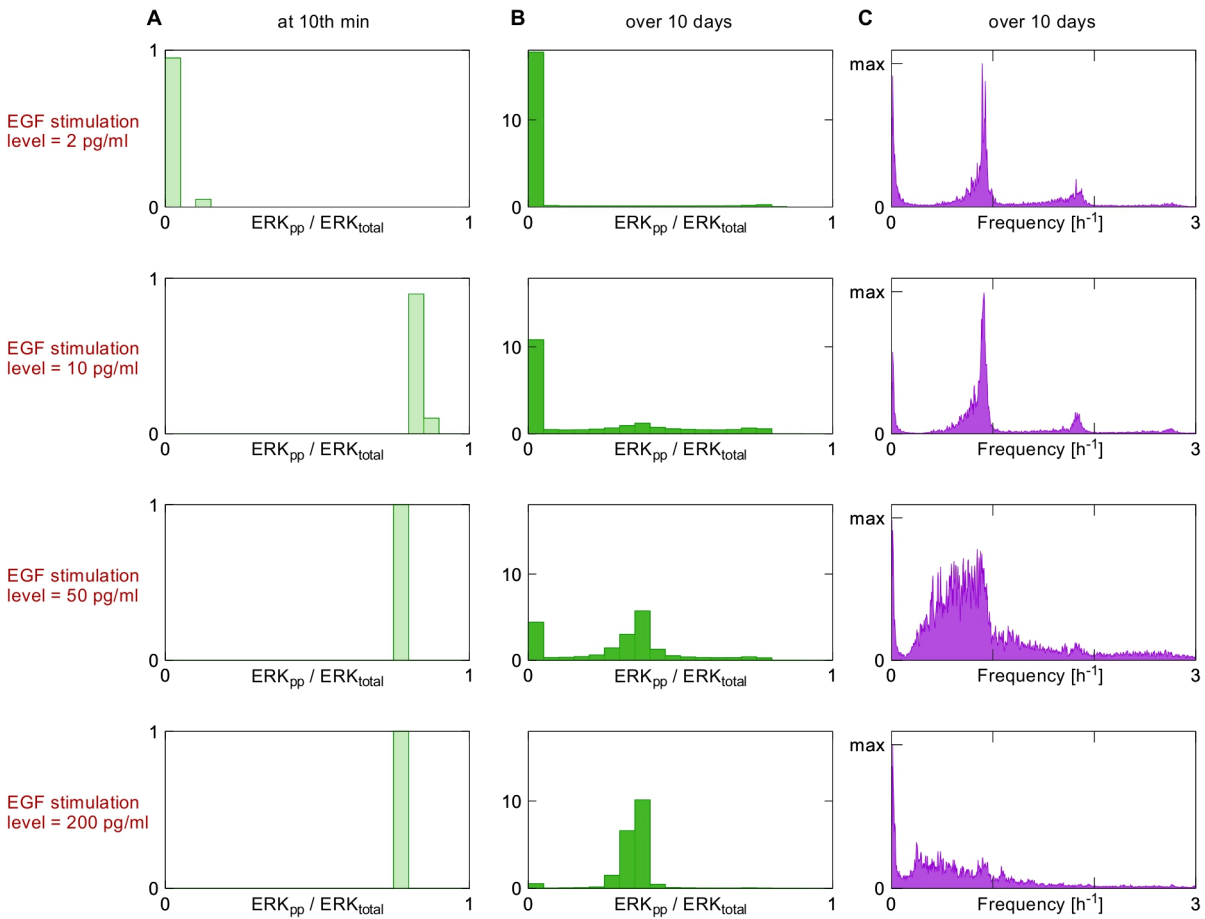
Supplementary Figure S8. Distributions of active ERK and its frequency spectrum. (**A**) Histograms of active ERK fractions at 10th min of EGF stimulation in simulations of 20 cells shown in panels of Fig. 8 in the main text. (**B**) Distributions of active ERK fractions over 10-day-long simulations of 20 cells. (**C**) Frequency spectrum of active ERK calculated from 10-day-long simulations of 20 cells.

Kochańczyk *et al.*: Relaxation oscillations and hierarchy of feedbacks in MAPK signaling – SUPPORTING INFORMATION

Video. Animation of COMSOL output. This video is provided as a separate MOV file. Activation of EGF receptors and RAS on the membrane, and activation of ERK in the cytoplasm (a cross-section is shown) in response to extracellular EGF bursts in the spatially extended, PDE-based model variant. Corresponding model source files are contained within Supplementary Dataset 4

Author contributions

In **Article A**,

Stochastic transitions in a bistable reaction system on the membrane,

published in the *Journal of the Royal Society Interface* **10**, 20130151 (2013),

Marek Kochańczyk:

- built the spatial stochastic simulator,

- set up and managed massively parallel simulations of the spatial stochastic kinetics,

- performed stochastic simulations in the well-mixed limit,

- analyzed and interpreted the results,

- wrote the manuscript and prepared all figures in the main text and in the supplementary information;

Joanna Jaruszewicz:

- performed finite-element method-based simulations of the reaction–diffusion system in COMSOL Multiphysics,

- contributed to numerical simulations of the stochastic spatially extended model;

Tomasz Lipniacki (corresponding author):

- conceived and supervised the study,

- helped to interpret the results,

- revised the manuscript.

Marek Kochańczyk   Joanna Jaruszewicz-Błońska   Tomasz Lipniacki

In **Article B**,

Effective reaction rates in diffusion-limited phosphorylation–dephosphorylation cycles,

published in *Physical Review E* **91**, 022702 (2015),

Paulina Szymańska (co-first author):

- derived analytical expressions for the steady-state fraction of the phosphorylated substrates in the zero-motility limit and in the well-mixed limit,

- performed stochastic simulations in the well-mixed limit in BioNetGen,

- managed massively parallel simulations of the spatial stochastic dynamics,

- wrote the manuscript and prepared figures 2, 5, 6, 7, 8;

Marek Kochańczyk (co-first author):

- built the spatial stochastic simulator,

- set up massively parallel simulations of the spatial stochastic dynamics,

- calculated spatial correlation functions,

- wrote the manuscript and prepared figures 1, 3, 4, 9, 10, 11;

Jacek Miękisz:

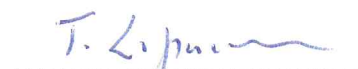- co-supervised the study,

- revised the manuscript;

Tomasz Lipniacki (corresponding author):

- conceived and co-supervised the study,

- analyzed and interpreted results,

- revised the manuscript.

Paulina Szymańska-Rożek

Marek Kochańczyk

Jacek Miękisz

Tomasz Lipniacki

In **Article C**,

Effective reaction rates for diffusion-limited reaction cycles,

published in *The Journal of Chemical Physics* **143**, 215102 (2015),

Paweł Nałęcz-Jawecki:

- derived analytical formulas for effective macroscopic reaction rates and their relation to the mean first-passage time (jointly with Paulina Szymańska),
- set up and managed massively parallel simulations of the spatial stochastic dynamics,
- analyzed simulation results,
- wrote the manuscript;

Paulina Szymańska:

- derived analytical formulas for effective macroscopic reaction rates and their relation to the mean first-passage time (jointly with Paweł Nałęcz-Jawecki),
- managed massively parallel simulations of the spatial stochastic chemical kinetics,
- wrote the manuscript;

Marek Kochańczyk:

- implemented the spatial stochastic simulator,
- helped to set up parallel simulations,
- analyzed simulation results,
- prepared all figures;

Jacek Miękisz:

- analyzed the results,
- co-supervised the study,
- edited the manuscript,

Tomasz Lipniacki (corresponding author):

- conceived and co-supervised the study,
- revised the manuscript.

....
Paweł Nałęcz-Jawecki   Paulina Szymańska-Rożek   Marek Kochańczyk

....
Jacek Miękisz   Tomasz Lipniacki

In **Article D**,

SPATKIN: a simulator for rule-based modeling of biomolecular site dynamics on surfaces,

accepted for publication in *Bioinformatics*,

Marek Kochańczyk (corresponding author):

- built, validated, benchmarked and optimized the software tool 'SPATKIN,'

- wrote the manuscript and software manual, and prepared all figures;

William S. Hlavacek:

- provided guidance on the rule-based modeling,

- proof-read software manual,

- revised the manuscript;

Tomasz Lipniacki:

- outlined expected software capabilities and supervised the project,

- revised the manuscript.

Marek Kochańczyk   William S. Hlavacek   Tomasz Lipniacki

In **Article E**,

Spontaneous NF-κB Activation by Autocrine TNFα Signaling:
A Computational Analysis,

published in *PLOS One* **8**, e78887 (2013),

Jakub Pękalski:

- build the model,
- wrote the numerical codes,
- performed stochastic simulations,
- analyzed the data;

Jakub Pękalski

Paweł J. Żuk:

- wrote the numerical codes;

Paweł J. Żuk

Marek Kochańczyk:

- performed bifurcation analysis in Matlab/MatCont,
- wrote the numerical codes;

Marek Kochańczyk

Michael Junkin:

- performed the experiments,
- analyzed the experimental data;

Signature provided on another page.

Michael Junkin

Ryan Kellogg:

- performed the experiments,
- analyzed the experimental data;

Signature provided on another page.

Ryan Kellogg

Savaş Tay

- designed the experiments;

Signature provided on another page.

Savaş Tay

Tomasz Lipniacki:

- conceived and designed the study,
- wrote the manuscript.

Tomasz Lipniacki

In Article E,

Spontaneous NF-κB Activation by Autocrine TNFα Signaling: A Computational Analysis,

published in *PLOS One* **8**, e78887 (2013),

Jakub Pękalski:

- build the model,
- wrote the numerical codes,
- performed stochastic simulations,
- analyzed the data;

Signature provided on another page.

Jakub Pękalski

Paweł J. Żuk:

- wrote the numerical codes;

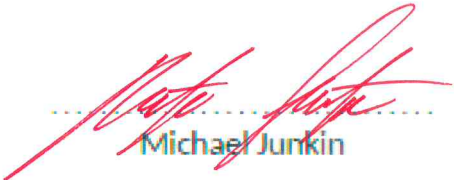Signature provided on another page.

Paweł J. Żuk

Marek Kochańczyk:

- performed bifurcation analysis in Matlab/MatCont,
- wrote the numerical codes;

Signature provided on another page.

Marek Kochańczyk

Michael Junkin:

- performed the experiments,
- analyzed the experimental data;

Michael Junkin

Ryan Kellogg:

- performed the experiments,
- analyzed the experimental data;

Signature provided on another page.

Ryan Kellogg

Savaş Tay

- designed the experiments;

Signature provided on another page.

Savaş Tay

Tomasz Lipniacki:

- conceived and designed the study,
- wrote the manuscript.

Signature provided on another page.

Tomasz Lipniacki

In **Article E**,

Spontaneous NF-κB Activation by Autocrine TNFα Signaling: A Computational Analysis,

published in *PLOS One* **8**, e78887 (2013),

Jakub Pękalski:

- build the model,
- wrote the numerical codes,
- **performed stochastic simulations,**
- analyzed the data;

Signature provided on another page.

Jakub Pękalski

Paweł J. Żuk:

- wrote the numerical codes;

Signature provided on another page.

Paweł J. Żuk

Marek Kochańczyk:

- performed bifurcation analysis in Matlab/MatCont,
- wrote the numerical codes;

Signature provided on another page.

Marek Kochańczyk

Michael Junkin:

- performed the experiments,
- analyzed the experimental data;

Signature provided on another page.

Michael Junkin

Ryan Kellogg:

- performed the experiments,
- **analyzed the experimental data;**

Ryan Kellogg

Savaş Tay:

- designed the experiments;

Signature provided on another page.

Savaş Tay

Tomasz Lipniacki:

- conceived and designed the study,
- wrote the manuscript.

Signature provided on another page.

Tomasz Lipniacki

In **Article E**,

Spontaneous NF-κB Activation by Autocrine TNFα Signaling: A Computational Analysis,

published in *PLOS One* **8**, e78887 (2013),

Jakub Pękalski:

- build the model,
- wrote the numerical codes,
- performed stochastic simulations,
- analyzed the data;

Paweł J. Żuk:

- wrote the numerical codes;

Marek Kochańczyk:

- performed bifurcation analysis in Matlab/MatCont,
- wrote the numerical codes;

Michael Junkin:

- performed the experiments,
- analyzed the experimental data;

Ryan Kellogg:

- performed the experiments,
- analyzed the experimental data;

Savaş Tay

- designed the experiments;

Tomasz Lipniacki:

- conceived and designed the study,
- wrote the manuscript.

Signature provided on another page.

Jakub Pękalski

Signature provided on another page.

Paweł J. Żuk

Signature provided on another page.

Marek Kochańczyk

Signature provided on another page.

Michael Junkin

Signature provided on another page.

Ryan Kellogg

Savaş Tay

Signature provided on another page.

Tomasz Lipniacki

In **Article F**,

Feedbacks, bifurcations, and cell fate decision-making in the p53 system,

published in *PLOS Computational Biology* **12**, e1004787 (2016),

Beata Hat (co-first author):

- build and analyzed the computational model in Matlab,

- wrote the manuscript;

Marek Kochańczyk (co-first author):

- performed bifurcation analysis in Matlab/Matcont,

- set up and managed massively parallel stochastic simulations,

- wrote the manuscript and prepared most of figures;

Marta N. Bogdał:

- analyzed the computational model in Matlab;

Tomasz Lipniacki (corresponding author):

- conceived and supervised the study,

- interpreted the results,

- revised the manuscript.

Beata Hat-Plewińska
Beata Hat-Plewińska

Marek Kochańczyk
Marek Kochańczyk

Marta N. Bogdał
Marta N. Bogdał

Tomasz Lipniacki
Tomasz Lipniacki

In **Article G**,

Relaxation oscillations and hierarchy of feedbacks in MAPK signaling,

published in *Scientific Reports* **6**, 38244 (2017),

<u>Marek Kochańczyk</u> (corresponding author):

- conceived and designed the study,
- built and analyzed models in BioNetGen and COMSOL,
- performed bifurcation analysis in Matlab/Matcont,
- interpreted the results,
- wrote the manuscript and prepared all figures;

Paweł Kocieniewski:

- built and analyzed the ODE-based model in BioNetGen;

Emilia Kozłowska:

- contributed to model analysis in Matlab/Matcont;

Joanna Jaruszewicz-Błońska:
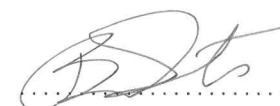
- analyzed the stochastic model in BioNetGen;

Breanne Sparta:
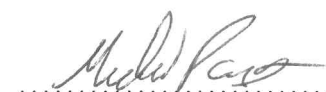
- performed the experiments,
- interpreted the experimental results;

Michael Pargett:
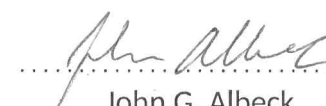
- interpreted the experimental results,
- edited the manuscript;

John G. Albeck:

- performed and designed the experiments,
- interpreted the results,
- revised the manuscript;

William S. Hlavacek:

- conceived and designed the study,
- interpreted the results,
- revised the manuscript;

Tomasz Lipniacki (corresponding author):

- conceived and designed the study,
- built and analyzed the models,
- interpreted the results,
- revised the manuscript.

Marek Kochańczyk

Paweł Kocieniewski

Signature provided
on another page.

Emilia Kozłowska

Joanna Jaruszewicz-Błońska

Breanne Sparta

Michael Pargett

John G. Albeck

Signature provided
on another page.

William S. Hlavacek

Tomasz Lipniacki

In **Article G**,

Relaxation oscillations and hierarchy of feedbacks in MAPK signaling,

published in *Scientific Reports* **6**, 38244 (2017),

<u>Marek Kochańczyk</u> (corresponding author):

- conceived and designed the study,
- built and analyzed models in BioNetGen and COMSOL,
- performed bifurcation analysis in Matlab/Matcont,
- interpreted the results,
- wrote the manuscript and prepared all figures;

Signature provided on another page.

Marek Kochańczyk

Paweł Kocieniewski:

- built and analyzed the ODE-based model in BioNetGen;

Signature provided on another page.

Paweł Kocieniewski

Emilia Kozłowska:

- contributed to model analysis in Matlab/Matcont;

Emilia Kozłowska

Joanna Jaruszewicz-Błońska:

- analyzed the stochastic model in BioNetGen;

Signature provided on another page.

Joanna Jaruszewicz-Błońska

Breanne Sparta:

- performed the experiments,
- interpreted the experimental results;

Signature provided on another page.

Breanne Sparta

Michael Pargett:

- interpreted the experimental results,
- edited the manuscript;

Signature provided on another page.

Michael Pargett

John G. Albeck:

- performed and designed the experiments,
- interpreted the results,
- revised the manuscript;

Signature provided on another page.

John G. Albeck

William S. Hlavacek:

- conceived and designed the study,
- interpreted the results,
- revised the manuscript;

Signature provided on another page.

William S. Hlavacek

Tomasz Lipniacki (corresponding author):

- conceived and designed the study,
- built and analyzed the models,
- interpreted the results,
- revised the manuscript.

Signature provided on another page.

Tomasz Lipniacki

In **Article G**,

Relaxation oscillations and hierarchy of feedbacks in MAPK signaling,

published in *Scientific Reports* **6**, 38244 (2017),

<u>Marek Kochańczyk</u> (corresponding author):

- conceived and designed the study,
- built and analyzed models in BioNetGen and COMSOL,
- performed bifurcation analysis in Matlab/Matcont,
- interpreted the results,
- wrote the manuscript and prepared all figures;

Paweł Kocieniewski:

- built and analyzed the ODE-based model in BioNetGen;

Emilia Kozłowska:

- contributed to model analysis in Matlab/Matcont;

Joanna Jaruszewicz-Błońska:

- analyzed the stochastic model in BioNetGen;

Breanne Sparta:

- performed the experiments,
- interpreted the experimental results;

Michael Pargett:

- interpreted the experimental results,
- edited the manuscript;

John G. Albeck:

- performed and designed the experiments,
- interpreted the results,
- revised the manuscript;

William S. Hlavacek:

- conceived and designed the study,
- interpreted the results,
- revised the manuscript;

Tomasz Lipniacki (corresponding author):

- conceived and designed the study,
- built and analyzed the models,
- interpreted the results,
- revised the manuscript.

Signature provided on another page.
Marek Kochańczyk

Signature provided on another page.
Paweł Kocieniewski

Signature provided on another page.
Emilia Kozłowska

Signature provided on another page.
Joanna Jaruszewicz-Błońska

Signature provided on another page.
Breanne Sparta

Signature provided on another page.
Michael Pargett

Signature provided on another page.
John G. Albeck

William S. Hlavacek

Signature provided on another page.
Tomasz Lipniacki